UNIVERSITY OF OKLAHOMA

GRADUATE COLLEGE

EVOLUTION OF THE TORNADO AND NEAR-TORNADO WIND FIELD OF THE SELDEN, KANSAS TORNADIC SUPERCELL ON 24 MAY 2021 USING A RAPID-SCAN, X-BAND, MOBILE, DOPPLER RADAR

A THESIS

SUBMITTED TO THE GRADUATE FACULTY

in partial fulfillment of the requirements for the

Degree of

MASTER OF SCIENCE

By

JACOB A. MARGRAF
Norman, Oklahoma
2023

EVOLUTION OF THE TORNADO AND NEAR-TORNADO WIND FIELD OF THE SELDEN, KANSAS TORNADIC SUPERCELL ON 24 MAY 2021 USING A RAPID-SCAN, X-BAND, MOBILE, DOPPLER RADAR

A THESIS APPROVED FOR THE
SCHOOL OF METEOROLOGY

BY THE COMMITTEE CONSISTING OF

Dr. Howard B. Bluestein, Chair

Dr. Jason C. Furtado

Dr. Jeffery C. Snyder

Dr. Louis J. Wicker

The views expressed in this thesis are those of the author and do not reflect the official policy or position of the United States Air Force, Department of Defense, or the U.S. Government.

Acknowledgements

First and foremost, I would like to thank the Air Force for allowing me to attend graduate school and experience the academic side of meteorology while I await pilot training. My opportunity to attend graduate school at one of the foremost institutions for meteorology and to have the chance to operate mobile radars was a once in a lifetime opportunity, and I thank the Air Force for allowing me to seize the moment and study weather for a bit longer before starting my career as a pilot.

I would also like to thank my parents for their support throughout my time at the University of Oklahoma and during my childhood years, without which this thesis would not have been possible. Ever since I first became enamored with the power of nature after a strong tornado passed through my childhood community and damaged my grandparents' property when I was 4 years old, my parents were there to foster my interest in weather. I remember standing outside to watch thunderstorms pass through many times and my parents always telling me when watches and warnings were issued; my excitement on these days made them all special occasions. My parents support also extended to my time at the University of Oklahoma. While I was navigating my accelerated program, phone calls with my parents would always offer a place for me to vent frustration and allow me to remain sane while work piled up to seemingly insurmountable levels at times. I could not have completed my graduate programs without my parents' unconditional support.

I would also like to thank my late Grandpa Baldosser for his role in fostering my interest in weather. Although my grandfather never pursued meteorology, he had an interest in it that he shared with me from a very young age. Whenever storms would move into the area, we would stand out on my grandfather's front porch and watch the storms pass. Perhaps owing to my grandfather's time as a volunteer EMT, we would pay close attention to any signs that storms were turning severe and report it to the Sheriff's office. I can remember one day when we watched a funnel cloud form from the base of one storm and watched the clouds rotate. Grandpa took notice and promptly called into the Sheriff's office as we watched the funnel cloud pass by. Besides watching storms on the front porch, my grandfather would also take a drive around the surrounding areas after storms came through to witness damage and take pictures, which he often shared with the family. The pictures of his property after being struck by the fateful tornado that occurred when I was 4 years old still hang on the wall in my grandparents' home to this day, including ones that show me walking around the debris left behind. These pictures were always some of my grandpa's favorites, especially ones of me pointing at an upturned shed that I was very upset about since it used to be the place where my grandparent's outdoor cats and kittens used to live.

I also extend my thanks to my friend, Drew Shearer, would often stop by the office to talk, giving me the chance to take a break from my work. We would also have lunches together on the Observation Deck, often discussing severe thunderstorm chances and the odds that Oklahoma would see storms worth chasing. The lunches we had together and severe storms we discussed often helped to alleviate some of the stress that came with graduate life. Additionally, times I had hanging out on the weekends or chasing storms

with my friends Drew, Connor Bruce, Brad Lamkin, and Elizabeth Spicer made the transition to Oklahoma and graduate school much more enjoyable, for which I am very grateful.

I would also like to thank Howie Bluestein, David Schvartzman, Trey Greenwood, and Sam Emmerson for showing me how to operate RaXPol and process radar data. I am indebted to David, for both the code he provided and the numerous questions he answered, which made it possible for me to complete my project. Sam and Trey also helped greatly, showing me how to operate RaXPol, obtain raw data, and then process the data, saving me a large amount of time and frustration. Finally, Howie helped me get a feel for the less technical side of storm chasing, showing me how to pick deployment spots, be aware of the storm environment, and predict the most likely areas for storm development.

The work presented in this thesis is supported by National Science Foundation grants AGS-0821231 and AGS-1947146.

Table of Contents

Acknowledgments ..... **v**

List of Tables ..... **xi**

List of Figures ..... **xii**

Abstract ..... **xxv**

1 Introduction **1**

1.1 A Brief History of High-Resolution Radar Observations 2

1.2 Current Understanding of the Supercell Tornado Lifecycle 9

1.2.1 From Clear Air to Supercell – Requisites for Tornadogenesis 9

1.2.2 Tornado Maintenance and Decay – Supercell Cycling Behavior 15

1.2.3 Selected Tornadic Supercell Signatures and Phenomena 21

1.2.3.1 RFD Surges and Their Role Throughout Tornado Lifecycles 21

1.2.3.2 Multiple Vortex Tornadoes 25

1.2.3.3 Anticyclonic Vortices and Tornadoes in Cyclonic Supercells 28

1.2.3.4 Weak Reflectivity Band (WRB) 30

1.2.3.5 Descending Reflectivity Core (DRC) 32

1.2.3.6 Streamwise Vorticity Current (SVC) 34

1.3 Overview 35

2 Data and Methods **37**

2.1 Instrumentation Overview: The *RaXPol* Mobile Radar 37

2.2 Available Data and Data Control 41

2.2.1 Data Collection 41

2.2.2 Data Quality Control 43

2.3 Cross Section Synthesis and Averaging 44

2.3.1 Constructing Cross Sections 44

2.3.2 Averaging 48

2.4 Radar Analysis Procedures....48
2.5 Video and Photo Analysis Procedures....50

3 Selden Supercell and Tornado Overview....53
3.1 Synoptic Environment....53
3.2 Storm Evolution and the Selden Supercell....57
3.3 Selden Tornado Overview....61

4 The Selden, Kansas Tornado During D6 – Before the Data Gap....67
4.1 Track Behavior....67
4.2 Evolution of the Near-Vortex Wind Field and RFD on Radar....73
4.3 Cross Section Analysis....80
4.4 Photogrammetric Analysis....89
4.5 Descending Reflectivity Core....97

5 The Selden, Kansas Tornado During D6 – After the Data Gap....101
5.1 Track Behavior....101
5.2 Evolution of the Near-Vortex Wind Field and RFD on Radar....103
5.3 Multiple Vortex Transition....111
5.4 Cross Section Analysis....115
5.5 Descending Reflectivity Core....119
5.6 Streamwise Vorticity Current....122

6 The Selden, Kansas Tornado During D7....129
6.1 Track Behavior....129
6.2 Evolution of the Near-Vortex Wind Field and RFD on Radar....139
6.2.1 Evolution in Early D7 – First Cyclonic Track Loop....139
6.2.2 Evolution in Mid D7 – Retrogression and Second Cyclonic Track Loop....147
6.2.3 Evolution in Late D7 – Tornado Dissipation....154
6.3 Cross Section Analysis....157
6.3.1 Analysis During Segment 4 and Transition Back to Single Vortex....157
6.3.2 Analysis During Mid D7....163

6.3.3 Analysis During Late D7 166
6.4 'Rogue' Anticyclonic Vortex 170
6.5 Weak Reflectivity Band 173

7 The Companion Anticyclonic Tornado 178
7.1 Vortex Genesis 178
7.2 Track Behavior 183
7.3 Evolution of the Vortex and Near-Vortex Wind Field on Radar 190
7.4 Cross Section Analysis 199

8 Summary of the Selden Tornado, Conclusions, and Future Work 205

Bibliography 218

List of Tables

2.1 Selected RaXPol Specifications 39

2.2 Details for all RaXPol deployments on 24 May 2021. Distances are measured from nearest town or village. Asterisk indicates deployments not on the Selden storm. 42

List of Figures

1.1 Schematic views of a supercell thunderstorm. Left: A top-down view of a mature supercell thunderstorm near the surface from Lemon and Doswell (1979). Both the RFGF and forward flank boundary are marked with frontal symbols and flow is denoted with arrows. Regions of updraft are finely stippled, while regions of downdraft are coarsely stippled. Right: A view looking west at a mature supercell with primary visual features labeled. Adapted from Grazulis (2001). 11

1.2 Schematic view of supercell airflow as the storm reaches maturity. The T marks the location of a tornado. Blue fronts mark the positions of the RFGF and forward flank convergence zone while blue arrows indicate flow. Air parcels labeled A, B, and C all possess streamwise vorticity that is ingested by the supercell updraft. From Rotunno et al. (2017) and adapted from Klemp (1987). 12

1.3 Visualization of the idealized evolution of RFD vortex rings into vortex arches. The view is from the south, looking north at a supercell thunderstorm. The vortex lines labeled 1 – 4 represent either a single vortex line evolving in time or 4 different vortex lines at different points in their evolution. An environmental vortex line is also shown coming from the inflow to help show the difference between mid-level and low-level rotation. From Markowski et al. (2008). 14

1.4 Conceptual model for the occlusion of a tornado. The ‘T’ marks the position of the tornado. In the last panel of the figure, the ‘X’ marks the location of the decaying tornado, and the ‘M’ marks the location of the new mesocyclone. From Marquis et al. (2016). 17

1.5 Diagram containing a summary of the results in Adlerman and Droegemeier (2005) where supercell cycling behavior was modeled in environments with differing amounts of shear and curvature in the hodograph. The type of supercell cycling behavior is plotted versus hodograph shape (ordinate) and amount of shear (abscissa). 19

1.6 RaXPol reflectivity (dBZ) and velocity (m s^{-1}) from the 4° elevation at a) 2326:38 and b) 2327:18 UTC on 24 May 2021 near Selden, Kansas. Range rings are spaced at 2.5 km intervals. An example of a RFD momentum surge is circled as it moves to the east, south of an ongoing tornado. The surge has a distinct velocity and reflectivity signature. 22

1.7 Conceptual model from Kurdzo et al. (2015) showing the 'failed' occlusion process for the Moore 2013 tornado. As surges on different trajectories move by the tornado at different times, the tornado track is affected. In this case, the pattern of RFD surges resulted in looping behavior. 24

1.8 Conceptual diagram of the effects of increasing swirl ratio on tornadic flow. As swirl ratio increases, an internal downdraft develops in response to an intensifying downward directed perturbation pressure gradient force. Upon reaching the ground, the downdraft splits the vortex into multiple cells. From Rotunno (2013). 26

1.9 RaXPol imagery at 2° of the El Reno 2013 tornado at 2327:54 UTC on 31 May 2013. a) Reflectivity, b) Radial velocity, c) Spectrum Width, and d) Correlation Coefficient. Arrows point to secondary vortices within the parent tornado. From Bluestein et al. (2015). 27

1.10 RaXPol imagery at 2° of the El Reno 2013 tornado at 2332:19 UTC on 31 May 2013. a) Reflectivity, b) Differential Reflectivity, c) Correlation Coefficient, and d) Radial Velocity. Arrows point to the cyclonic and anticyclonic tornadoes, labeled 'C' and 'A'. The anticyclonic tornado formed along the trailing edge of the RFGF. From Bluestein et al. (2015). 29

1.11 RaXPol a) Reflectivity and b) Radial velocity at 1° elevation on 24 May 2011 at 2057:17 UTC. Red lines denote the WRB, the black dashed circle marks the part of the WRB observed visually by the radar crew that collected the data, small black circles mark the positions of small vortices along the trailing part of the WRB, and red arrows show the convergence pattern around the WRB. From Houser et al. (2016). 31

1.12 Example of an DRC adapted from Rasmussen et al. (2006). In this example, a core of reflectivity develops and descends from the supercell overhang, contacting the ground near the location of the tornado. 33

1.13 Example of the SVC from Orf et al. (2017). A concentrated area of streamwise vorticity develops near the surface position of the forward flank convergence zone, highlighted with yellow vortex lines. 35

2.1 The RaXPol radar, photographed by the author outside of the Advanced Radar Research Center. 38

2.2 Example of cross sections at 2319:13 UTC at 4° elevation. The white line is the azimuthal cross section, connecting the velocity maxima marked with white diamonds. The black line is the radial wind cross section. Red arrows point out the different centers, with the white circle denoting the geometric center. 47

2.3 Example analysis of a panel from the D6 tornado video. The scale object (railroad grain silos) and tornado are annotated with the information required to calculate lengths at the tornado location. The desired parameters, condensation funnel width and distance of the tornado from the grain silos, are marked in orange. 51

3.1 a) 500 hPa height (black lines, dam), temperature (red lines, °C) and winds (barbs and fill, kt) valid at 1800 UTC, near the time of convection initiation. The low and weak shortwave are marked. b) 700 hPa height (black lines, dam), temperature (red and blue lines, °C), dewpoint (green lines and fill, °C), and wind (barbs, kt) valid at 1800 UTC. c) Surface based CAPE (red lines, J kg^{-1}) and CIN (fill, J kg^{-1}) valid at 1800 UTC. d) 0 – 6 km bulk shear (contours, kt) and storm motion (barbs, kt) valid at 1800 UTC. Adapted from the Storm Prediction Center (SPC) event archive. 54

3.2 Surface observations at 1800 UTC, near the time of initiation. The first radar echoes are denoted by a black arrow. The surface low and weak stationary fronts (dashed black lines) along with the remnant outflow boundary (double black line) are marked. Adapted from the SPC surface map archive. 55

3.3 KDDC (Dodge City, Kansas) sounding from 0000 UTC on 25 May. This was the nearest sounding in time and space to the Selden storm that was within the favorable storm environment. Taken from the SPC event archive. 56

3.4 a) Surface observations valid at 2100 UTC, 2 hours before the start time of the Selden tornado. The Selden storm is marked with a black arrow and the remnant outflow is denoted (double black line). b) Surface based CAPE (red lines, J kg^{-1}) and CIN (fill, J kg^{-1}) valid at 200 UTC. c) 0 – 3 km storm relative helicity (lines, m^2 s^{-2}) and storm motion (barbs, kt) valid at 2300 UTC. Adapted from the SPC event archive and surface map archive. 58

3.5 RaXPol reflectivity and velocity during D3 showing a period in which the Selden storm underwent mergers with non-supercells approaching from the southwest (white arrows and numbers). The weak velocity couplet is marked in the first panel before it is disrupted by the collision of the first cell (black circles). Range ring spacing is 2.5 km. 59

3.6 RaXPol derived track of the Selden tornado at 4° elevation overlayed with the estimated damage swath based on the low correlation coefficient area associated with the tornado. Various pictures of the tornadoes are also included on the track. Photos courtesy of Howard Bluestein, Sam Emmerson, and Trey Greenwood. 62

3.7 Comparison of the RaxPol derived tracks at 4°, 8°, 12°, and 16°. The 4° and 16° elevation tracks are representative of lower and upper elevation scans, respectively. 64

3.8 RaXPol derived track (using objective geometric centers) for the cyclonic tornado at 4°. Track segments 1 – 8 are marked, identified by changes in tornado behavior. Red dots mark the locations for D6 and D7. 65

3.9 Timeline of track segments at all elevations. Different colors represent the various segments, with boxes of the same color representing segments with similar behavior. Segment 4 is also broken down into subsections to isolate the track loop, which is represented by the red boxes. 66

4.1 Track of the Selden tornado at the 4°(top) and 16° (bottom) elevation scans. Zoomed insets of the tracks prior to the D6 data gap are provided on the right, along with descriptions of the segment motion vectors. 68

4.2 Schematic showing the track for segments 1 and 2 at every 4° in elevation. The increasingly chaotic areas of track are circled in the 12° and 16° maps. Grids have 1 km spacing. 69

4.3 Interpolated plot of ΔVmax for the Selden tornado, measured from the wind maxima on either side of the vortex. The red box denotes the portion of the graph corresponding to track segments 1 and 2 while the red arrows highlight the nearly simultaneous or slight upward trend in vortex development and intensification during segments 1 and 2. 71

4.4 RaXPol imagery at the 4° elevation taken every 2 scans (40 s) during segment 1. In each radar panel, reflectivity is on the left and Doppler velocity on the right. Range ring spacing is 2.5 km. Black lines denote RFD surge fronts, which are also numbered. Black arrows also point to associated reflectivity appendages. Finally, red lines mark the approximate positions of the forward flank boundary and RFGF. 74

4.5 Timeseries at 4° of the ΔVmax for the Selden tornado. The portion of the series corresponding to segments 1 and 2 is boxed and a zoomed inset of the boxed portion is provided to the right of the figure with surge related bursts in ΔVmax circled. Gridlines in the inset are spaced 10 m s^{-1} apart. 75

4.6 RaXPol imagery at the 4° elevation taken every 3 scans (60 s) during segment 2. In each radar panel, reflectivity is on the left and Doppler velocity on the right. Range ring spacing is 2.5 km. Black lines denote RFD surge fronts, which are also numbered. Black arrows also point to associated reflectivity appendages. Finally, red lines mark the approximate positions of the forward flank boundary and RFGF. 79

4.7 Average cross section for the Selden tornado during segment 2 with error bars plotted. Error bars represent 1 standard deviation of the data. 81

4.8 Azimuthal Cross Sections through the Selden Tornado at 4° elevation for track segments 1 (top) and 2 (bottom). Pictures of the Selden tornado from each segment are also included. Photos courtesy of Trey Greenwood. 82

4.9 Picture of the Selden tornado at 2309:30 UTC, looking to the west southwest towards the town of Selden from the D6 RaXPol location.

The condensation funnel and debris cloud diameters were estimated with the use of the tall grain silos near the middle of the image. The edges of the debris cloud are marked. Photo courtesy of Trey Greenwood. 84

4.10 Comparison of the segment 2 cross section at 4° (top) and 16° (bottom). Example PPI maps of radial velocity are provided from the volume starting at 2309:43 UTC to further show the typical changes in the tornadic vortex with height. 86

4.11 Height comparison of all nine segment 1 cross sections. The 9 scan elevations are color coded in groups of three (lower group – blue, middle group – green, upper group – pink). Each group then has a solid profile, dashed profile, and dotted-dashed profile in increasing height. 87

4.12 Radial wind cross sections through the Selden tornado at the 4° elevation for segment 1 (top) and segment 2 (bottom). 1-D divergence is also included. 88

4.13 Top panel contains a timeseries of the tornado condensation funnel width at 250 m ARL (dark green) and 500 m ARL (green) and TVS width at the 4° scan elevation (bright green). Bottom panel contains a timeseries of tornado ΔV (red) and vorticity (blue). 90

4.14 Comparison of the video estimated and radar derived tornado tracks during D6. The bottom panel contains a rotated map showing that the track discrepancies are likely due to a systematic azimuth bias in the radar data resulting from an incorrect GPS heading. A yellow star marks the location of the grain silos, and the gray line denotes the line of sight from the D6 deployment location to the grain silos. 94

4.15 Volumes enclosing reflectivity values greater than or equal to 55 dBZ. The domain is centered on the tornado in each panel, and the view is from the northeast. All distances are in meters (m). For clarity, the DRC is circled and denoted with an arrow. 98

4.16 Reconstructed cross sections through the tornado at the same 4 scans as in Figure 4.15. Reflectivity is on the left and Doppler velocity on the right. Black arrows point to the DRC, while white arrows indicate the potentially related velocity disruption. 99

5.1 Track of the Selden tornado at the 4°(top) and 16° (bottom) elevation scans. Zoomed insets of the tracks leading up to and during segment 3 are provided on the right, along with descriptions of the segment motion vectors. 102

5.2 RaXPol imagery at the 16° elevation taken every 2 scans (40 s) during segment 3. In each radar panel, reflectivity is on the left and Doppler velocity on the right. Range ring spacing is 2.5 km. Black lines denote RFD surge fronts, which are also numbered. Black arrows also point to associated reflectivity appendages. Finally, a red dotted line marks the approximate position of the RFD front aloft. 104

5.3 RaXPol imagery at the 4° elevation taken every 2 scans (40 s) during segment 3. In each radar panel, reflectivity is on the left and Doppler velocity on the right. Range ring spacing is 2.5 km. Black lines denote RFD surge fronts, which are also numbered. Black arrows also point to associated reflectivity appendages. Finally, red lines mark the approximate positions of the forward flank and RFGF. 107

5.4 Schematic showing how a pulse in occlusion downdraft outflow could generate RFD surges. The location of the tornado is marked by a T, the occlusion downdraft outflow by a blue circle, the RFD flow by a blue arrow, and enhanced areas of convergence, or RFD surges, by red lines. 110

5.5 Radar analysis during segment 3 at the 4° elevation depicting the multiple vortex transition for the Selden tornado. Doppler velocity is on the left and correlation coefficient on the right. Range ring spacing is 2.5 km. Black arrows point to secondary vortex related features. 112

5.6 Video grabs of the Selden tornado at 2318:16 UTC (top) and 2318:26 (bottom), taken looking to the west southwest into the town of Selden from the D6 location. A white arrow denotes the first visible secondary vortex in the bottom image. Video courtesy of Trey Greenwood. 114

5.7 Azimuthal Cross Sections through the Selden Tornado at 4° elevation for track segments 1 (top) and 2 (bottom). Pictures of the Selden tornado from each segment are also included. Photo courtesy of Trey Greenwood. 116

5.8 Radial wind cross section through the Selden tornado at the 4° elevation for segment 3 (top) and 1-D divergence (bottom). 118

5.9 Volumes enclosing reflectivity values greater than or equal to 45 dBz. The domain is centered on the tornado in each panel, and the view is from the northeast. All distances are in meters (m). For clarity, the DRC is circled and denoted with an arrow. The dotted arrow and circle denote that the DRC is reaching the ground and has passed through the bottom of the domain. 120

5.10 Reconstructed cross sections through the tornado at the same 4 scans as in Figure 5.9. Reflectivity is on the left and Doppler velocity on the right. Black arrows point to the DRC, while a white arrow indicates the potentially related low-level velocity increase. 121

5.11 Comparison of raw (top) and interpolated (bottom) reconstructed reflectivity and velocity RHIs from 2319:09 UTC at an azimuth angle of 275°. 123

5.12 Reconstructed RHIs from 2319:09 UTC at azimuth 265°. The reconstructed velocity (top right), reconstructed reflectivity (bottom left), and calculated 1-dimensional horizontal vorticity (bottom right) are provided along with the corresponding 4° elevation PPI plot that shows where the RHI was reconstructed. Black circles denote the SVC feature. 124

5.13 Averaged reconstructed RHIs taken every 2° in azimuth for a 2 km arc along the forward flank boundary. The panels on the left show analysis for 2317:49 UTC, with averaged velocity (top) and averaged reflectivity (middle). The panels on the right show analysis for 2319:09 UTC, with averaged velocity (top) and averaged reflectivity (middle). Radar PPIs are provided on the bottom of the figure to show the wedge that is represented by the average RHIs. Black circles denote the approximate location of the strongest horizontal vorticity. 126

6.1 Track of the Selden tornado at the 4°(top) and 16° (bottom) elevation scans. Zoomed insets of the tracks leading up to and during D7 are provided, along with descriptions of the segment motion vectors. 130

6.2 Comparison of the first cyclonic track loop at 4° increments. The evolving area of the track which represents the track loop is circled in each diagram. Axes are measured from D7 RaXPol position (km). 131

6.3 Comparison of the second cyclonic track loop at 4° increments. The evolving area of the track which completes a transition to a track loop by the 16° level is circled in each diagram. Axes are measured from D7 RaXPol position (km). 136

6.4 Tilt analysis for the Selden tornado, highlighting features associated with height dependent movement during D7. Analysis is done from the 4° level to the 16° level. 137

6.5 RaXPol imagery at the 4° elevation taken every 2 scans (40 s) during segment 4. In each radar panel, reflectivity is on the left and Doppler velocity on the right. Range ring spacing is 2.5 km. Black lines denote RFD surge fronts, which are also numbered. Black arrows also point to associated reflectivity appendages. Red lines mark the approximate positions of the forward flank and RFGF. A black circle also marks the location of an anticyclonic vortex, which will be investigated in section 6.4. 140

6.6 Conceptual model adapted from Kurdzo et al. (2015) to show the impact of surges at the 4° elevation during segment 4. During segment 4, RFD surge 1 from Figure 6.5 corresponds to the red surge while RFD surge 3 matches to the blue surge. 144

6.7 RaXPol imagery at the 16° elevation taken every 2 scans (40 s) during segment 4. In each radar panel, reflectivity is on the left and Doppler velocity on the right. Range ring spacing is 2.5 km. Black lines denote RFD surge fronts, which are also numbered. Black arrows also point to associated reflectivity appendages. Red lines mark the approximate positions of the forward flank and RFGF. A black circle also marks the location of an anticyclonic vortex, which will be investigated in section 6.4. 145

6.8 RaXPol imagery at the 4° elevation taken every 3 scans (60 s) during segments 5 and 6. In each radar panel, reflectivity is on the left and Doppler velocity on the right. Range ring spacing is 2.5 km. Black lines denote RFD surge fronts, which are also numbered. Black arrows also

point to associated reflectivity appendages. Finally, red lines mark the approximate positions of the forward flank and RFGF. 148

6.9 RaXPol imagery at the 4° elevation taken every 3 scans (60 s) during segments 6 and 7. In each radar panel, reflectivity is on the left, Doppler velocity is in the center, and correlation coefficient is on the right. Range ring spacing is 2.5 km. Black lines denote RFD surge fronts, which are also numbered. Black arrows also point to associated reflectivity appendages. Reded lines mark the approximate positions of the forward flank and RFGF. In the correlation coefficient images, the white circles denoted the correlation coefficient minima and white arrows indicate direction of movement. 150

6.10 RaXPol imagery at the 16° elevation taken every 3 scans (60 s) during segments 5 and 6. In each radar panel, reflectivity is on the left and Doppler velocity on the right. Range ring spacing is 2.5 km. Black lines denote RFD surge fronts, which are also numbered. Black arrows also point to associated reflectivity appendages. Finally, red lines mark the approximate positions of the forward flank and RFGF. 152

6.11 Radar analysis of RaXPol data at 4° elevation during the 2 minutes leading up to dissipation of the Selden tornado. Range ring spacing is 2.5 km. The vortex signature is marked by a black circle. Once the vortex signature breaks down, a line marks the remnant enhanced shear zone. A black arrow also points to the WEH in the reflectivity field. 156

6.12 Azimuthal Cross Section through the Selden Tornado at 4° elevation for track segment 4. Photo courtesy of Howard Bluestein. 158

6.13 Photo of the tornado at 2327:22 UTC, mid-way through segment 4 at the end of the track loop. Photo is taken looking west from the D7 deployment location; the tornado is approximately 6 km away. Photo courtesy of Howard Bluestein. 159

6.14 Azimuthal Cross Sections through the Selden Tornado at 4° elevation for track segment 4 subsections. The first subsection (top) represents the loop portion of segment 4, the second subsection (bottom) represents the rapid northeasterly movement after the track loop. 160

6.15 Radial wind cross section through the Selden tornado at the 4° elevation for segment 4 (top) and 1-D divergence (bottom). 162

6.16 Azimuthal Cross Sections through the Selden Tornado at 6° elevation for track segments 5 (top) and 6 (bottom). A picture of the Selden tornado from segment 5 is also included. Photo courtesy of Howard Bluestein 164

6.17 Radial wind cross sections through the Selden tornado at the 4° elevation for segment 5 (top) and segment 6 (bottom). 1-D divergence is also included. 166

6.18 Azimuthal Cross Sections through the Selden Tornado at 4° elevation for track segments 7 (top) and 8 (bottom). 167

6.19 Radial wind cross sections through the Selden tornado at the 4° elevation for segment 7 (top) and segment 8 (bottom). 1-D divergence is also included. 169

6.20 Radar analysis at 8° showing the 'rogue' anticyclonic vortex during early D7. Panels are taken every other scan, or 40 s apart. Range ring spacing is 2.5 km. The black circles denote the 'rogue' anticyclonic vortex, and its movement is tracked on the reflectivity field. 171

6.21 Reflectivity and velocity timeseries lasting about 2.5 minutes from 2334:38 to 2336:58 UTC. Black arrows on the reflectivity plots denote the WRB, while black circles on the velocity field mark the pronounced convergence signature. Range ring spacing is 2.5 km. 174

7.1 Radar analysis at the 4° level during early D7 showing development of an incipient anticyclonic vortex on the southern flank of the RFD. Panels are every 2 scans (40 s) and range rings are spaced every 2.5 km. Red lines mark the positions of the RFGF and forward flank boundary. The instigating RFD surge is marked in black, and a black arrow denotes the surge core. Dotted black lines and arrows mark the dissipating surge. In the first panel, a black circle marks slightly enhanced anticyclonic vorticity likely due to RFD vortex ring tilting, while the black circle in the last panel denotes the incipient anticyclonic vortex. 181

7.2 Track of the Selden companion anticyclonic tornado at the 4°(top) and 16° (bottom) elevation scans. Descriptions of the segment track vectors are provided to the right. 184

7.3 Comparison of the first anticyclonic tornado track segment at 4° increments. The segment 1 track is shorter with height reflecting longer development times aloft and is somewhat more erratic with height. Grid is at 1 km intervals. 185

7.4 Comparison of the right turn between segments 3 and 4 at 4° increments. The right turn is persistent with height and generally sharp, occurring in 1 or 2 scans. Grid is at 1 km intervals. 189

7.5 RaXPol imagery at the 4° elevation taken every 2 scans (40 s) during segment 1. In each radar panel, reflectivity is on the left and Doppler velocity on the right. Range ring spacing is 1.0 km. Black circles denote the anticyclonic vortex. Red lines mark the approximate positions of RFGF near the vortex. 191

7.6 RaXPol imagery at the 4° elevation taken every 2 scans (40 s) during segment 2. In each radar panel, reflectivity is on the left and Doppler velocity on the right. Range ring spacing is 1.0 km. Black circles denote the anticyclonic vortex. Red lines mark the approximate positions of RFGF near the vortex. 192

7.7 Conceptual diagram comparing the anticyclonic tornado occlusion process to the more familiar cyclonic tornado occlusion process. Red lines represent the major near-tornado boundaries. A dotted area shaded light blue denotes the approximate location of the occlusion downdraft. Gray arrows show where momentum is surging because of the occlusion downdraft. There is a scale difference between the two diagrams. 194

7.8 Radar analysis at the 4° scan elevation depicting a possible RFD surge brushing by the north side of the anticyclonic tornado. Black circles denote the area of enhanced momentum, while arrows indicate direction of movement. A dotted circle and arrow mark weakening of the possible surge in the last panel. 197

7.9 RaXPol imagery at the 4° elevation taken every 2 scans (40 s) during segments 3 and 4. In each radar panel, reflectivity is on the left and

Doppler velocity on the right. Range ring spacing is 1.0 km. Black circles denote the anticyclonic vortex. Red lines mark the approximate positions of RFGF near the vortex. 199

7.10 Azimuthal Cross Sections through the Selden anticyclonic Tornado at 4° elevation for track segments 1 (top) and 2 (bottom). 200

7.11 Picture of the anticyclonic vortex looking straight up as it passed overhead of the radar. The vortex is roughly in the center of the image, with a small funnel cloud or protrusion visible in the center of the vortex. Photo courtesy of Sam Emmerson. 202

7.12 Azimuthal Cross Sections through the Selden anticyclonic Tornado at 4° elevation for track segments 3 (top) and 4 (bottom). 204

Abstract

On 24 May 2021, a supercell in Selden, KS produced tornadoes which were probed by RaXPol, the University of Oklahoma's rapid-scan, mobile, X-band, polarimetric Doppler radar. According to the National Weather Service, the primary tornado was on the ground for 30 minutes and attained a maximum width of 850 yards as a multiple vortex tornado. Throughout this time, the tornado produced EF-1 damage in and around Selden. RaXPol was deployed twice on this tornado; RaXPol moved once as the tornado was approaching. During the first deployment, data from shortly after tornadogenesis to right after a transition to multiple vortex phase were collected. After rapidly redeploying to a safer location, data were then recorded from the end of the tornado's multiple vortex phase through its dissipation. While the cyclonic tornado was ongoing during the second deployment, a strong anticyclonic vortex or marginal tornado at the southern end of the Rear Flank Gust Front (RFGF) passed directly over RaXPol. Along with a high-definition video taken of the cyclonic tornado from the first deployment location, the high-resolution data collected by RaXPol throughout the lifespan of both vortices provide a rare opportunity to correlate structural features of the cyclonic tornado, anticyclonic vortex, and cyclonically rotating parent supercell to changes in tornado movement and behavior. Using the data captured by RaXPol, a thorough analysis of the tornado pair and the parent supercell was completed and cross sections through both vortices were constructed through their respective Doppler velocity couplets roughly perpendicular to the radar beam.

Ultimately, the RaXPol data help to construct a detailed narrative of the Selden tornado pair.

RaXPol observed several important phenomena concerning the Selden tornado pair. Numerous significant shifts in the track of the primary cyclonic tornado were identified, and the tornado as well as its parent low-level mesocyclone were observed to occlude with time leading up to the tornado's dissipation. During analysis, various Rear Flank Downdraft momentum surges (RFD surges) were identified, and they were found to be of critical importance to the occlusion and track behavior of the Selden tornado. The transition of the Selden tornado into and out of a multiple vortex phase were also observed, and the initial transition of the tornado into its multiple vortex phase was found to be the result of a temporary inflow disruption associated with RFD surges. While the primary cyclonic tornado was ongoing, RaXPol observed two independent anticyclonic vortices with different behavior, including a 'rogue' anticyclonic vortex and the marginally tornadic anticyclonic member of the Selden tornado pair. The 'rogue' anticyclonic vortex appeared very near the Selden tornado for a brief time, and numerous ideas for its origin and nature are discussed. The marginally tornadic anticyclonic vortex was found to form when a potent RFD surge impinged on the southern end of the RFGF, and the vortex was observed to occlude in a similar manner as the primary Selden tornado leading up to its dissipation.

Chapter 1

Introduction

Tornadoes are perhaps the most enigmatic of meteorological events, displaying awe inspiring strength and power. Although tornadoes occur over a wide range of environments and in conjunction with storms of multiple scales, no subset of tornadoes has garnered as much attention as the supercell tornado. Often visually stunning, supercell tornadoes enrapture the imagination. However, it is the supercell tornado's propensity for destruction that has likely resulted in the plethora of research focused on them. Nearly all violent tornadoes (rated EF2+) occur with supercells, highlighting the importance of the supercell despite only one-fifth to one-quarter of supercells being tornadic (Trapp et al. 2005; Markowski and Richardson 2009). Illustrative examples of the destruction wrought by tornadic supercells include such storms as the Joplin 2011 supercell or Mayfield 2021 supercell. Although these events were devastating, they pale in comparison to a worst-case scenario. In their study of a hypothetical violent tornado occurring in Chicago, Wurman et al. (2007a) estimated that the tornado could kill thousands to tens of thousands of people and damage or destroy nearly 400,000 homes – a testament to the destruction a tornadic supercell can cause should it strike a major city.

Yet, despite their power, supercell tornadoes are not a fully understood phenomenon. The tornadogenesis problem has received the most attention from researchers and is likely the best understood portion of the supercell tornado lifecycle.

However, our understanding of tornado behavior during mature and decay phases continues to be limited. For example, supercell tornadoes have been observed to make sudden turns, deviating significantly from their initial tracks. In 2007, a large and violent tornado in Kansas made a sudden left turn during its mature phase, making direct impact to the town of Greensburg (Tanamachi et al. 2012). In 2013, the largest tornado ever recorded, the El Reno tornado, made a significant left turn resulting in the deaths of several chasers and researchers who were caught off-guard by the odd tornado motion (Bluestein et al. 2015). Deviant track motion is a common phenomenon amongst supercell tornadoes that continues to surprise both scientists and operational forecasters. Nixon and Allen (2021) found 102 cases in which tornadoes displayed deviant leftward motion from 2005 to 2019, and that in 25% of these cases the tornado travelled entirely out of the National Weather Service warning polygon. Witness to the lack of operational knowledge concerning tornado behavior post-genesis, the Nixon and Allen (2021) findings and potential for loss of life posed by the failure to anticipate deviant motion underscore the need to study tornadoes throughout their entire lifecycles.

1.1: A Brief History of High-Resolution Radar Observations

Perhaps the most revolutionary tool for advancing tornado research has been the mobile Doppler radar. Prior to the use of radars that could be deployed in proximity to tornadic supercells, meteorologists were limited by use of the fixed site WSR-88D radar. Although the WSR-88D has a relatively small beamwidth of 1°, it is meant to cover a wide area of hundreds of kilometers in each direction (Doviak and Zrnic 1993). As distance from the radar continues to increase, the beam spread will render many smaller scale features

unresolvable. For example, at 100 km range, the beam is approximately 1750 meters wide. Furthermore, the height of the radar beam above the ground will continue to increase with distance from the radar due to the Earth's curvature and atmospheric refraction, with a 0° elevation beam being roughly 500 meters above the ground at 100 km or over 2000 meters above the ground at 200 km (Doviak and Zrnic 1993). As a result, remote near-surface features are not observable from a WSR-88D. Finally, the WSR-88D can only rotate at 30° s^{-1} (Doviak and Zrnic 1993). This results in volume update times of 4 to 5 minutes on average. Because of these factors, it became necessary to deploy radars in the vicinity of supercells to observe tornadoes with appreciable resolution.

For the first time in 1987 and 1988, Bluestein and Unruh (1989) deployed a mobile radar on tornadic supercells in the Southern Plains. The radar used was a second-hand Los Alamos National Laboratory (LANL) bistatic, continuous wave, 3 cm (X-band) radar with a 5° beamwidth not originally designed for meteorological applications. To operate the radar, it was set on a stand and then pointed by hand at storms. Data were then received and recorded as audio signals. Despite the crudeness of this set up, approaching and receding velocities associated with supercell and tornado circulations were able to be detected. Following on the success of the proof of concept for the LANL radar, Bluestein et al. (1993) continued to deploy the system near tornadic supercells in the Southern Plains throughout 1990 and 1991. One tornado in Red Rock, Oklahoma, which was rated F-4, was observed with the LANL radar which detected F-5 wind speeds of 120 to 125 m s^{-1} and strong winds all the way through the decay phase of the tornado. These winds were found to greatly exceed the 'thermodynamic speed limit', in which all parcel CAPE is converted to kinetic energy in cyclostrophic balance. In addition, several wind maxima

were observed on either side of the tornado, perhaps the first observations of what may have been secondary vortices in a multiple vortex tornado.

After initial experience with the LANL radar, it became clear that a higher-resolution, computer-controlled radar system would be needed to continue advancing tornado observations. In response to this need, Bluestein et al. (1995) field tested the U-Mass W-Band radar in 1993 and 1994. The U-Mass W-band radar was a van mounted pulsed Doppler radar that had a narrow beam width of 0.7° and was able to achieve 30-meter range resolution, allowing for the identification of small-scale features in tornadic supercells and rapid deployments. Bluestein et al. (1995) were able to collect the highest resolution datasets of supercells available at the time, proving the practicality of using vehicle mounted radar systems to probe severe convection.

Following on recent successes with mobile radar systems, Wurman et al. (1997) tested the first truck mounted mobile radar, the Doppler on Wheels (DOW), in 1995 during the Verification on the Origins of Rotation in Tornadoes Experiment (VORTEX). The DOW was a 3 cm wavelength (X-band), pencil-beam, pulsed Doppler radar which was able to collect a high-resolution dataset of the mature and decay phases of a violent tornado near Dimmitt, Texas. In their analysis of this data, Wurman and Gill (2000) were able to identify several small-scale features of tornadoes. A defined weak echo region was found inside the tornado, called the Weak Echo Hole (WEH), which was surrounded by concentric rings of high reflectivity. Evidence for a strong central downdraft in the tornado core with a magnitude of 30 m s^{-1} was also found. In another VORTEX dataset collected by an airborne radar (ELECTRA), Dowell and Bluestein (2002) described the cycling behavior of a supercell in McLean, Texas in which they identified a surging Rear Flank

Downdraft (RFD) as the primary cause for cycling. When the RFD surged ahead of the tornado, rearward storm relative flow sometimes increased near the tornado, causing it to move westward away from the parent updraft and dissipate.

In 1999, a major outbreak of tornadoes occurred in Kansas and Oklahoma. One tornado, which tracked through Moore, Oklahoma, was a violent F-5. Both the U-Mass W-band and DOW collected data on this supercell. Bluestein and Pazmany (2000), using U-Mass data of an earlier tornado produced by the same supercell as the Moore tornado, noted spiral like bands of reflectivity around the tornado and identified small, wave-like perturbations in the edge of the tornado that were likely manifestations of secondary vortices. Using the DOW data of the Moore tornado, Burgess et al. (2002) found wind speeds near those reported from damage surveys. Later in the day, the DOW collected additional data of another violent tornado near Mulhall, Oklahoma. Wurman (2002) analyzed this data, finding the first concrete evidence of secondary vortices within a multiple vortex tornado. Secondary vortices were observed to possess total vorticity values of up to 8 s^{-1}, which are the highest values ever measured in tornadoes.

Throughout the early 2000's, mobile radar observations continued to yield exciting results. In their analysis of tornadoes near Attica, Kansas, Bluestein et al. (2007b) found that the highest velocities associated with tornadoes occurred outside of the visible condensation funnel and that velocities changed most rapidly within 25 meters of the ground. Additionally, horizontal rolls were noted in proximity to the tornado and a band of reflectivity was found wrapping around the hook echo, both of which were likely the manifestation of one or more RFD surges. RFD surges are discrete areas of higher momentum within the RFD outflow, accompanied by enhanced vorticity and convergence,

that can influence the tornado throughout its lifecycle (Finley and Lee 2004; Finley and Lee 2008; Lee et al. 2012; Skinner et al. 2014). Similar patterns within the RFD region of tornadic supercells were being noted repeatedly in mobile radar observations. Wurman et al. (2010) identified several RFD surges in their analysis of a tornado occurring near Orleans, Nebraska. Surge positions were found to not be conducive to tornado maintenance, separating the tornado from buoyant inflow.

In the mid 2000's, new technology was being developed for mobile weather radars. The Mobile Weather Radar, 2005 X-Band, Phased Array (MWR-05XP) was built using a second-hand military phased array antenna grid. Although the technology had been used in military applications for decades (phased array radars have been in use in Air Force fighter aircraft since the 1960's), the MWR-05XP marks the first time the technology was used for a mobile weather radar. Phased array antennas allow for the rapid collection of volumes without needing to mechanically move the antenna through electronic beam steering (Bluestein et al. 2010). Using this radar, French et al. (2014) found that tornadoes may not be entirely continuous with height and that dissipation occurred in an inside out manner following the tornado being displaced from the parent updraft by a momentum imbalance that may have been the result of RFD surges.

In 2009-2010, the second VORTEX experiment was conducted to further understanding of tornadogenesis and the tornado lifecycle. Numerous mobile radar systems participated, resulting in the documentation of several tornado cases including the well-studied Goshen County, Wyoming tornado. Kosiba et al. (2013) found that the Goshen tornado formed as a secondary RFD, or RFD surge, wrapped the low-level mesocyclone. Vorticity for the tornado came from both the Rear Flank Gust Front (RFGF) and forward

flank leading edge, and it was found that only modest vorticity generation at the RFGF was necessary for genesis. In another supercell in Dumas, Texas, Skinner et al. (2014) again found several RFD surges, noting that they are important for the evolution of the low-level mesocyclone. Tornadogenesis never occurred in the Dumas storm, likely the result of less buoyant air in RFD surges surrounding the low-level mesocyclone. Another feature, the Low Reflectivity Ribbon (LRR), was also observed repeatedly during VORTEX2 (e.g., Griffin et al. 2018 and Kosiba et al. 2013). The LRR is a narrow channel of low reflectivity that starts near the rear side of the supercell hook echo and heads into the storm, separating the Forward Flank Downdraft (FFD) from the RFD. It was also concluded that the LRR was likely a region of sparse, large hail (Griffin 2018). However, Kosiba et al. (2013) noted that inflow air for the tornado did not pass through the LRR and that the LRR did not affect tornado evolution.

Around the same time as the VORTEX2 project, dual polarization became practical for use in mobile radars. Polarimetric variables allow radars to detect differences in the size and shape of scatterers since both horizontally and vertically polarized radiation is transmitted. Differential reflectivity (Z_{DR}), or the difference between horizontal and vertical returns for reflectivity, can reveal the shape of scatterers in a volume since the particles will give higher returns in the channel that is more aligned with their larger dimension. Correlation coefficient (ρ_{HV}) can also be calculated between the horizontal and vertical returns, representing how homogeneous the scatterers are in a volume. One consistent feature that can be detected using these variables is the Tornadic Debris Signatures (TDS) first described by Zrnic and Ryzhkov (1999). The TDS is a region of low differential reflectivity (due to the lack of large, oblate drops and presence of debris) and

low correlation coefficient (due to the heterogeneity of the scatterers, which include rain drops, debris, and dirt). Bluestein et al. (2007a) later showed the validity of the idea that polarimetric radars could detect tornadoes remotely using the TDS. Additional polarimetric supercell signatures have also been defined. In their review of polarimetric data of supercells, Kumjian and Ryzhkov (2008) found several features, including Z_{DR} arcs and Z_{DR} and correlation coefficient mid-level rings and columns that resulted from precipitation size sorting at the leading edge of the forward flank and from updraft related melting layer perturbations respectively.

In 2011, the Rapid-Scan, X-band, Polarimetric (RaXPol) radar became operational. For the first time, RaXPol combined polarimetric capability with the ability to scan at rates of up to 180° s^{-1} with a 1° beamwidth (Pazmany et al. 2013). More details of the RaXPol system will be given in Chapter 2. One of the first tornadoes observed by RaXPol in the spring of 2011 was the El Reno 2011 tornado. In their analysis of the data, Houser et al. (2015) observed tornadogenesis to proceed in a non-descending pattern, with rotation developing first at low levels. It was also found that tornado dissipation proceeded nearly simultaneously at all heights within a 30 second period, but that this was sensitive to the shear criteria used to define the tornado. RFD surges were also noted to contribute to both genesis and decay. RaXPol data have also been used to study polarimetric signatures. Snyder et al. (2013) identified that the LRR also had a well-defined Z_{DR} depression in their review of supercell data.

Perhaps the most analyzed case documented by RaXPol is the massive and violent El Reno 2013 tornado (Bluestein et al. 2015). In their analysis of data collected early in the El Reno tornado's lifecycle, Bluestein et al. (2019) found that tornadogenesis proceeded

nearly simultaneously in an upward fashion. Bluestein et al. (2018) analyzed the tornado during its mature multiple vortex phase, finding that secondary vortices formed and dissipated in different areas of the tornado. Comprehensive damage surveys were also completed with the help of RaXPol data. Wakimoto et al. (2016) found a damage swath that could be associated with a secondary vortex for the first time. Radar data were also used to study the TDS (Wakimoto et al. 2015 and Wakimoto et al. 2016). Findings included that the WEH within the tornado is filled in by debris near the ground, a band of convergence within the tornado results from the centrifuging of large debris, a low correlation coefficient zone exists north of the tornado in the inflow where smaller debris and dust is being lofted, and a ridge of high ZDR wraps around the tornado to the south as large raindrops are advected around the hook echo. While RaXPol continues to collect valuable scientific data, phased array mobile radars with polarimetric capability are currently being developed as the next step in mobile radar technology. With their ability to complete large volumes in a rapid manner, these radars will likely advance our understanding of tornadic supercells in the coming years.

1.2: Current Understanding of the Supercell Tornado Lifecycle

1.2.1: From Clear Air to Supercell – Requisites for Tornadogenesis

The process of generating a tornado from a supercell can be visualized as a three-step sequence, with rotation first developing at mid-levels and then low-levels before needing to be concentrated near the ground for a tornado to develop. Supercells initially acquire rotation from the tilting of horizontal vorticity associated with environmental wind

shear (Davies-Jones 1984). When a storm updraft initiates and begins ingesting air in an environment with vertical wind shear, it tilts the horizontal vorticity into the vertical and stretches it. As a result, a pair of counterrotating circulations develop straddling the updraft at mid-levels. If the hodograph veers (turns clockwise) with height, then the environmental horizontal vorticity vector has a component aligned with the storm relative wind at low-levels and vorticity is streamwise. The storm updraft will become collocated with the cyclonic member of the circulation pair by advection of vorticity. The supercell updraft then begins to propagate right of the mean wind because of changing shear with height in the veering hodograph. Shear induces linear dynamic pressure forces when interacting with the supercell updraft, with high pressure occurring on the upshear side of the updraft and low pressure on the downshear side; because the hodograph veers with height, the shear vector is oriented with height such that high pressure is induced at low-levels and low pressure at upper-levels on the right flank of the updraft. As a result, there is an upward directed pressure gradient force on the right flank of the updraft that drives rightward propagation of the supercell (Klemp 1987). If the hodograph backs (turns counter-clockwise) with height, vorticity is anti-streamwise and a left-moving supercell develops. If the hodograph is straight, vorticity is instead mostly crosswise (perpendicular to storm relative inflow), and the updraft does not become collocated with either member of the circulation pair. In this scenario, the nonlinear dynamic pressure minimum associated with both the vorticity maximum and minimum drive upward vertical motion on opposite flanks of the updraft, and storm splitting occurs; subsequent off hodograph motion then generates streamwise or anti-streamwise vorticity for right and left moving storms and the shear mechanism described above becomes dominant in supercell propagation (Klemp 1987).

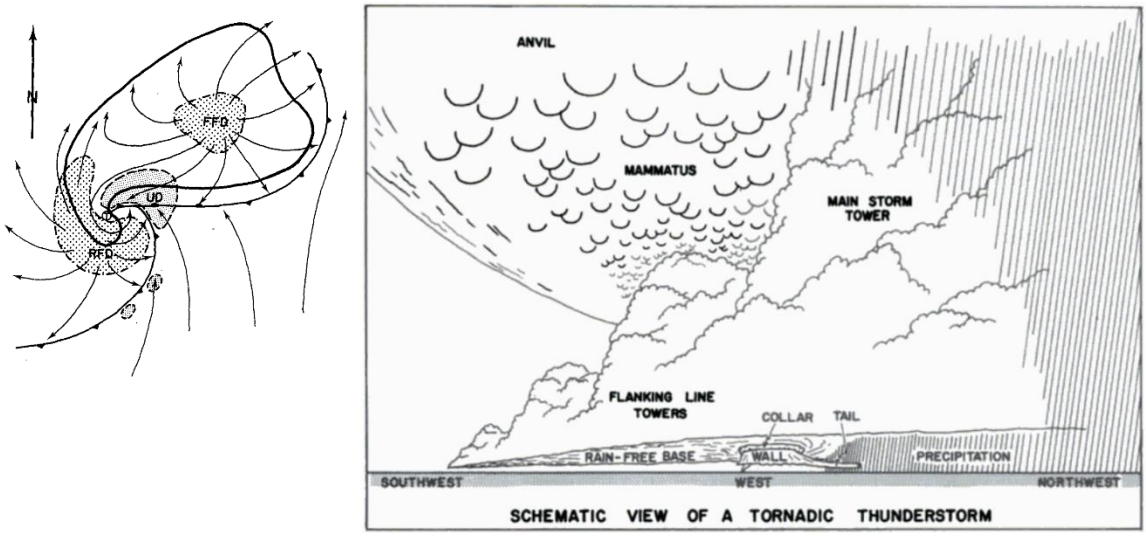

Figure 1.1: Schematic views of a supercell thunderstorm. Left: A top-down view of a mature supercell thunderstorm near the surface from Lemon and Doswell (1979). Both the RFGF and forward flank boundary are marked with frontal symbols and flow is denoted with arrows. Regions of updraft are finely stippled, while regions of downdraft are coarsely stippled. Right: A view looking west at a mature supercell with primary visual features labeled. Adapted from Grazulis (2001).

Winds in the northern hemisphere tend to increase in magnitude and veer with height, favoring streamwise environmental vorticity and the resulting right-moving, cyclonic supercells (Davies-Jones 1984; Klemp 1987). Schematics of a mature right-moving supercell are shown in Figure 1.1. A concentrated area of rotation, the mesocyclone, develops within the broader supercell updraft and two areas of downdraft develop on the front and rear flanks of the storm. The mesocyclone and tornado, if it develops, are located at the juncture of the forward flank precipitation area and rain-free cloud base at the RFGF where a wall cloud may become visible.

After the supercell acquires mid-level rotation, the incipient mesocyclone must strengthen, and rotation needs to develop at lower levels if a tornado is to occur. Numerical simulations of supercell thunderstorms have shown that this can be accomplished by the baroclinic generation of vorticity along the forward flank of the storm (Klemp and Rotunno

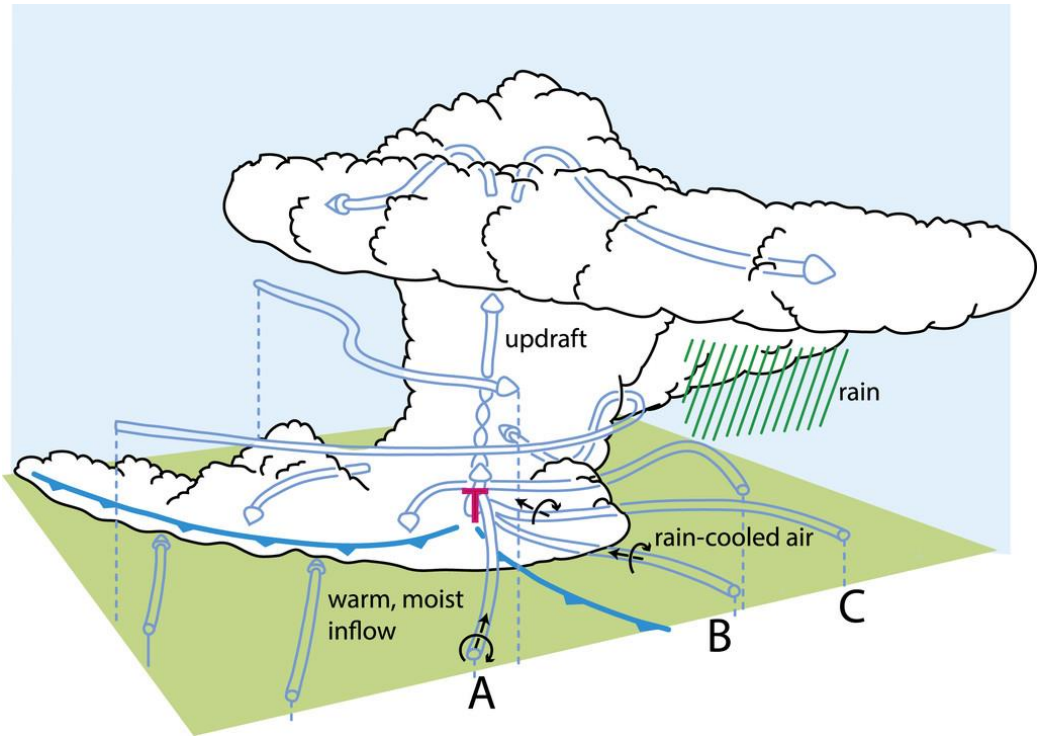

Figure 1.2: Schematic view of supercell airflow as the storm reaches maturity. The T marks the location of a tornado. Blue fronts mark the positions of the RFGF and forward flank convergence zone while blue arrows indicate flow. Air parcels labeled A, B, and C all possess streamwise vorticity that is ingested by the supercell updraft. From Rotunno et al. (2017) and adapted from Klemp (1987).

1983; Rotunno and Klemp 1985). Colder, negatively buoyant air within the forward flank downdraft region creates a buoyancy gradient with the neutrally stable ambient air, resulting in horizontal vorticity generation. Figure 1.2 shows how vorticity generated along the forward flank is ingested into the supercell. Since storm relative winds in the vicinity of the forward flank are moving towards the updraft as part of the storm inflow, the vorticity vector and wind are parallel, and vorticity is streamwise. The tilting and subsequent stretching of this baroclinically produced vorticity can result in significant enhancement of low-level rotation (Markowski and Richardson 2009). In their studies, both Klemp and Rotunno (1983) and Rotunno and Klemp (1985) found that the low-level

mesocyclone in supercells cannot develop until the forward flank becomes established and baroclinic vorticity generation begins.

Finally, for a tornado to form, vorticity must be somehow concentrated near the surface so it can be tilted and stretched into an intense vortex. When there is insufficient pre-existing vertical vorticity near the ground, a downdraft is required in proximity to the storm updraft for tornadogenesis to occur (Markowski and Richardson 2009). The supercell RFD fills this role. The RFD forms as ingested dry mid-level air is cooled by precipitation processes and loading as it is advected around the rotating updraft (Brandes 1981; Klemp et al. 1981). As the ingested air cools, it acquires negative buoyancy and descends, hitting the ground behind the storm updraft. The cool outflow continues to spread out and is advected cyclonically around the supercell updraft, forming a distinct boundary, the RFGF, where the RFD outflow meets with the ambient air. In addition to moving environmental vorticity closer to the surface and tilting it, Markowski et al. (2008) have shown that the baroclinically generated vortex lines associated with the RFD cold pool form vortex line arches as they are lifted at the RFGF by flanking line updrafts as shown in figure 1.3. These vortex arches create counterrotating vortices on either side of the RFD, enhancing the near-surface vorticity. One of these is the cyclonic tornado associated with the parent supercell, while the other is an anticyclonic vortex that has been observed to sometimes develop into an additional anticyclonic tornado (e.g., Bluestein et al. 2016).

The process by which tornadoes develop is still not completely understood. At a fundamental level, tornadogenesis requires that there be some sort of low-level convergence, an updraft, and a low-level vorticity source (Markowski and Richardson 2009). The RFGF and forward flank boundary provide near-surface vorticity and a zone of

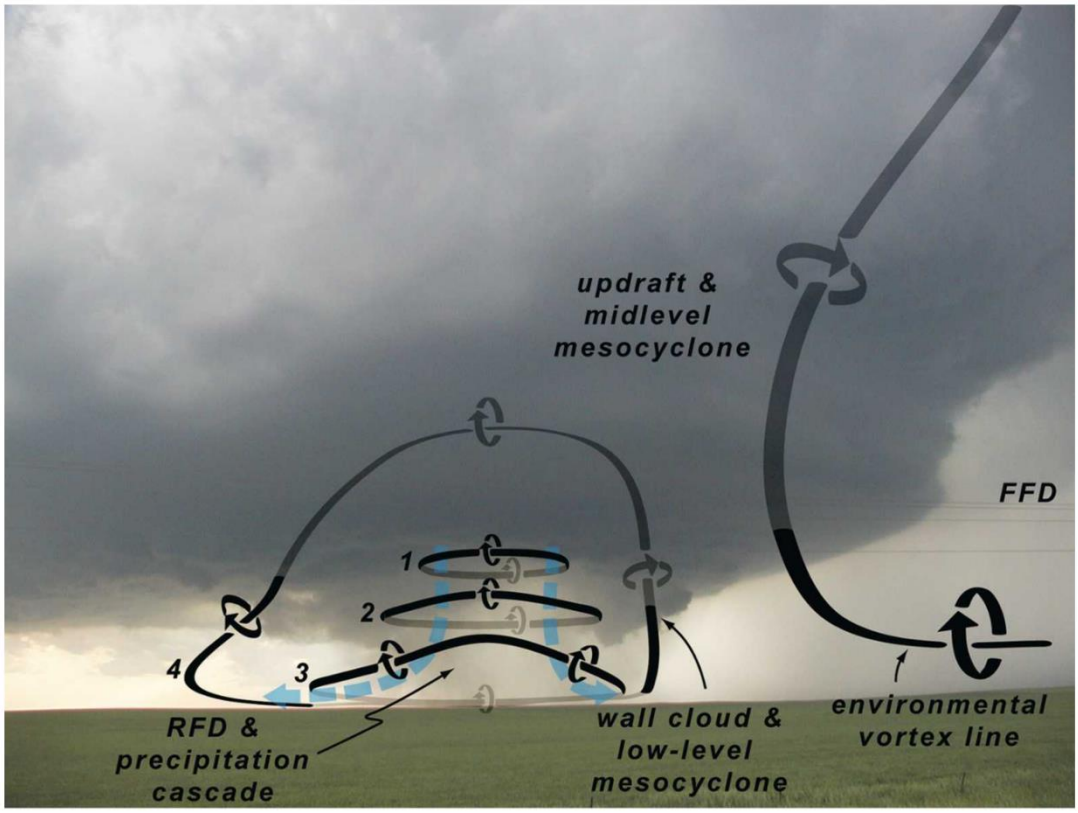

Figure 1.3: Visualization of the idealized evolution of RFD vortex rings into vortex arches. The view is from the south, looking north at a supercell thunderstorm. The vortex lines labeled 1 – 4 represent either a single vortex line evolving in time or 4 different vortex lines at different points in their evolution. An environmental vortex line is also shown coming from the inflow to help show the difference between mid-level and low-level rotation. From Markowski et al. (2008).

enhanced surface convergence where the two boundaries meet. Finally, the supercell updraft, if it is in place overhead of the forward flank convergence zone and RFGF apex, satisfies the last requirement for tornadogenesis. However, tornadogenesis is a nuanced process and often proceeds non-monotonically (Kosiba et al. 2013; Wurman et al. 2007b). The supercell RFD exerts considerable influence over tornadogenesis and can vary significantly from storm to storm. Tornadic RFDs have been found to only have small negative potential temperature perturbations, being only slightly cooler than the storm inflow (Grzych et al. 2007 and Hirth et al. 2008). Markowski et al. (2002) discusses a 'goldilocks' nature for RFD strength. An RFD that is too cold undercuts the supercell

updraft, while one that is not cold enough fails to produce enough baroclinic vorticity. Kosiba et al. (2013) reinforce this idea, finding that only modest vorticity generation within the RFD was required for tornadogenesis in the Goshen County, Wyoming case.

The broad scale characteristics of the supercell RFD are far from the only factor influencing tornadogenesis. Most supercells also display cyclic behavior to some degree, where the supercell updraft and relevant surface features propagate away from each other before tornadogenesis can take place, such as was described by Beck et al. (2006) when they analyzed a cyclic supercell in Kress, Texas. Storm mergers can also cause tornadogenesis by enhancing low-level convergence (Wurman et al. 2007b). Furthermore, numerous studies have documented tornadogenesis coincident with the development of RFD surges (e.g., Houser et al. 2015; Kosiba et al. 2013; Lee et al. 2012). Given these observations, it is tempting to conclude that RFD surges are a key ingredient for tornadogenesis, such as is suggested by Lee et al. (2012) in their analysis of RFD surges occurring throughout the lifecycle of the Bowdle, South Dakota tornado.

1.2.2: Tornado Maintenance and Decay – Supercell Cycling Behavior

At a fundamental level, tornadoes will persist so long as there is significant near-surface vorticity, near-surface convergence, and an overlying updraft. The ideal position relative to the parent supercell for the tornado to meet these requirements is at the apex of the RFGF and forward flank convergence zone underneath the supercell updraft (Dowell and Bluestein 2002). The supercell updraft provides some amount of near-surface convergence and allows for air to pass into and up through the tornado. Vertical vorticity is produced near the surface at the RFGF in the process of RFD vortex ring tilting, which

the tornado can ingest and stretch. The RFGF is also associated with a zone of significant near-surface convergence, which aids in transporting angular momentum inwards to the tornado. Horizontal near-surface vorticity is also generated along the forward flank, which the tornado tilts and stretches. However, numerous forces work against the tornado that prevent it from staying in this mature phase.

Commonly, tornadic supercells undergo an 'occlusion process' that is summarized in Figure 1.4 in which the supercell RFD eventually occludes the tornado and low-level mesocyclone, severing them from warm inflow. The occlusion of supercells was first formally described in Adlerman and Droegemeier (1999). During early intensification of the supercell, the RFD will develop and spread outwards, driving forward the RFGF. This increases near surface convergence, which results in intensification of the tornado and is represented by the first panel in Figure 1.4. Dowell and Bluestein (2002) observed this behavior in their analysis of the 1995 McLean, Texas tornado, in which continued intensification of the tornado was observed to cause the RFGF to advance outwards, causing additional increases in near-surface convergence.

Strengthening of the low-level mesocyclone continues, and the magnitude of vertical vorticity near the surface surpasses the strength of vorticity aloft in the mid-level mesocyclone. Because vorticity is associated with a nonlinear dynamic pressure drop, a downward directed pressure gradient force develops and drives a downdraft called the 'occlusion downdraft', which is shown in the second panel of Figure 1.4 (Klemp and Rotunno 1983). The occlusion downdraft is near but not collocated with the surface vorticity maximum at the tornado; this offset may occur because of tilting of the mesocyclone with height, misalignment between the tornado and low-level mesocyclone,

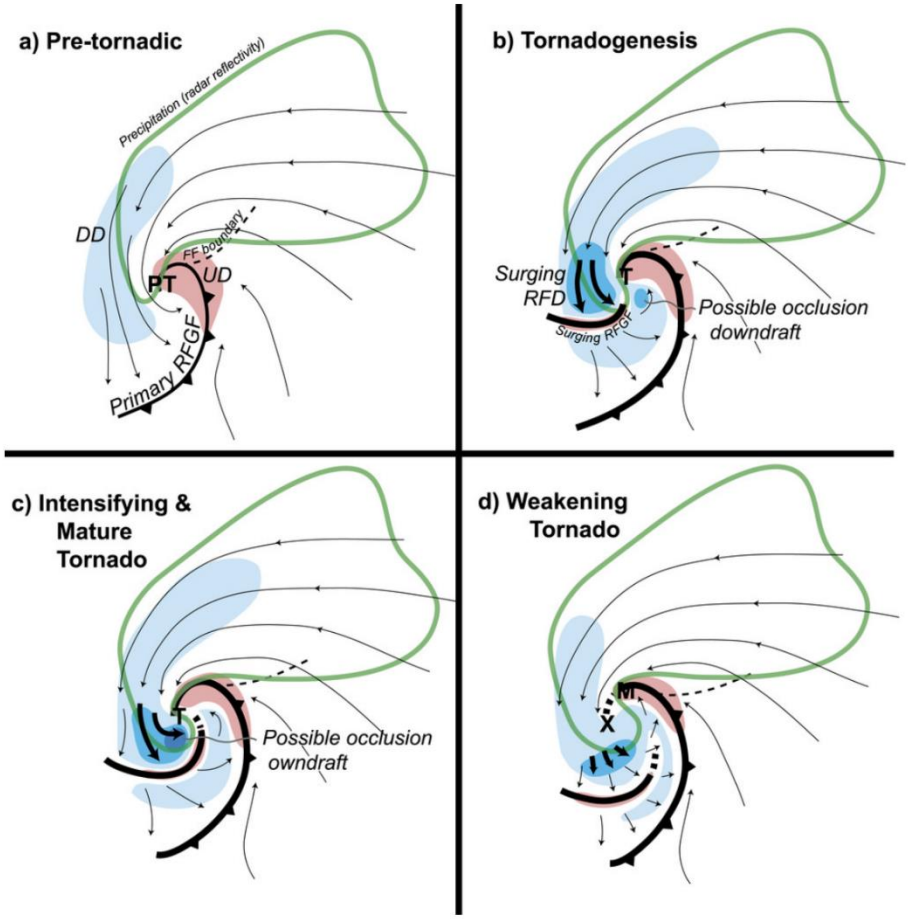

Figure 1.4: Conceptual model for the occlusion of a tornado. The 'T' marks the position of the tornado. In the last panel of the figure, the 'X' marks the location of the decaying tornado, and the 'M' marks the location of the new mesocyclone. From Marquis et al. (2016).

or contributions to the downward directed pressure force associated with buoyancy (Bluestein 2013). As shown in the third and fourth panels of Figure 1.4, RFD surges and surging momentum within the RFD displace the RFGF; the occlusion downdraft, as well as other mechanisms, contribute to the surging momentum within the RFD. If surging momentum is strong enough, the RFGF becomes decoupled from the tornado and occlusion occurs; the tornado and low-level mesocyclone move westwards with respect to the parent supercell and become enveloped in downdraft air. The surrounding air may be too negatively buoyant to be lifted as it is ingested by the tornado and vorticity available to be

tilted and stretched may be nearly non-existent, leading to decay (Dowell and Bluestein 2002; Skinner et al. 2014; Wurman et al. 2010). While the RFGF continues to move forward with time and attempts to occlude the low-level mesocyclone in a process conceptually like the occlusion of synoptic lows, it is the occlusion downdraft that provides the impetus for occlusion (Adlerman and Droegemeier 1999).

The pattern of occluding supercell behavior described above often occurs in repeated cycles as a new low-level mesocyclone then forms to the east of the occluding mesocyclone, which is shown at the 'M' in the fourth panel of Figure 1.4 (Adlerman and Droegemeier 2005). The new low-level mesocyclone forms underneath the updraft which has propagated along with the leading edge of the RFGF as it surged ahead of the tornado and low-level mesocyclone. The new low-level mesocyclone then often follows a similar lifecycle as the first mesocyclone. Adlerman and Droegemeier (2005) further explored the nature of cycling supercell behavior, finding two primary modes of cycling that include the occluding cyclic mesocyclogenesis described above and a non-occluding model.

To further describe supercell cycling behavior, Adlerman and Droegemeier (2005) ran numerous model simulations in which supercells were subjected to environments with differing magnitudes of shear and hodograph curvature. Their results are summarized in Figure 1.5. According to Figure 1.5, occluding supercells tend to occur in environments which have low to moderate amounts of shear and have quarter to three-quarter circle hodographs. At both very low and high amounts of shear and in environments with an extreme amount of veering of the winds throughout the entire troposphere, supercells may attain a steady, non-cycling structure. The spectrum of supercell structure with increasing shear for quarter to three-quarter circle hodographs reveals an important aspect of

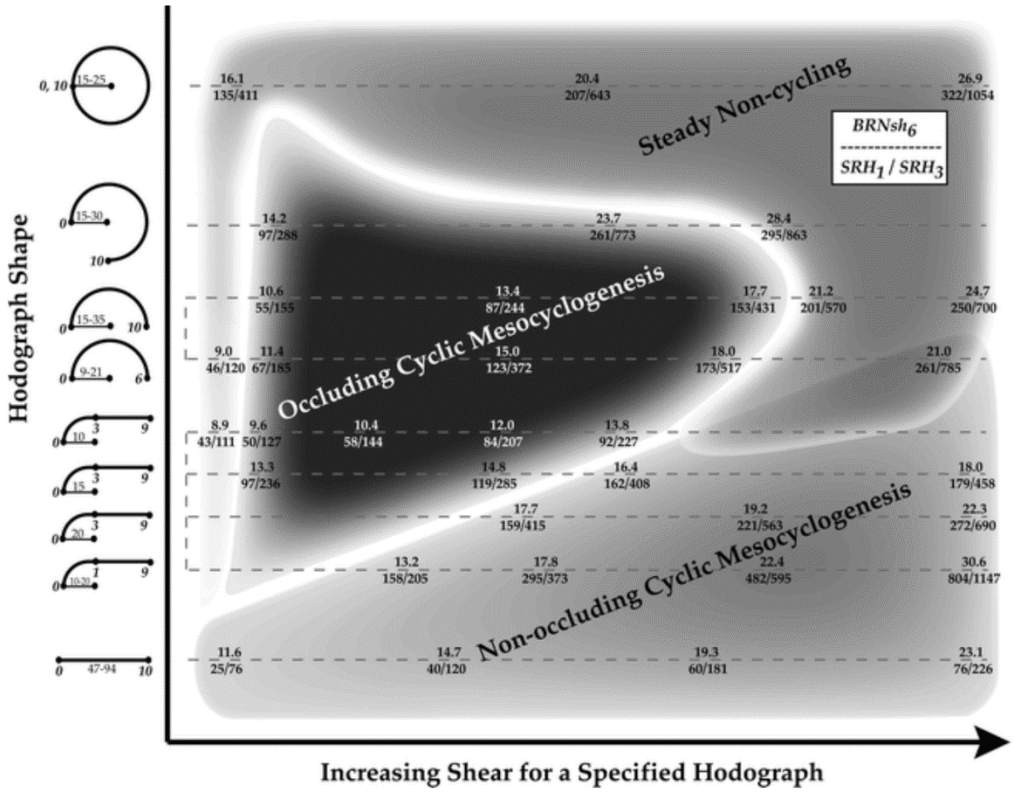

Figure 1.5: Diagram containing a summary of the results in Adlerman and Droegemeier (2005) where supercell cycling behavior was modeled in environments with differing amounts of shear and curvature in the hodograph. The type of supercell cycling behavior is plotted versus hodograph shape (ordinate) and amount of shear (abscissa).

occluding behavior. Adlerman and Droegemeier (2005) explain that at very low shear, updraft rotation is so weak that a mature RFD and RFGF never develop, preventing occlusion. At the opposite end of the shear spectrum, very high environmental shear results in a very strong supercell mesocyclone with strong inflow which resists displacement of the RFGF from the low-level mesocyclone, thereby preventing occlusion. Furthermore, a strong mid-level mesocyclone also delays the formation of the occlusion downdraft since the tornado will need to intensify further for its vorticity to exceed the vorticity aloft; occlusion may not occur at all if the tornado becomes very intense and is able to drive large amounts of surface convergence that keep the RFGF coupled to the tornado and low level

mesocyclone even as the occlusion downdraft becomes established. For full circle hodographs, a steady non-cycling structure is obtained as precipitation falls into the inflow and updraft regions of the supercell, disrupting normal structure and occlusion cycles.

Non-occluding mesocyclogenesis is poorly understood in comparison to the occluding model (Adlerman and Droegemeier 2005). For reasons that are not entirely clear, the supercell low-level mesocyclone and updraft propagate away from each other, with the low-level mesocyclone moving south along the RFGF and updraft along the forward flank. While the low-level mesocyclone remains coupled to the RFGF, it loses the support of the primary supercell updraft, and it starts to decay. A new low-level mesocyclone forms underneath the supercell updraft, which is to the north of the decaying, original mesocyclone. The physical processes controlling non-occluding cyclic mesocyclogenesis are not well understood, but the diagram in Figure 1.5 from Adlerman and Droegemeier (2005) may point to a governing mechanism. The dichotomy present in hodograph curvature between non-occluding and occluding supercells suggests that the dominant dynamic pressure forces controlling supercell propagation may be important in determining the cycling tendency of the supercell. In the non-occluding regime where hodographs are straight, supercell propagation is governed by nonlinear dynamic pressure forces and significant crosswise vorticity is being ingested into the updraft from the environment. As a result, the vorticity maximum within the updraft is advected towards the front (east) of the updraft as opposed to the right flank of the updraft in the curved hodograph case where significant streamwise vorticity is being ingested. It may be possible that the position of the vorticity maximum within the supercell updraft further forward in the straight hodograph case favors updraft propagation up the forward flank away from the

low-level mesocyclone in the non-occluding case. This is opposed to the occlusion case, where the updraft remains on the RFGF while the low-level mesocyclone becomes decoupled from the RFGF and moves away from the updraft.

1.2.3: Selected Tornadic Supercell Signatures and Phenomena

1.2.3.1: RFD Surges and Their Role Throughout Tornado Lifecycles

No other storm-scale feature exerts as much influence on a tornado through its lifecycle than the supercell RFD. Interest in the RFD culminated with project Analysis of the Near-Surface Wind and Environment along the Rear-flank of Supercells (ANSWERS) in 2003. During the ANSWERS campaign, mobile mesonets were deployed in the path of supercells with the intention of measuring the characteristics of supercell RFDs. In their analysis of data collected during project ANSWERS on the Basset, Nebraska supercell, Finley and Lee (2004) found at least 3 distinct areas of high momentum that moved through the RFD, or RFD surges. Although RFD surges have been sporadically noted in observations for decades and have gone by many different names such as outflow surges (Dowell and Bluestein 2002), embedded surge (Hirth et al. 2008), and secondary RFD gust front (Kosiba et al. 2013; Finley and Lee 2008; Marquis et al. 2012; Wurman et al. 2010) just to name a few, it appears that all of the different names actually refer to the same phenomenon (Skinner et al. 2014).

RFD surges are distinct regions or ‘surges’ of momentum within the RFD outflow, an example of which is shown in figure 1.6 (Lee and Finley, 2022). Since RFD surges constitute an area of enhanced momentum, there is an area of convergence at the front of the surge where significant vorticity can be generated (Finley and Lee 2004). Finley and

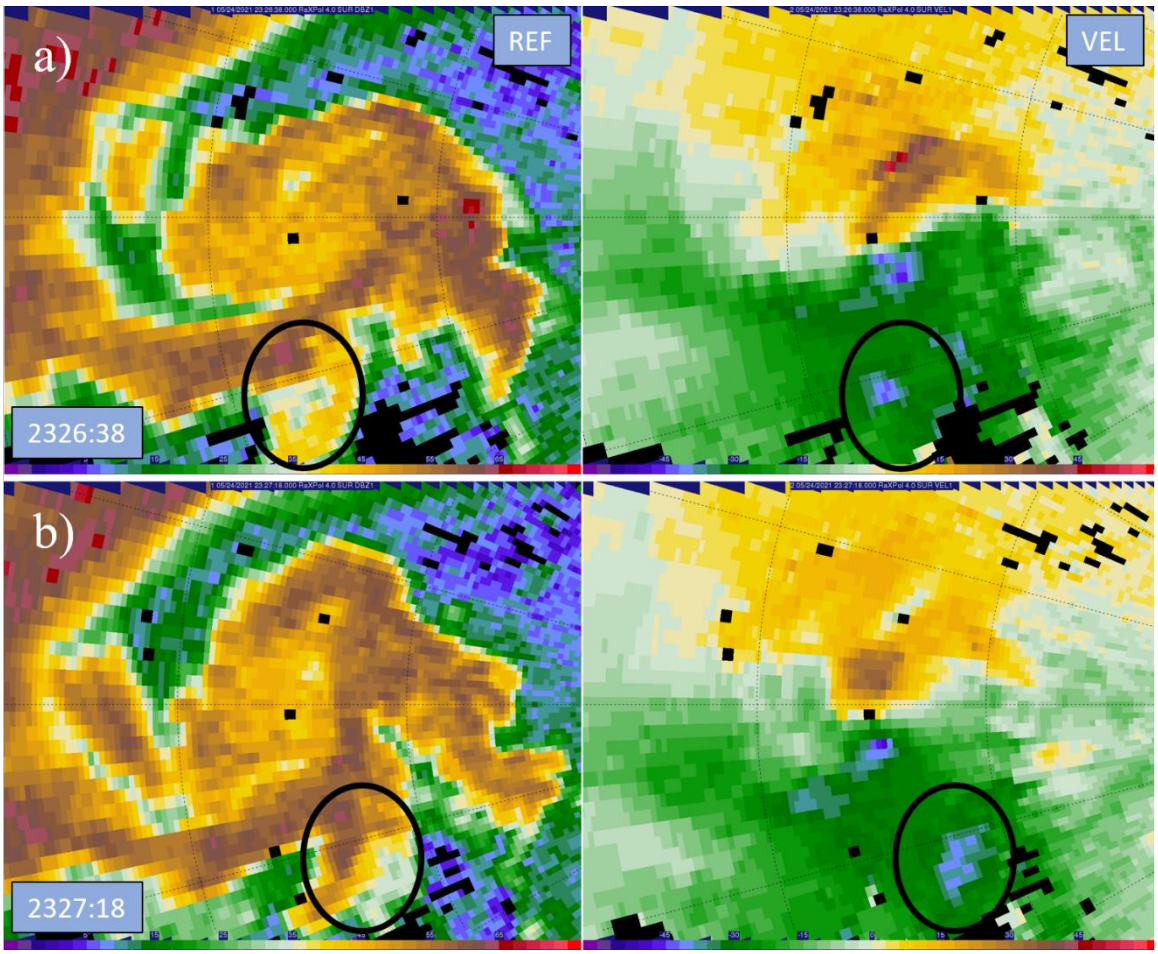

Figure 1.6: RaXPol reflectivity (dBZ) and velocity (m s^{-1}) from the 4° elevation at a) 2326:38 and b) 2327:18 UTC on 24 May 2021 near Selden, Kansas. Range rings are spaced at 2.5 km intervals. An example of a RFD momentum surge is circled as it moves to the east, south of an ongoing tornado. The surge has a distinct velocity and reflectivity signature.

Lee (2008) later found that the vorticity and convergence values associated with RFD surges were on the order of 0.05 s^{-1} using mobile mesonet data. In both studies, tornadogenesis was coincident with the time of a surge passage, suggesting their importance for the formation of tornadoes. Further studies, such as Houser et al. (2015), Kosiba et al. (2013), and Lee et al. (2012), have observed tornadoes forming near the northern apex of RFD surges. In their study of the genesis of the Goshen County tornado, Markowski et al. (2012) implicated vorticity generated along RFD surges for the rapid

enhancement of low-level rotation within the pre-tornadic vortex. Marquis et al. (2012) also found that tornadoes could persist entirely wrapped in downdraft air because of the convergence associated with RFD surges. RFD surges also have a variety of thermodynamic characteristics. RFD surges are generally characterized by small potential temperature perturbations and are very potentially buoyant (Finley and Lee 2004; Lee et al., 2004). However, RFD surges have also been documented with widely varying potential temperatures, ranging from as warm as the storm inflow to significantly colder than the broader RFD. Lee et al. (2004) found that warmer surges coincided with tornadogenesis. Skinner et al. (2014) noted that tornado dissipation occurred coincident with a very cold surge. Strong RFD surges have also been noted to be associated with the occlusion downdraft, making them potentially important to the occlusion process (Skinner et al. 2014). Despite the recent attention on RFD surges and their apparent importance, however, the reasons for surge formation are not yet entirely clear.

The kinematics of surges also have a demonstrative effect on the tornado track during its lifecycle. While a tornado is ongoing, RFD surges can redistribute momentum around the tornado in such a way that the balance of bounding momentum around the tornado is changed. A change in the momentum balance around tornadoes was implicated by Dowell and Bluestein (2002) for the leftward turn of a tornado. Since then, further studies have provided more evidence that a specific distribution of RFD surge momentum can cause the tornado to change track heading or execute track loops. Lee and Finley (2022) found that the hard left turns of three major tornadoes occurred along with the passage of a strong RFD surge that changed the balance of momentum around the tornado. Kurdzo et al. (2015) saw a ‘failed occlusion’ take place as the 2013 Moore tornado ejected from a

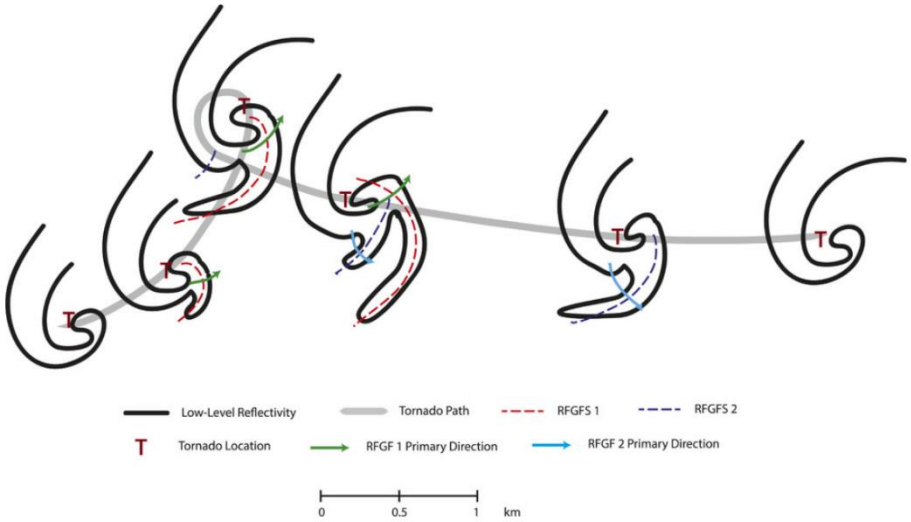

Figure 1.7: Conceptual model from Kurdzo et al. (2015) showing the 'failed' occlusion process for the Moore 2013 tornado. As surges on different trajectories move by the tornado at different times, the tornado track is affected. In this case, the pattern of RFD surges resulted in looping behavior.

track loop in an easterly direction instead of in a northerly one due to a specific arrangement of surges. The Kurdzo et al. (2015) conceptual model is given in Figure 1.7, showing how a combination of surges resulted in looping behavior. Kurdzo et al. (2015) and Wienhoff et al. (2020) have also shown that internal RFD surges are accompanied by debris ejections. Consequently, Wienhoff et (2020) found that the TDS grows most rapidly and reaches a maximum diameter when RFD surges pass through the tornado circulation.

Houser et al. (2015), Lee and Finley (2022), and McKeown et al. (2020) have also shown that RFD surges are coincident with tornado dissipation. In their study of a violent tornado near Sulphur, OK, McKeown et al. (2020) provide a specific hypothesis, arguing that an RFD surge instigated tornado decay by launching the lower parts of the tornado eastward as it made impact, displacing the tornado from the mid-level updraft. In their numerical analysis. Marquis et al. (2012) found that surges can initiate occlusion by forcing

the RFGF to surge forward and decouple from the tornado as the surges merge with the RFGF and displace it; the tornado is then wrapped with RFD air and begins to dissipate.

1.2.3.2: Multiple-Vortex Tornadoes

Odd, cycloidal scouring marks were first noted by Ted Fujita in his aerial assessments of tornadoes in the 1960's. In their paper, Fujita et al. (1970) referred to these marks as suction spots. However, their true nature remained a mystery since no radar at the time possessed high enough resolution to resolve small scale features within a tornado. Instead, laboratory and numerical simulations were utilized to study the nature of large and intense vortices. In the 1980's, Rotunno (1984) completed a comprehensive study of what he called a 'three-dimensional axisymmetric vortex'. In this study, the vortex was observed to breakdown into a multiple celled structure when a central downdraft formed, separating the vortex into two cells with an updraft remaining around the edges. The central downdraft was forced by a downward directed pressure gradient which developed in response to the vortex and resultant nonlinear pressure deficit being most intense at lower heights. Finally, the flow was also found to be unstable to perturbations at the updraft and downdraft interface, which when disturbed, resulted in the growth of small secondary vortices. A summary for vortex transition, in which a central downdraft forms and splits the vortex into two cells, is given in Figure 1.8. Winds encountered on the outside edges of secondary vortices, once superimposed on the mean azimuthal flow, result in locally higher velocities.

Beginning in the late 1990's and early 2000's, the multiple vortex phenomenon was documented by radar in tornadoes for the first time. Early studies, such as Wurman and Gill (2000), noted the presence of multiple Doppler velocity maxima on both sides of

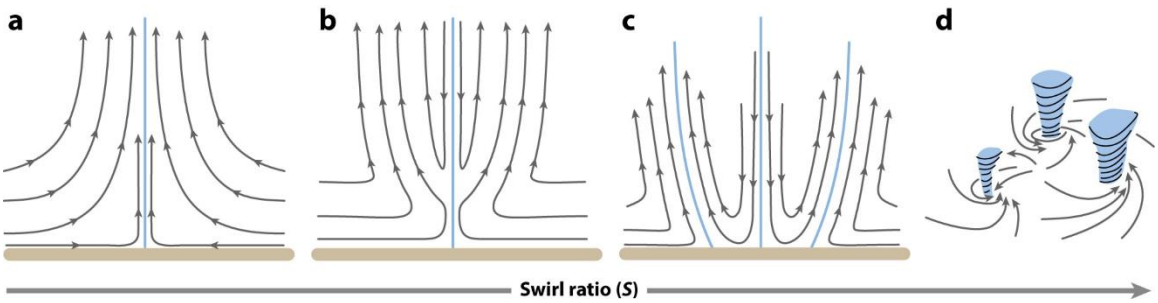

Figure 1.8: Conceptual diagram of the effects of increasing swirl ratio on tornadic flow. As swirl ratio increases, an internal downdraft develops in response to an intensifying downward directed perturbation pressure gradient force. Upon reaching the ground, the downdraft splits the vortex into multiple cells. From Rotunno (2013).

tornadoes. These multiple maxima were likely the manifestations of secondary vortices within a multiple vortex tornado. Wurman and Gill (2000) also found evidence of an internal downdraft with a magnitude of roughly 30 m s^{-1}. Following these early radar observations, Wurman (2002) formally documented for the first time finescale mobile radar observations of a multiple vortex tornado. Numerous secondary vortices were identified, lasting for at least 40 s. While the wind fields associated with the secondary vortices was approximately 250 m wide on average, at least half of the total azimuthal shear across the secondary vortex was concentrated in a zone of just 50 m. As a result, the vorticity within the secondary vortices was measured at 4 to 8 s^{-1}, the highest vorticity measurements ever made in tornadic circulations. An example of secondary vortices in radar data is given in Figure 1.9 below.

Since the seminal Wurman (2002) study, numerous cases of multiple vortex tornadoes have been recorded. Marquis et al. (2008) postulated that a tornado in Crowell, TX may have evolved into a multiple vortex tornado due to perturbations to the tornadic flow caused by strong outflow. Although it was not known at the time, the observation of strong, surging outflow within the RFD was likely an RFD surge. Lewellen et al. (2000)

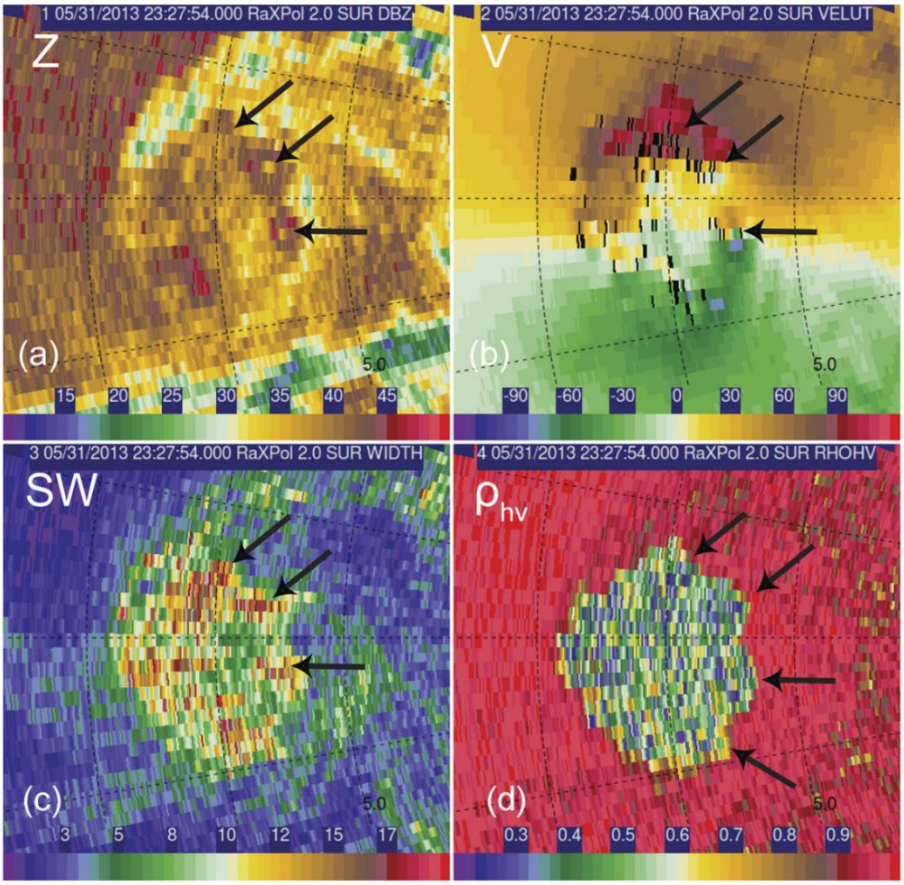

Figure 1.9: RaXPol imagery at 2° of the El Reno 2013 tornado at 2327:54 UTC on 31 May 2013. a) Reflectivity, b) Radial velocity, c) Spectrum Width, and d) Correlation Coefficient. Arrows point to secondary vortices within the parent tornado. From Bluestein et al. (2015).

have shown that tornado structure is highly sensitive to the character of surface inflow, making it possible that changes brought about by RFD surges could instigate a multiple vortex transition. In their study of tornado and mesocyclone structure, Wurman and Kosiba (2013) found that multiple vortex tornadoes do not have a specific spatial scale associated with them. Some multiple vortex tornadoes were observed to be smaller than large single vortex tornadoes, while some secondary vortices were found to be larger than small single vortex tornadoes.

Perhaps the most studied case of a multiple vortex tornado is the extremely large and powerful El Reno tornado of 2013. Aside from being 2.6 miles wide at its greatest

extent, this tornado is notable for its multiple vortex structure. Extensive damage surveys (Wakimoto et al. 2015 and Wakimoto et al. 2016) of the El Reno tornado have been completed, in which Wakimoto et al. (2016) were able to identify a damage swath and prove that it resulted from a secondary vortex for the first time. Bluestein et al. (2018) documents the tornado structure as seen from mobile radar. In this study, secondary vortices were found to form preferentially in areas of high azimuthal shear in the left-rear quadrant of the tornado. Secondary vortices were then tracked as they revolved around the parent circulation with an inward component of motion where they tended to dissipate in the front quadrants of the parent tornado. As the authors noted, the secondary vortices appeared to form from small wavelike oscillations in the parent tornado, reminiscent of 'Rossby waves in a vortex'. In their analysis of mobile radar data, Wurman et al. (2014) found maximum ground relative winds of 130 to 150 m s^{-1} in the El Reno tornado within the most intense secondary vortices, among the highest winds ever observed in tornadoes. An example of secondary vortices in the El Reno 2013 tornado is shown in Figure 1.9.

1.2.3.3: Anticyclonic Vortices and Tornadoes in Cyclonic Supercells

Anticyclonic tornadoes have occasionally been observed in right-moving cyclonic supercells along the trailing flank of the RFGF, sometimes resulting in a tornado pair where both the cyclonic and anticyclonic tornadoes are visible at the same time (e.g., Bluestein et al. 2015; Fujita 1981; Finley and Lee 2008). While other anticyclonic tornadoes, such as satellite tornadoes and gust front tornadoes (e.g., Bluestein et al. 2003; Finley and Lee 2004; 2008; Tanamachi et al. 2012; Tanamachi et al. 2013) have been observed, they are not the same type of anticyclonic tornadoes considered here. Anticyclonic members of

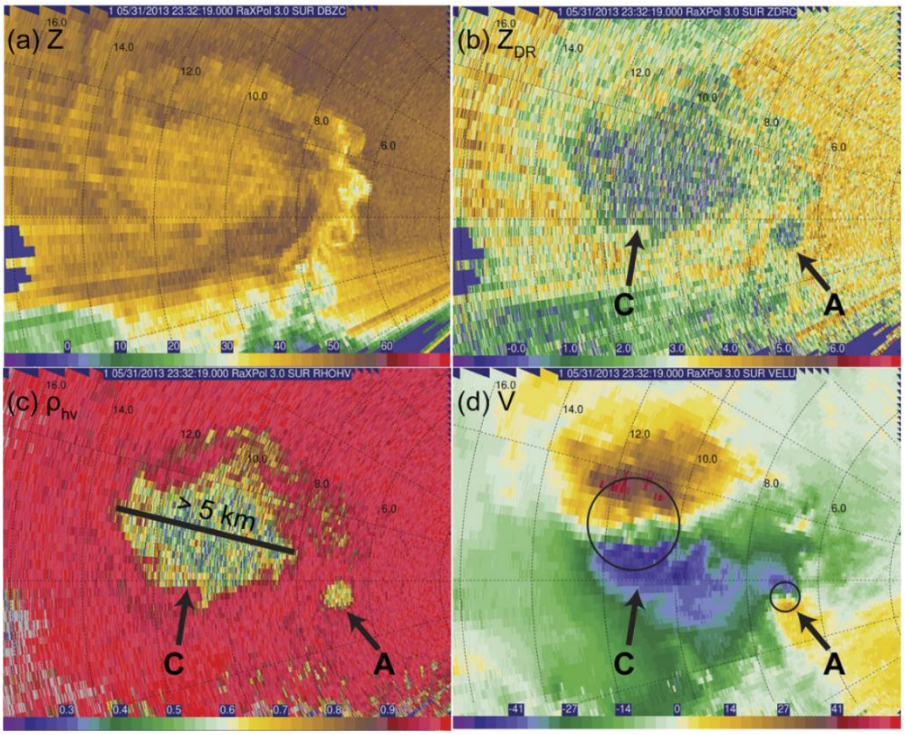

Figure 1.10: RaXPol imagery at 2° of the El Reno 2013 tornado at 2332:19 UTC on 31 May 2013. a) Reflectivity, b) Differential Reflectivity, c) Correlation Coefficient, and d) Radial Velocity. Arrows point to the cyclonic and anticyclonic tornadoes, labeled 'C' and 'A'. The anticyclonic tornado formed along the trailing edge of the RFGF. From Bluestein et al. (2015).

tornado pairs are generally found to be weaker than the cyclonic member, and the anticyclonic tornado often occurs later in the cyclonic tornado's lifecycle. In their study of the violent El Reno 2013 storm, Bluestein et al. (2015) documented a strong anticyclonic tornado with roughly 75 m s^{-1} of shear across a diameter of 500 m which is shown in Figure 1.10. The anticyclonic tornado was large and strong enough to develop its own debris signature as it curved to the right, away from the cyclonic tornado. This is perhaps the strongest companion anticyclonic tornado ever observed, with Wurman et al. (2014) noting that the anticyclonic tornado may have briefly displayed multiple vortex structure.

Companion anticyclonic tornadoes that form on the trailing edge of the RFGF have a different formation process than the primary cyclonic tornado. Before a cyclonic tornado

can form, the low-level mesocyclone must intensify. The additional vorticity for this comes from baroclinic generation along the forward flank of the supercell (Markowski and Richardson 2009). However, a corresponding structure does not exist at the trailing edge of the RFGF where companion anticyclonic tornadoes commonly develop. In their study, Bluestein et al. (2016) provide two possible answers to this conundrum. The first possibility is that vortex arches associated with the supercell RFD provide vorticity for anticyclonic tornadoes. Once vortex lines are lifted into arches, they produce anticyclonic vertical vorticity on the right side of the RFD relative to storm motion (Markowski et al. 2008). Another possibility is that preexisting shear vorticity at the southern edge of the RFGF or at the southern end of an RFD surge is concentrated by flanking line updrafts. Indeed, Finley and Lee (2008) have observed an anticyclonic tornado to form near the southern end of an RFD surge. Bluestein et al. (2016) conclude that anticyclonic tornadoes likely form from both mechanisms, and that it is possible that both work in tandem to result in anticyclonic tornadogenesis.

1.2.3.4: Weak Reflectivity Band (WRB)

The Weak Reflectivity Band (WRB) has only been described recently and is formally documented in one case. In their analysis of mobile radar data collected on the 2011 El Reno tornado, Houser et al. (2016) observed a band of weak reflectivity returns collocated with adjacent bands of enhanced convergence and divergence which is shown in Figure 1.11. The leading edge of the feature was associated with an area of divergence while convergence was present to the rear of the feature, implying that a horizontal circulation was present. This horizontal circulation was also observed visually. A band of

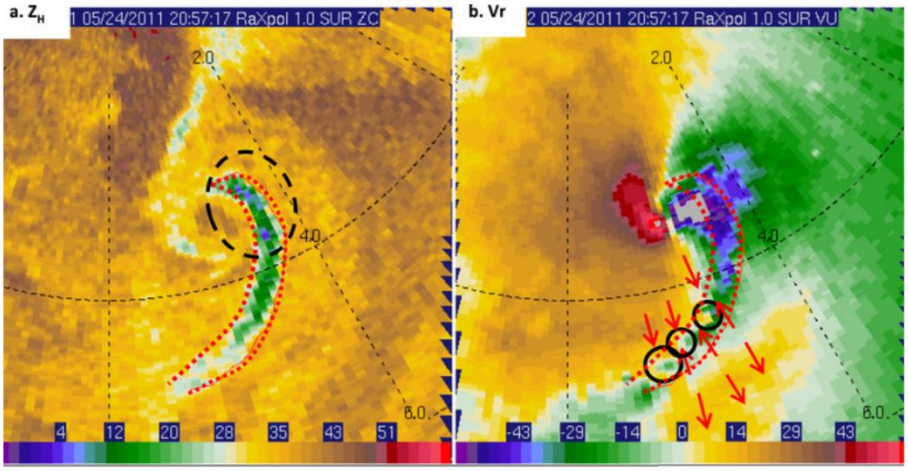

Figure 1.11: RaXPol a) Reflectivity and b) Radial velocity at 1° elevation on 24 May 2011 at 2057:17 UTC. Red lines denote the WRB, the black dashed circle marks the part of the WRB observed visually by the radar crew that collected the data, small black circles mark the positions of small vortices along the trailing part of the WRB, and red arrows show the convergence pattern around the WRB. From Houser et al. (2016).

inflow was apparent in radial velocity returns, bounded on both sides by outflow. Houser et al. (2016) postulated that the WRB formed within the descending branch of the horizontal circulation associated with the evident RFD surge. Three generation mechanisms were given for the horizontal circulation: 1) baroclinic generation with warmer air behind the RFD surge, 2) frictional generation behind the RFD surge with higher winds above the surface, and 3) tilting of near-tornado vertical vorticity into the horizontal. Unfortunately, the small sample size and data limitations made it difficult to make any definitive conclusions regarding WRB formation.

Houser et al. (2016) observed the WRB in Figure 1.11 for approximately 3 minutes as it progressively wrapped around the tornado. Tornado intensification was observed during this time, leading Houser et al. (2016) to conclude that the WRB may have been at least partially responsible as the horizontal vorticity within the WRB circulation was being ingested and tilted by the tornado. However, it is also possible that the tornado was

strengthening due to increasing inflow or other processes, and that the strengthening of the tornado amplified ambient horizontal vorticity through stretching, resulting in the WRB.

1.2.3.5: Descending Reflectivity Core (DRC)

The Descending Reflectivity Core (DRC) was first defined by Rasmussen et al. (2006) as a core or 'blob' of high reflectivity roughly 1 – 2 km across that descends from the supercell overhang above the weak echo region of a supercell as shown in Figure 1.12. Upon impacting the ground, DRCs became associated with a distinct velocity signature. The velocity signature consisted of a region of greatly enhanced rear to front flow, convergence at the front of the signature, and counter rotating vortices on either side similar in form to an RFD surge. When these cores descend, they fall near developing tornadoes since the weak echo region, or inflow, of a supercell is located adjacent to the hook echo and developing low-level mesocyclone. As the enhanced vorticity and convergence associated with the DRC impacting the ground nears the low-level mesocyclone, it may result in its intensification. In their study, Rasmussen et al. (2006) found that the DRC signature was a recurring feature in supercells but that not all supercells produced DRCs.

Following the suggestion made by Rasmussen et al. (2006) that DRC's may be connected to tornadogenesis, interest in DRCs increased. Byko et al. (2009), however, found that there was not a general relationship between the occurrence of DRCs and tornadogenesis, and that this could be explained by a difference in formation mechanisms for DRCs. Three different types of DRCs were identified. The first type of DRC formed due to mid-level flow stagnation in the supercell inflow. As air is ingested by the storm updraft, it stagnates, and precipitation falls out. The second type of DRC occurs when

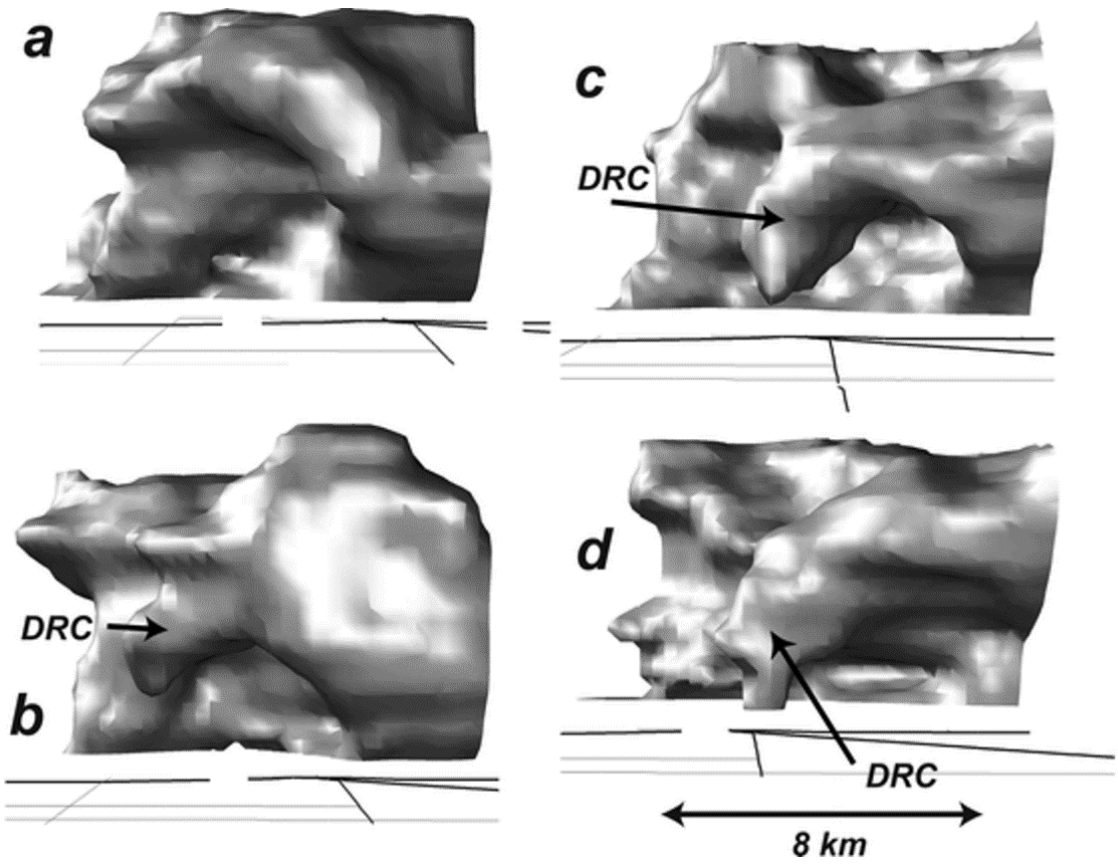

Figure 1.12: Example of an DRC adapted from Rasmussen et al. (2006). In this example, a core of reflectivity develops and descends from the supercell overhang, contacting the ground near the location of the tornado.

precipitation caught in a developing flanking line updraft collects and then begins to fall towards the ground when the flanking line updraft merges with the primary supercell updraft. Finally, a third type of DRC forms as a core of precipitation gets caught in downward directed pressure gradient caused by rotation being strongest at low levels. Byko et al. (2009) were only able to identify intensifying low-level rotation with DRC type 1, showing why there was no general rule connecting DRCs to tornadogenesis. Observations continue to provide evidence that DRCs are connected to tornadogenesis. In their study of the genesis of the El Reno 2013 tornado, Bluestein et al. (2019) connected a surge in radial

velocity near the developing tornado to a DRC. Intensification of the low-level mesocyclone was evident, suggesting that genesis may have been a result of the DRC.

1.2.3.6: Streamwise Vorticity Current (SVC)

More recently, the generation of streamwise vorticity along the forward flank has been observed in increasingly high-resolution simulations to be a concentrated 'river' of vorticity. In an extremely high resolution (30m grid spacing) simulation of a supercell, Orf et al. (2017) found that there was a concentrated, intense 'tube' of horizontal vorticity along the forward flank, dubbing it the 'Streamwise Vorticity Current' (SVC). The authors found that the feature was persistent and that it developed leading up to tornadogenesis and decayed coincident with tornado dissipation. An image of an SVC from the Orf et al. (2017) model is shown in Figure 1.13.

Schueth et al. (2021) have documented the SVC in both numerical simulations and in mobile radar data. In two real storms, a distinct SVC was found at and just behind the forward flank leading edge at the front of the forward flank cold pool around 500 m above the ground. Within a high-resolution simulation, Schueth et al. (2021) found that the SVC extended 1 – 10 km to the north and east along the forward flank leading edge upstream from the updraft. Magnitudes of horizontal vorticity within the simulated SVC were 0.08 s^{-1}, generated primarily by stretching of weak baroclinic vorticity in accelerating inflow. While these values are from simulation, Schueth et al. (2021) conclude that they may be representative of real SVCs. In contrast to the Orf et al. (2017) findings, Schueth et al. (2021) observed that the SVC was a transient feature occurring in the heads of breaking Kelvin-Helmholtz waves located at the front of the forward flank cold pool in both

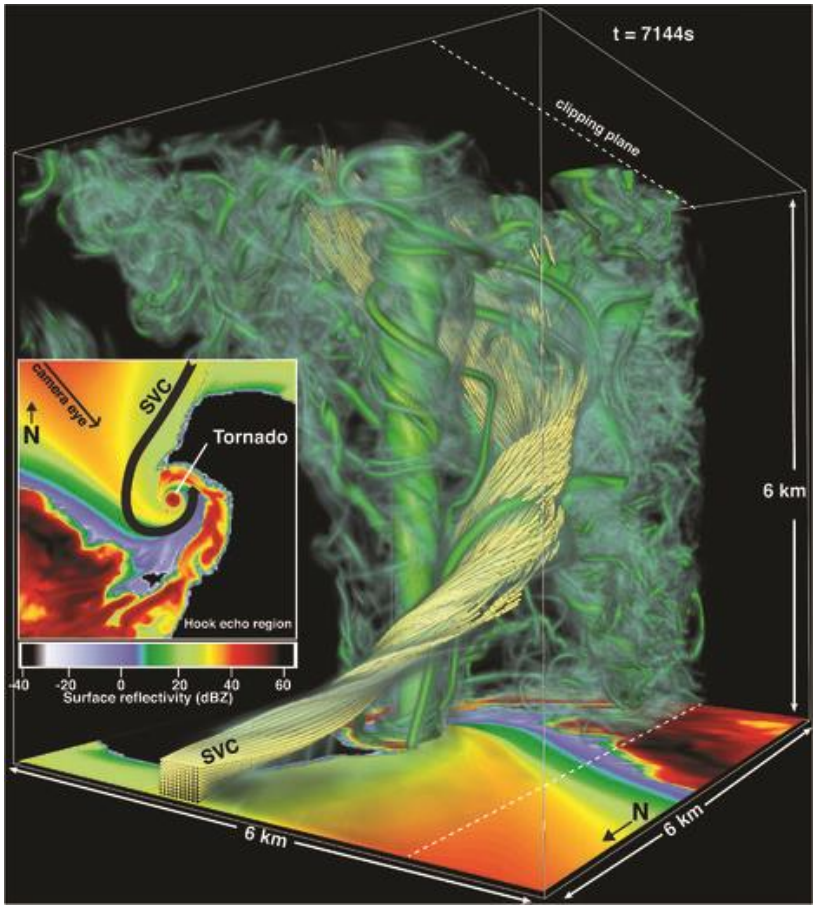

Figure 1.13: Example of the SVC from Orf et al. (2017). A concentrated area of streamwise vorticity develops near the surface position of the forward flank convergence zone, highlighted with yellow vortex lines.

simulation and in the analyzed storms. Conclusions regarding how SVCs impact a tornado are still uncertain because SVCs appear to be transient and air passing through SVCs may not be ingested by tornadoes; regardless, SVCs are certainly important for the health of the supercell and have a role to play in governing the strength of the supercell mesocyclone (Schueth et al. 2021).

1.3: Overview

In May of 2021, a tornadic supercell in northwest Kansas was documented by RaXPol over the course of eight deployments. Near the town of Selden, this supercell

produced a large multiple vortex tornado and anticyclonic tornado pair after several failed attempts at tornadogenesis. RaXPol had two deployments during the lifecycle of the Selden tornado, documenting the primary cyclonic tornado from near the time of genesis through dissipation. The focus of this study is to closely analyze the RaXPol data of the Selden tornado pair for structural features of the vortex and any storm scale features that effect the behavior of the tornadoes throughout their lifecycles. Questions addressed by this study include: 1) What observable features, such as RFD surges, yield a change in tornado behavior? 2) How do the tornadoes appear in velocity cross sections (both azimuthal and radial) throughout their lifecycles, and how does tornado cross section appearance change with evolving behavior? 3) How do the features identified in radar scans, cross sections, and video correlate to each other? 4) How do cross sectional analyses and identified finescale features compare with previous findings? Ultimately, this study aims to enhance understanding of tornadic supercells and tornado behavior, presenting possible explanations for why the Selden tornadoes behaved as they did. Chapter 2 will describe RaXPol, the mobile radar used to collect the data for this study. Data procedures and methods, specifically those concerning the synthesis of cross sections, will be discussed. A synoptic overview for the Selden supercell will be given in Chapter 3. Chapters 4 – 7 will cover the Selden tornado pair, presenting analysis of the cyclonic tornado and anticyclonic tornado. Finally, Chapter 8 will present discussion and conclusions of the most salient findings and recommend future work.

Chapter 2

Data and Methods

2.1: Instrumentation Overview: The *RaXPol* Mobile Radar

The Rapid, X-Band, Polarimetric (RaXPol) mobile Doppler radar is a rapid scanning radar that operates at a 3 cm wavelength housed and maintained at the University of Oklahoma's Advanced Radar Research Center. RaXPol features a mechanically rotating 2.4 m parabolic dish mounted on the bed of a medium-duty Chevrolet 5500 series truck (Figure 2.1; Pazmany et al. 2013). Becoming operational in 2011, RaXPol is a novel tool for the study of rapidly evolving storm and sub-storm scale processes owing to its polarimetric capability and fast scanning rates. Selected specifications for the RaXPol radar system are given in Table 2.1.

RaXPol features a heavy-duty pedestal which allows for scanning rates of up to 180° s^{-1}. While rotating at this speed in rapid scan mode, RaXPol has a dwell time of only 5.6 ms at each radial, which is not long enough for samples to decorrelate and be considered independent. For a modest spectrum width of 1 m s^{-1}, the decorrelation time for samples at X-band is 3.85 ms (Doviak and Zrnic 1993; Pazmany et al. 2013). As a result, only 1 to 2 independent samples would be collected at each radial no matter how rapid the Pulse Repetition Frequency (PRF). Consequently, RaXPol is unable to obtain high quality moment estimations given a standard pulse strategy (Pazmany et al. 2013). To overcome

Figure 2.1: The RaXPol radar, photographed by the author outside of the Advanced Radar Research Center.

this hurdle, RaXPol employs a frequency hopping strategy in which 24 pulses are transmitted in 12 pulse pairs with each pulse pair shifted in frequency by at least the pulse width. Each pulse is transmitted 200 μs apart to give an averaging period of 4.8 ms when using a PRF of 5000 Hz. (Pazmany et al. 2013). Using this strategy, RaXPol can treat each pulse pair as an independent sample because each pulse pair is on a different frequency and retrieve at least 24 samples at each radial even at maximum scanning speed, allowing for higher quality moment estimations. Another benefit of frequency hopping is that second-trip echoes are suppressed if the first sample in a pulse pair is used to estimate signal power (both horizontal and vertical channels, Z_H and Z_V) and correlation coefficient (ρ_{HV}) since each consecutive pulse pair is on a different frequency (Pazmany et al. 2013).

RaXPol has a 2.4 m dish, which at 3 cm wavelength results in a 3 dB beamwidth, or angular resolution, of 1°. However, in the frequency hopping strategy described above,

Table 2.1: Selected RaXPol specifications.

Center Operating Frequency	9.73 GHz ± 20 MHz
Transmit Power	20 kW peak, 200 W avg
Pulse Width	0.1 – 40 μs
Pulse Repetition Time (PRT)	Uniform or Staggered
Antenna Diameter	2.4 m
Antenna 3 dB Beamwidth	1°
First Sidelobe	27 dB
Pedestal Scan rate	180° s^{-1} azimuth 36° s^{-1} elevation
Range Gate Spacing	7.5 – 75 m

the averaging window is 4.8 ms. As RaXPol rotates rapidly at 180° s^{-1}, the radar will rotate nearly a whole degree in azimuth over the averaging period as samples from each pulse pair return. As result, the effective angular resolution of the radar is larger than 1° as beam smearing occurs. According to Pazmany et al. (2013) the effective resolution of RaXPol is 1.4° to 1.5° as result of the temporal averaging when using high PRFs at maximum scanning speed. Fortunately, this beam smearing can be negated by operating RaXPol in strobed mode. In strobed mode, all the first pulses of each pulse pair are combined into a single first pulse while the second pulses of each pulse pair are combined into a single second pulse, resulting in the transmission of a large single pulse pair (Pazmany et al. 2013). Consequently, the averaging time is reduced to the length of a single pulse pair, greatly reducing beam smearing. However, the blind range of the radar will increase since the radar is in transmit mode for 12 times longer to send the strobed pulse (Pazmany et al. 2013).

RaXPol's ability to scan at 180° s^{-1}, ability to be rapidly deployed near storms in 1 – 2 minutes, and 1° bandwidth make possible the collection of very high resolution spatial-temporal data. A typical 10 elevation scan, such as a 0° to 18° volume incremented by 2°, can be completed in as little as 20 seconds. The polarimetric capability of RaXPol allows for the collection of three additional moments, differential reflectivity (Z_{DR}), correlation coefficient (ρ_{HV}), and differential phase (Φ_{DP}), yielding much more information that can be used to study storm and sub-storm scale features and processes. Examples include the TDS, which can be used to track tornadoes remotely; the Z_{DR} arc, which can be used to infer supercell intensity; and precipitation size and shape, which can yield information about the microphysical processes within storms (e.g., Bluestein et al. 2007a; Kumjian and Ryzhkov 2008; Ryzhkov et al. 2005; Wakimoto et al. 2016). Despite the incredible capabilities of RaXPol, there are a couple factors to be aware of when deploying. Like most mobile radars, the large dish on the back of the truck is heavy (~17000 lbs. total weight for RaXPol) and acts as a wind sail (Pazmany et al. 2013). As a result, RaXPol may not be able to keep up with storms or follow them onto unpaved roads. While scanning, caution must also be exercised to build in additional time for the radar to come back down from its top scan elevation to its lowest. Since RaXPol can only scan at 36° s^{-1} in elevation, if a buffer is not inserted into the scanning strategy, the surface level scan will be at an angle as the dish moves back down to 0°. Finally, RaXPol also suffers from significant attenuation in heavy precipitation because it operates at X-band. To account for this, attenuation correction techniques, such as those outlined in Snyder et al. (2010), need to be applied to the data depending on the type of analysis being considered.

2.2: Available Data and Data Control

2.2.1: Data Collection

On 24 May 2021, RaXPol followed the supercell that would eventually produce the Selden tornado through northwestern Kansas as it moved northeasterly after briefly pursuing an initial target farther to the south in west-central Kansas. Throughout the afternoon and evening, the Selden storm attempted tornadogenesis several times until a tornado finally developed near the town of Selden, Kansas. RaXPol had eight total deployments on 24 May. Deployments 1 and 2 were on the separate, earlier storm while deployments 3 – 5 occurred before the Selden tornado and deployment 8 afterwards, capturing numerous attempts at cloud base lowering and several funnel clouds. Deployments 6 and 7 (hereafter D6 and D7) occurred during the Selden tornado. During D6 data were collected from near the time of tornadogenesis to right after the tornado transitioned to a multiple vortex tornado, from 2304:43 UTC (1804:43 CDT – local time) to 2320:42 UTC (1820:42 CDT). During D6, there was a brief ~3-minute gap in data collection (hereafter the D6 gap) lasting from 2313:41 UTC (1813:41 CDT) to 2316:29 UTC (1816:29 CDT). During this gap, raw I/Q radar data were being collected, but failure to turn off frequency hopping by the radar operator at this time renders the data unusable. By the end of D6, it became necessary to redeploy RaXPol to a safer location further away from the approaching tornado. Consequently, there is a 6-minute gap in data collection. After arriving at the D7 location 5 km to the east of D6, RaXPol resumed data collection at 2326:34 UTC (1826:34 CDT), continuing through the Selden tornado's dissipation until 2343:14 UTC (1843:14 CDT). Deployment details are given in Table 2.2.

Table 2.2: Details for all RaXPol deployments on 24 May 2021. Distances are measured from nearest town or village. Asterisk indicates deployments not on the Selden storm.

Deployment and Location	**Times (UTC)**	**Distance to Tornado**
D1 (13 km W of Leoti, KS) *	1900:09 – 1917:53	N/A
D2 (18 km N of Leoti, KS) *	1941:41 – 1950:04	N/A
D3 (11 km WSW of Rexford, KS)	2144:17 – 2205:48	N/A
D4 (2.5 km WSW of Rexford, KS)	2226:08 – 2237:01	N/A
D5 (2 km ENE of Rexford, KS)	2244:23 – 2250:55	N/A
D6 (3 km ENE of Selden, KS)	2304:43 – 2320:42	11.2 decreasing to 3.3 km
D7 (8 km E of Selden, KS; 5km east of D6)	2326:34 – 2343:14	5.0 to 6.5 km
D8 (16 km SE of Dresden, KS)	2354:45 – 0014:28	N/A

All data during the Selden tornado was collected in rapid scan mode using a 10-elevation scanning strategy from 0° to 18° incremented by 2°. This resulted in update times of 20 seconds. While data were being collected, the radar PRF was 4000 Hz, resulting in a maximum unambiguous range of 37.5 km and maximum unambiguous velocity of 30.8 m s^{-1}. Data resolution is 60 m in range and 1° in azimuth after oversampling the beam-smeared data. Unfortunately, some of the data collected during D6 and D7 are unusable. The available 0° scans are rendered irrecoverable because the scan was taken as the dish moved back down from 18° elevation. While the travel time of the dish from 18° to 0° is only 0.5 s, or one quarter of the 0° scan, the tornado and supercell fell within the affected quadrant of the 0° scan and data around the tornado are taken at differing elevation angles. Significant low ground clutter also contaminated the data at the 2° elevation near the radar, causing scans to be irrecoverable at the very end of D6 as the tornado moved into the area of high ground clutter and noise. However, this only occurred for the last two scans at 2° in D6.

2.2.2: Data Quality Control

Data collected from weather radars often need to be corrected to remove low-quality portions of the data. Both the characteristics of the radar and the environment being sampled influence data quality. A primary concern is the selection of radar pulse width and PRF, which must be chosen carefully to ensure proper sensitivity to the environment. Longer pulse widths allow better detection in clear air and selecting a PRF leads to the so called 'Doppler Dilemma', where a faster PRF results in a greater unambiguous velocity but smaller unambiguous range and vice versa (Doviak and Zrnic 1993). The Selden data were collected with a high PRF since RaXPol was very close to the tornado, resulting in less velocity folding and generally improving the quality of the radial velocity field by making it easier to unfold. However, there are numerous factors that result in a decrease of quality in the Selden data. In the case of RaXPol, rapid rotation leads to beam smearing (Pazmany et al. 2013). In addition to being affected by beam smearing, mobile radars like RaXPol are susceptible to ground clutter since deployment locations are hardly ever perfect. Small hills and short trees combined with the radar being on the ground make it difficult to avoid ground clutter, so lower-level data is usually contaminated to some degree. Furthermore, some meteorological phenomena, such as highly turbulent motions and debris lofting in gust fronts or tornadoes also degrade the quality of radar data samples. When necessary, areas of poor data quality and artifacts were subjected to a data control process and edited as appropriate.

Data were manually edited using SOLO3, a software package provided by the National Center for Atmospheric Research (Oye et al. 1995). First, the data were copied and cleaned using SOLO3's 'despeckle' command, which removes individual and very

small groups consisting of 2 to 3 isolated pixels from the field. After basic clean up, radial velocities were manually unfolded in and around the tornado. Since the Nyquist velocity was 30.8 m s^{-1} and the Selden tornado was relatively weak, data were only folded once around the tornado, making the unfolding process straightforward. After unfolding, tornado velocities were in good agreement with National Weather Service (NWS) damage surveys. Significant ground clutter was also present around RaXPol, especially at the 2° elevation. In previous studies (e.g., Snyder and Bluestein 2014), a signal quality index using spectrum width and Normalized Coherent Power (NCP) was used to remove data that had a poor signal to noise ratio. However, the NCP field was not available for the Selden data. Instead, ground clutter was subjectively determined to be contaminating pixels when high reflectivity values were paired with low velocity values, creating a discontinuity in the moment fields that was especially apparent in animations (Doviak and Zrnic 1993). When ground clutter was encountered, pixels were ignored and neighboring, uncontaminated pixels were used when necessary. Finally, attenuation was not an issue for the Selden case since the radar was observing the tornado from the east where there was no intervening precipitation; correction techniques like those described by Snyder et al. (2010) were not applied.

2.3: Cross Section Synthesis and Averaging

2.3.1: Constructing Cross Sections

In addition to a visual analysis of radar data and animations, cross sections were constructed for both the cyclonic and anticyclonic tornadoes at all available elevations.

Two cross sections were drawn across the tornadoes for each scan, one containing vortex azimuthal winds and the other radial winds. Notably, these cross sections were drawn without using the Ground Based Velocity Track Display (GBVTD) procedure. GBVTD is a method for retrieving the vortex flow field (tangential and radial winds) that takes advantage of radar observed Doppler velocities of vortices (Lee et al. 1999). GBVTD was developed for use in tropical cyclones but has also been adapted to tornadic vortices to elucidate details of tornado wind field structure (Bluestein et al. 2003; Kosiba and Wurman 2010; Kosiba and Wurman 2013; Tanamachi et al. 2012). During analysis, data are used to construct sine and cosine functions that represent tangential and radial winds at different radii within the vortex. However, the set of resulting equations is underdetermined, and assumptions must be made to solve them (Lee et al. 1999). These assumptions, such as assuming vortex axial symmetry or assuming all non-axisymmetric vortex radial winds are 0, have the effect of filtering out numerous aspects of vortices, giving a smooth solution that often washes out important vortex features. Furthermore, GBVTD strives to isolate tornado circulations from all other flow, aggressively suppressing winds around tornadoes that may be important to their structures. Nonetheless, GBVTD has aided in the study of several tornado features, including the multiple vortex structure of a tornado with the associated internal downdraft (Kosiba and Wurman 2010), shallow inflow confined to below 14 meters above the ground (Kosiba and Wurman 2013), and varying modes of tornado intensification (Tanamachi et al. 2012).

Despite its usefulness, the GBVTD technique can make critical errors handling tornadic vortices. First, the GBVTD analysis assumes the vortex is axisymmetric, which is certainly not the case for many tornadoes, especially multiple vortex tornadoes (Bluestein

et al. 2003). Translational movement has also been observed to create artifacts in the analysis (Tanamachi et al. 2012). Wakimoto et al. (2012) also noted that centrifuging of debris and hydrometeors within the tornado causes error in the GBVTD wind profiles. Furthermore, GBVTD suppresses winds outside of the idealized tornadic vortex, potentially altering or eliminating important details from the analysis. These factors call into question how useful GBVTD may be for studying small-scale tornadic structure. While previous GBVTD studies have produced cross sections that resemble Burgers-Rott vortices (Tanamachi et al. 2012), cross sections need to be constructed systematically using unaltered data to reveal how tornado structure appears without any filtering or assumptions.

As previously discussed, cross sections were drawn across both the cyclonic and anticyclonic tornadoes to capture both the vortex tangential and radial winds. An example of the two types of cross sections is shown in Figure 2.2. The white line in Figure 2.2 is an example of the tangential, or azimuthal, wind cross sections that were constructed by locating the velocity maxima on either side of the tornado. This needed to be accomplished manually, since locating the tornado associated wind maxima is not straightforward. Multiple maxima can often be present since the tornado is embedded within the larger scale mesocyclone (Bluestein 2013). Other features, such as an RFD surge or strong RFD can also create additional maxima. Furthermore, when the Selden tornado transitioned to a multiple vortex tornado, particular care had to be taken to accurately represent the parent vortex rather than any secondary vortices. A line was then drawn connecting the maxima, which extended beyond the radius of maximum wind to approximately twice the vortex size and the velocity values for all the pixels on the line were collected. The line connecting the two velocity maxima was not necessarily perpendicular to the radar beam or at a

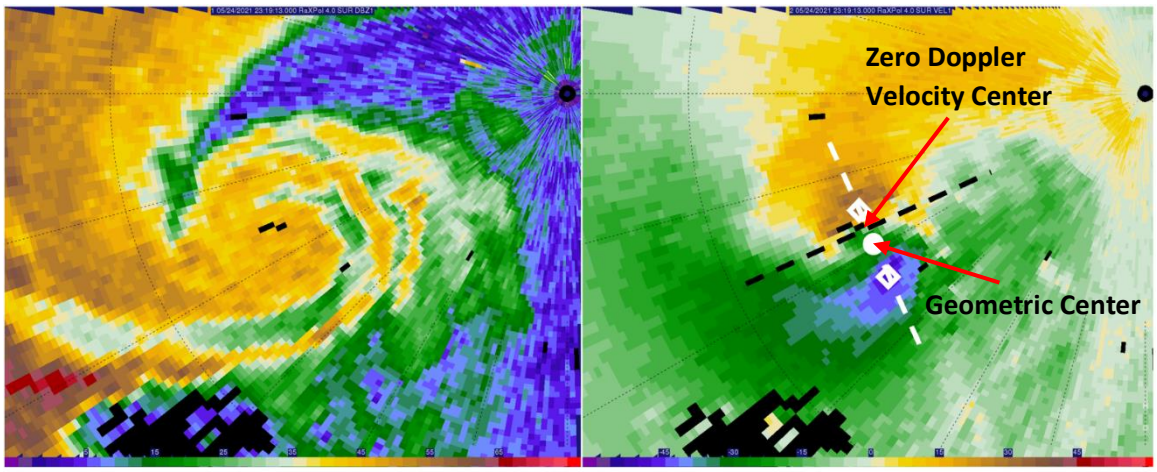

Figure 2.2: Example of cross sections at 2319:13 UTC at 4° elevation. The white line is the azimuthal cross section, connecting the velocity maxima marked with white diamonds. The black line is the radial wind cross section. Red arrows point out the different centers, with the white circle denoting the geometric center.

constant radius owing to the positions of the velocity maxima, although it was often very close to these criteria. Since range did not change much along the cross sections and to simplify data collection, a constant radius was assumed for cross section construction.

The black line in Figure 2.2 represents an example of the radial wind cross sections, which were constructed by taking data along a radial, or constant azimuth, through the center of the vortex. However, data could not simply be taken along a radial using the middle point in between the velocity maxima on either side of the vortex. This 'geometric center' in between the velocity maxima did not necessarily match the zero Doppler velocity point inside the tornado due to vortex asymmetries; the two different definitions for the tornado center are highlighted in Figure 2.2. If the data for radial wind cross sections were not taken as close as possible to the point corresponding to zero Doppler velocity inside the tornado, then vortex azimuthal winds would contaminate the radial wind cross section. Especially during the Selden tornado's multiple vortex phase, particular care had to be taken to redefine vortex centers by subtracting vortex motion and then locating the zero

Doppler velocity point. Data were then taken along the radial passing through the zero Doppler velocity point in a 3 km zone centered on the vortex.

2.3.2: Averaging

The cross sections taken by themselves are inherently noisy owing to the nature of high-resolution data. To parse important features from the cross sections, they were first interpolated to a uniform grid and then averaged with each other in discrete groups. Instead of simply averaging cross sections with a set window of neighboring ones, cross sections were grouped by tornado track segments based on movement behavior. Therefore, each of the resulting average cross sections represent the vortex structure of the tornado during a segment of time containing distinct tornado behavior. Track segments were determined subjectively from the RaXPol derived track at all elevations (2° to 18°). To eliminate much of the noise in individual cross sections but also preserve important changes in the tornado through time, segments required that there be at least 3 scans to average (1 minute of data) and no more than 15 scans (5 minutes of data). Using these criteria, 8 to 9 different track segments were identified at each elevation for the cyclonic tornado, while 4 were identified at all elevations for the anticyclonic vortex. Details concerning the individual track segments will be discussed in the following chapters. After grouping into segments, the vortex velocity over each segment is subtracted to produce the final cross sections.

2.4: Radar Analysis Procedures

During this study, radar data were analyzed to locate tornado proximate boundaries and features. Locating tornado proximate boundaries, RFD surges, and other features was

done methodically to reduce the inherent subjectivity in locating the features in single-Doppler data. First and most importantly, animations of RaXPol PPIs for both reflectivity and Doppler velocity fields were analyzed to locate storm scale features such as the RFGF, forward flank convergence zone, and RFD surges. While the high spatial and temporal resolution of the RaXPol data allows RFD surges to be easily tracked, caution must be taken since all data are from a single Doppler radar and the full 3-D wind field was not available. Despite this limitation, animations of the data with update times of 20 seconds have great value in locating RFD surges and other finescale features. While any particular boundary or RFD surge is often difficult to locate in a single scan, animations allow boundaries and features to be identified much more easily because of the time continuity offered in the animations.

Often, the first features to be located were the RFGF and forward flank convergence zone. These boundaries generate significant areas of radial convergence, which were easy to locate. In some cases, especially early, the forward flank boundary placement is ambiguous based on radial convergence alone. Because of this, it became necessary to rely on the forward flank reflectivity gradient as well. When only a broad convergence signature is identified, the forward flank reflectivity gradient is used to help locate the forward flank boundary.

After locating tornado proximate boundaries, RFD surges were identified and located. Most information needed to identify surges came from close inspection of the reflectivity and velocity animations. To locate an RFD surge, an enhancement of velocities within the RFD was required, and this area of velocity enhancement needed to have time continuity. A transient area of enhanced velocities, appearing in only one scan, was not

identified as an RFD surge; movement or persistence of the enhanced velocities within the RFD was required to identify the enhanced velocities as a surge. The RFD surge front was then located at the area of strongest radial convergence. Secondary to this were any reflectivity appendages on the hook echo, which almost always accompanied RFD surges. The combination of both velocity and reflectivity features provided reasonably accurate placement of RFD surges, even as velocity signatures became more ambiguous. However, after initial analysis of radar animations, other factors were considered to ensure placement of RFD surges was as accurate as possible. Especially for surges traveling perpendicular to the radar such that no velocity signature was trackable, the correlation coefficient field was analyzed. Correlation coefficient often decreases at RFD surge fronts as debris collects in the convergence zone at the RFD surge front (Kurdzo et al. 2015). Therefore, if a correlation coefficient minimum was identified, had time continuity, and was collocated with a reflectivity appendage or feature, an RFD surge was identified. Finally, as a last resort, height continuity was used to locate surges. However, because the RFD is relatively shallow, the use of height continuity is somewhat limited.

2.5: Video and Photo Analysis Procedures

One of the most valuable and unique aspects of this study is that a video of the tornado was taken during the entirety of D6 from the radar location. As such, the video provides a rare opportunity to compare and contrast visual evidence with radar data. Two primary types of analysis were conducted on the tornado video, condensation funnel width estimation and tornado track estimation. Figure 2.3 presents an example analysis of one of the tornado video frames and shows how both the funnel width and tornado track were

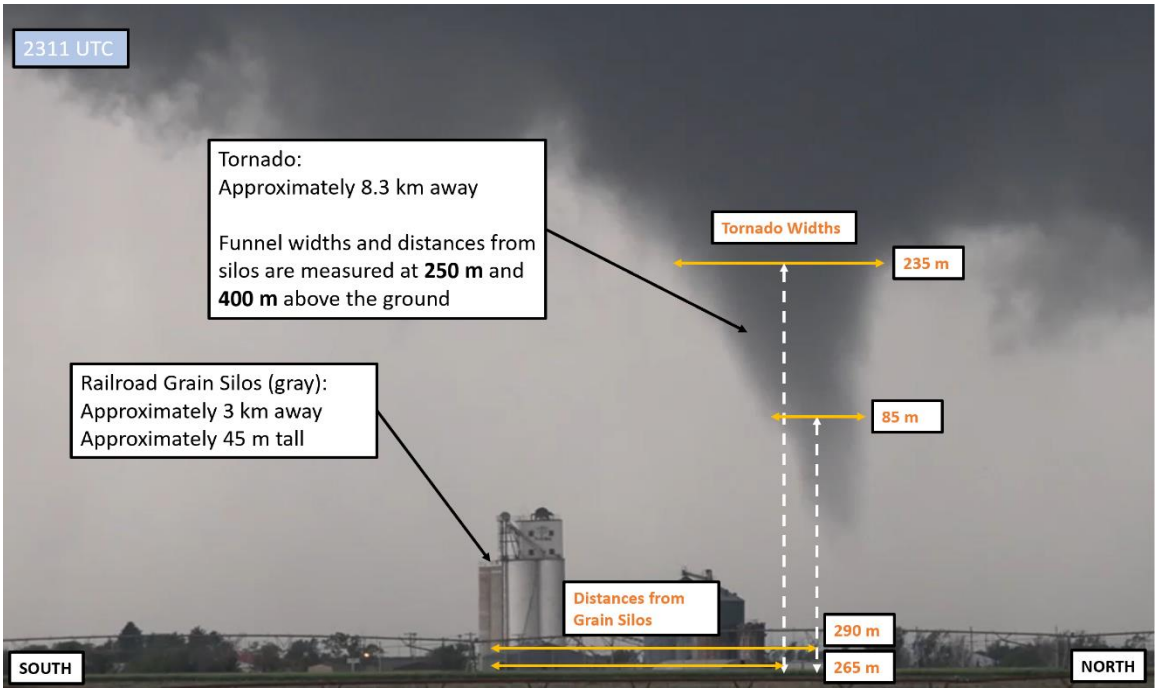

Figure 2.3: Example analysis of a panel from the D6 tornado video. The scale object (railroad grain silos) and tornado are annotated with the information required to calculate lengths at the tornado location. The desired parameters, condensation funnel width and distance of the tornado from the grain silos, are marked in orange.

estimated from video. To approximate lengths on frames of the video, a known scale object is required. Fortunately, a grouping of tall railroad grain silos appear throughout the entirety of the video. Using a map resource such as Google Maps with satellite view, it was possible to pinpoint the precise location of the grain silos relative to the radar; the silos were roughly 3 km away from the D6 deployment site. Then, the height of the grain silos was needed. Because railroad grain silos are a common structure with relatively standard heights, a reasonably accurate silo height estimate was able to be determined from web sources. According to the University of Nebraska's Agriculture Department website, railroad grain silos are commonly about 150 ft (or 45 m) tall.

Using the railroad grain silos as the scale object in the tornado video and the radar indicated positions of the tornado at the lowest available scan elevation, it was then possible

to estimate lengths at the tornado location. To obtain the estimations, a simple ratio of the distance to the tornado and distance to the grain silos was calculated to account for the different distances of the tornado and grain silos relative to the radar. After the ratio was calculated, the 45 m grain silo height was measured in the video frame, which was then used with the ratio of distances to find the desired lengths at the tornado location. The widths of the tornado's condensation funnel were measured at both 250 m and 400 m above the ground, as was the distance of the center of the condensation funnel to the left or right of the grain silos. Using the grain silo relative position of the tornado, it was then possible to estimate the track of the tornado during D6. To do so, the recorded grain silo relative positions of the tornado were plotted by hand on a map relative to the line of sight between the D6 deployment site and the grain silos.

Chapter 3

Selden Supercell and Tornado Overview

3.1: Synoptic Environment

On 24 May 2021, a broad longwave trough was slowly ejecting to the northeast from the northern Rocky Mountains into the northern High Plains in Montana and southern Canada. By 1800 UTC, the trough axis was progged to extend from the upper-level low in Saskatchewan southwards towards southern California (Fig. 3.1a). Numerous shortwaves were progressing through the upper-level flow pattern, with a weak shortwave located over Wyoming and Colorado at 1800 UTC (Fig 3.1a), close to the initiation time of convection on the afternoon of the 24th. Ahead of the shortwave, a prominent 70 knot jet streak was rounding the eastern flank of the trough, centered over the Dakotas. Farther south in the entrance region of the jet streak, southwesterly 500 hPa winds of roughly 50 knots were oriented at a 45-degree angle to the spine of the Rockies; the upward motion present in the right entrance region of the jet combined with vertical stretching lee of the Rocky Mountains and height falls ahead of the advancing shortwave resulted in moderate cyclogenesis in east central Colorado. Slow propagation of the trough and distance from the primary synoptic forcing resulted in the surface low remaining broad and nearly stationary over the Colorado plains throughout the day.

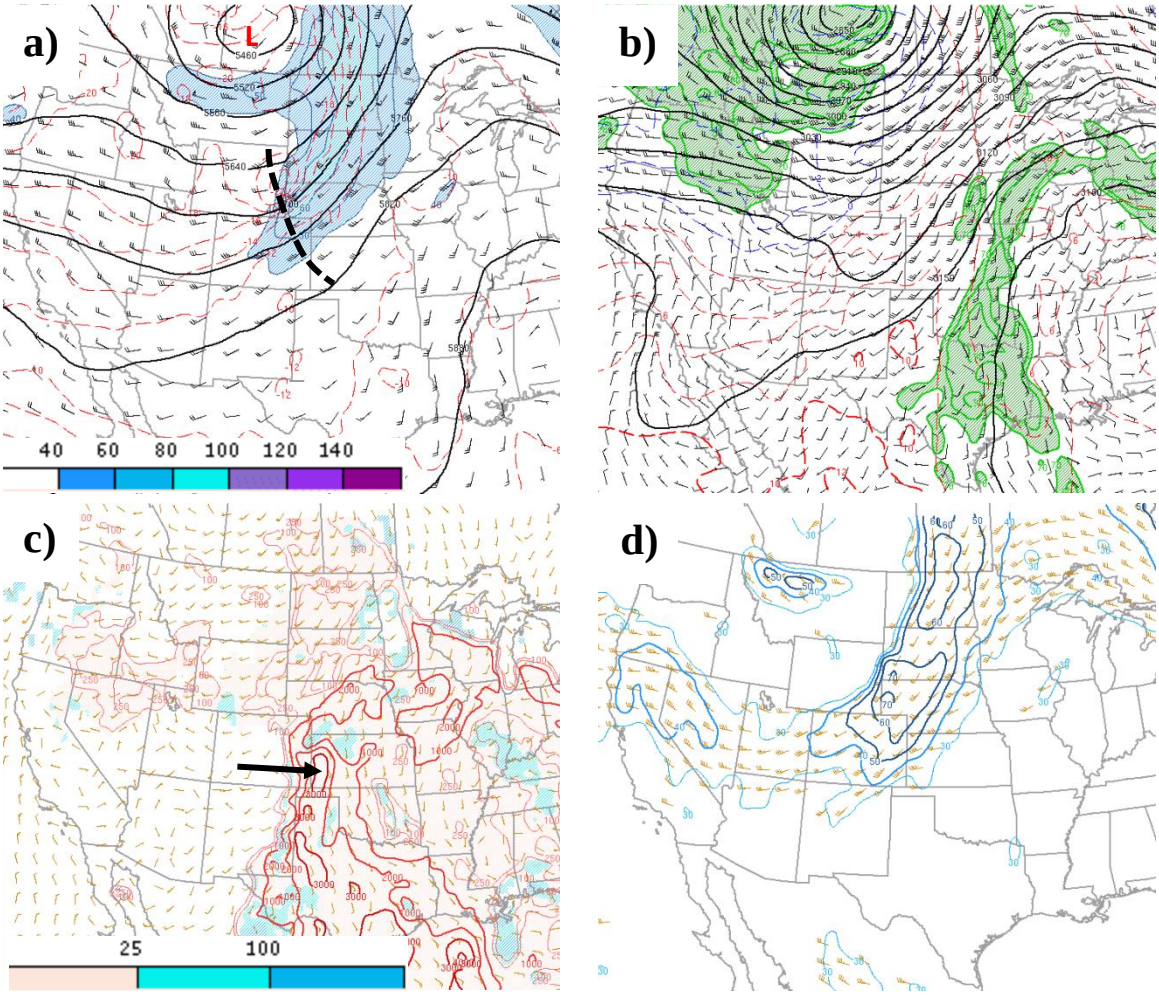

Figure 3.1: a) 500 hPa height (black lines, dam), temperature (red lines, °C) and winds (barbs and fill, kt) valid at 1800 UTC, near the time of convection initiation. The low and weak shortwave are marked. b) 700 hPa height (black lines, dam), temperature (red and blue lines, °C), dewpoint (green lines and fill, °C), and wind (barbs, kt) valid at 1800 UTC. c) Surface based CAPE (red lines, J kg^{-1}) and CIN (fill, J kg^{-1}) valid at 1800 UTC. d) 0 – 6 km bulk shear (contours, kt) and storm motion (barbs, kt) valid at 1800 UTC. Adapted from the Storm Prediction Center (SPC) event archive.

Surface observations and boundaries are shown in Figure 3.2 at 1800 UTC. A stationary boundary predominately associated with a wind shift developed around the surface low oriented south to north near the Colorado and Kansas state line. An additional remnant outflow boundary from convection the night before was present running west to east from near the surface low into west central Kansas and was associated with a

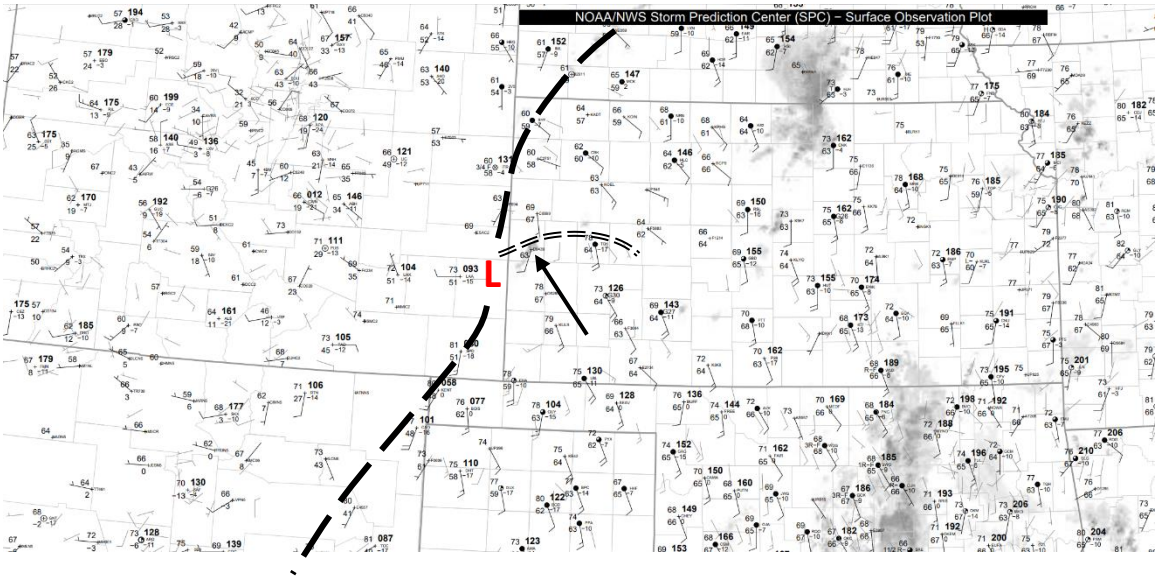

Figure 3.2: Surface observations at 1800 UTC, near the time of initiation. The first radar echoes are denoted by a black arrow. The surface low and weak stationary fronts (dashed black lines) along with the remnant outflow boundary (double black line) are marked. Adapted from the SPC surface map archive.

significant wind shift boundary and temperature gradient. East of the stationary fronts and south of the outflow boundary, surface temperatures rose into the 70's and dewpoints into the mid 60's as southeasterly mass flux continued throughout the day along with solar heating. The nearest sounding from Dodge City at 0000 UTC (Fig. 3.3) sampled the moist boundary layer, which was overlain by a modest elevated mixed layer with steep mid-level lapse rates over 7 K/km. As a result, a corridor of CAPE exceeding 3000 J kg^{-1} was in place over southwestern Kansas as shown in Figure 3.1c. Convection initiation first occurred in this unstable airmass aided by the enhanced convergence at the intersection of the remnant outflow boundary and stationary frontal zone in a weakly capped environment at 1755 UTC. As time progressed, the outflow boundary would continue to act as a focal point for convection initiation.

Despite the favorable thermodynamic environment, weak shear present in much of western Kansas was not supportive of supercells and tornadoes. Southwesterly 0 – 6 km

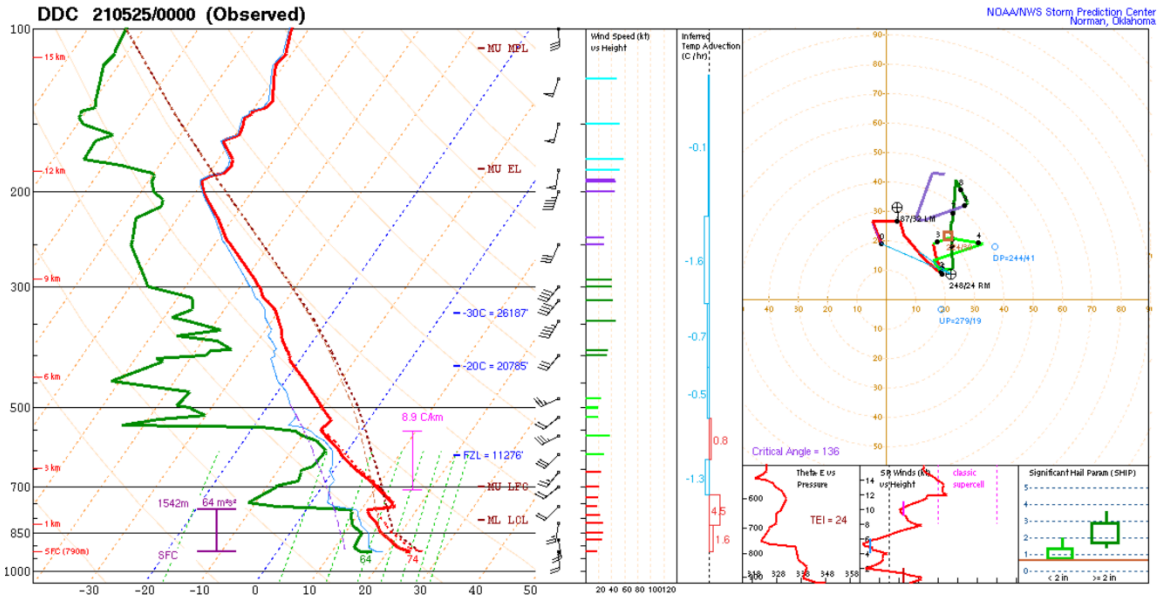

Figure 3.3: KDDC (Dodge City, Kansas) sounding from 0000 UTC on 25 May. This was the nearest sounding in time and space to the Selden storm that was within the favorable storm environment. Taken from the SPC event archive.

bulk shear of 30 to 40 knots was in place (Fig. 3.1d), which is not sufficient for strong updraft rotation. Additionally, 700 hPa winds were only 25 knots out of the southwest (Fig. 3.1b), and weak synoptic forcing prevented the development of a strong low-level jet as the afternoon progressed. Consequently, only 50 to 100 $m^2 s^{-2}$ of 0 – 3 km storm relative helicity was present (Fig. 3.4c) throughout the day as shown by the near unidirectional and weak wind profile from Dodge City at 0000 UTC (Fig. 3.3). The result was a marginal supercell environment. However, there was a significant south to north gradient of 0 – 6 km shear because of the jet streak, with bulk shear of 50 knots in place over northwestern Kansas (Fig. 3.1d). Initial storms occurred south of the conducive shear zone and low-level shear remained weak; any tornado potential would be conditional on if storms moved or initiated to the north and confined to storms interacting with the remnant outflow boundary where low-level convergence and vorticity were enhanced.

3.2: Storm Evolution and the Selden Supercell

By 1800 UTC on 24 May, the airmass over southwestern Kansas was very unstable with surface-based CAPE of over 3000 J kg^{-1} and was only weakly capped because of solar heating (Fig. 3.1c). In the weakly capped unstable environment, any lifting would result in storm initiation. At 1755 UTC, the first radar echoes appeared in west central Kansas within the unstable airmass at the intersection between the remnant outflow boundary and stationary frontal zone where lifting was strongest. The first cell grew rapidly in response to the unstable environment with other cells quickly initiating along the outflow boundary. Because of the high instability, lack of a significant cap, and moderate shear, storms rapidly built into semi-discrete storms and storm clusters. By 2000 UTC, three discrete storm clusters were ongoing and beginning to interact, forming a broken line. Storms continued to stay semi-discrete, however, resulting in numerous hail reports and a few very brief tornadoes where semi-discrete marginal supercells were interacting with the remnant outflow boundary. As storms persisted, the remnant outflow boundary continued to move northward, initiating more storms as it did so. The surge of the remnant boundary to the north may have been instigated by thunderstorm outflow, but lack of substantiating data makes this far from certain. The evolution of surface features is shown in Figure 3.4a.

The storm that would produce the Selden tornado first appeared on radar at 2015 UTC along the remnant outflow boundary just to the east of the loose convective line. In the intervening time between the initial storms and the formation of the Selden storm, the remnant boundary had moved to the north, bringing unstable air into the higher shear zone in northwest Kansas (Fig. 3.4b). Consequently, the nascent Selden storm quickly evolved into a supercell as it moved northeasterly. As the Selden storm took on supercell structure

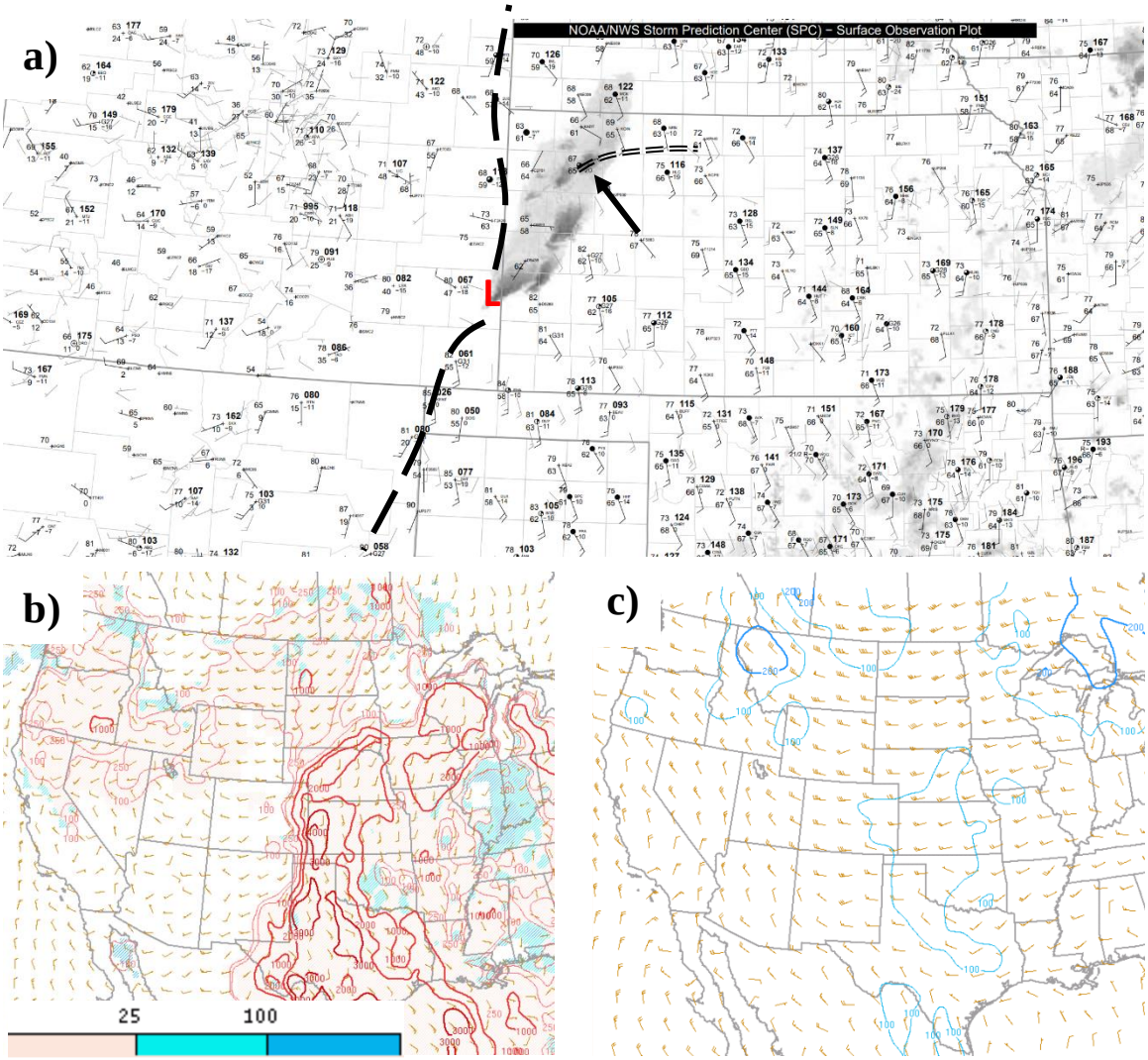

Figure 3.4: a) Surface observations valid at 2100 UTC, 2 hours before the start time of the Selden tornado. The Selden storm is marked with a black arrow and the remnant outflow is denoted (double black line). b) Surface based CAPE (red lines, J kg^{-1}) and CIN (fill, J kg^{-1}) valid at 200 UTC. c) 0 – 3 km storm relative helicity (lines, m^2 s^{-2}) and storm motion (barbs, kt) valid at 2300 UTC. Adapted from the SPC event archive and surface map archive.

and turned right, its motion roughly paralleled the remnant outflow boundary and the storm started to interact with it, allowing the storm to overcome the poor low-level shear environment to achieve tornadogenesis (Fig. 3.4c). At 2115 UTC, the Selden storm produced its first brief tornado near Colby, Kansas. At least two additional tornadoes or

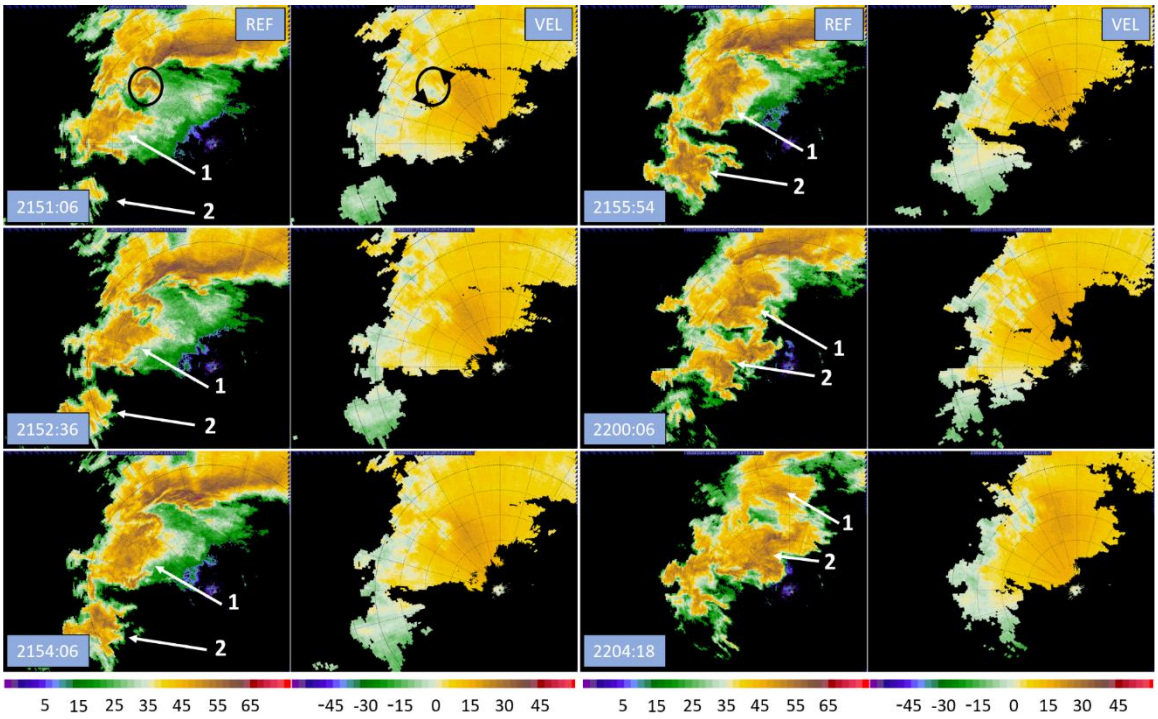

Figure 3.5: RaXPol reflectivity and velocity during D3 showing a period in which the Selden storm underwent mergers with non-supercells approaching from the southwest (white arrows and numbers). Merger 1 is on the left, merger 2 is on the right. The weak velocity couplet is marked in the first panel before it is disrupted by the collision of the first cell (black circles). Range ring spacing is 2.5 km.

funnel clouds occurred as the Selden storm continued northeasterly along the outflow boundary, with the final tornado report prior to the Selden tornado occurring at 2145 UTC.

Shown in Figure 3.5, the Selden storm began undergoing mergers with approaching weaker cells to its southwest around 2140 UTC. At least two separate mergers occurred between 2140 and 2215 UTC, with the first merger shown on the left of Figure 3.5 and the second on the right. By the time of the 2145 UTC report, the first approaching cell and the Selden storm were colliding, and the structure of the Selden storm was disrupted while rotation within the mesocyclone weakened considerably. Mergers continued over at least the next half hour, during which the Selden storm became disorganized. By 2215 UTC, the Selden storm finished undergoing mergers but was very disorganized, taking almost 45

minutes to regain supercell structure as it restrengthened before producing the Selden tornado shortly after 2300 UTC. During the mergers, no tornadoes were reported. The final tornado report leading up to the first merger also occurred coincident with the initial collision between the Selden storm and the first approaching cell. This is like the findings of Wurman et al. (2007b), in which it was observed that mergers between a supercell and another non-supercell storm would cause a brief tornado as near surface convergence temporarily increased before the merger would disrupt the supercell's structure and cause the tornado to decay.

Over a 45-minute period, the Selden storm slowly reorganized and strengthened as it remained in the vicinity of the remnant outflow boundary. In addition to the enhanced low-level shear and vorticity at the remnant outflow boundary, the winds in the low-level jet were increasing slightly as the evening progressed. At 2304 UTC, the storm underwent tornadogenesis again, this time producing the more significant Selden tornado. At the time of the Selden tornado, the parent supercell was at the peak of its strength while realizing the higher shear environment enhanced at low levels by the remnant outflow boundary and slightly strengthened low level jet. Consequently, the Selden tornado persisted for over 30 minutes and reached EF-1 strength; it was not transient like prior activity. The tornado tracked into the town of Selden where one person was injured, and the tornado sustained a multiple vortex phase. After passing through Selden, the tornado reverted to a single-celled vortex as it turned left and occluded, completely dissipating by 2340 UTC. Further details of the Selden tornado lifecycle will be explored in Chapters 4 through 6. This would be the end of tornadic activity from the Selden storm. During the lifecycle of the Selden tornado, new convection initiated in front of the parent supercell. The new convection appears to

have formed along merging outflows from the broken line of storms that overtook the Selden supercell from the west and southwest. By the conclusion of the Selden tornado, a new line of storms was building along the merging outflows, blocking the Selden storm from unstable inflow. Consequently, the Selden storm began to weaken and completely dissipated by 0030 UTC behind the new convective line.

3.3: Selden Tornado Overview

On the afternoon of 24 May 2021, a supercell was tracking northeasterly towards the town of Selden. As it rode along the remnant outflow boundary, the storm attempted tornadogenesis several times. However, the storm was disrupted when it started undergoing mergers, and the low-level mesocyclone diminished before any significant tornado was produced. After undergoing a reorganization period for over an hour, the storm regained supercell characteristics and the low-level mesocyclone redeveloped as it continued to track in vicinity of the low-level remnant outflow boundary towards the town of Selden. At or around 2304 UTC (1804 CDT), the supercell spawned a tornado 5 miles to the west southwest of Selden near US highway 83. The tornado tracked parallel to highway 83 into the town of Selden over the course of the next 20 minutes where it would damage numerous structures and injure 1. After passing through Selden, the tornado slowly occluded and turned to the left into its parent supercell. The tornado circulation completely dissipated around 2340 UTC (1840 CDT) about 2.5 miles to the northeast of Selden before crossing US Highway 83 as the road turns north on the east side of town. The RaXPol derived track of the 36-minute Selden tornado at the 4° elevation is shown below in Figure 3.6.

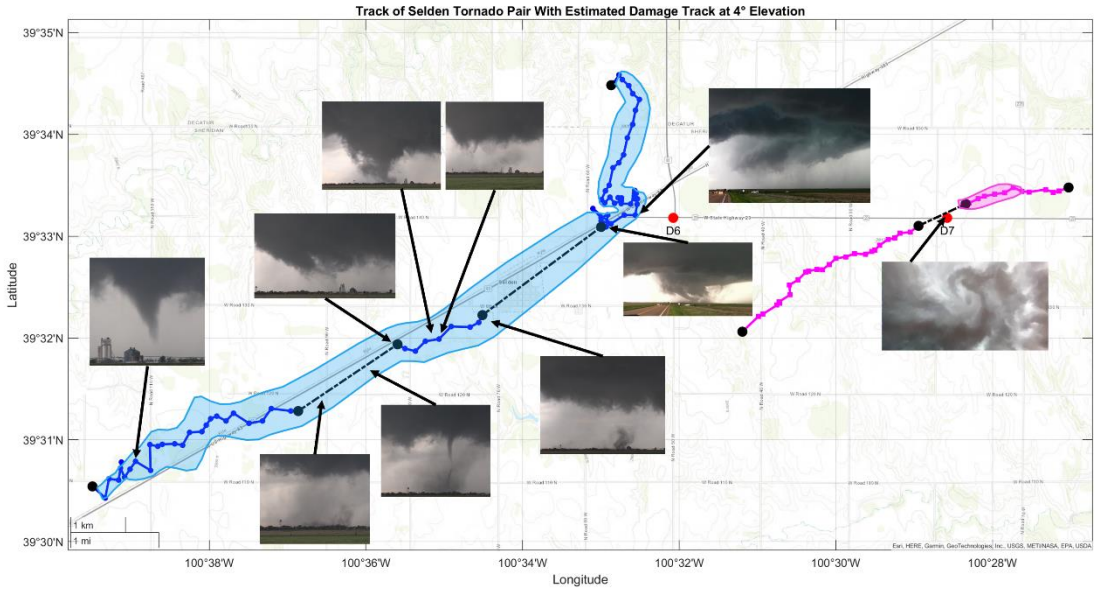

Figure 3.6: RaXPol derived track of the Selden tornado at 4° elevation overlayed with the estimated damage swath based on the low correlation coefficient area associated with the tornado. Various pictures of the tornadoes are also included on the track. Photos courtesy of Howard Bluestein, Sam Emmerson, and Trey Greenwood.

RaXPol was deployed twice just to the east of Selden where it collected data throughout the lifecycle of the Selden Tornado. In total, 32 minutes of data were collected, with almost 30 of those minutes containing a tornado circulation. Throughout the deployments, RaXPol observed the tornado to shift track several times while also capturing several interesting features. The RaXPol derived track from the 4° elevation is shown above in Figure 3.6, overlayed with the approximate damage swath estimated from the edges of the correlation coefficient minima associated with the tornado circulation. The map also includes the track of a companion anticyclonic vortex. Serendipitously, this vortex caught the radar crew by surprise and the radar was not moved, resulting in it passing right over the radar site. Consequently, the data provide a rare opportunity to take a very high-resolution look at a vortex. Various pictures of the tornado are included on the map in Figure 3.6, which display the wide variety of structures the tornado had during its life.

Early in D6, the tornado did not have a consistent condensation funnel. Especially leading up to and during the D6 data gap, the tornado had no visible funnel. Pictures then reveal a transition to multiple vortex structure with a large funnel developing and then rapidly dissipating as secondary vortices become visible. During early D7, pictures show the rapid dissipation of the condensation funnel as the tornado begins to turn northward. Finally, a picture of the anticyclonic vortex taken looking straight up from the radar site reveals the intensity of the anticyclonic circulation as the clouds form a circular pattern around a central downward extension which may be a small funnel cloud.

During its lifespan, the Selden tornado underwent several track shifts which are visible in Figure 3.6. During D6, the tornado followed the motion of the parent storm but then sustained several track shifts in D7. Early in D7, the tornado executed a cyclonic track loop and then accelerated out of it to the northeast. Suddenly, the tornado became nearly stationary for just over two minutes before starting to retrograde. After two minutes of retrograding movement, the tornado finally turns north and dissipates. However, the behavior of the tornado during D7 shows stark differences with height. Figure 3.7 shows the RaXPol tracks at 4° intervals of elevation angle. In upper elevation scans, the tornado instead continues to gradually curve northward out of the cyclonic track loop in early D7. Interestingly, the tornado then executes a second cyclonic track loop shortly after the first in upper elevation scans while the tornado becomes stationary and retrogrades in lower elevation scans. After exiting the second track loop, the tornado then turns north and dissipates as the behavior between upper and lower elevation scans once again becomes similar. Figure 3.7 also shows that the tornado was generally tilted towards the north for most of its life until dissipation, at which point tilt became easterly.

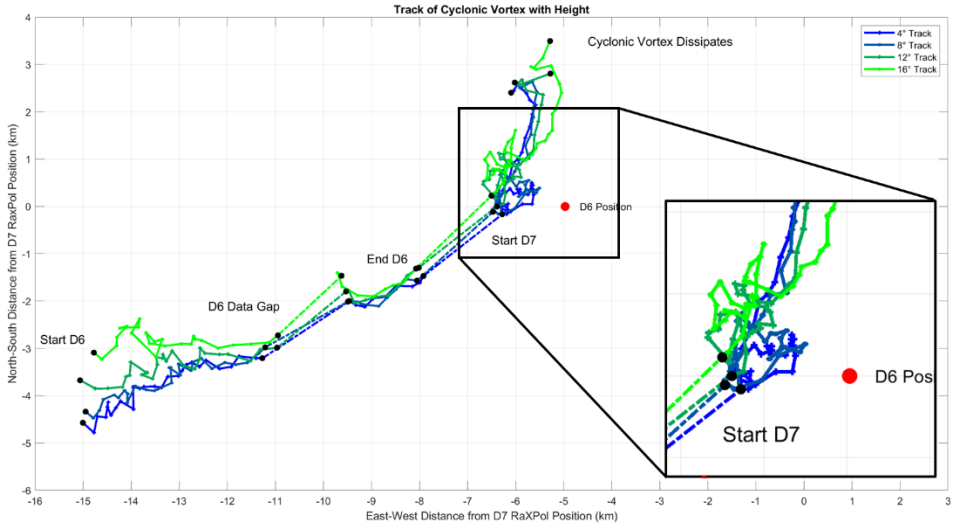

Figure 3.7: Comparison of the RaxPol derived tracks at 4°, 8°, 12°, and 16°. The 4° and 16° elevation tracks are representative of lower and upper elevation scans, respectively.

The marked differences in track behavior with time and height allow for the dividing of the track into several segments, which is then leveraged to perform cross section analysis of the tornado based on tornado movement behavior. An example of a divided track at the 4° elevation for the cyclonic tornado is provided below in Figure 3.8. While the details of each segment and how segments changed with height will be discussed in following chapters, eight distinct segments were identified. The first two segments contain the early development of the Selden cyclonic tornado, with the second segment having a slightly different track heading to the right of the heading in segment 1. Segment 3 was defined by the data in between the D6 data gap and the end of D6. Segment 4 runs from the start of D7 through a cyclonic track loop to a point when the tornado suddenly stops moving. Segment 5 contains this stationary behavior, while segment 6 marks a time when the tornado retrograded. Finally, segment 7 begins when the tornado makes a northward turn, and segment 8 marks a final left hook as the tornado fully dissipates.

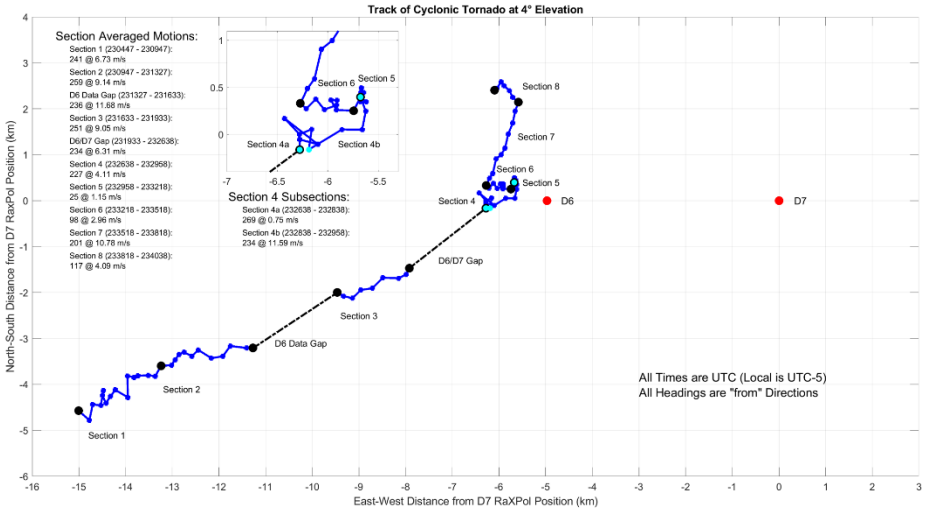

Figure 3.8: RaXPol derived track (using objective geometric centers) for the cyclonic tornado at 4°. Track segments 1 – 8 are marked, identified by changes in tornado behavior. Red dots mark the locations for D6 and D7.

A summary of track segments at all scan elevations is presented in a timeline shown below in Figure 3.9. During D6, there are three segments at all elevations. For all scan elevations, the first two segments represent the development and intensification phases of the tornado. The next segment contains the data between the D6 data gap and the end of the deployment. Once D7 begins, the vortex begins to shift track and behavior diverges with height. The first segment in D7, segment 4, contains the first track loop and is broken down further to isolate the track loop which is highlighted in red on the timeline. After this, the track segments split into two groups based on elevation with a transition height that is somewhat like a hybrid of the two archetypes. At lower elevations, segment 5 represents a time when the tornado was stationary. Segment 6 is a retrograde phase while segments 7 and 8 represent the northward turn and dissipation of the tornado. At the transition scan elevation of 8°, the vortex becomes quasi-stationary during segment 5 before retrograding. Then, a new distinct phase of eastward movement occurs during segment 7 and the tornado track begins to take on the shape of a secondary track loop. Segments 8 and 9 then contain

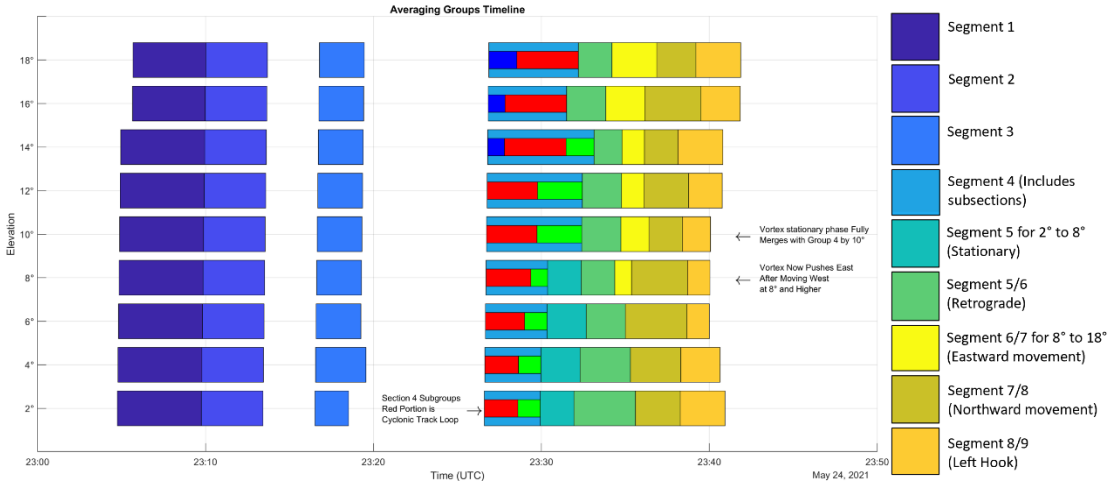

Figure 3.9: Timeline of track segments at all elevations. Different colors represent the various segments, with boxes of the same color representing segments with similar behavior. Segment 4 is also broken down into subsections to isolate the track loop, which is represented by the red boxes.

the tornado's northward turn and dissipation. In higher elevation scans, the stationary phase disappears and becomes absorbed into segment 4. Consequently, the tornado moves directly into the retrograde phase in segment 5. Segment 6 then contains easterly movement, which together with segment 5 makes up the second track loop present in upper elevation scans. Finally, segments 7 and 8 represent the tornado's dissipation. In general, the stationary phase of the tornado gradually vanishes with height while the retrograde phase takes on a smaller westward component at higher scan elevations.

Chapter 4

The Selden, Kansas Tornado During D6 – Before the Data Gap

4.1: Track Behavior

Before the D6 data gap from 2304:45 to 2313:41 UTC, the Selden tornado closely matches the motion of the parent supercell while intensifying. There are two track segments prior to the data gap at all elevations. The segment 1 and 2 tracks from the 4° and 16° elevation are detailed in Figure 4.1 below. The estimated track vectors used here and throughout this study are accurate to within ±1 m s^{-1} for speed and ±5° for heading given that center positions of the tornado could only be determined to within 0.5° azimuth and to one-half of a range gate (30 m). For especially short segments where not much distance is covered by the tornado, the error in estimates grows but is still within acceptable limits.

The first segment represents a time when the tornado was developing, lasting from the start of data collection at 2304 to approximately 2310 UTC. Motion during this time was markedly slow when compared to the motion of the parent storm, which was moving to the east northeast at in between 9.5 and 10 m s^{-1}; the track vector at 4° elevation was roughly 7 m s^{-1} from 240° (WSW). This is a trend that becomes more pronounced at higher elevations. At the 16° elevation, the motion of the vortex was only 4.5 m s^{-1}. An additional key difference between the track at 4° and 16° is that the track direction at the 16° elevation was from 260° as compared to 240° at the 4° elevation. Widely disparate tracks at different

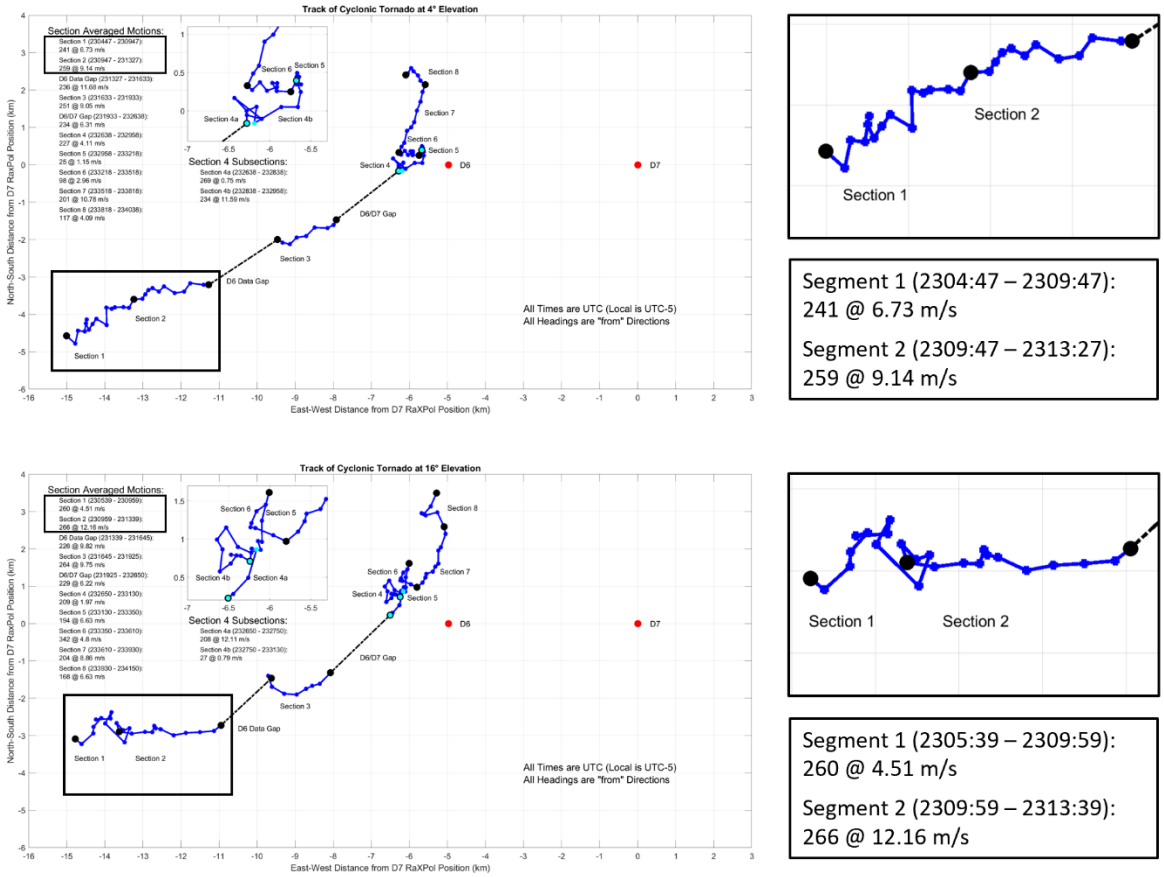

Figure 4.1: Track of the Selden tornado at the 4°(top) and 16° (bottom) elevation scans. Zoomed insets of the tracks prior to the D6 data gap are provided on the right, along with descriptions of the segment motion vectors.

heights above the surface and motion that does not match the parent supercell are indicative of a tornado that has yet to reach a stable mature position with regards to the supercell updraft and RFGF; the tornado fails to strengthen significantly as it continues to change position relative to the parent supercell (e.g., Dowell and Bluestein 2002).

The nearly 20° contrast in track heading and notable 3 m s^{-1} difference in speed during segment 1 between the 4° and 16° elevations reflect a tornado still in early stages of development. At both the 4° and 16° elevations, the tornado track is unsteady. Instead of following a relatively straight line, the center of the tornado wobbles back and forth, giving the track a jagged appearance on a map. Some of the aberrations in the track are

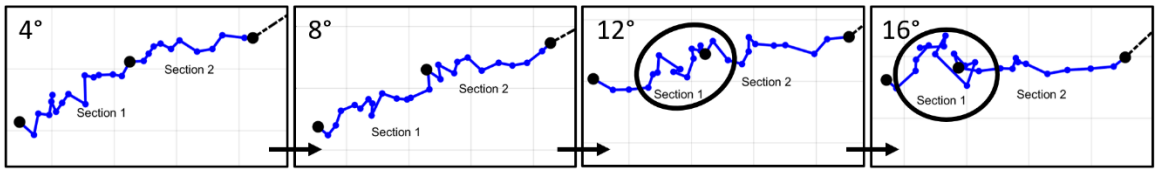

Figure 4.2: Schematic showing the track for segments 1 and 2 at every 4° in elevation. The increasingly chaotic areas of track are circled in the 12° and 16° maps. Grids have 1 km spacing.

certainly a function of angular resolution since the center position of the vortex can only be determined to within a half degree, but the numerous track deviations are far larger than can be expected from this alone. Furthermore, the distance travelled in every 20 second scan is variable, with the tornado sometimes barely moving at all. The unsteadiness of the track is a feature that becomes more apparent with height, evincing the greater deviations of the tornado track from the motion of the parent supercell in higher elevation scans. At the 16° elevation, the vortex was observed to move westwards twice, and there appeared to be no rhyme or reason to the pattern of vortex motion. Early in segment 1, the 16° track heads northeasterly before the vortex center meanders about. Then the vortex center shifts to the southeast. After repositioning to the southeast, the vortex center once again meanders about, remaining nearly stationary and moving backwards slightly as segment 1 ends. Furthermore, the trend of increasing track unsteadiness with height is not linear. Shown in Figure 4.2, the course of the tornado during segment 1 gradually becomes more unsteady with height from the 4° elevation to the 12° elevation, at which point the track suddenly becomes much more unsettled.

The tendency for track deviations to grow more extreme with height testifies to a non-descending pattern of vertical development for the Selden tornado. Moderate unsteadiness of the tornado tracks below the 12° level, which is roughly 1800 m Above Radar Level (ARL) during segment 1, overlain by tracks of a highly volatile nature seem

to indicate that a coherent tornado circulation first appears at low levels before developing upward. Small differences between the appearance of the tracks below 12° are minimal and indicate near simultaneous development with height at low levels. This is like the findings of Houser et al. (2022), in which it was found that tornadoes developed in non-descending patterns, either nearly simultaneously or upward from 0 to approximately 1.5 to 2 km. The marked difference in the stability of the tracks between the 10° and 12° level, which are roughly 1800 m and 2100 m ARL respectively, is also of note. The presence of a dividing line near the 2 km level may reveal the top of the tornadic circulation, or at least, that the tornadic circulation does not attain significant depth until well into its lifecycle. It is possible that the Selden tornado struggles to attain significant vertical depth above 2 km due low shear in the synoptic environment (See Figure 3.1). Weaker shear results in a less intense supercell mesocyclone, which results in a weaker tornado and one that may not become very deep.

If track steadiness is taken as a proxy for how well established the tornado is, as is implied here, then the tendency for the track to become slightly less stable with height and then chaotic above the 2 km level would support the notion that the tornado develops first nearer to the ground or nearly simultaneously at low-levels (non-descending pattern) and may not be very deep as in Houser et al. (2022). Further evidence from a plot of ΔV_{max} in Figure 4.3 is supportive of the idea that the vortex develops in a non-descending pattern as shear values increase nearly simultaneously across the depth of observations up to 2.5 km, above which velocities decrease to under the commonly accepted tornadic threshold of 40 m s^{-1} of total shear across the vortex (Wurman and Kosiba 2013). The way in which tornadogenesis proceeds, whether upwards, downwards, or simultaneously, has been a

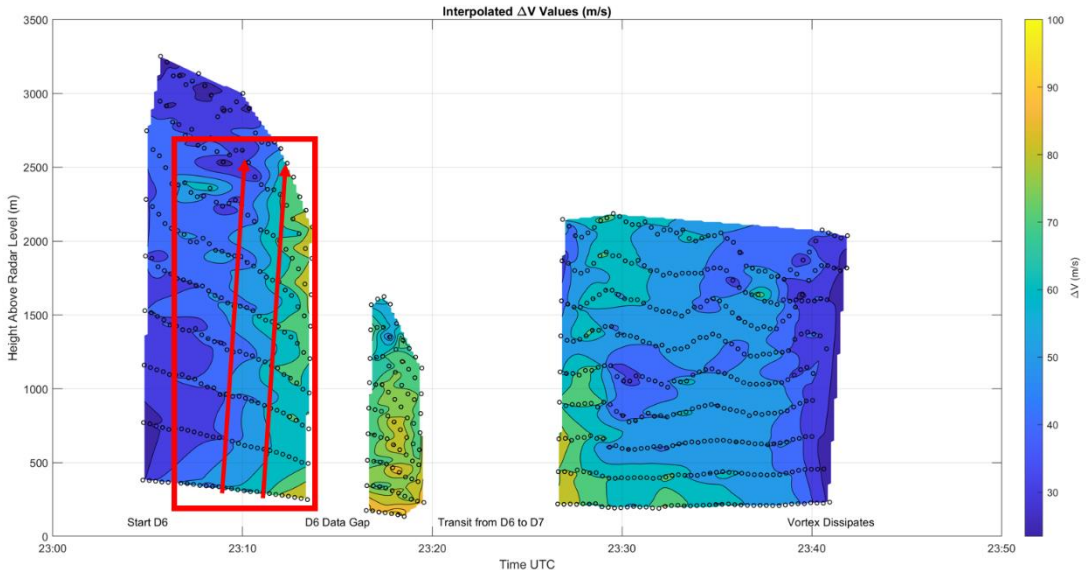

Figure 4.3: Interpolated plot of ΔV_{max} for the Selden tornado, measured from the wind maxima on either side of the vortex. The red box denotes the portion of the graph corresponding to track segments 1 and 2 while the red arrows highlight the nearly simultaneous or slight upward trend in vortex development and intensification during segments 1 and 2.

frequently asked question. In this case and in the Houser et al. (2022) case, tornadoes were found to build upwards or nearly simultaneously with height. While an in-depth analysis of the Selden tornado's genesis is precluded by a lack of data during that time, perhaps the level of environmental shear in which the parent supercell is embedded plays a role in tornado development. Since the Selden supercell is in a low shear environment, upward or near simultaneous vertical development may be favored because the Selden supercell's mid-level mesocyclone is relatively weak, and the tornado must rely to a greater degree on near-surface processes to drive intensification. Finally, the small area of higher shear centered just under 2.5 km early in segment 1 is likely a result of tracking velocity maxima associated with the supercell mesocyclone at low levels, not the tornadic circulation; it is not necessarily an indicator that the tornado developed first aloft.

During segment 2, which lasted from 2310 to 2313 UTC, the track of the tornado becomes typical of the parent supercell motion as the tornado reaches a stable position under the supercell updraft at the apex of the supercell RFGF and forward flank convergence zone. Particularly at low levels, the motion of the supercell and tornado are nearly identical; the 4° track vector is 9 m s^{-1} from 260° (W). The change in track vector between segments 1 and 2 at the 4° level is evidence for a transition of the tornado to a 'mature' position. During segment 1, the tornado is moving northwestwards with respect to the parent supercell. Then, in segment 2, the tornado turns right by almost 20° and its forward speed increases to over 9 m s^{-1}, such that the motion of the tornado is nearly identical to that of the parent supercell. In their study, Dowell and Bluestein (2002) noted that their tornado began its lifecycle by being advected north or northwestwards up the RFGF towards the supercell updraft and the forward flank convergence zone as the supercell RFD intensified and matured. Once the tornado reached the northern apex of the RFGF underneath the supercell updraft, it was said to be in a mature position and rapid intensification took place. The Selden case shows a similar progression, with the tornado moving northwestwards with respect to the parent supercell during segment 1. Then the tornado reached a 'mature' position by the start of segment 2, at which point the tornado became coupled to the northern apex of the RFGF and the forward flank convergence zone; the tornado began moving along with the parent supercell and the pace of intensification increased (See Figure 4.3). The idea that the transition from segment 1 to segment 2 represents the evolution of the tornado from a precarious development stage to a more stable mature phase will be revisited in the following sections.

The stark change in the 16° track from segment 1 to 2 also clearly shows that the behavior of the tornado changed significantly. Suddenly, at the start of segment 2, the tornado begins to move to the east at a steady pace and the track becomes remarkably stable as the tornado traces out a nearly straight line. The steadiness of the segment 2 track and closer match to storm motion are typical of a more established vortex that stands in juxtaposition to the chaotic track in segment 1. Yet, there is a significant difference in vortex forward speed during segment 2. However, this appears to simply be a result of the more chaotic and overall slower motion at 16° during segment 1. During segment 1, the vortex at 16° fell behind its near ground position. Following this in segment 2, the vortex at 16° slowly caught up to its near ground position. A tilt analysis of the vortex from 4° to 16° is supportive of this finding. Throughout segments 1 and 2, the tilt off vertical decreased from over 40° to 15°. Given variability of ±5° in tilt due to errors in determining the tornado center, the large decrease in tilt is significant. While this is indicative of a vortex that is becoming more vertically aligned and coherent, caution must be exercised Because the tornado is moving directly towards the radar during D6; the decrease of tilt likely contains a component that is the result of decreasing sample depth, where the upper sample bound descends below a potential threshold height where the tornado bends and acquires significant tilt.

4.2: Evolution of the Near-Vortex Wind Field and RFD on Radar

Shown in Figure 4.4, radar analysis during segment 1 reveals an interesting development sequence for the flow field near the tornado. At the start of the analysis, there is a zone of enhanced convergence running from southwest to northeast to the west of the

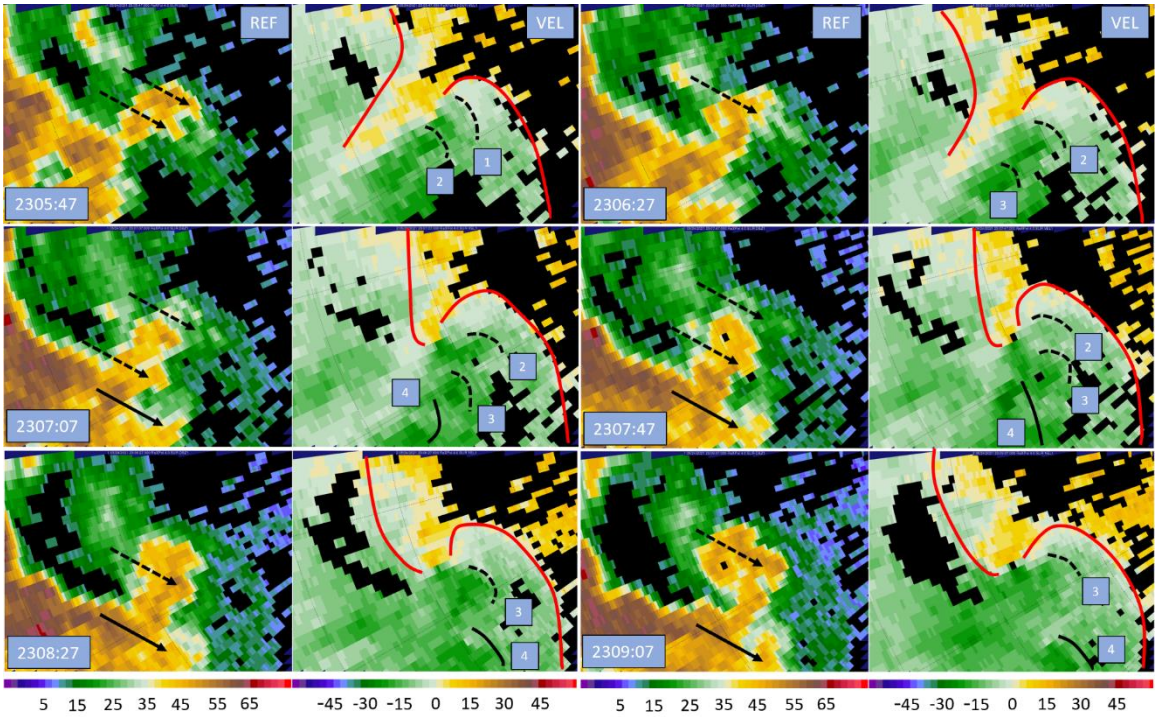

Figure 4.4: RaXPol imagery at the 4° elevation taken every 2 scans (40 s) during segment 1. In each radar panel, reflectivity is on the left and Doppler velocity on the right. Range ring spacing is 2.5 km. Black lines denote RFD surge fronts, which are also numbered. Black arrows also point to associated reflectivity appendages. Finally, red lines mark the approximate positions of the forward flank boundary and RFGF.

tornado, and a defined tight circulation has yet to develop although video taken of the Selden tornado confirms that a condensation funnel has already formed. In the first panel, the forward flank boundary has yet to wrap towards the low-level mesocyclone and is marked along the area of enhanced convergence behind the tornado location at the back of the receding velocities in the storm inflow. As time passes, the forward flank boundary eventually becomes linked to the tornadic circulation as the supercell becomes wrapped due to the action of the intensifying low-level mesocyclone. As has been suggested by Orf et al. (2017) and Scheuth et al. (2021), the linking of the forward flank convergence band to the tornado will make it possible for vorticity generated baroclinically in the supercell FFD to be ingested by the tornado or low-level mesocyclone. While a detailed examination

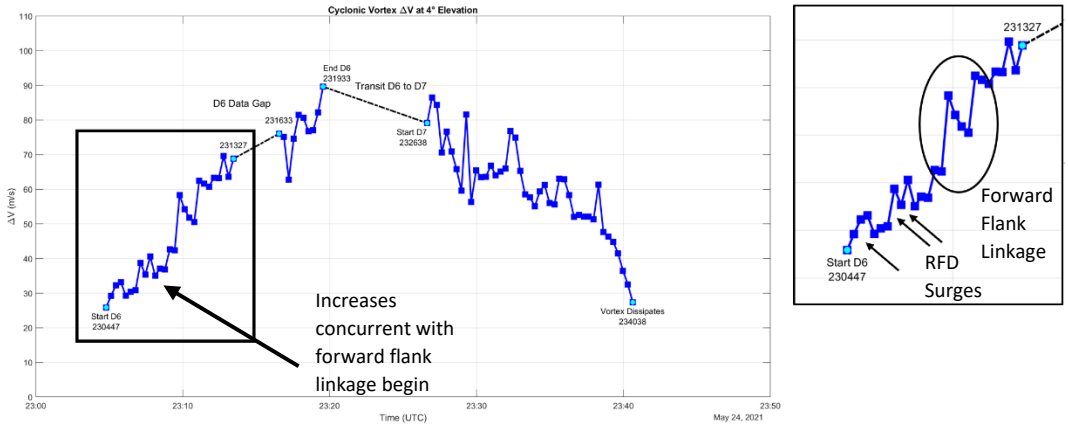

Figure 4.5: Timeseries at 4° of the ΔV_{max} for the Selden tornado. The portion of the series corresponding to segments 1 and 2 is boxed and a zoomed inset of the boxed portion is provided to the right of the figure with surge related bursts in ΔV_{max} circled. Gridlines in the inset are spaced 10 m s^{-1} apart.

of the possible presence of SVCs is presented in a later section, the tornado starts to strengthen once the forward flank boundary becomes established. A timeseries of ΔV_{max} shown in Figure 4.5 is supportive; the tornado's rate of strengthening increases markedly at 2308 UTC shortly after the forward flank convergence zone becomes established at 2307 UTC. The timing of forward flank establishment near the tornado and strengthening in Figure 4.5 also occur shortly before the rightward track shift between segments 1 and 2 at 2310 UTC, providing more evidence that the tornado was slowly migrating towards a stable mature position relative to the parent supercell during segment 1. As the tornado moved northwest relative to the parent storm and neared a mature position, it became coupled to the forward flank convergence zone; shortly thereafter, the tornado turned right as it reached its mature position at the northern end of the RFGF.

Of key interest in Figure 4.4 is the rapid evolution of the supercell RFD. By the start of D6, the RFD has already been established and is linked to the tornadic circulation. As described by Dowell and Bluestein (2002), the enhanced convergence at the RFGF likely played a role in tornadogenesis and is causing the tornado to intensify along with the

vorticity being baroclinically produced and tilted into arches at the RFGF like those found by Markowski and Richardson (2008). While the RFD has been established by the start of the analysis, it is relatively weak. Despite the weak RFD, however, surges are still apparent. There are at least 4 small surges throughout the analysis, three of which move through the RFD towards the RFGF while being advected around the tornado circulation. As these surges pass near the tornado, it is likely that the enhanced convergence and vorticity at the northern apex of the surges is causing the tornado to intensify slightly or experience a pulse in strength (Finley and Lee 2008; Houser et al. 2015; Kosiba et al. 2013; Markowski 2012). A timeseries of the shear across the vortex at the 4° level shown in Figure 4.5 indicates that there were responses to the surges, with total shear undergoing pulsing behavior while the tornado generally strengthens. When surge 1 passed by the tornado, shear across the vortex increased by roughly 7 m s^{-1}. However, since the tornado is also strengthening due to other processes such as the establishment of the forward flank boundary, it is unclear how much of the jump in shear is attributable to the surge. As surge 2 approaches and passes the tornado, shear jumps by 8 m s^{-1} in one scan. This is followed closely by surge 3, which causes a smaller shear response of roughly 4 m s^{-1} when it impacts the tornado. It should be noted, however, that most of these jumps represent relatively small changes in ΔV that are often transient, occurring in only one radar scan. Since the standard deviation of the velocity data is generally near ± 10 m s^{-1} around the Radius of Maximum Wind (RMW) where ΔV is obtained, caution should be taken when investigating these changes in ΔV. More on the error of cross section estimations will be discussed in the following section.

The RFD expands in coverage and becomes more intense by the end of segment 1. As documented by Dowell and Bluestein (2002), the stronger RFD enhances the vorticity

and convergence near the tornado, causing the tornado to steadily intensify. At the same time, the tornado has been migrating to a mature position within the supercell; during segment 1, the tornado has moved northwestward with respect to the parent supercell (See Figure 4.1). The movement of the tornado towards its mature position underneath the supercell updraft is also visible in Figure 4.4 as the hook echo and vortex signature shift northwards with respect to the forward flank precipitation region with time. Since the primary supercell updraft is located above the inflow region south of the forward flank, the tornado is moving closer to the updraft base with time.

The strengthening of the RFD and the arrival of the tornado underneath the supercell updraft and position at the RFGF and forward flank convergence zone juncture all allow the tornado to intensify as is reflected in the ΔV_{max} timeseries in Figure 4.5. Continued strengthening of the tornado circulation will then in turn cause the RFGF to advance outwards, enhancing near surface convergence in the vicinity of the tornado, which causes the tornado to strengthen further. If the RFGF resists significant displacement from RFD surges or the occlusion downdraft that will develop as the near-ground vorticity continues to intensify, then the tornado can remain in a mature position. However, as soon as the tornado becomes decoupled from the RFGF, the tornado begins to decay and move away from its favorable position in enhanced convergence under the parent updraft as was found in the case studied by Dowell and Bluestein (2002) or simulations of Marquis et al. (2012; 2016). In other words, temporary positive feedback exists between the strength of the tornado and RFGF related convergence near the tornado. However, this situation does not persist forever since continued intensification of the tornado will eventually result in the formation of the occlusion downdraft, the outflow of which will displace the RFGF and

decouple it from the tornado and low-level mesocyclone; the temporary positive feedback is best contextualized as an important step in the advancement of the tornado lifecycle.

The track of the tornado can also be affected by the configuration of enhanced momentum created by RFD surges (e.g., Kurdzo et al. 2015 and Lee and Finley 2022). While the surges are not yet intense enough to directly affect the track of the Selden tornado, the higher momentum within the surges helps to advance the RFGF forward as they reach and merge with it. Especially important is the action of the surges to potentially displace the RFGF from the low-level mesocyclone and tornado. Each successive surge is advected cyclonically by the tornado circulation to varying extents depending on surge trajectory where they can then merge with the RFGF near its northern end and potentially dislodge the RFGF and force it to move into the inflow channel. However, no such large displacements to the RFGF position occur during segment 1; the RFD surges are too weak and the pressure minimum at the center of the tornado too strong to allow for decoupling between the RFGF and tornado. Therefore, the RFGF continues outwards gradually with time as the low-level mesocyclone and tornado continue to intensify. However, continued intensification of the tornado will eventually result in the formation of the occlusion downdraft (Adlerman and Droegemeier 2005). Momentum within the RFD will surge in response to the occlusion downdraft's outflow and the RFGF will likely become decoupled from the tornado since the environmental shear conditions are not high enough to generate a sufficiently strong supercell mesocyclone capable of achieving a steady, non-cycling structure (See Figure 3.1).

A similar radar analysis produced during segment 2 is shown in Figure 4.6. During the analysis period, the RFGF continues to surge outward from the parent supercell and the

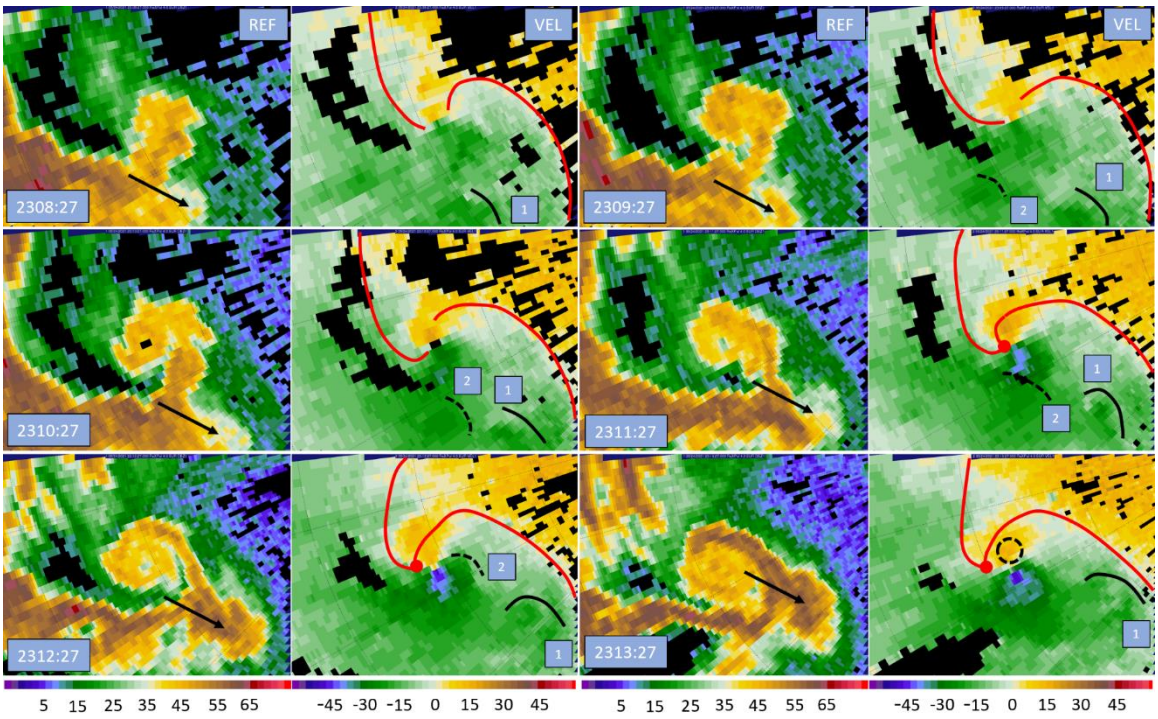

Figure 4.6: RaXPol imagery at the 4° elevation taken every 3 scans (60 s) during segment 2. In each radar panel, reflectivity is on the left and Doppler velocity on the right. Range ring spacing is 2.5 km. Black lines denote RFD surge fronts, which are also numbered. Black arrows also point to associated reflectivity appendages. Finally, red lines mark the approximate positions of the forward flank boundary and RFGF.

forward flank boundary and RFGF become joined at an apex point just behind the tornado. This marks a maturation of the supercell, and the tornado will thrive off of the greatly enhanced convergence at the apex as discussed by Dowell and Bluestein (2002). During segment 2, additional discrete surges appear and eventually merge with the RFGF. The first surge passed well south of the tornado and does not appear to have impacted the tornado. The second surge, however, initially builds to the southwest of the tornado and then passes through the southern half of the vortex on a northeasterly trajectory as velocities on the southern branch of the tornado circulation increase significantly. However, this higher area of velocities persist well after surge 2 passes; it is unclear what affect, if any, surge 2 had on the intensity of the vortex. Despite this, the greatly enhanced

convergence at the norther apex of the surge can be expected to have at least contributed to the sudden uptick in vortex strength and ΔV_{max} shown in Figure 4.5 as the fourth noted shear increase (Finley and Lee 2008). After surge 2 moves through the tornadic circulation, it pivots around the vortex and starts to move northwesterly as it merges with the northern end of the RFGF. For the first time, an increase in easterly momentum is detectable north of the vortex as surging momentum intrudes north of the tornado and attempts to displace the RFGF from the tornado. However, the tornado and low-level mesocyclone are able to remain coupled to the RFGF during segment 2 and RFD surges fail to cause occlusion; the tornado continues to reside in a mature position where it steadily strengthens.

4.3: Cross Section Analysis

The average cross sections presented here and in following chapters are an estimation of the average velocity profiles of the Selden tornado. The rapidly evolving nature of the tornado and scan-to-scan variability in radar measurements produce average cross sections with a substantial amount of variability. In Figure 4.7, an average cross section of the tornado from segment 2 with error bars representing one standard deviation is plotted to provide a visualization of the error within the cross sections. The error bars reveal that the standard deviation within the data can be large, with a magnitude of ±10 to ±15 m s^{-1} within the tornado core and near the RMW. In some instances, the standard deviation can approach almost ±20 m s^{-1} within the tornado core. Outside of the tornado, the standard deviation of the data is generally within ±5 m s^{-1}. The highest variability occurs within zones where it would be expected, namely, within the core of the tornado and near its edges where the cross section is sensitive to changes in vortex size and intensity. Error

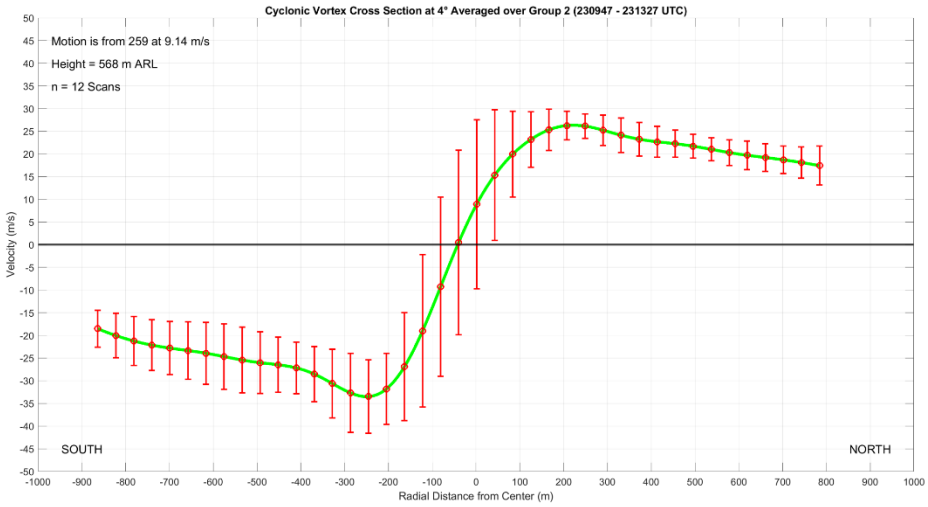

Figure 4.7: Average cross section for the Selden tornado during segment 2 with error bars plotted. Error bars represent 1 standard deviation of the data.

within the cross sections is therefore greatest during segments when the vortex is undergoing rapid changes, such as near the start of the tornado's lifecycle when it is growing and intensifying quickly. Given these error estimates, caution must be taken when interpreting the average cross sections since individual values of velocity possess a large spread within the tornado core and near the RMW. Additionally, transient changes in ΔV_{max} of the tornado less than 10 m s^{-1} should be treated carefully since ΔV is readily impacted by changes in the values for maximum velocity at the RMW.

Presented in Figure 4.8 are the averaged azimuthal cross sections for track segments 1 and 2 at the 4° elevation, which was chosen because it is the lowest elevation available which was not contaminated by significant ground clutter. During segments 1 and 2, the average height of the sampled cross sections was roughly 700 m and 570 m respectively, placing the cross sections well above the frictional inflow layer noted in Bluestein et al. (2004) or Wakimoto et al. (2011). Consequently, it is not possible to see near-surface convergence within 20 to 30 m of the ground. Because the cloud base near the tornado is

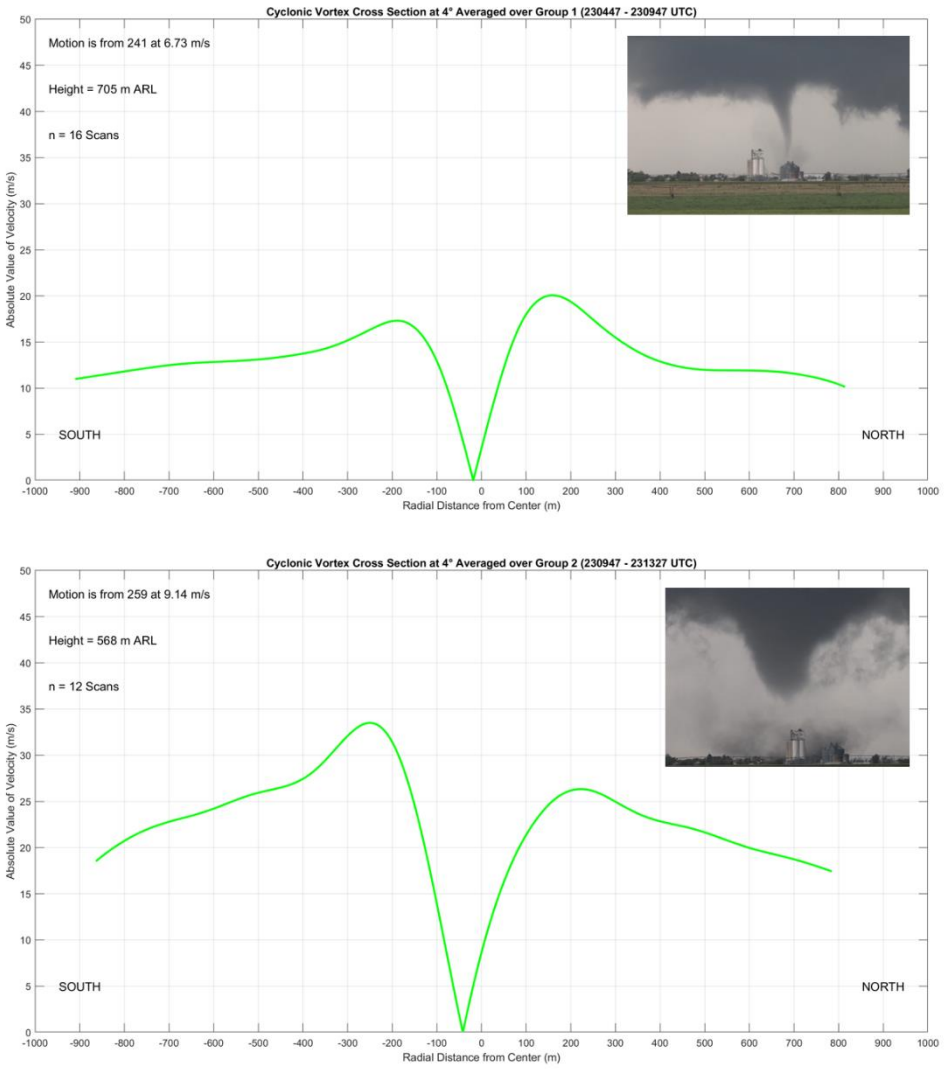

Figure 4.8: Azimuthal Cross Sections through the Selden Tornado at 4° elevation for track segments 1 (top) and 2 (bottom). Pictures of the Selden tornado from each segment are also included. Photos courtesy of Trey Greenwood.

approximately 600 m, the cross sections represent a point through the top of the visible condensation funnel. The azimuthal cross section for segment 1 contains a weakly tornadic vortex with ΔV_{max} of slightly less than 40 m s^{-1}. The marginally tornadic shear is a clear indicator that the tornado is still developing, matching findings from the vortex track and radar analysis. Like previous studies in which cross sections have been retrieved, such as in Kosiba and Wurman (2010) and Tanamachi et al. (2007), the core of the vortex largely

obeys solid body rotation and the velocity maxima on either side of the vortex have similar magnitudes.

An unanticipated finding in the cross sections is that the winds do not fall off exponentially outside of the RMW as would be expected in potential flow. Previous studies have consistently shown that azimuthal wind cross sections have potential flow outside the RMW (e.g., Tanamachi et al. 2007), but many of these cross sections were produced using the GBVTD technique. It is important to realize that in the GBVTD technique, the tornado is isolated from other flows such as the storm scale mesocyclone. Since GBVTD is not done in this study, the primary reason for the higher winds outside of the RMW is likely the superposition of the tornadic circulation on storm scale flows such as the mesocyclone. Another feature of the segment 1 cross section related to the superposition of the tornado on larger scale flows is the large width of the vortex when gauged by the RMW. Even though the vortex is still developing, the width is roughly 340 m and high winds cover a broad area. While the width of the vortex is large and winds outside of the RMW only slowly decrease radially outwards, they remain a true representation of the coverage of tornadic winds at the surface. Figure 4.9 provides a visual example, showing that the debris cloud is nearly 500 m in diameter, even during segment 1 while the tornado is still relatively weak. The 500 m diameter of the debris cloud is close to, but is slightly larger than, the tornado velocity signature on the radar and is nearly identical to the width of the damage swath estimated from the correlation coefficient (See Figure 3.6). Figure 4.9 clearly shows that dust and dirt is being scoured and lofted well outside the visible edge of the condensation funnel; the debris cloud, and thusly, the area of high winds near the surface, cover a diameter that is four to five times the width of the condensation funnel. The findings

Figure 4.9: Picture of the Selden tornado at 2309:30 UTC, looking to the west southwest towards the town of Selden from the D6 RaXPol location. The condensation funnel and debris cloud diameters were estimated with the use of the tall grain silos near the middle of the image. The edges of the debris cloud are marked. Photo courtesy of Trey Greenwood.

that the tornado has a large diameter and persistently high velocities outside the RMW are consistent through this study, forcing consideration of important questions regarding how far out from the vortex center winds matter for the tornado circulation and where the tornado truly ends.

The structure of the segment 2 cross section is significantly different from that in segment 1. The shear across the tornado is now nearly 60 m s^{-1} and the width has grown to approximately 450 m. In segment 1, the total circulation at the RMW was approximately 20000 m^2 s^{-1}, but by segment 2 the circulation has more than doubled to almost 45000 m^2 s^{-1}. In the intervening time from segment 1 to segment 2, circulation was not conserved as both the averaged azimuthal wind and RMW increased; angular momentum is being ingested by the tornado from external sources including the RFGF. This is a clear indicator that the tornado is growing more intense.

Also of note is that the segment 2 cross section is now significantly off center, with the vortex being shifted nearly 50 m to the south. There are three primary factors that can force the profile to not be centered. First is that the vortex is significantly asymmetrical, but this is unlikely given that tornadoes are nearly axisymmetric except when in a multiple vortex phase (e.g., Tanamachi et al 2012). Second is that velocity correction was performed with an unrepresentative vortex velocity, which is possible since an average motion vector for the segment is used. Third is superposition of larger scale flows on the vortex, such as the RFD, which can bias the cross section towards the north or south. If the vortex motion is chosen differently, such that the tornado's zero azimuthal velocity point occurs at a radius of 0 m, the new vortex velocity required would be only 0.5 m s^{-1} from the west southwest. This velocity does not match any other observations and is far too low. Regardless of how realistic the new vortex velocity is, it results in a severely unbalanced cross section where the winds on the RFD side of the tornado are several times those on the inflow side. If instead the vortex velocity is chosen to balance the velocity maxima on either side of the tornado, the vortex becomes even more off center. Because of these factors, it is likely that the vortex velocity subtracted in the original cross section is close to the true value and that the vortex may be slightly asymmetrical. However, radar analysis indicated that the RFD became intense during segment 2, which is reflected in the preference of the segment 2 cross section towards the RFD side of the tornado. The maximum on this side of the vortex is 33 m s^{-1}, while it is only 27 m s^{-1} on the other side. Because the RFD is intense, it is more likely that the third primary cause of profile asymmetry, flow superposition, is causing the segment 2 cross section to be off-center as a strong RFD biases the velocity values towards the south.

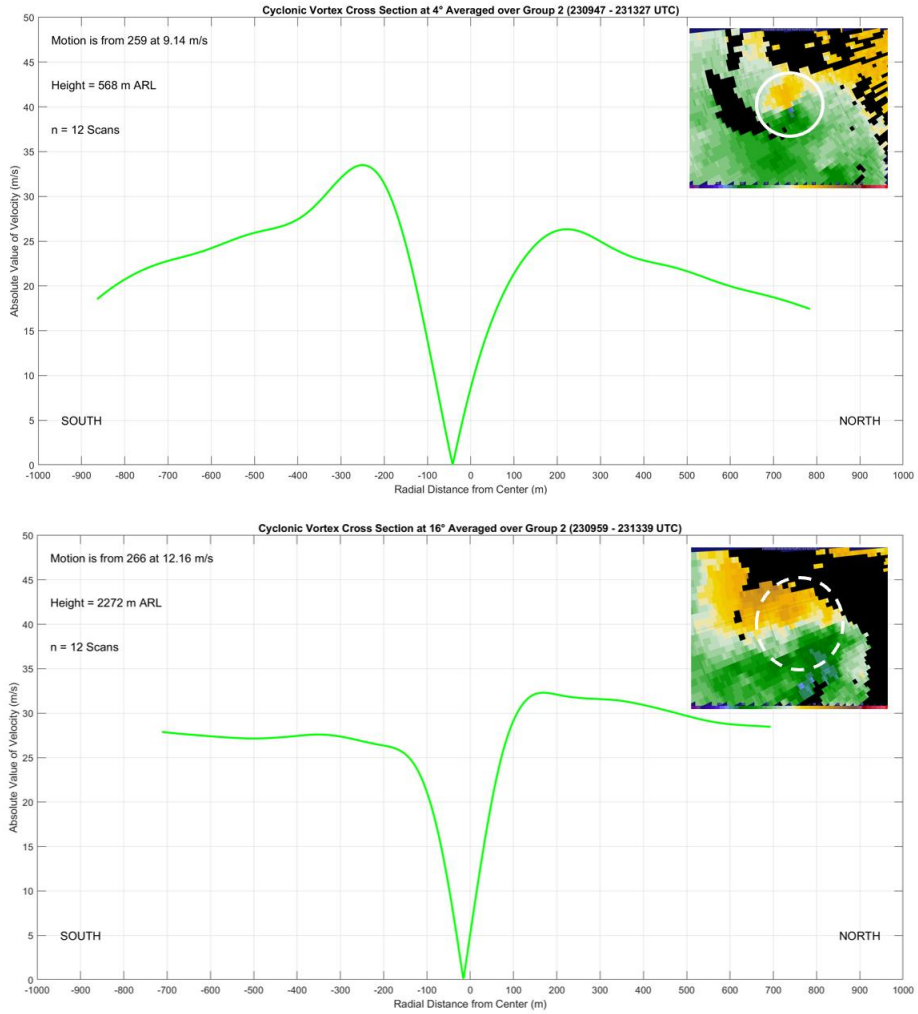

Figure 4.10: Comparison of the segment 2 cross section at 4° (top) and 16° (bottom). Example PPI maps of radial velocity are provided from the volume starting at 2309:43 UTC to further show the typical changes in the tornadic vortex with height.

The segment 1 and 2 cross sections also change significantly with height. As with the track analysis, changes with height become most pronounced above the 2 km level. Figure 4.10 shows the segment 2 cross section from the 4° and 16° elevation. At the 16° height, the vortex still contains a solid body rotation core, but no longer has defined velocity maxima. Instead, the velocity values plateau heading radially outwards from the vortex center. In general, the vortex becomes less defined with height, especially above the 2 km level because the mid-level supercell mesocyclone is overwhelming the velocity

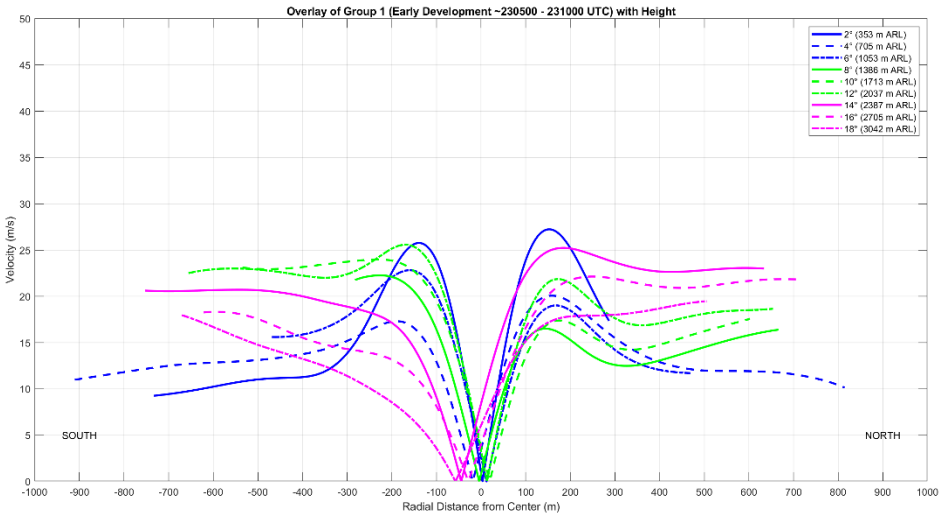

Figure 4.11: Height comparison of all nine segment 1 cross sections. The 9 scan elevations are color coded in groups of three (lower group – blue, middle group – green, upper group – pink). Each group then has a solid profile, dashed profile, and dotted-dashed profile in increasing height.

signatures related to the tornado. Since the background circulation is much stronger as the cross sections approach the mid-level mesocyclone, the vortex becomes much less defined, being marked only by a locally higher shear zone and sometimes a WEH.

A comparison of all nine segment 1 cross sections over height yields additional details aside from a general decrease in definition. Shown in Figure 4.11 are overlays of all the segment 1 cross sections with height, color coded in batches of three with increasing height. Especially in segment 1, the vortex becomes much less defined with height, reflecting the finding that the vortex took longer to become established aloft and was not coherent in the entire 3 km vertical column in segment 1. In the segment 1 height comparison, the middle elevation scans from 8° to 12° (green profiles) are biased to the RFD side of the tornado, while the top three elevation scans (magenta profiles) are biased towards the inflow. This is a product of tornado proximate supercell structure; the RFD outflow is strongest near the surface (Grzych et al. 2007) and the inflow is moving up and

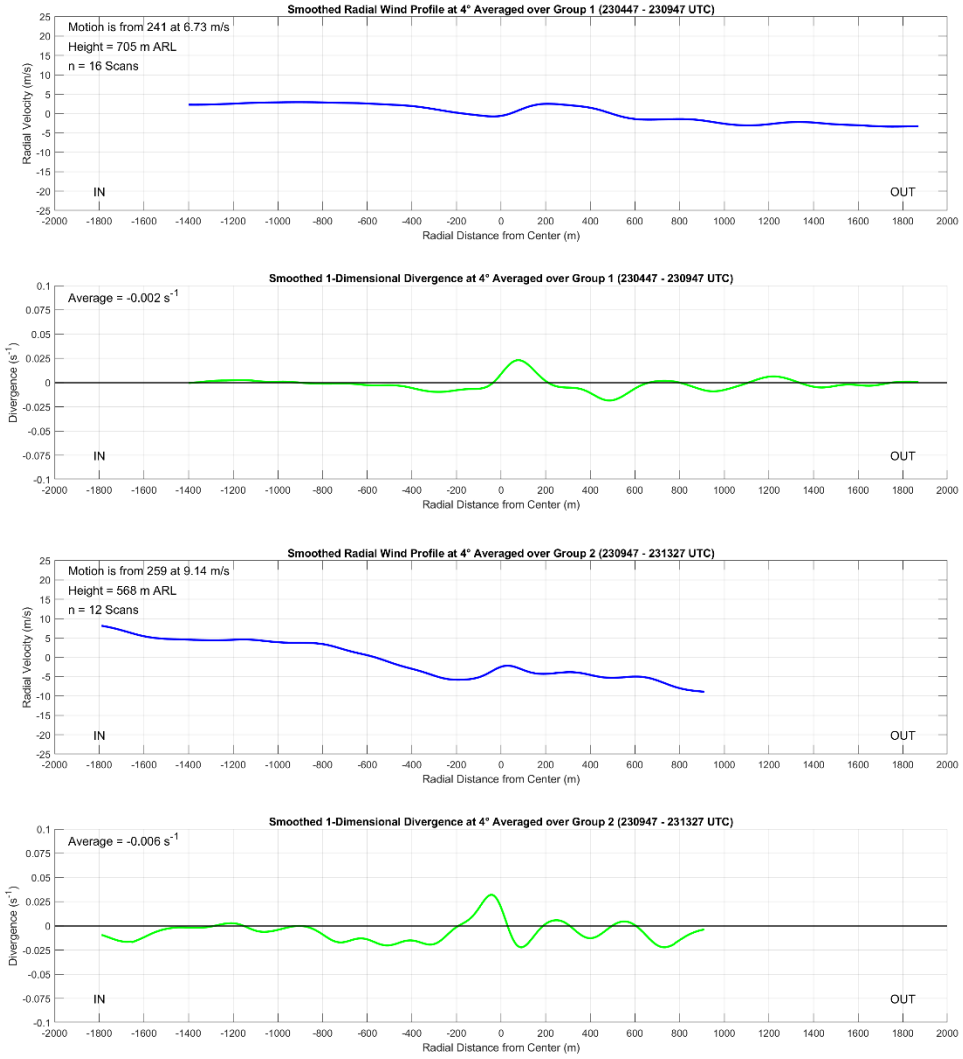

Figure 4.12: Radial wind cross sections through the Selden tornado at the 4° elevation for segment 1 (top) and segment 2 (bottom). 1-D divergence is also included.

into the supercell updraft. As cross section sample heights increase and then pass above 2 km, they are increasingly capturing weaker RFD outflow and stronger supercell inflow. While the RFD dominates within the lower 2 km of the observation column, inflow winds are stronger above this as the supercell inflow 'jet' becomes increasingly sampled. Many of the trends seen in the segment 1 height comparison vanish in the segment 2 comparison (not shown). The profiles during segment 2 are remarkedly similar, which is likely a

function of the vortex becoming more coherent as it matures and because of decreasing sample heights, such that the upper bound of observation is still within the RFD outflow.

Shown in Figure 4.12 are the radial wind cross sections for segments 1 and 2, produced to capture the tornado radial winds by passing through the zero Doppler velocity point within the tornado. While the sample heights are far too great to capture radial inflow, the cross sections do contain well defined peaks of 1-dimensional divergence roughly centered on the tornado as would be expected due to centrifuging above the inflow layer. The same processes lead to the formation of the WEH (e.g., Bluestein et al. 2004 or Bluestein et al. 2007b), and the cross sections corroborate the existence of persistent divergence. The magnitude of the divergence is also high, with both cross sections having divergence on the order of 0.025 s^{-1}. A sign change in the radial velocity, going from negative to positive outwards from the radar, is also commonly associated with the increase of radial velocity heading outwards from the radar in and near the tornado. This sign change does not always occur, as it is very sensitive to the vortex motion that was subtracted from the cross section. Overall, the profiles are slightly convergent over the domain sampled, indicating that the supercell mesocyclone and associated circulation are slowly strengthening which is supported by radar observations and expected since the tornado is also intensifying.

4.4: Photogrammetric Analyses

Utilizing the video of the Selden tornado taken from the D6 deployment location, an analysis of the width of the condensation funnel and track of the tornado were completed. Figure 4.13 presents results of the condensation funnel analysis, showing a

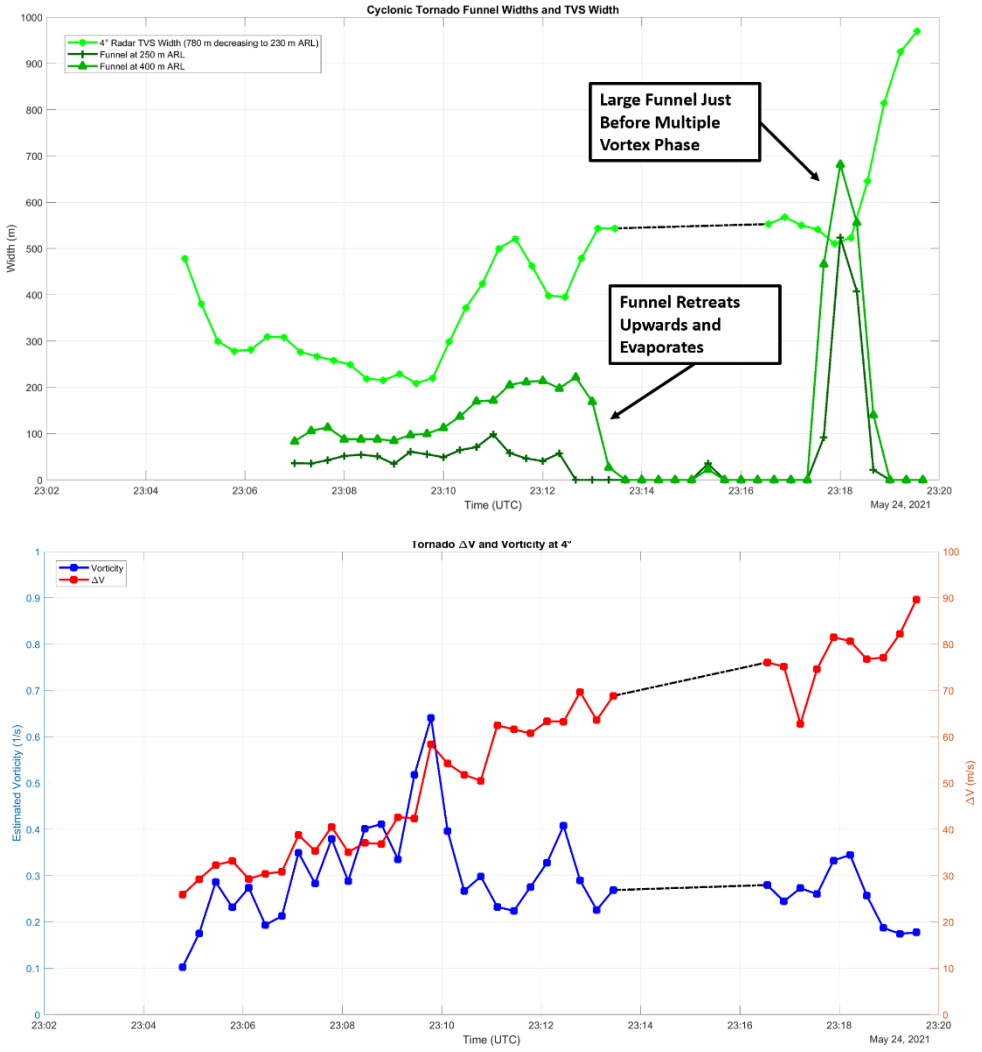

Figure 4.13: Top panel contains a timeseries of the tornado condensation funnel width at 250 m ARL (dark green) and 500 m ARL (green) and TVS width at the 4° scan elevation (bright green). Bottom panel contains a timeseries of tornado ΔV (red) and vorticity (blue).

timeseries of the funnel width and Tornado Velocity Signature (TVS) width along with timeseries of the ΔV and vorticity of the tornado. In the top panel of Figure 4.13, the width of the condensation funnel is much smaller than that of the TVS, reflecting the prior finding that the visible condensation funnel is much smaller than the debris cloud (See Figure 4.9). The width of the condensation funnel also increases with height, being smallest close to the ground.

The changes to condensation funnel width with time also reveal an important aspect of the Selden tornado. While the tornado ΔV is consistently growing more intense on radar, the condensation funnel of the tornado does not always appear. These times are annotated on Figure 4.13, with the first occurring from approximately 2313 to 2317 UTC and second from roughly 2319 UTC through the end of the analysis at 2320 UTC. Despite continued intensification, the tornado condensation funnel first disappears around 2313 UTC. The formation of the condensation funnel is dependent on both the environmental relative humidity and the strength of the dynamically driven low pressure minima at the center of the tornado. While no tornado proximate environmental data are available, the estimated vorticity timeseries in the bottom panel of Figure 4.13 provides a likely explanation for the disappearance of the condensation funnel since the dynamic pressure minimum at the tornado center is directly proportional to the square of vorticity (Klemp and Rotunno 1983). Leading up to when the funnel disappeared, the vorticity of the tornado increases steadily. Then, shortly before the condensation funnel begins retreating upwards in the video and disappears, the vorticity peaks and then decreases before becoming steady. As a result, the magnitude of the tornado's central pressure minimum decreases from 2310 to 2312 UTC before stabilizing. Because of the higher central pressure, the tornado is unable to force the condensation of water from the air it is ingesting, and the funnel disappears. However, there are no direct pressure or moisture measurements to confirm this hypothesis.

The reappearance of the tornado condensation funnel and then subsequent disappearance at the end of the analysis in Figure 4.13 are related to the transition of the Selden tornado to a multiple vortex structure, which is discussed in greater detail in Chapter 5. However, Figure 4.13 still provides a likely explanation. According to Figure 4.13, both

tornado ΔV and vorticity are slightly increasing as segment 3 begins, causing a large condensation funnel to form. However, once the tornado undergoes transition to multiple vortex structure, the magnitude of vorticity once again decreases as the vortex broadens significantly without attendant increases in azimuthal flow speed. As a result, the central pressure within the tornado decreases and the condensation funnel disappears.

Because the presence of the condensation funnel is tied intimately to the magnitude of vortex vorticity, the size of the condensation funnel should also be directly related to the magnitude of vorticity; the size of the funnel depends not just on the bulk shear across the vortex but also on how tight the gradient in velocities is within the vortex. Figure 4.13 shows that for the periods in which the condensation funnel is present during segments 1 and 2, the width of the funnel appears directly proportional to the magnitude of vorticity. As the Selden tornado gradually strengthens and vorticity increases, so too does the width of the condensation funnel. However, by 2313 UTC, the funnel disappears as the Selden tornado's central pressure increases due to decreases in vorticity; the relationship between vorticity and condensation funnel width is not linear since the vorticity can sometimes decrease below a minimum threshold required to form a condensation funnel. If the vorticity decreases beyond this threshold, then the funnel will entirely disappear. The proportional relationship between condensation funnel width and vorticity does not hold during segment 3, likely as a result of changing tornado structure during its multiple vortex transition. While condensation funnel width and vorticity appear to be directly proportional to each other, there exists no simple relationship between condensation funnel width and ΔV. Since vorticity is a combined parameter that contains both the TVS width and ΔV, vortex vorticity and ΔV do not necessarily directly relate to each other; one can decrease

while the other increases (e.g., Kosiba et al. 2013). The bottom panel of Figure 4.13 reflects this, showing that vorticity and ΔV both increase at first. However, by 2310 UTC, vorticity begins decreasing and then remains constant while shear continues to increase.

The relationship between the width of the TVS and tornado intensity, whether it is measured by shear across the vortex or by vorticity, is more complicated. Early in the analysis, the TVS width decreases rapidly before stabilizing around 2306 UTC while both vortex shear and vorticity increase. This likely reflects the early development of the Selden tornado as the pre-tornadic circulation finishes contracting and intensifies into a nascent tornado. Then, from 2306 to 2310 UTC, the TVS continues to slowly contract while both vorticity and shear across the vortex increase. At 2310 UTC, the TVS diameter begins to expand rapidly. When the TVS diameter rapidly expands, the azimuthal flow speed of the tornado only gradually continues to increase. As a result, the magnitude of vorticity decreases, and the condensation funnel evaporates. After 2313 UTC, the width of the TVS stabilizes before its diameter rapidly expands again during multiple vortex transition as vorticity decreases and shear across the vortex continues to slowly increase. The complex relationship displayed between the TVS, vorticity, and ΔV displayed in this case has also been documented in prior cases, such as Greenwood (2021). In their Putnam, OK case, plots of ΔV, TVS width, and vorticity revealed a complex relationship and showed that the TVS width was not directly proportional to either the vortex ΔV or vorticity.

The track of the Selden tornado was also estimated using video analysis. The top panel of Figure 4.14 shows a comparison between the radar indicated track of the tornado at the 4° elevation and the video derived track of the tornado. The gray line shows the line of sight from the D6 deployment location to the railroad grain silos, which are marked by

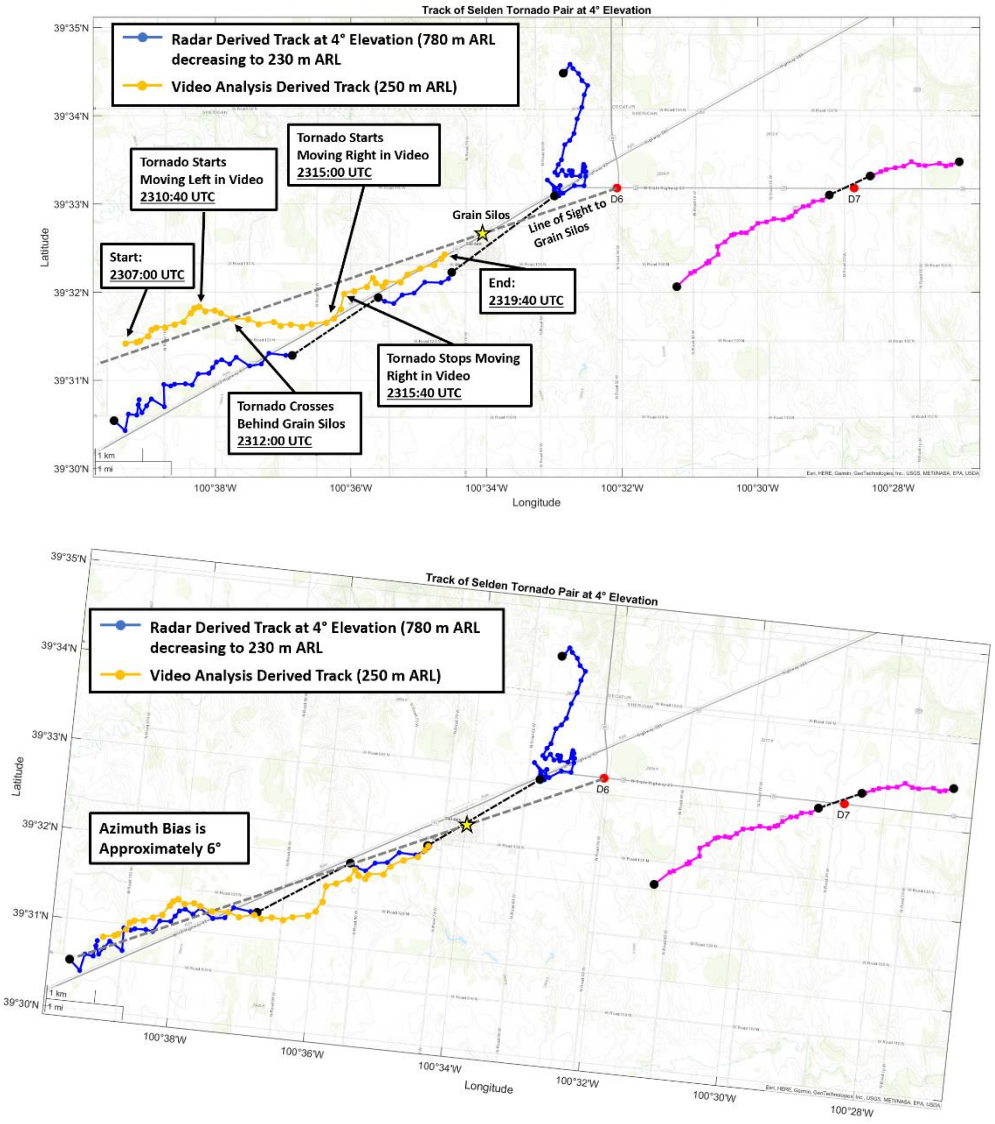

Figure 4.14: Comparison of the video estimated and radar derived tornado tracks during D6. The bottom panel contains a rotated map showing that the track discrepancies are likely due to a systematic azimuth bias in the radar data resulting from an incorrect GPS heading. A yellow star marks the location of the grain silos, and the gray line denotes the line of sight from the D6 deployment location to the grain silos.

a star. Using the line of sight, the track of the tornado was estimated from the distances of the tornado to the left or right of the silos obtained from analysis of the video and is plotted in orange. During the video, the Selden tornado was observed to shift slowly to the right on the north side of the grain silos from the start of the video to approximately 2310:40

UTC before starting to move abruptly to the left. At 2312:00 UTC, the tornado crossed behind the grain silos and continued moving to left to the south side of the grain silos. This continued until the Selden tornado reached its furthest point south of the grain silos at roughly 2315:00 UTC, at which point the tornado began to move rapidly rightwards in the video. The tornado then stopped moving right at about 2316:00 UTC when it was just to the south side of the grain silos; the tornado remained just to the south of the grain silos for the rest of the video. This movement is reflected on Figure 4.14 by how the video estimated track (orange line) shifts relative to the line of sight to the grain silos (gray line). The initial shift of the tornado towards the left correlates well with the track shift noted earlier between segments 1 and 2. The reversal of leftward movement to rightward occurs during the D6 data gap, but the rapidity of the shift and temporary nature of the rightward motion suggests that RFD surges may have had an influence. While no radar data are available during the data gap, Chapter 5 presents some evidence that implicates RFD surges for the track shift.

At first, the results in the top panel of Figure 4.14 seem to indicate a significant deviation between the radar and video derived tornado tracks. However, the video estimated tornado track is persistently to the north of the radar indicated track, suggesting a systematic error in the collection of radar data. Furthermore, the increasing displacement to the north of the video estimated track from the radar indicated track with increasing distance from the radar implies that there is an error in the recorded azimuths of each radar pixel. To check for this type of error, the radar track map was rotated about the D6 RaXPol location until the two tracks were the most aligned. The result is presented in the bottom panel of Figure 4.14, where it is revealed that a 6° azimuth correction for each radar pixel causes the two different tracks to become nearly perfectly aligned. Because of how well

the two tornado tracks align, it is likely that the displacement between the two tracks in the top panel of Figure 4.14 is an artifact of the bias and is not a representation of a meaningful physical characteristic of the tornado. This type of error is easily generated when an incorrect heading is given to the RaXPol system by the truck's GPS. Because the GPS unit was having known problems during the 2021 and 2022 seasons, it is likely that the differences between the two tracks were the result of an incorrect GPS heading. However, since the 4° scan elevation derived track does not have a constant height ARL because of the decreasing distance of the tornado to the radar, it is still possible that some of the disagreement between the two tracks is due to vortex tilt. Another possibility is that there is a misalignment between the tornado below the cloud base and the tornado and low-level mesocyclone above the cloud base (e.g., Bluestein et al. 2019).

Fortunately, the 6° azimuth bias in radar data does not impact the results of this study. While an azimuth bias does exist, it applies to all the data equally, such that the resulting tornado track is rotated by 6° about the radar from where its true position is. Calculated track headings are affected by this, but the tornado forward speeds and overall pattern of the track are not. As a result, all of the analyzed track shifts and features remain the same whether or not an azimuth bias exists in the radar data. However, one of the effects of the azimuth bias is that the absolute positions of the tornado derived from radar relative to other physical objects and places on a map, such as the town of Selden, are not entirely correct. Therefore, the most accurate tornado track relative to ground features is given by the tornado video estimated track in the top panel of Figure 4.14. Other analyses in this study, such as cross section and radar analyses, are entirely unaffected by the azimuth bias.

4.5: Descending Reflectivity Core

Leading up to the D6 data gap, at least one DRC was identified in the RaXPol dataset. Produced to visualize the area of descending reflectivity, Figure 4.15 contains 4 volumes centered on the tornado created by enclosing the areas of reflectivity at or above 55 dBZ. Starting at 2311:03, an area of high reflectivity begins to descend into the top of the domain at 2.7 km ARL to the east of the tornado. Over the course of the remaining 2 minutes of D6 before the data gap, the high reflectivity core slowly descends towards the ground. At 2311:43, the blob of reflectivity has visibly descended into the domain; the volume at or above 55 dBZ has grown significantly and includes areas north of the tornado. By 2312:23, the upper part of the reflectivity core has passed into the domain as the lower portion starts contacting the ground. Finally, in the last scans of D6, the portion of the reflectivity core north of the tornado nears the ground. As first described by Rasmussen et al. (2006), a DRC often falls from the top of the vault from the supercell reflectivity overhang, which is overhead of the RFGF, forward flank boundary, and updraft interface where tornadoes are generally located. On the order of minutes, the DRC makes it to the ground near the tornado. The identified DRC fits the Rasmussen et al. (2006) definition closely as the reflectivity core falls through the lowest 3 km of the storm over the course of 2 to 3 minutes, contacting the ground just to the north and east of the tornado.

The impacts of DRCs on tornado formation and intensification have been the subject of several studies. Rasmussen et al. (2006) found a DRC coincident with tornadogenesis in a subset of supercells and noted that DRCs were associated with strengthening of the tornado. Unfortunately, in this case, it is not possible to ascertain with certainty what the effects of the identified DRC were on the Selden tornado. As the main

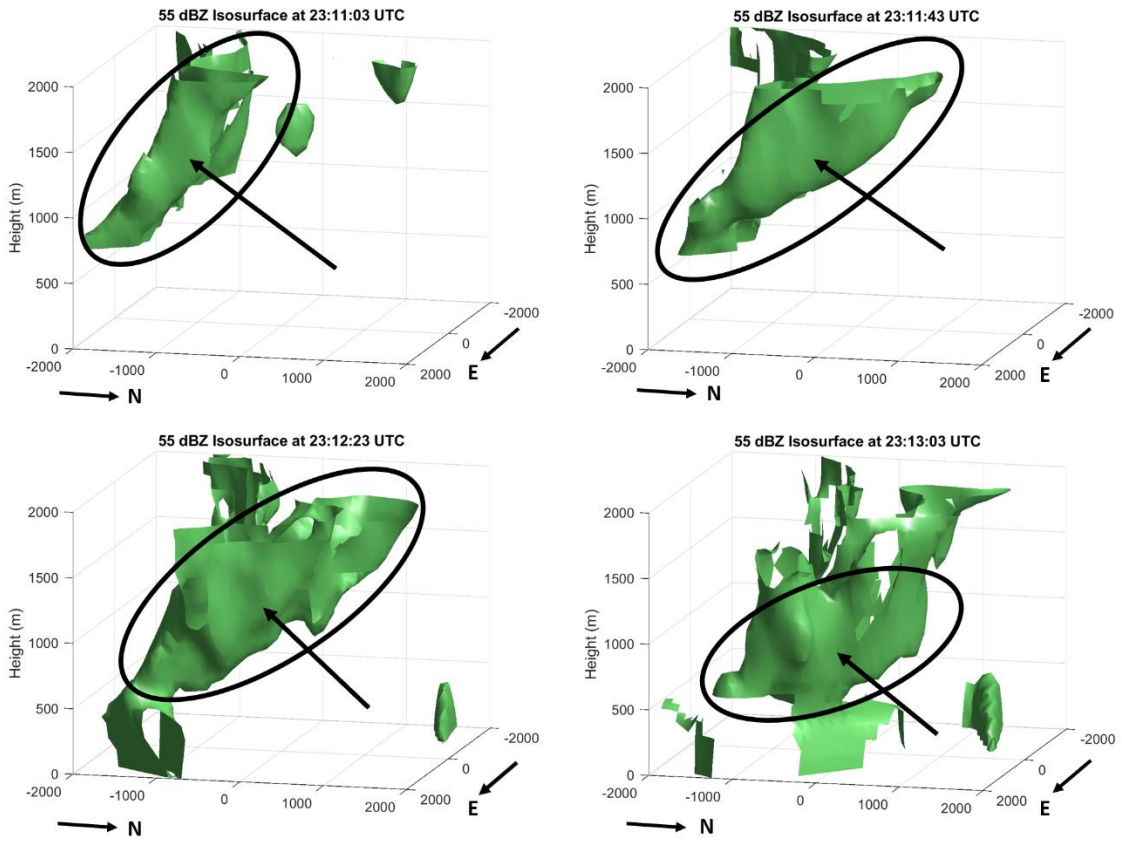

Figure 4.15: Volumes enclosing reflectivity values greater than or equal to 55 dBZ. The domain is centered on the tornado in each panel, and the view is from the northeast. All distances are in meters (m). For clarity, the DRC is circled and denoted with an arrow.

body of the reflectivity core nears the surface, the D6 data gap occurs, and no data are available over the next 2.5 minutes. However, reconstructed cross sections provided in Figure 4.16 offer some clues to the nature of the DRC. The cross sections run roughly south to north, cutting through the center of the tornado at the same scans as the volumes in Figure 4.15. On the reflectivity panels, the descending blob of high reflectivity centered 500 to 600 m north of the tornado is seen falling from the top of the domain to roughly 800 m ARL by the last scans before the D6 data gap. This matches closely to what was observed in Figure 4.15, with the portion of the reflectivity element north of the tornado falling through the domain at a slightly later time than the portion to the east. Meanwhile, the velocity field may respond to the DRC. By the second panel, the receding velocities on the

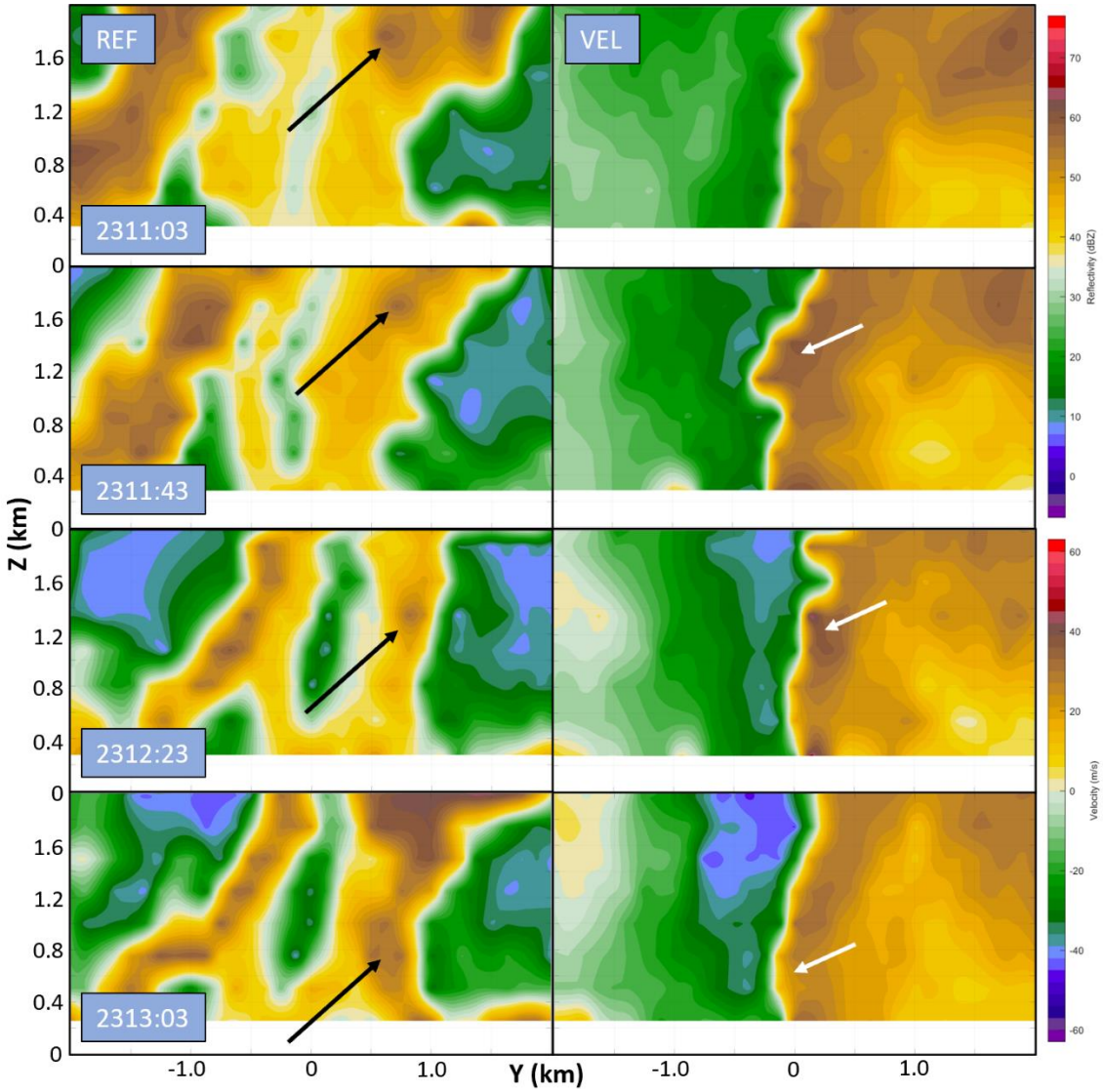

Figure 4.16: Reconstructed cross sections through the tornado at the same 4 scans as in Figure 4.15. Reflectivity is on the left and Doppler velocity on the right. Black arrows point to the DRC, while white arrows indicate the potentially related velocity disruption.

north side of the tornadic circulation have become visibly displaced from the center of the vortex, coming out in a notch into the other side of the vortex. This notch of anomalously high positive Doppler velocities continues to fall through the tornado, roughly correlating with the position of the DRC. However, there may be many other factors creating this notch of velocities with the tornado, and its position is not very well correlated to that of the DRC.

Since the DRC contacts the ground during the D6 data gap, there is no near-surface velocity evidence to confirm that the DRC influenced the Selden tornado. However, determining the DRC type according to the categories in Byko et al. (2009) can help to further characterize the DRC. In their study, Byko et al. (2009) found that there were three categories of DRCs, with only one category being correlated with tornado formation and intensification. Type 1 DRCs were those of the nature described by Rasmussen et al. (2006) and are the DRCs that effect tornadoes. These DRCs formed from the supercell overhang were flow stagnation in the supercell inflow resulted in heavily precipitation loaded air beginning to fall; the DRC ultimately reached the surface near the tornado, often immediately to its north or east. Type 2 DRCs form as precipitation laden air within flanking line updrafts begins to descend when the parent flanking line updraft merges with the primary supercell updraft; these DRCs often contact the ground on the RFD side of the supercell updraft too far from tornadoes to have an impact on them. Finally, type 3 DRCs form when precipitation loaded air becomes caught in a downward directed pressure gradient that results when vorticity is most intense at low levels. These DRCs are more typical later in a tornado's lifecycle (Byko et al. 2009). Based on the location of the DRC in the RaXPol data and timing relative to the tornado lifecycle, it is likely a type 1 DRC. Consequently, it is probable that the DRC will have a strengthening effect on the tornado when it reaches the surface as its outflow impinges on the tornado during the D6 data gap. While the vortex continues to strengthen in an average sense over the data gap, with ΔV_{max} increasing from 70 to 77 m s^{-1} at 4° elevation (See Figure 4.5), it is not possible to ascertain how much, if any, of this strengthening is attributable to the DRC.

Chapter 5

The Selden, Kansas Tornado During D6 – After the Data Gap

5.1: Track Behavior

After the D6 data gap, the motion of the Selden tornado is largely the same as it was before the gap. In between the data gap and the end of D6, a timespan of 3 minutes, there is one track segment and no significant changes in motion. The segment 3 track at the 4° and 16° elevations is shown in Figure 5.1. At the 4° level, which is now only 300 m ARL due to the increasing proximity of the tornado to the radar, the track vector is 9 m s^{-1} from 250° (WSW). Nearly identical to the segment 2 motion, the segment 3 motion continues to largely match the track of the parent supercell. As observed by Dowell and Bluestein (2002) in their study, the tornado and the supercell are remaining in the same positions relative to each other and the tornado is locked into its mature location at the apex of the RFGF and forward flank boundary underneath the supercell updraft. Until the RFGF and the Selden tornado become decoupled, or the parent supercell weakens as the result of external forcing, the tornado will continue to strengthen or at least remain intense. However, it is noteworthy that the average movement of the tornado required over the data gap to reach the starting position of segment 3 is more southwesterly than the track before and after it, with the tornado moving from approximately 235°. This suggests that some force nudged the tornado more northerly before the start of segment 3 during the gap.

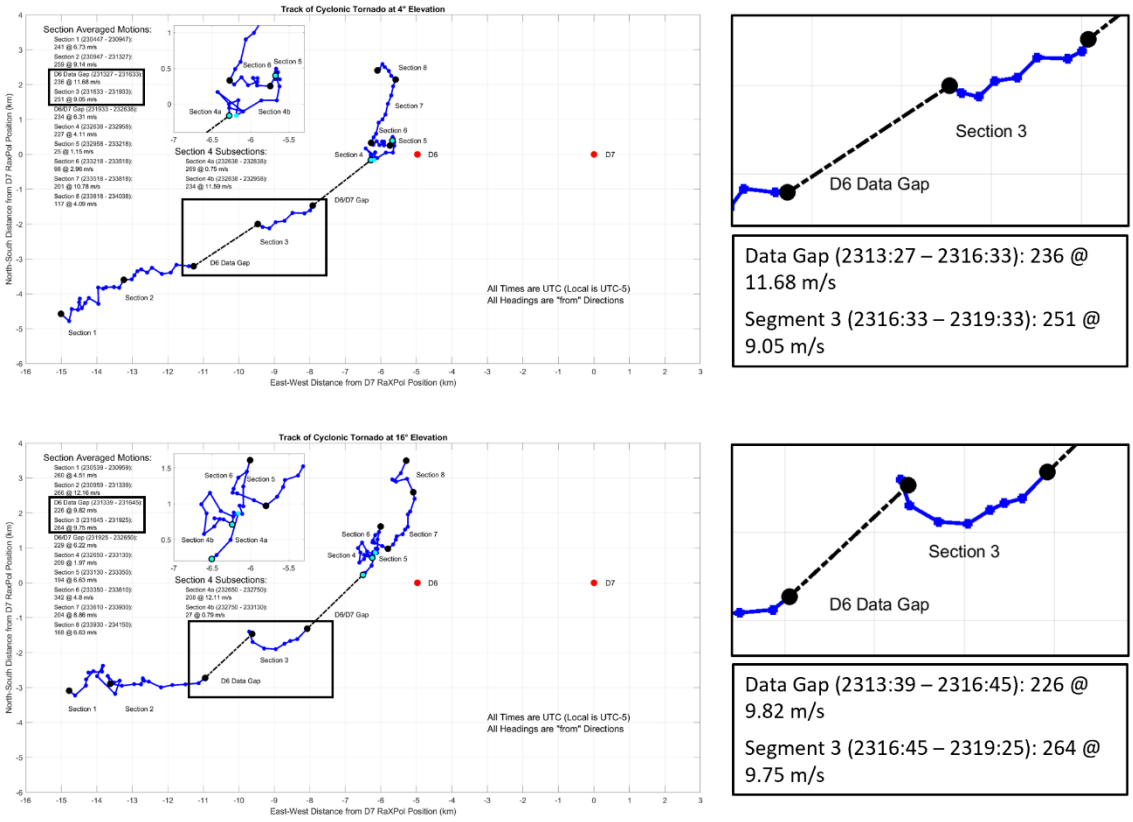

Figure 5.1: Track of the Selden tornado at the 4°(top) and 16° (bottom) elevation scans. Zoomed insets of the tracks leading up to and during segment 3 are provided on the right, along with descriptions of the segment motion vectors.

Furthermore, the very start of the segment 3 track has a slight southerly trend before the tornado resumes along a track heading from 240° following the parent supercell.

The slight aberration in the Selden tornado track at 4° becomes much more pronounced at the 16° level, which is now approximately 1200 m ARL. Overall, the track vector remains similar in speed but not in direction at higher elevations, with the 16° track vector being roughly 10 m s^{-1} from 265° (W). The apparent northward shift of the tornado during the data gap leading into segment 3 is much greater at 16°, causing the tornado to move almost due easterly in an average sense over segment 3. Looking at the tracks in Figure 5.1, much of the track during segment 3 is nearly identical, with east northeasterly motion at approximately 9.5 m s^{-1} from roughly 240° after the tornado at higher elevation

scans settles into a track following the parent supercell. When compared to the apparent northward nudging of the tornado at 4° during the data gap, the force that caused the northward movement was clearly much stronger at the 16° elevation. In fact, the data gap heading at 16° was southwesterly at 225°, which reflects more northward movement at this level than below. Southward movement at the start of segment 3 then follows the northward displacement in what appears to be an adjustment of the tornado back to its base state before interference of the track during the data gap. The changes in tilt of the vortex are also reflective of the Selden tornado undergoing and then recovering from a disturbance strongest in upper elevation scans. During the data gap, the tilt of the tornado from 4° to 16° increased from roughly 20° off vertical to just over 30° despite decreasing sample depth. Then, the tilt of the tornado rapidly decreases to approximately 5° off vertical as the southward adjustment at higher heights results in the position of the tornado becoming uniform across all elevations. The potential causes of this track disturbance will be further explored in the radar analysis of the following section.

5.2: Evolution of the Near-Vortex Wind Field and RFD on Radar

An analysis of radar PPI plots from segment 3 at the 16° elevation is provided in Figure 5.2 in which momentum surges were once again tracked by leveraging the high temporal and spatial resolution of the RaXPol data. During segment 3, the 16° level is roughly 1200 m ARL. Consequently, the RFD outflow is not as well defined, and the near vortex wind field is more of a circularly symmetric circulation rather than a bifurcated flow field between RFD outflow and inflow like at the surface. Because of this, the surges of momentum within the tornado proximate flow pivot around the tornado to a much greater

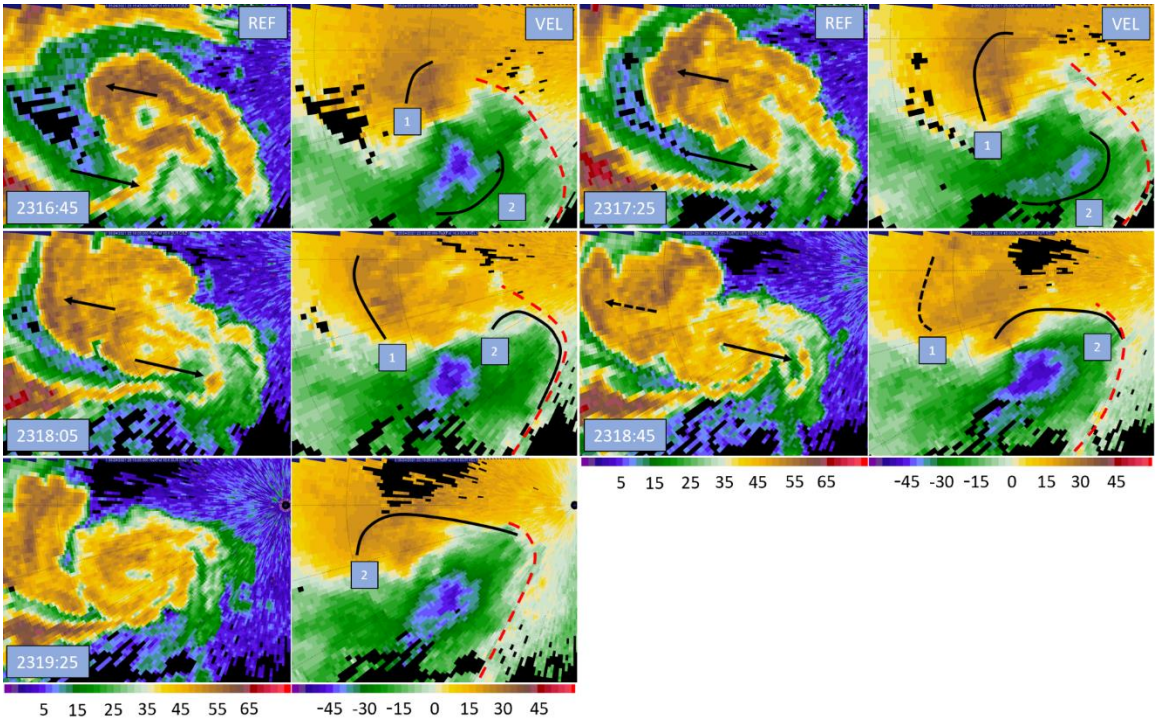

Figure 5.2: RaXPol imagery at the 16° elevation taken every 2 scans (40 s) during segment 3. In each radar panel, reflectivity is on the left and Doppler velocity on the right. Range ring spacing is 2.5 km. Black lines denote RFD surge fronts, which are also numbered. Black arrows also point to associated reflectivity appendages. Finally, a red dotted line marks the approximate position of the RFD front aloft.

extent since there is no intervening RFGF for the surges to merge with aloft; while RFD surges often meet with and then merge with the RFGF at lower scan elevations, a similar feature to the RFGF does not exist aloft and the surges of momentum that are present continue to be advected around the circulation.

Starting at the first scan in segment 3, two surges can be found. The first surge is north of the tornado and is moving west as it pivots around the vortex. Its progression can easily be tracked by following the reflectivity protrusion out of the northwest side of the hook echo, which by the last panel in the analysis is just a remnant of the decayed first surge. Compared to the first surge, the second surge is very potent. By the time data collection resumes after the data gap, a large area of enhanced momentum is already

surging to the southeast of the tornado. Throughout the next four scans (80 s later), the burst of elevated momentum begins to pivot to the east as it curves around the tornado circulation. While doing so, the surge spreads out and its magnitude decreases somewhat. By 2318:05 UTC, the second surge starts merging with the weakly defined RFD front as some momentum begins impinging north of the tornado. In the last two analysis scans, the second surge continues to dissipate as easterly momentum intrudes north of the tornado.

The second surge in Figure 5.2 occurs coincident with the southward motion at the 16° elevation noted in the track analysis. The strength of the surge is also key; the surge is one of the strongest identified in the data. Recent work by Kurdzo et al. (2015) and Lee and Finley (2022) have focused specifically on how RFD surges can alter vortex motion by transporting momentum. Kurdzo et al. (2015) investigated a track loop occurring during the lifecycle of the Moore 2013 tornado. They found that a specific arrangement of surges in time and space resulted in the execution of a cyclonic track loop. Specifically, a surge approached from the southwest and pivoted around the tornado, merging with the RFGF to the north and northeast of the tornado. Then, a second surge built and approached from the northwest of the tornado, pivoting around the vortex before ejecting to the east. As the first surge approached the tornado and passed by its eastern flank, the vortex was forced northward under the influence of enhanced southerly momentum on its eastern side. Remnant momentum from the first surge leaks north of the tornado, causing the tornado to track westward. Finally, the second surge passes to the west and then south of the tornado, forcing it to track to the south and then to the east under the influence of the pivoting momentum. Lee and Finley (2022) have documented similar behavior as it relates to persistent left turns in tornado tracks long before tornado decay. In three separate cases,

high momentum on the right flank of the tornado (relative to tornado motion) always preceded significant leftward turns. Surge momentum would be advected around the tornado and arrive on its left flank; as the enhanced momentum pivoted around the tornado from its right to left flank, surge momentum would be directed to the left with respect to tornado motion and a leftward track turn would occur.

In Figure 5.2, the strong second surge passes near the tornado on its western flank and then pivots to the tornado's south before its primary thrust of momentum spreads out to the east and merges with the RFD front. This pattern of momentum transfer is like the second portion of the looping schematic presented in Kurdzo et al. (2015); the result is a southward adjustment of the tornado before it resumes moving to the east northeast. The similarity of the observed surge and momentum configuration to the second half of the Kurdzo et al. (2015) track loop model makes it tempting to call the 16° southward track curve the exit from a track loop which only occurred in upper elevation scans, but owing to the data gap, it is impossible to see what the configuration of RFD surges was leading up to the start of segment 3. Video analysis also revealed a low-level track shift, revealing that the tornado track underwent changes near the ground as well as aloft leading up to segment 3 (See Figure 4.14). While the low-level track does not resemble a loop, its rapidity and short duration suggested that RFD surges may have been the cause; it appears likely that RFD surges were present and influencing the track of the tornado leading up to segment 3. Since RFD surges can appear in different vortex relative positions around the tornado at different heights due to vortex tilt and vertical surge structure, it is possible that RFD surges caused a track loop aloft and a brief, sharp track shift near the surface. However, a lack of radar data during the gap remains problematic and limits analysis.

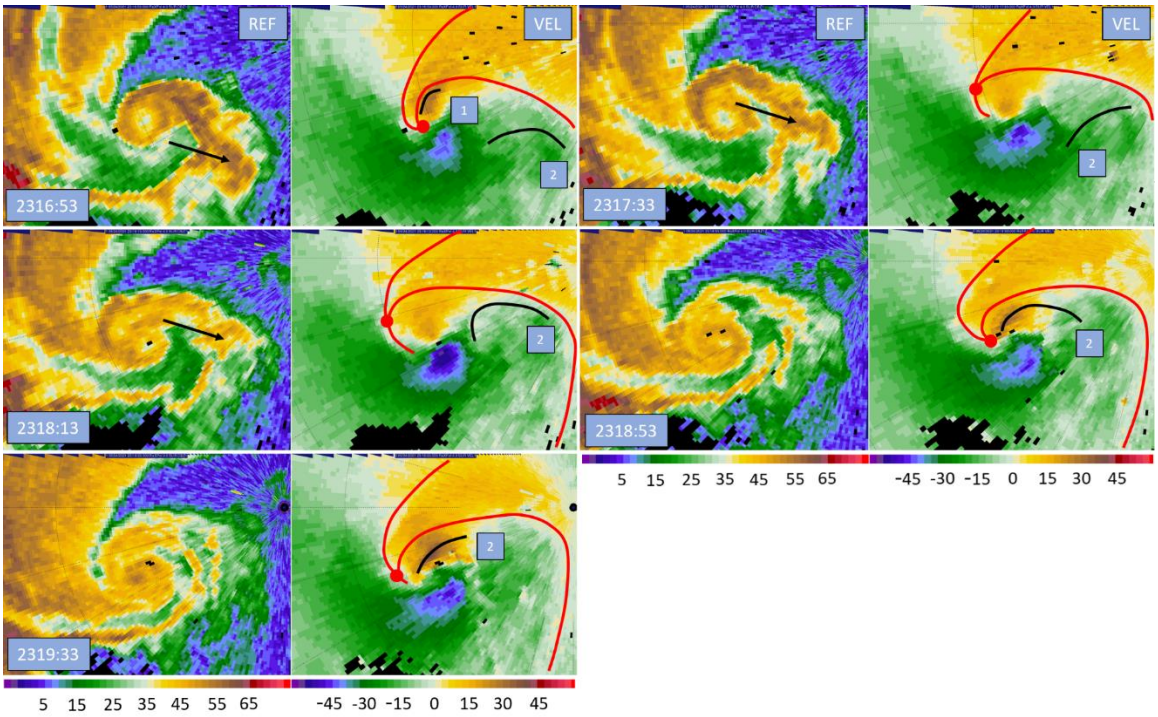

Figure 5.3: RaXPol imagery at the 4° elevation taken every 2 scans (40 s) during segment 3. In each radar panel, reflectivity is on the left and Doppler velocity on the right. Range ring spacing is 2.5 km. Black lines denote RFD surge fronts, which are also numbered. Black arrows also point to associated reflectivity appendages. Finally, red lines mark the approximate positions of the forward flank and RFGF.

The radar analysis for 4° provided in Figure 5.3 reveals similar evolution within the near-tornado flow as that for the 16° level. Notably, two surges are also present. At first, these features do not seem to correlate well with the surges aloft. However, the air within the RFD and RFD surges acts as a density current or large momentum surge depending on whether the RFD is fueled by cold, dense air or by its own momentum if air has warmed to or above the environmental temperature on descent (Lee et al. 2004). Both driving mechanisms result in surge fronts that generally tilt back with height since the descending parcels of air reach the ground and then spread out at the surface. Because RFD surge fronts tend to be tilted back with height, it does appear that the surges at both elevations are parts of the same features. The second surge at the 4° analysis has already pivoted to the east of

the tornado, and when traced backwards with height (backwards around the tornado circulation), is likely the same feature as surge 2 at 16°, which is south of the tornado. The same is true for surge 1 at 4° and 16°; if surge 1 is tilted back with height the position of the surge further to the east in the 16° data aligns with its position at 4°. Note that since the tornado is also tilted northeast with height at this time, the surge appears in similar vortex relative positions at both levels.

Although the surges at the 4° level are likely the same features as the surges aloft, their contrasting positions and trajectories relative to the tornado and presence of surface boundaries result in important differences in the evolution of the near-tornado flow field. By the start of segment 3, the first surge is already almost entirely merged with the RFGF. Most importantly, this surge has been advected to the north of the tornado, and a localized pocket of high easterly momentum is poised to potentially displace the RFGF from the tornado. In the next 40 seconds, the momentum merges with and dislodges the RFGF, causing it to move back into the tornado inflow channel. The forward flank convergence zone and RFGF meet, and the inflow to the tornado is disrupted. Because its inflow is disrupted, the tornado has been wrapped to a greater extent in colder downdraft air that is less buoyant; the tornado will start to weaken if the inflow does not recover. However, the tornado is intense, and the pressure minimum located at its center is driving enough convergence as to recover the inflow and prevent decoupling from the RFGF; the inflow channel recovers within 1.5 minutes as gauged by the likely positions of the forward flank convergence boundary and RFGF in Figure 5.3. As the Selden tornado recovers from inflow disruption, the second surge in Figure 5.3 continues to be advected around the tornado. As it passes to the east of the tornado, its velocity signature becomes masked since

it is travelling perpendicular to the radar beam and the velocities cannot be measured due to the single-Doppler nature of the data. However, the velocity signature reappears as the surge impinges north of the tornado. By the end of the analysis, the second surge is once again threatening the tornado inflow and is poised to displace the RFGF. However, the end of data collection for D6 makes it impossible to know what effect the surge had on the tornado after this point.

During D6, Figure 4.3 shows that the Selden tornado reaches its peak measured intensity. Moreover, the analysis in Figure 4.3 also reveals that the tornado is much stronger near the surface than aloft; shear across the tornado near the ground is close to 90 m s^{-1} while it is only 70 m s^{-1} at the top of the domain near 1200 to 1300 m ARL. The tornado width is also close to 700 m at both the bottom and top of the domain. Vertical vorticity is therefore greatest near the surface, creating a downward directed pressure gradient force that drives the development of the occlusion downdraft. Adlerman and Droegemeier (1999) show that the occlusion downdraft forms within the RFD, generally on the southern flank of the tornado and that the occlusion downdraft is slowly advected around the low-level circulation with time. Numerous possible explanations have been given for why the occlusion downdraft is not collocated with the tornado, including tilt to the vorticity maximum with height, misalignment between the tornado and mesocyclone above it, and contributions from buoyancy (Bluestein 2013). While it is not possible to ascertain the degree to which buoyancy is contributing to the formation of the occlusion downdraft, the vorticity maximum does tilt significantly to the north with height (See Figure 4.5). The appearance of generally stronger, larger, and vertically coherent RFD surges is also suggestive of the development of the occlusion downdraft and helps to determine its

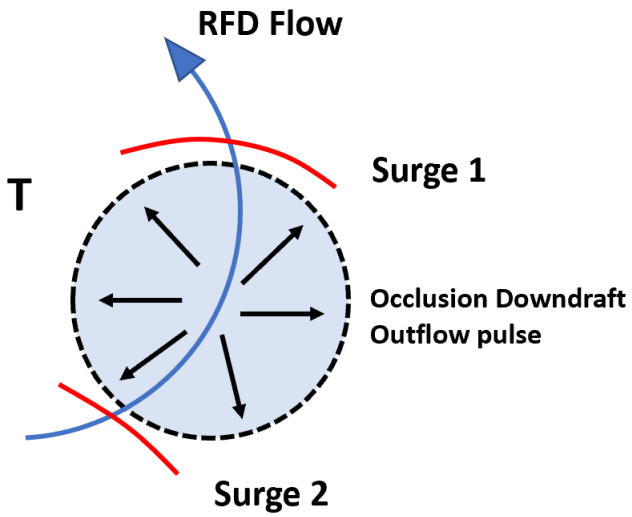

Figure 5.4: Schematic showing how a pulse in occlusion downdraft outflow could generate RFD surges. The location of the tornado is marked by a T, the occlusion downdraft outflow by a blue circle, the RFD flow by a blue arrow, and enhanced areas of convergence, or RFD surges, by red lines.

location. In their study, Skinner et al. (2014) noted that the manifestation of the occlusion downdraft at the surface would resemble RFD momentum surges, with areas of enhanced convergence appearing at its peripheries. Because the strong RFD surges are seen to appear to the south or southwest of the tornado and momentum generally increases on the tornado's southern flank during segment 3 (See Figure 5.3), it is likely that the occlusion downdraft has become established within the RFD just to the south of the tornado.

While no specific physical mechanism was given for how the occlusion downdraft produces RFD surges in Skinner et al. (2014), Figure 5.4 attempts to provide a possible explanation. The occlusion downdraft, like the broader RFD, is sensitive to changes in the magnitude of its forcing mechanisms. If the vertical gradient of vorticity, and thusly, the dynamic pressure gradient, undergo any pulses in strength, then the occlusion downdraft would also undergo pulses. A burst in intensity of the occlusion downdraft generates an outflow surge, around which significant convergence is found. Figure 5.4 then shows that

interaction with the background RFD flow creates two stronger zones of enhanced convergence around the outflow surge. One is situated in front of the occlusion downdraft where convergence is enhanced as the RFD flow forces that portion of the outflow boundary forward, and the second is located to the rear of the occlusion downdraft where opposing flow enhances convergence. As time passes, the two areas of enhanced convergence are advected by the RFD flow and present as momentum surges; the process then repeats if the occlusion downdraft experiences any further pulses in intensity. However, even though RFD surges likely result from the outflow of the occlusion downdraft near the surface (Skinner et al. 2014), it is still possible that the RFD surges appearing during segment 3 are driven by some other mechanism. Both Marquis et al. (2016) and Lee et al. (2012) documented the vital role surging RFD momentum and RFD surges play in causing occlusion; whether the RFD surges are directly generated by the occlusion downdraft or not, their appearance is an indication that the Selden tornado is nearing occlusion.

5.3: Multiple Vortex Transition

At or around 2318:20 UTC, the Selden tornado sustains a multiple vortex transition. A radar analysis covering the period depicting this transition is shown in Figure 5.5. At the start of the analysis period, the velocity field portrays a tight, symmetric vortex. This remains the case for the next 40 seconds, with the tornado intensifying a bit. Then, at 2318:33 UTC, the velocity field in and around the tornado begins to become irregular. Small areas of intense shear appear within the tornadic vortex and asymmetry develops. The intense pockets of shear have a magnitude sometimes over 40 m s^{-1} and a size on the

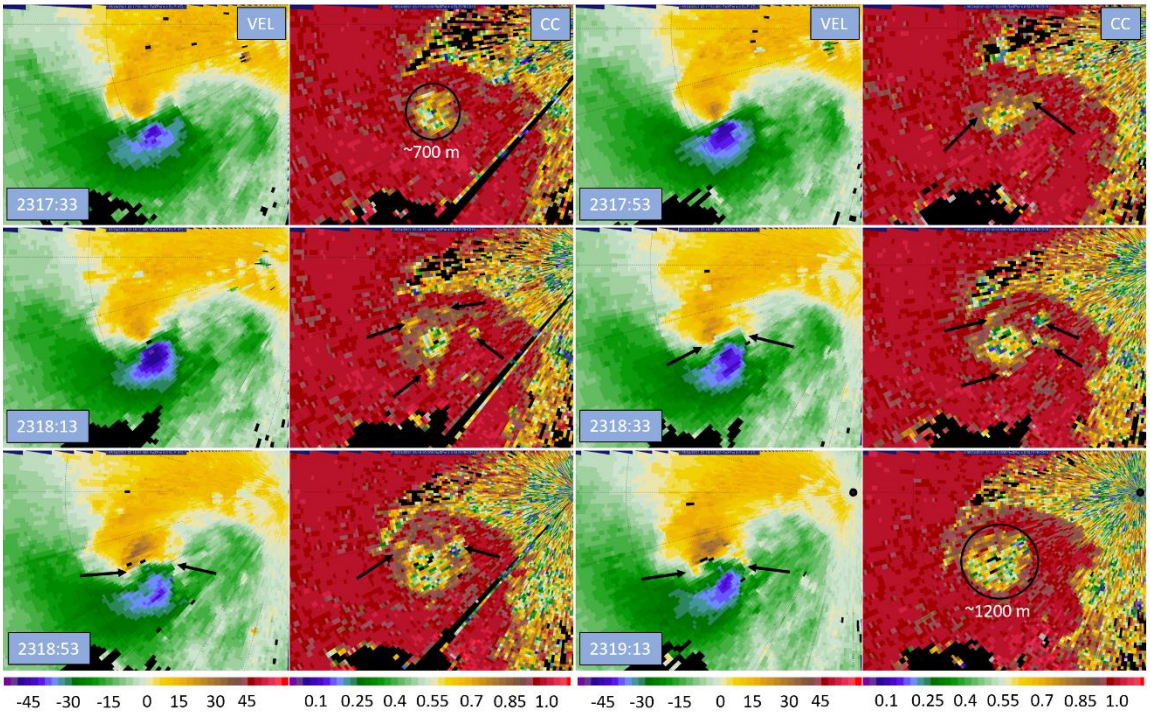

Figure 5.5: Radar analysis during segment 3 at the 4° elevation depicting the multiple vortex transition for the Selden tornado. Doppler velocity is on the left and correlation coefficient on the right. Range ring spacing is 2.5 km. Black arrows point to secondary vortex related features.

order of 10 to 100 m while the parent tornado in which the pockets are embedded has a ΔV_{max} of approximately 80 m s^{-1} and a width near 700 m. (See Figures 4.5, 5.7). Furthermore, the shear pockets appear to revolve about the parent vortex slower than the vortex azimuthal flow in radar animations, propagating into the flow. These characteristics closely resemble the definition of secondary vortices set forth by Wurman (2002); secondary vortices were found to be on the order of 50 m across and had a ΔV_{max} magnitude of approximately half of the parent vortex while moving about the parent tornado at a slower pace than the average azimuthal flow. Both the asymmetry and secondary vortices become more defined by the end of D6 as the multiple vortex transition completes. Finally, the tornadic vortex velocity signature expands greatly in size during the transition, another hallmark of multiple vortex tornadoes.

Evidence from the ρ_{HV} field also confirms the presence of secondary vortices. At the start of the analysis, the ρ_{HV} field shows a circular minimum associated with the dust and debris in the tornado about 700 m across. In the following panels, the ρ_{HV} minimum becomes irregular as small discrete minima appear outside the primary minimum. These new minima are associated with the secondary vortices. As time goes forward, the area of low ρ_{HV} grows as dust and debris get increasingly lofted and disturbed by the new secondary vortices appearing around the edge of the parent tornado. By the end of the analysis, the ρ_{HV} minimum has grown significantly, to over 1200 m in diameter reflecting the new large size of the tornado.

Photos taken from video of the Selden tornado provided in Figure 5.6 provide more detail on the timing and pace of multiple vortex transition. The first image, taken looking to the west southwest into the town of Selden at 2318:16 UTC, shows a large single celled tornado with a visible condensation funnel. Just 10 seconds later, a second image from the same vantage point shows an entirely different scenario. No longer is there a complete condensation funnel reaching the ground, and the area of lofted dust has notably increased. The first visible secondary vortex also appears in the second photo to the right (north) side of the tornado, marking the completion of multiple vortex transition. These photos display the rapidity of the transition, with the vortex taking only 10 seconds to go from a fully condensed funnel around a single celled vortex to the appearance of the first secondary vortex. In video, the vortex undergoes rapid changes, with the condensation funnel suddenly evaporating and appearing to spread out as the tornado's internal downdraft reaches the ground and forces the vortex to breakdown. The photos also pinpoint the time of transition to approximately 2318:20 UTC.

Figure 5.6: Video grabs of the Selden tornado at 2318:16 UTC (top) and 2318:26 (bottom), taken looking to the west southwest into the town of Selden from the D6 location. A white arrow denotes the first visible secondary vortex in the bottom image. Video courtesy of Trey Greenwood.

In observations of a tornado in Crowell, Texas, Marquis et al. (2012) noted that the tornado's multiple vortex transition may have been instigated by the presence of enhanced outflow that was associated with particularly cold air. Lewellen et al. (2000) also noted that a tornado could sustain a multiple vortex transition if outflow air wrapped around a tornado and blocked its warm inflow in a process called corner flow collapse. The time of the Selden tornado's multiple vortex transition correlates very well with the greatest extent of

inflow channel disruption visible at the 4° elevation at 2318:13 UTC in Figure 5.3. It is possible that the Selden tornado sustained its multiple vortex transition because its inflow was briefly disrupted. Multiple vortex tornadoes are generally associated with high swirl ratios, which can be interpreted simply as a ratio of azimuthal flow over radial flow (Rotunno 1984). While the tornado had access to buoyant inflow which could be easily lifted by the tornado updraft, radial inflow was high near the surface, resulting in a low swirl ratio. But once the tornado became enveloped in heavier, less buoyant downdraft air, the tornado could no longer force its ascent as easily and radial inflow decreased. As a result, the swirl ratio increased, and the internal downdraft was able to penetrate to the surface to cause multiple vortex transition.

After the tornado recovers its inflow, it does not transition back to single vortex. It appears that the primary cause was that the dynamic pressure minimum at the center of the tornado was weaker due to the multiple vortex transition. When transition occurred, the vortex broadened significantly while azimuthal flow speed did not increase, resulting in a significant decrease to the magnitude of the tornado's central pressure drop. Consequently, even after inflow recovered, the pressure minimum could not drive enough near-surface convergence to restore the vortex inflow to the level it was previously, and the swirl ratio remained high.

5.4: Cross Section Analysis

The tornado azimuthal wind cross section for segment 3 at 4° is provided in Figure 5.7. Because the tornado has moved to within 4 km of RaXPol, the cross section now represents a height under 300 m ARL, well underneath the cloud base and potentially

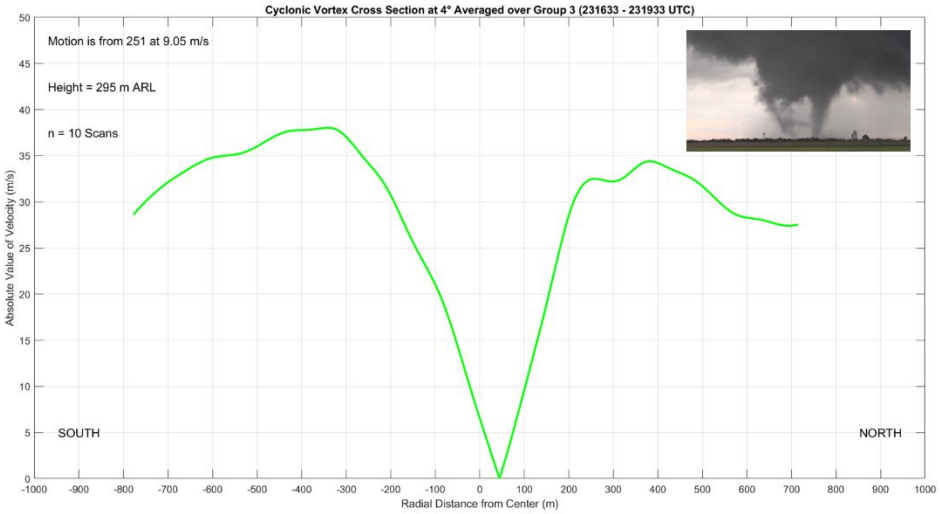

Figure 5.7: Azimuthal Cross Sections through the Selden Tornado at 4° elevation for track segments 1 (top) and 2 (bottom). Pictures of the Selden tornado from each segment are also included. Photo courtesy of Trey Greenwood.

within weak inflow, which may occur up to 600 m above the surface according to Kosiba and Wurman (2010). The segment 3 cross section also samples the tornado at peak intensity, with an average ΔV_{max} of 73 m s^{-1} during the period. Reflecting this, circulation has also greatly increased again, from nearly 45000 m^2 s^{-1} to almost 80000 m^2 s^{-1}. Notably, the tornado has attained a very large width of approximately 700 m, and the profile has begun to take on some irregularity. There is a double relative maximum feature on the north side of the cross section, and the solid body core is slightly disrupted on the south side. Both irregularities and the large width are indicative of a multiple vortex tornado. The action of secondary vortices and breakdown of the tornado into multiple cells will cause the vortex core to deviate from solid body rotation since velocities will be enhanced on the outer edge of secondary vortices and lessened on their inner side. The presence of the double maximum on the north side of the profile is likely a reflection of the change in size of the tornado during transition; the tornado did not undergo transition until mid-way into segment 3, so the double maximum is capturing both the smaller and larger radius of the

tornado before and after transition. While the signature is not present on the south side of the tornado, the maximum on this side is broad, likely because of the same process. Finally, the winds outside the RMW are slow to decrease. Wurman and Gill (2000) noted that azimuthal winds decreased particularly slowly outside the RMW, especially when their tornado was in its multiple vortex phase; this appears to also be the case here.

The segment 3 cross section may also appear to document an asymmetrical tornado at first glance. However, if a slightly different vortex velocity is chosen such that the velocity maxima on either side are made more equal, then the profile becomes much closer to being centered on 0 m; a small change in vortex velocity subtracted to make the profile results in both a more symmetric vortex and a reasonable vortex speed given the motion of the parent supercell. Even though the tornado became quite asymmetrical on radar during its multiple vortex phase, the presence of analysis times in the segment 3 cross section from before the transition seem to be washing out any significant signal of asymmetry. Yet, if the segment 3 profiles from each elevation angle are compared with height (figure not shown), a clear chaotic trend emerges in the center positions of the tornado; vortex center positions cover a wide range of ±50 m from the profile center. The wide variety in center asymmetries is likely a reflection of the multiple vortex nature of the tornado later in segment 3 as the development of secondary vortices generate differing vortex asymmetries with height since secondary vortices have significant vertical tilt (Rotunno 1984).

Further evidence for a multiple vortex transition during segment 3 can be found in the pattern of standard deviation within the cross section. Error bars are exceptionally large within the vortex core region, with a magnitude of ±15 to ±20 m s^{-1}. Large variability within the vortex core reflects the disruptions occurring because of secondary vortices,

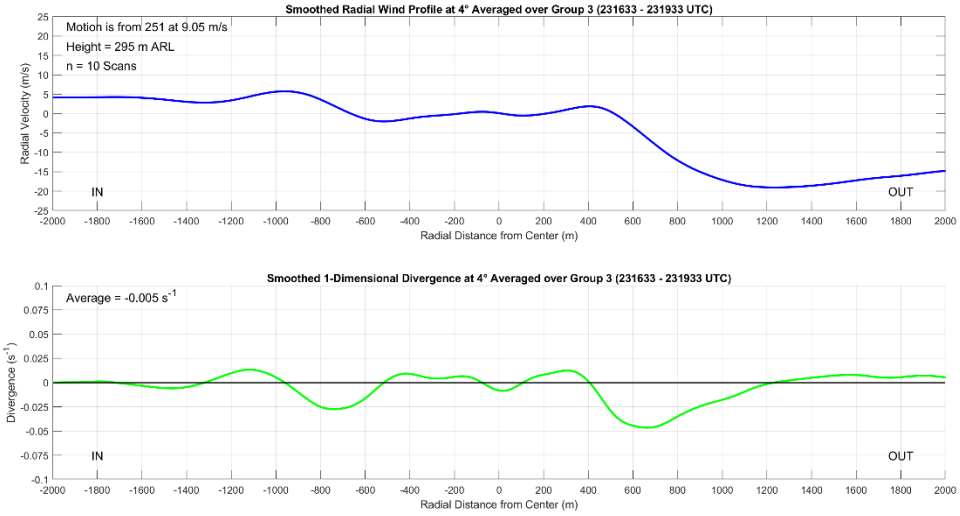

Figure 5.8: Radial wind cross section through the Selden tornado at the 4° elevation for segment 3 (top) and 1-D divergence (bottom).

which are orbiting the center of the tornado and producing wide ranges of velocity measurements at the radar from scan to scan. The standard deviation of the velocity values in the segment 3 cross section also reaches relative maxima near the RMW, again suggesting a wide range of measured values near the RMW in the individual scans that make up the average cross section, and thusly, a tornado that is changing size.

The vortex radial wind profile for segment 3 is shown in Figure 5.8. Near the center of the cross section in and around the tornado, there is now a very broad area of divergence that is over 800 m in diameter. Additionally, unlike previous radial wind profile divergence maxima, this area of divergence is weak and has no defined maximum near the middle of the cross section. Because the Selden tornado has undergone a multiple vortex transition, the tornado has become much wider, causing there to be a larger area of centrifuging. However, the magnitude of ΔV_{max} did not increase with the increased radius of the tornado, decreasing the magnitude of the centrifugal force within the tornado and decreasing overall divergence within the vortex. This finding supports the notion that the magnitude of the

dynamic pressure minimum within the tornado decreased significantly during the multiple vortex phase, and that it was unable to drive enough near surface convergence into the tornado even after the inflow channel disruption ended to spur transition of the tornado back to a single celled vortex. Another notable feature of the radial wind profile is the convergence on either side of the tornado, perhaps marking where inflow is slowing down as it turns upwards at the edges of the tornado. The convergence signatures could also be a result of inflow slowing as it encounters debris (Wakimoto et al. 2020). Finally, the profile is overall convergent, reflective of a strong and strengthening supercell mesocyclone.

5.5: Descending Reflectivity Core

During segment 3, a second DRC was identified as depicted in Figure 5.9. Over a 2-minute period beginning at the start of segment 3 at 2316:29 UTC, a large area of high reflectivity greater than 45 dBZ is observed to fall through the domain all the way to the ground. In the first analysis panel, the DRC is located at roughly 1000 m ARL and includes areas to the east and north of the tornado. The weak echo column of the tornado is also clearly visible in this volume. Over the next two analysis times, the DRC continues its descent, first to the east and then north of the tornado. Finally, by the last panel in the analysis at 2318:29 UTC, the DRC has passed entirely through the bottom of the domain very near the surface as it contacts the ground. The DRC is again falling on the east and north sides of the tornado as would be expected for a DRC coming off the overhang of the parent supercell. Since the DRC falls through the lowest 1 km of the storm in less than 2 minutes and is likely descending from the supercell overhang, it closely matches the Rasmussen et al. (2006) definition and is likely a type 1 DRC (Byko et al. 2009).

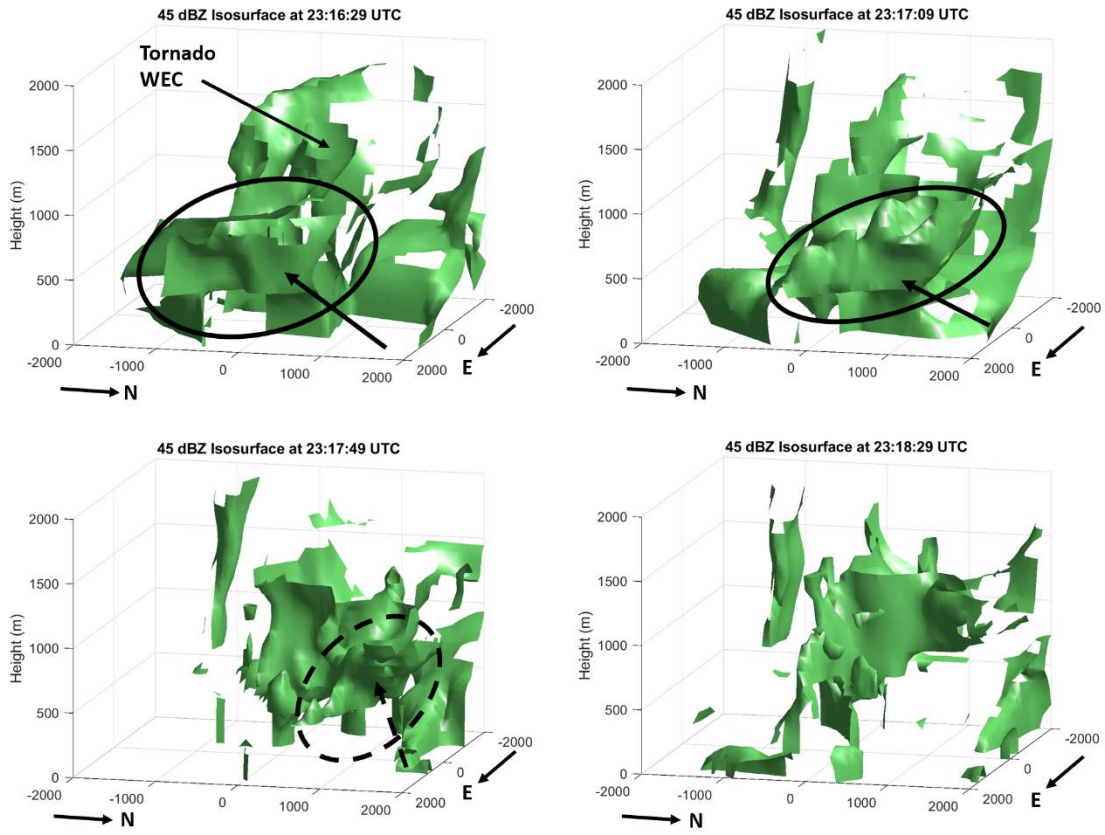

Figure 5.9: Volumes enclosing reflectivity values greater than or equal to 45 dBz. The domain is centered on the tornado in each panel, and the view is from the northeast. All distances are in meters (m). For clarity, the DRC is circled and denoted with an arrow. The dotted arrow and circle denote that the DRC is reaching the ground and has passed through the bottom of the domain.

Since the identified DRC is likely type 1, it is close enough to the tornado that it may have an impact on the vortex wind field. Figure 5.10 contains south to north reconstructed cross sections through the tornado center at the same times as the volumes in Figure 5.9. The DRC is clearly visible in the reflectivity cross sections. In the first panel at 2316:29 UTC, the high reflectivity core is centered at 1 to 1.2 km ARL. In the second panel 40 seconds later, the DRC is now at 0.8 km ARL, and in the third panel, is roughly 0.5 km ARL. By 2318:29, only the top of the DRC is visible, and the core of high reflectivity is below 0.2 km ARL. As compared to the first DRC from segment 2, this DRC is falling a bit farther from the tornado, located around 0.8 km north of its center. Nearly

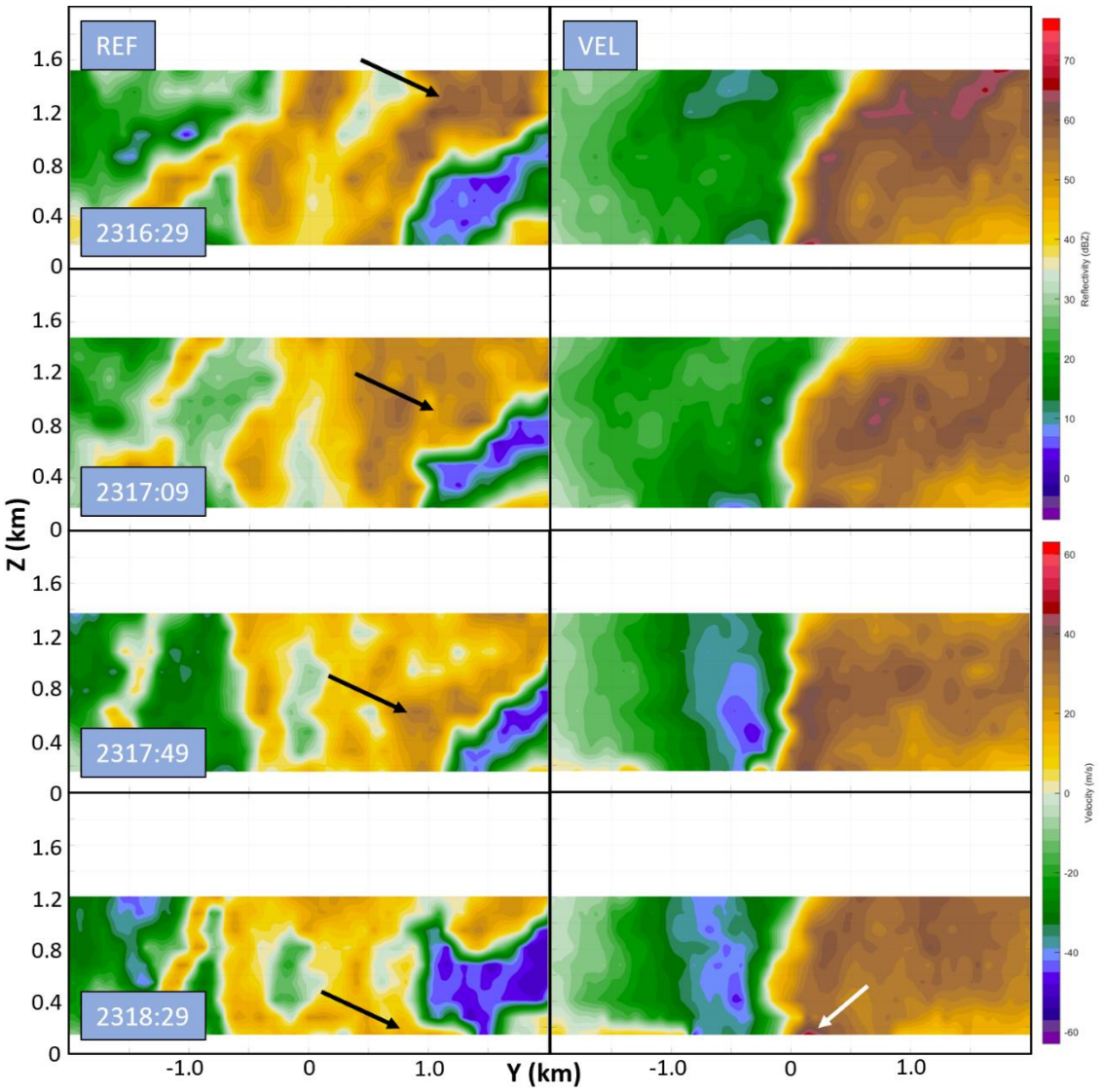

Figure 5.10: Reconstructed cross sections through the tornado at the same 4 scans as in Figure 5.9. Reflectivity is on the left and Doppler velocity on the right. Black arrows point to the DRC, while a white arrow indicates the potentially related low-level velocity increase.

double the tornado radius from the tornado center, this DRC is likely too far away from the tornado to have an effect before hitting the ground. The velocity cross sections reflect this, with no clear protrusions of the positive Doppler velocities following the DRC downwards. However, there does appear to be an increase in the velocities on the north side of the tornado in the last analysis panel at 2318:29, perhaps because of the enhanced convergence on the DRC outflow impinging the tornado from the north.

Interestingly, the DRC contacts the ground shortly after 2318 UTC. This is coincidental with peak inflow disruption (See Figure 5.3) and the Selden tornado's multiple vortex transition (See Figures 5.5 and 5.6). While the DRC is relatively far from the vortex, perhaps it may have played a role in enhancing momentum north of the tornado along with the RFD surge present at the same time. If this were the case, the additional enhancement of momentum north of the tornado from the DRC may have increased the severity of the inflow disruption, causing the multiple vortex transition to take place. However, because of the presence of the high momentum within the RFD surge, it is not possible to find a distinct DRC outflow velocity signature within the RaXPol data. Furthermore, limitations of 1-dimensional Doppler velocity preclude the analysis of the divergence field and previously described issues with the 2° and 0° RaXPol data prevent investigation at the lowest levels where the DRC response would be largest.

5.6: Streamwise Vorticity Current

During segment 3, the Selden tornado continues to strengthen and then reaches a plateau at a ΔV_{max} approaching 80 m s^{-1}. While the tornado is certainly intensifying because of a favorable position within enhanced convergence and vorticity near the apex of the RFGF and forward flank boundary, part of this strengthening may be the consequence of an SVC. While current research has not yet answered the question as to whether air from an SVC is actually ingested by tornadoes, they certainly have direct impacts on the health of the parent supercell and mesocyclone (e.g., Schueth et al. 2021). To search for a potential SVC feature, RHI's were reconstructed using RaXPol data from segment 3 since both the supercell and tornado reached their peak intensities during this time, radar data were very

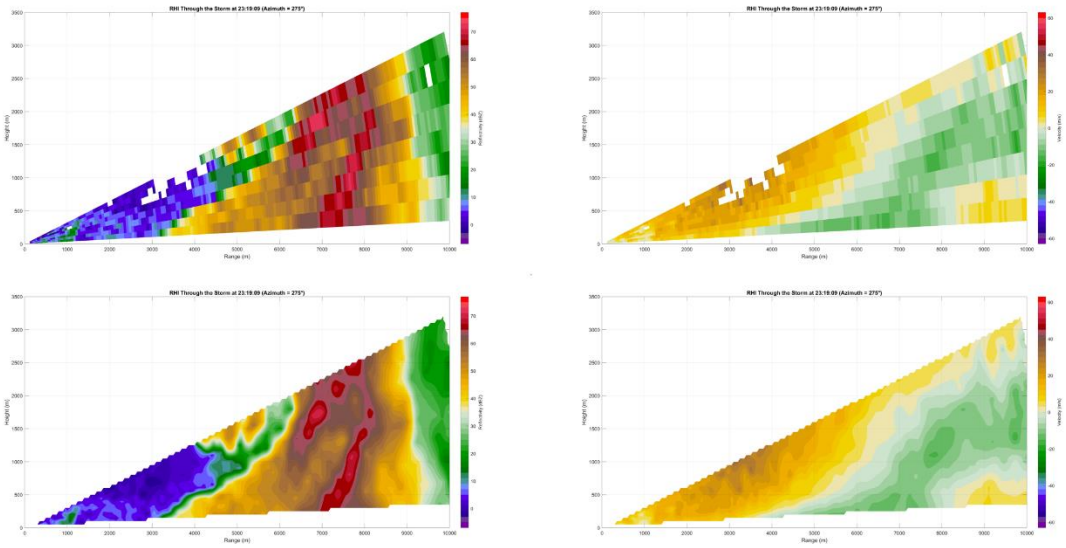

Figure 5.11: Comparison of raw (top) and interpolated (bottom) reconstructed reflectivity and velocity RHIs from 2319:09 UTC at an azimuth angle of 275°.

high resolution due to storm proximity, and angles from the radar to the supercell forward flank were favorable for analysis. Figure 5.11 contains an example of the RHI's in their raw form compared to those after interpolation to a grid. There are minimal differences between the two; interpolated RHIs will be used in lieu of raw forms for analysis.

Provided in Figure 5.11 is the best example of a potential SVC feature found in any of the reconstructed RHIs. The position of the RHI in Figure 5.12 is roughly 1 km upwind from the forward flank boundary and RFGF apex along the forward flank boundary. Within the velocity RHI on the top right of Figure 5.12, the negative inbound velocities within the forward flank outflow underlie the positive outbound velocities within the supercell inflow. Centered at a range of 4.9 km and a height of 0.5 km, a distinct velocity signature appears, with inbound and outbound radial velocities extending towards each other to form a relatively tight vertical gradient. The spike in vertical shear indicates the presence of a circulation, with outbound velocities over inbound ones giving the circulation a clockwise sense and vorticity oriented into the figure. Because the RHI was constructed upwind of

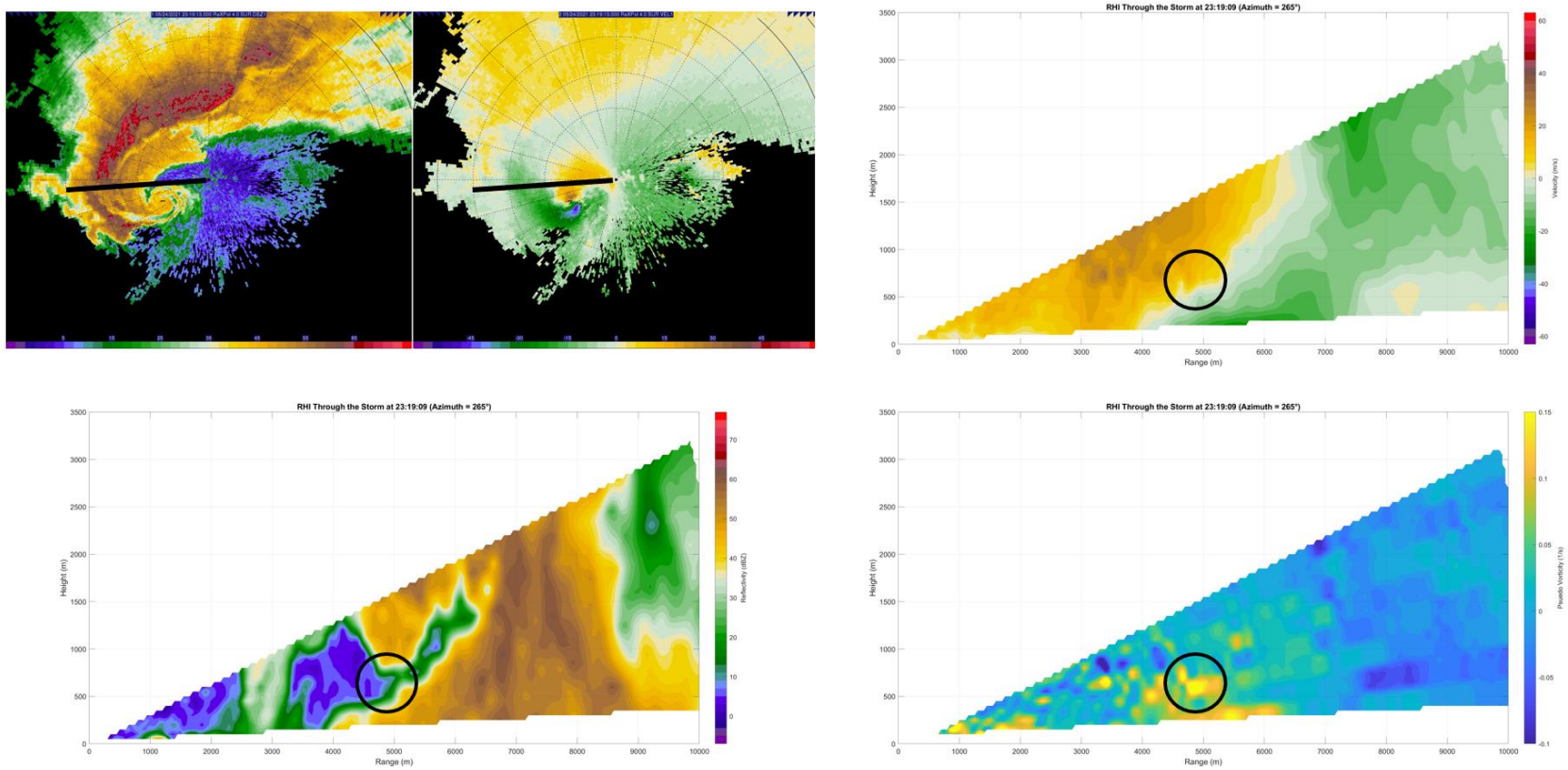

Figure 5.12: Reconstructed RHIs from 2319:09 UTC at azimuth 265°. The reconstructed velocity (top right), reconstructed reflectivity (bottom left), and calculated 1-dimensional horizontal vorticity (bottom right) are provided along with the corresponding 4° elevation PPI plot that shows where the RHI was reconstructed. Black circles denote the SVC feature.

the supercell mesocyclone along the forward flank region, the vorticity vector is pointing towards the mesocyclone.

The tightest gradient in velocities in Figure 5.12 appears just above the forward flank outflow, putting the resultant horizontal vorticity generated by the circulation within the inflow region. Winds within the inflow region likely contain a component directed towards the supercell mesocyclone, creating streamwise horizontal vorticity. Owing to the single-Doppler nature of the data and position of the supercell relative to the radar, it is not possible to prove that a component of wind directed towards the supercell mesocyclone is present during segment 3. However, earlier scans from segments 1 and 2 from when the supercell was farther to the west and the inflow region was at a different angle from the radar do show a significant component of the wind within the inflow region directed towards the mesocyclone. The same component of wind directed towards the mesocyclone is inferred to exist during segment 3 as well, creating significant streamwise horizontal vorticity. The 1-dimensional vorticity associated with the velocity signature is approximately 0.15 s^{-1}, as shown in the bottom right panel of Figure 5.12. Strong positive vorticity below the identified vorticity maxima is related to surface interaction. Finally, the SVC feature also lies within the entry to the supercell vault directly under the overhang.

The height ARL and location of the SVC feature agree closely with what was found in Schueth et al. (2021), which showed that SVCs were located right behind the surface position of the forward flank convergence boundary and were typically centered 0.5 km above the ground and generally occurred within 5 km along the forward flank boundary upwind from the RFGF and forward flank apex. However, the 1-dimensional horizontal vorticity calculation yields values that are close to double the horizontal vorticity

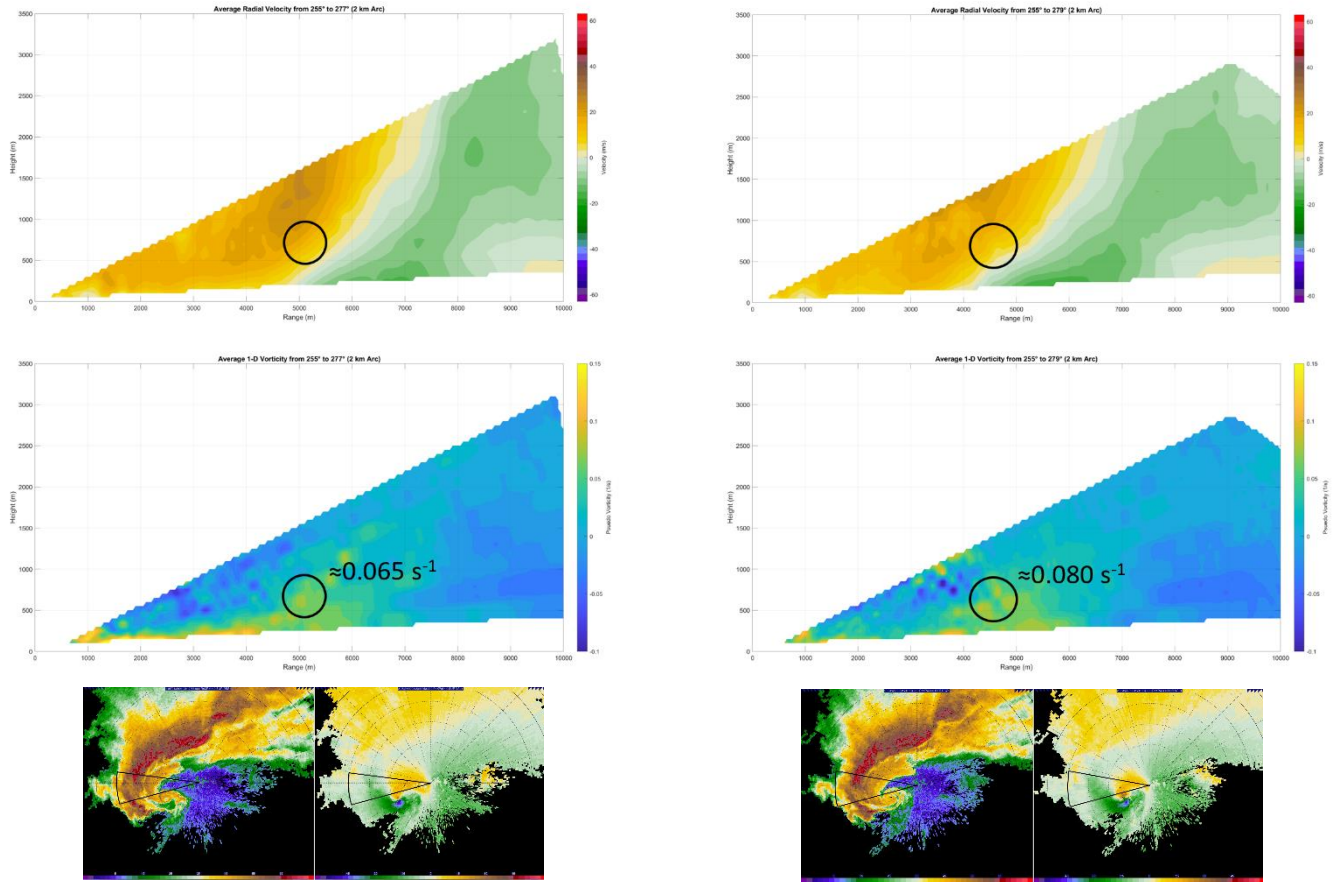

Figure 5.13: Averaged reconstructed RHIs taken every 2° in azimuth for a 2 km arc along the forward flank boundary. The panels on the left show analysis for 2317:49 UTC, with averaged velocity (top) and averaged reflectivity (middle). The panels on the right show analysis for 2319:09 UTC, with averaged velocity (top) and averaged reflectivity (middle). Radar PPIs are provided on the bottom of the figure to show the wedge that is represented by the average RHIs. Black circles denote the approximate location of the strongest horizontal vorticity.

magnitude of 0.08 s^{-1} found by Orf et al. (2017) and Schueth et al. (2021). Much of the overestimate is likely a result of the crudeness of the 1-dimensional vorticity calculation, which is limited by use of the Doppler velocity. Nonetheless, the vorticity maxima collocated with a velocity signature is a good match for a potential SVC.

When several reconstructed RHIs are taken spaced equidistant from each other along the forward flank boundary and averaged, the SVC feature vanishes and the RHIs simply reveal a velocity pattern that is expected from the density current at the edge of the forward flank cold pool. Figure 5.13 contains this type of analysis at two times, 2317:49 and 2319:09 UTC. The first time is mid-way through segment 3, while the second is the last complete volume before D6 data collection ends. In both analyses, RHIs were reconstructed at 2° azimuth increments from the northern edge of the supercell hook echo near the forward flank and RFGF apex to a point roughly 2 km upwind along the forward flank boundary. At 2317:49 UTC, a broad area of enhanced horizontal vorticity is centered about 0.6 km ARL and has a magnitude of approximately 0.065 s^{-1}. Similarly, a horizontal vorticity maximum appears at 2319:09 UTC, but its magnitude has increased to roughly 0.08 s^{-1}. While the increase in approximated horizontal vorticity indicates that the supercell may have been strengthening or developing through segment 3 or that an SVC had become established, the area of enhanced vorticity is broad and rather diffuse. In Schueth et al. (2021), SVCs were found to be transient features, appearing in the heads of breaking Kelvin-Helmholtz waves at the leading edge of the forward flank cold pool. Because of this, an SVC does not appear in the averaged RHIs. Instead, only the density current from the forward flank remains, with colder outflow moving towards the radar at the surface and supercell inflow moving away from the radar aloft; only broad horizontal vorticity exists

within the transition from forward flank outflow to the ambient inflow above it. While Figure 5.12 contains the best example of an SVC, Figure 5.13 reveals their transient nature, with the SVC velocity and vorticity signature disappearing in the average.

Chapter 6

The Selden, Kansas Tornado During D7

6.1: Track Behavior

During D7, the track of the Selden Tornado becomes irregular and undergoes many significant shifts as seen in Figure 6.1. The many track deviations apparent from Figure 6.1 are embedded within a larger scale pattern of movement typified by a gradual left turn towards the north, with the tornado eventually moving to the north-northeast shortly before dissipation in segment 7 at all scan elevations. In addition to making a gradual leftward turn, the tornado also slows down. During most of D6, the Selden tornado was moving along with its parent supercell at roughly 9.5 m s^{-1} from 240° (SW). In between D6 and D7 the forward speed of the tornado averaged only slightly more than 6 m s^{-1} at the 4° elevation, which then continues to decrease in segment 4 to only about 4 m s^{-1}. In both direction and forward speed, the track of the tornado no longer resembles that of the parent supercell after segment 4; the differing motions between the parent storm and tornado indicate a disconnect between the tornado and low-level supercell mesocyclone from the rest of the storm. The differential motion vectors between the tornado and parent supercell reflect a decoupling between the tornado and RFGF as occlusion takes place. Described by Dowell and Bluestein (2002) and Tanamachi et al. (2007), the occlusion of a tornado occurs as it becomes enveloped in downdraft air and buoyant inflow ceases, which results in decay

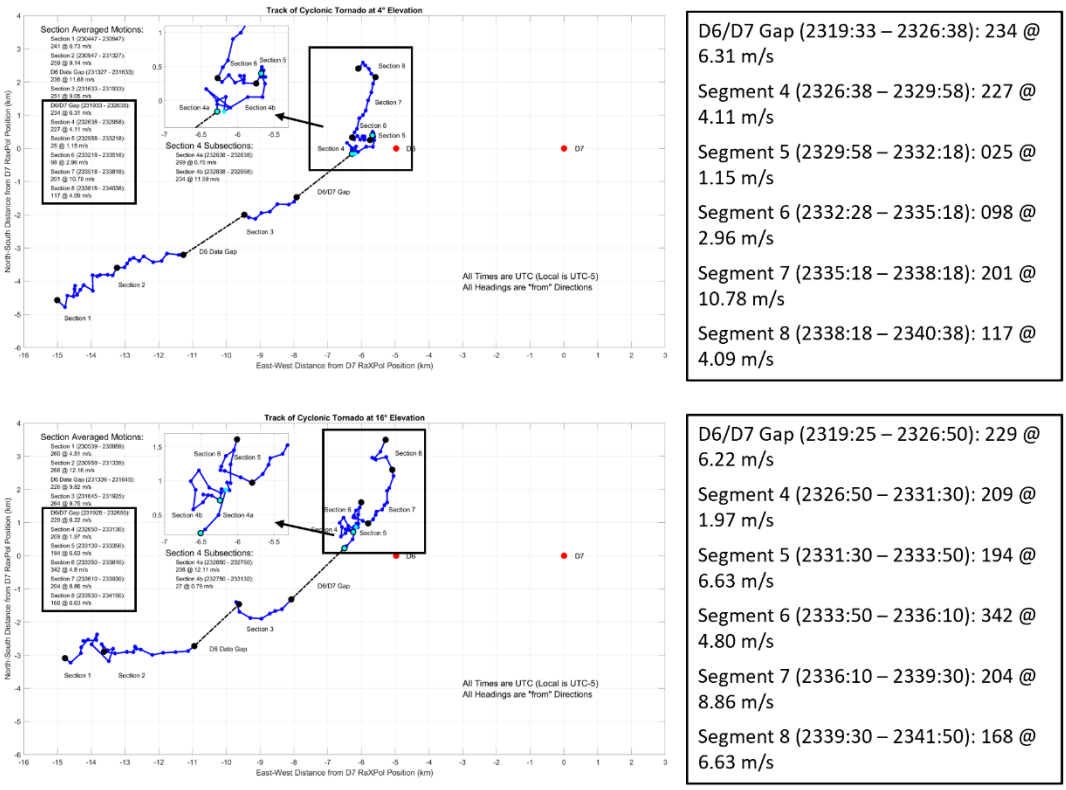

Figure 6.1: Track of the Selden tornado at the 4°(top) and 16° (bottom) elevation scans. Zoomed insets of the tracks leading up to and during D7 are provided, along with descriptions of the segment motion vectors.

of the tornado. In addition, decoupling from the RFGF means that the tornado and low-level mesocyclone are no longer 'anchored' to the parent supercell; in effect, there are no longer any near-surface features or boundaries to force movement of the tornado along with the parent supercell and the tornado falls behind (Adlerman and Droegemeier 1999). Since storm motion is east northeastward, the tornado and low-level mesocyclone move predominantly westward with respect to the parent supercell. Concurrently, the tornado track also trends leftwards with respect to the track of the parent supercell after occlusion. Persistent leftward motion of the tornado is likely a result of RFD surge influence; additional details will be addressed in the following radar analysis in section 6.2.

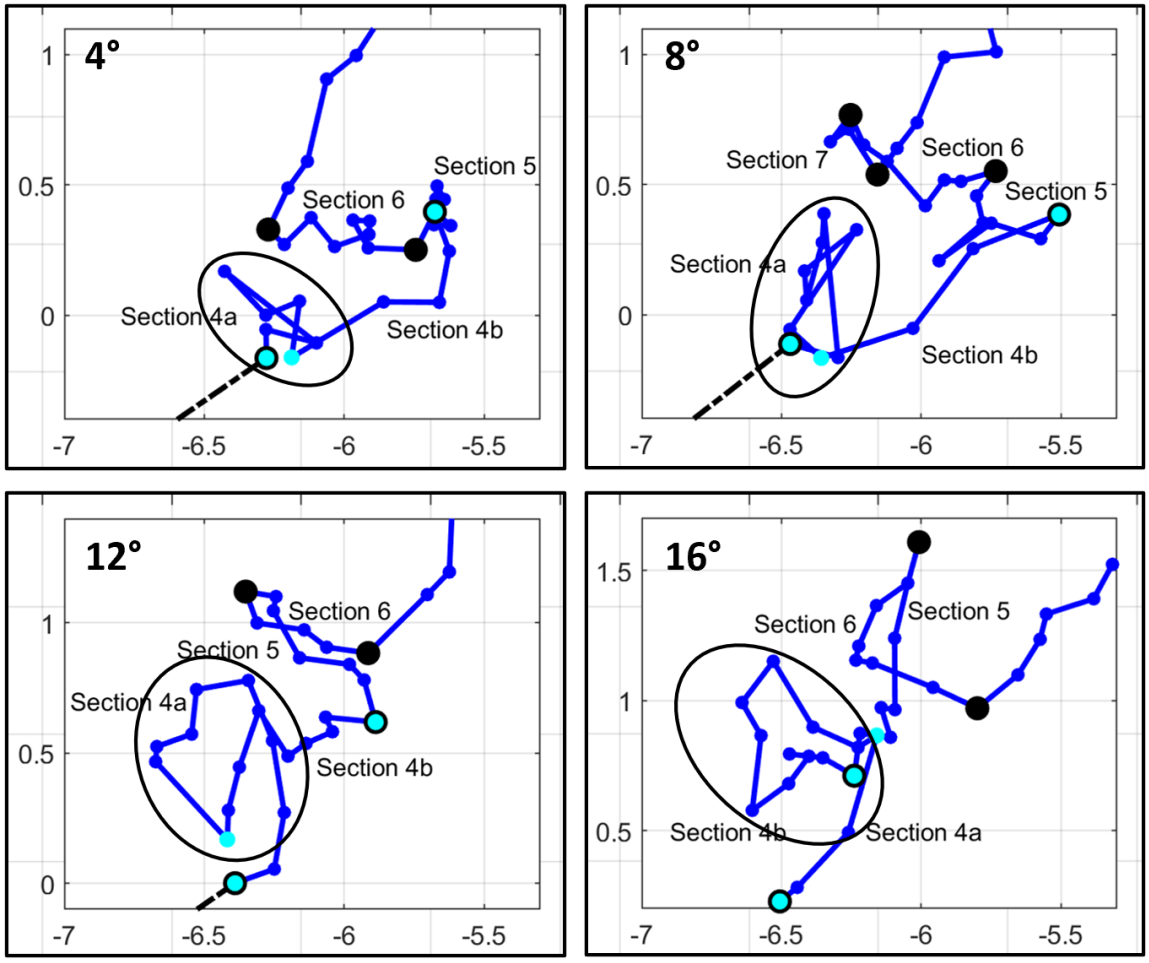

Figure 6.2: Comparison of the first cyclonic track loop at 4° increments. The evolving area of the track which represents the track loop is circled in each diagram. Axes are measured from D7 RaXPol position (km).

As the tornado becomes further separated from the RFGF and the supercell inflow channel, smaller scale forcings such as RFD surges have a greater effect on the tornado track, resulting in a sequence of unique movement patterns. At the 4° elevation, which during D7 remains at roughly 400 m ARL, the tornado track was separated into 5 segments based on numerous track shifts. Segment 4, the first of D7, contains generally northeasterly motion from roughly 225° (SW) at slightly greater than 4 m s^{-1}. Notably, this track vector represents an average for a segment in which the tornado sustains a significant track deviation which can be seen in Figures 6.1 and 6.2. At the very start of D7, the tornado

begins moving northwestward before moving back southeastward onto the previous track. A similar feature is seen in the 16° map in Figure 6.1 and throughout all scan elevations, a breakout of which is shown in Figure 6.2 at 4° elevation increments. At the 16° elevation, which is roughly 1700 m ARL during D7, the feature is clearly a track loop; the tornado enters the loop curving to the northwest, passes through the top of the loop moving to the south, then completes the loop and exits it heading back to the east before resuming a northeasterly track. Because of the motion of the parent supercell, which even after occlusion is still forcing the tornado to the east at a reduced speed, the track loop does not appear to be a loop at the 4° elevation; while the tornado is moving west at the top of the loop, it is doing so into the eastward component of motion forced by the parent storm such that the two motions sum to zero zonal movement. In the 12° and 16° track map, the cyclonic track loop is notably more pronounced. The tornado has a longer dwell time in the loop, resulting in a much slower average segment 4 motion at 16° of about 2 m s^{-1} from approximately 210° (SSW). The track loop of segment 4 and its similarity to the one analyzed by Kurdzo et al. (2015) will be a focus during radar and RFD surge analysis.

Following the track loop at the 4° elevation, the Selden tornado's forward speed rapidly increases. Because of this significant speed change, segment 4 is also subdivided into two sections. The first subsection at the 4° level contains the track loop while the second subsection is typified by the rapid northeasterly movement right after the loop. During the second subsection, the tornado moves forward at nearly 12 m s^{-1} from 235° (SW). While the track direction is typical of the parent supercell, the speed is not. For the brief duration of the subsection, the tornado moves faster than at any other observed portion of its lifecycle. A similar speed increase was observed by Lee and Finley (2022) associated

with RFD surges, albeit accompanying a leftward track turn. While the resulting motion from changes in bounding momentum brought on by RFD surges was different in the Lee and Finely (2022) cases, it is likely that the brief movement speed burst and rapidity of track changes during segment 4 are the result of RFD surges. More details will be examined during radar analysis.

Meanwhile, at the 16° elevation, the tornado continues to execute the cyclonic track loop, which takes much longer to complete at higher elevations. The first segment 4 subsection at 16° represents a brief period just before the track loop, which is slightly delayed with height. Then, the second subsection constitutes the track loop. At 16°, the track loop and second subsection last until 2331:30 UTC, which is well after the end of the loop at 4° (2328:38 UTC) and even segment 4 at 4° (2329:58 UTC). Because of the much longer dwell time in the track loop at 16°, the burst of rapid movement at the 4° level is happening while the tornado is still executing the track loop at 16°; the tilt of the tornado from 4° to 16° elevation increases to over 40° off vertical towards the north and then northwest during segment 4 (See Figure 6.4). As a result of continuing occlusion and perhaps due to rapidly increasing tilt of the vortex, it is at about 2330 UTC that the Selden tornado's condensation funnel completely dissipates. Although the correlation coefficient minimum from debris lofting and the WEH associated with the tornadic vortex remain, the tornado itself is no longer readily visible to any observer due to the lack of any condensation funnel and decreasing amounts of lofted dirt and dust.

After rapid tornado motion during the latter part of segment 4 at the 4° level, the Selden tornado comes to an abrupt stop during segment 5. For a period of 2.5 minutes, the tornado barely moves. As with the track in segment 4, RFD surges and the momentum they

transport are likely playing a role in keeping the tornado stationary by causing the tornado to move westward at the same speed as the parent supercell's eastward component of motion. Interestingly, segment 5 changes significantly with height. As height increases, the motion in segment 5 becomes less stationary, slowly appearing more like an extension of northeasterly movement during segment 4. By the 10° elevation, segment 5 is no longer distinct, and it merges into segment 4 (See timeline in Figure 3.8, map in Figure 6.1). Furthermore, the sharp changes in track seen at the end of segment 4 at the 4° elevation also disappear with height; the tornado no longer picks up so much speed after the track loop before coming to an abrupt stop. Consequently, the tracks at higher elevations during the first 4 to 5 minutes of D7 are closer to a gradual leftward turn and are less impacted by the action of RFD surges. Because RFD outflow is usually strongest near the surface, it would be expected that the tornado track would be dominantly governed by the occlusion process at higher elevations. As a result, the tornado moves at a more consistent pace westwards into the parent supercell and any track shifts are more subtle and smoother; a more thorough investigation will follow during radar analysis.

Especially at lower scan elevations, the Selden tornado unexpectedly begins retrograding after segment 5. At the 4° elevation, the tornado moves almost due west for a period of 3 minutes, tracking from 100° at roughly 3 m s^{-1}. The transition from segments 5 to 6 at the 4° scan level likely represents an amplification of the bounding momentum balance that led to the stationary motion in segment 5, causing the tornado to have a larger westward component of motion than the eastward component of motion forced by the parent supercell. Also, like the stationary movement of the preceding segment, the nature of the retrograding movement of segment 6 (from 2° to 8° scan elevation) and segment 5

(from 10° to 18° scan elevation due to loss of stationary phase) changes greatly with height. As height increases, the motion during the segment representing retrograding movement becomes less westward and starts to take on a northward component. By the 16° elevation at 1.7 km ARL, the motion during the retrograde phase is not actually westward any longer; the tornado's track vector at the 16° level is north-northeasterly at almost 7 m s^{-1} from 190° (S). Once again, the changes in retrogression at higher elevations reflect the waning influence of the RFD outflow and growing dominance of the occlusion process with height.

After the tornado retrogrades, the track becomes increasingly disjointed with height. At the 4° elevation, the tornado takes an abrupt turn towards the north and forward speed increases markedly. The transition from segment 6 to segment 7 is sharp, with the track vector becoming 11 m s^{-1} from 200° (SSW); the track heading changes by more than 100° and average forward speed more than triples. However, transition to a northward heading does not happen right away at the 16° level. As seen in Figure 6.1, there is an intervening secondary cyclonic track loop at the 16° elevation before the track takes on a north heading like it does below at the 4° level. At the 16° elevation, the tornado is on a due northward track during segment 5, which is the segment representing the retrograde phase at 16°. Suddenly, the tornado then stops and moves slightly to the west as it transitions back south at the start of segment 6. After moving south for 4 scans (80 s), the tornado then recovers back to the east before turning north during segment 7, where the motion of the tornado becomes very similar to that at the 4° level. If segments 5 and 6 at 16° are combined, they constitute a feature that presents as another cyclonic track loop.

The second track loop is not continuous with height like the first one. Provided in Figure 6.3 are zoomed in portions of the track showing the second track loop at 4°

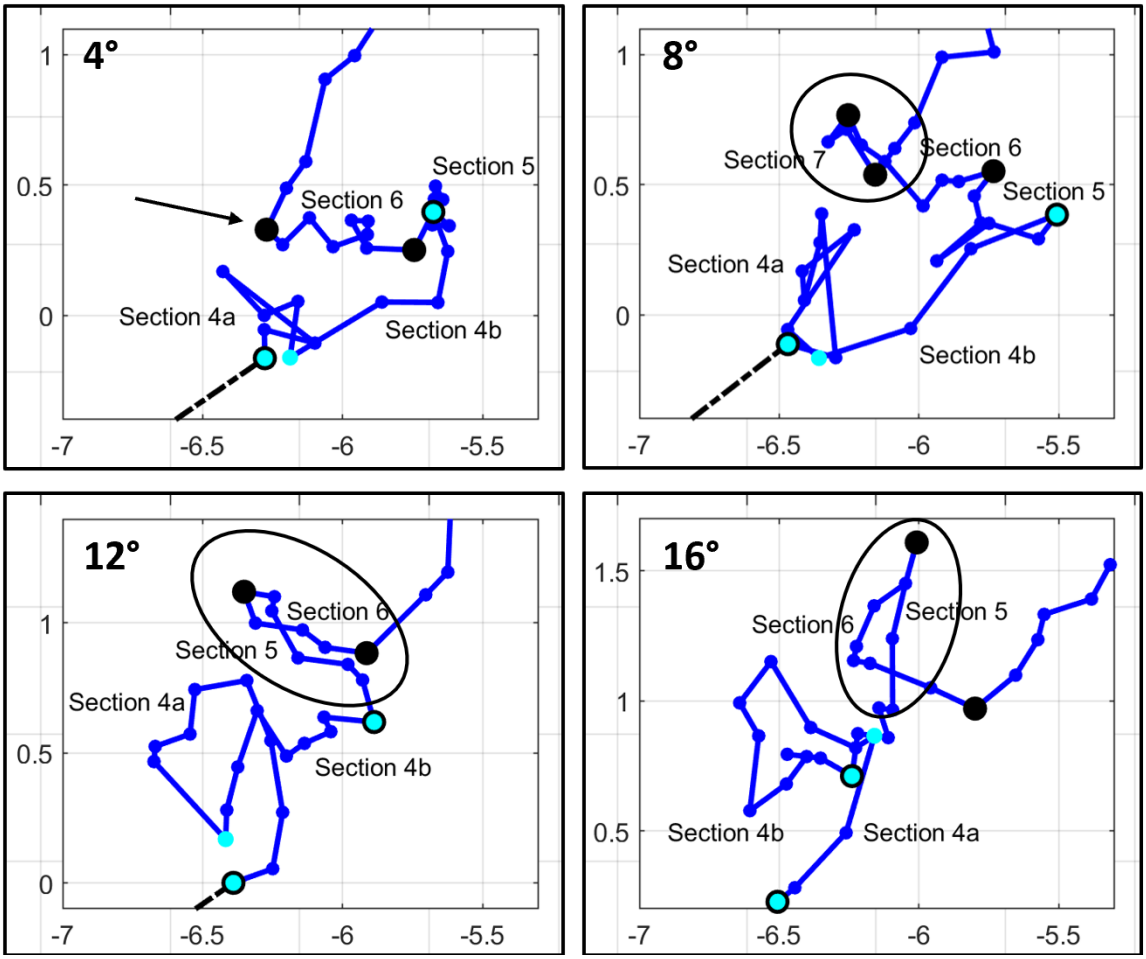

Figure 6.3: Comparison of the second cyclonic track loop at 4° increments. The evolving area of the track which completes a transition to a track loop by the 16° level is circled in each diagram. Axes are measured from D7 RaXPol position (km).

increments from the 4° to 16° level. While there is no hint of a track loop at the bottom of the domain at 4° besides for the sudden turn to the north, the loop starts to appear higher up. At the 8° elevation, a short burst of southeasterly movement, which lasts for only 3 scans (60 s), occurs in between the end of the retrograde phase and northward movement phase. The trend of increasing track loop resemblance continues at the 12° level, where the burst of eastward movement has become drawn out; segment 6 at the 12° elevation sees the tornado moving back east as far as it had to the west in the previous segment. Finally, by the 16° elevation, the loop becomes fully visible.

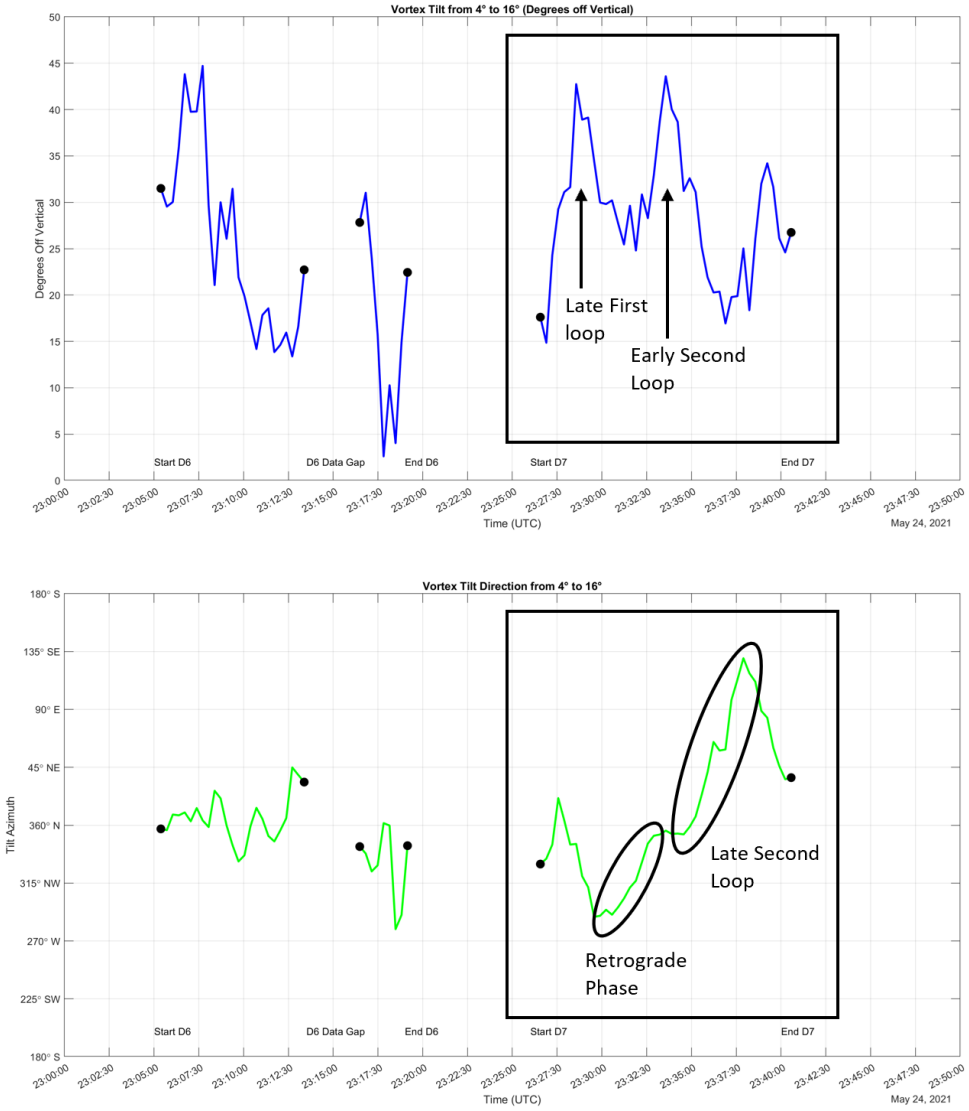

Figure 6.4: Tilt analysis for the Selden tornado, highlighting features associated with height dependent movement during D7. Analysis is done from the 4° level to the 16° level.

Further indications for the height dependent motions during D7 can be found in tilt analysis presented in Figure 6.4, which is accurate to within 5° for tilt magnitude and to within 5° for tilt azimuth when tilt is sufficiently large. The upper panel of Figure 6.4 displays the tilt in degrees off vertical from the 4° to 16° scan elevation while the lower panel shows the direction of the vortex tilt with height from the 4° to 16° scans. During the second track loop at 16°, the tilt of the tornado first spiked to over 40° off vertical and tilt

became almost due north as the tornado tracked slowly westward at low-levels and northward aloft. Then, the tilt decreased to about 20° off vertical and the tilt took on an easterly component during the latter half of the second track loop as the tornado at 16° moved south and then back east over the lower-level track. Once the tornado at 16° crossed over the track at 4°, tilt increased again towards 30° off vertical. The widely variable vortex motions around the second track loop are likely the result of differing RFD surge and momentum configurations around the tornado with height, which will be investigated further in radar analysis.

After the second track loop, the tornado track becomes uniform with height as the tornado picks up speed at all scan elevations on a north-northeasterly track during segment 7 (segment 8 at 8° due to appearance of second track loop, see Figure 3.8). The track vector at 16° during segment 7 is 205° (SSW) at nearly 9 m s^{-1}, which matches closely to the track vector at 4° of 200° at 11 m s^{-1}. Notably, the forward speed at lower levels is still greater than that aloft. Consequently, the northward component of the tornado tilt completely vanishes, and the tornado becomes tilted towards the southeast by the end of the segment at over 30° off vertical (see Figure 6.4). The track during segment 7 is also remarkably smooth and stable compared to previous segments in D7; the track continues in nearly a straight line with no major perturbations. This stability likely reflects waning influence of RFD surges as the RFD and proximate tornado wind field decay due to deepening occlusion. The transition will be seen more clearly in radar analysis in the following section, but as the tornado continues occluding along with the low-level mesocyclone, the RFD begins to rapidly weaken in segment 7 and RFD surges cease to be generated. Finally, segment 8 represents the complete occlusion and dissipation of the tornadic vortex. A final

left hook appears in the track, with the vortex moving westward again as it migrates into active downdraft regions within the parent supercell and dissipates in short order.

6.2: Evolution of the Near-Vortex Wind Field and RFD on Radar

6.2.1: Evolution in Early D7 – First Cyclonic Track Loop

A radar analysis at the 4° elevation (400 m ARL) covering segment 4 from 2326 to 2330 UTC is presented in Figure 6.5. In the first analysis time at 2326:38 UTC, two ongoing RFD surges are apparent. The leading surge is quite potent and is already wrapping around the tornado to its east and north; notably, very high easterly momentum is impinging north of the tornado with this surge. The strength and extent of surging momentum is reflective of a strong occlusion downdraft (Skinner et al. 2014). By analysis time 4 at 2328:38 UTC, surge 1 merges with the RFGF, displacing it from the tornado circulation. By the following analysis time, the RFGF breaks away from the tornado and the inflow channel on the western flank of the hook echo becomes cut off from the tornado. The tornado is unable to drive enough surface convergence to keep persistent surging momentum from displacing the RFGF; the RFGF and tornado become decoupled. Figure 6.5 indicates that occlusion occurs at a time close to 23:29 UTC, when the low reflectivity channel representing the inflow fills. An occluded portion of the RFGF still extends back to the tornado, as evident from the significant zone of radial convergence on the tornado's western flank. However, the occluded extension of the RFGF is not forced forward (eastwards) by the RFD outflow like the un-occluded leading portion of the RFGF and the tornado motion slows; the tornado begins to lag the parent storm. Furthermore, warm

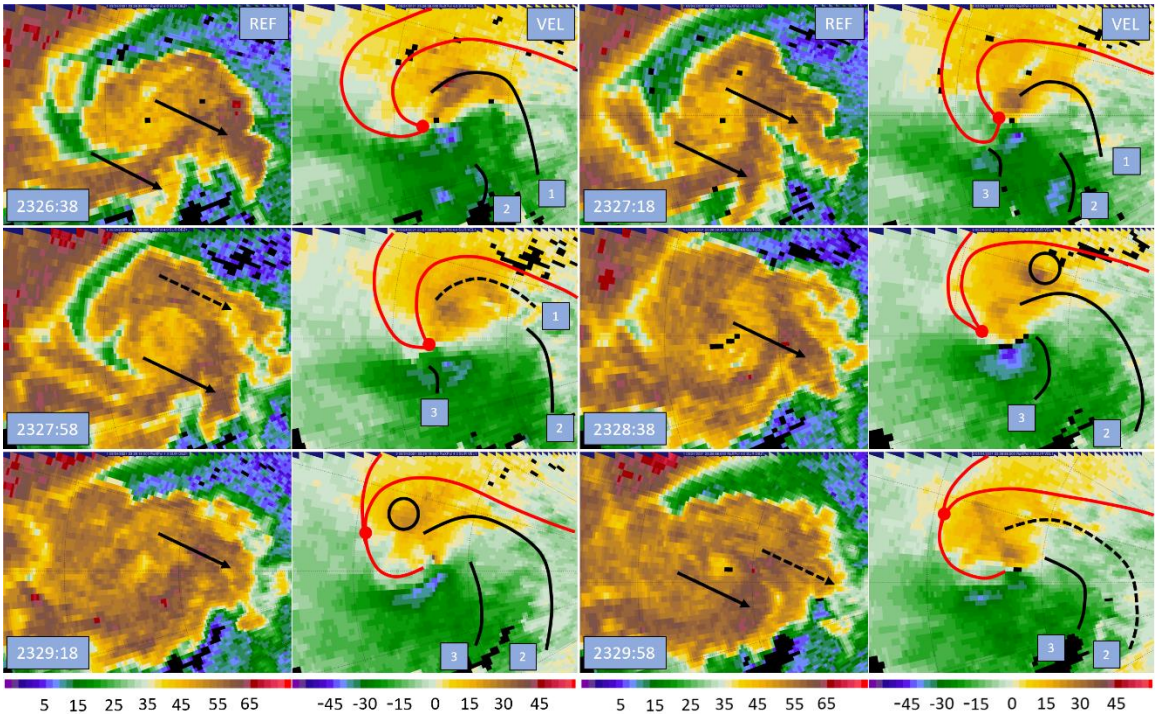

Figure 6.5: RaXPol imagery at the 4° elevation taken every 2 scans (40 s) during segment 4. In each radar panel, reflectivity is on the left and Doppler velocity on the right. Range ring spacing is 2.5 km. Black lines denote RFD surge fronts, which are also numbered. Black arrows also point to associated reflectivity appendages. Red lines mark the approximate positions of the forward flank and RFGF. A black circle also marks the location of an anticyclonic vortex, which will be investigated in section 6.4.

inflow is no longer reaching the tornado and is instead being forced up and over the occlusion, which is located at the triple point indicated by a red dot in Figure 6.5; the tornado begins to gradually weaken.

Both Lee et al. (2012) and Marquis et al. (2016) showed that RFD surges advance the tornado lifecycle, noting that a surging RFD eventually caused the near tornado air to become dominated by less buoyant downdraft air (See Figure 1.4). Similar evolution is seen in Figure 6.5, in which RFD surges cause the Selden tornado to become occluded. In their case, Skinner et al. (2014) tied the appearance of strong RFD surges near the low-level mesocyclone to the occlusion downdraft; Figure 5.4 shows how the occlusion

downdraft could generate RFD surges through pulsing behavior. These surges then go on to cause occlusion by displacing the RFGF from the tornado and surrounding the tornado in downdraft air.

As shown in the ΔV_{max} analysis of Figure 4.3, the tornado was much stronger near the ground than aloft during segments 3 and 4. In segment 3, the shear across the tornado was often close to 90 m s^{-1} near ground level, decreasing to under 70 m s^{-1} at the top of the domain near 1300 m ARL. A similar trend continues into early segment 4 leading up to occlusion, where the shear across the tornado is near 80 m s^{-1} close to the surface and is approximately 60 m s^{-1} at 2 km ARL. In both segments, the vortex had similar widths at both the bottom and top of the domain, causing vorticity to be greatest near the surface. As a result, the occlusion downdraft was found to form during Segment 3, and it is likely still present during segment 4. By the middle of segment 4, the occlusion downdraft has become established enough to create significant surging momentum within the RFD near the surface, especially on the eastern and northern flanks of the tornado. In analysis of segment 3, it was found that the occlusion downdraft was likely south of the tornado; the shift of surging momentum during segment 4 to the eastern and northern flanks of the tornado is expected given that the occlusion downdraft slowly wraps around the tornado circulation with time (Adlerman and Droegemeier 1999). Due to the surging momentum, the RFGF is displaced and breaks away from the tornado. Ultimately, the RFGF and tornado become decoupled as the RFGF displacement grows, and occlusion occurs.

Occlusion of the tornado has profound consequences for its movement. First, as explained in the track analysis section, decoupling from the RFGF means that the tornado no longer moves with the RFGF as RFD outflow pushes it forward. As a result, the

tornado's forward movement slows, and the tornado moves rearwards (westwards) into the parent supercell. In addition to westward storm relative motion, the Selden tornado also tracks persistently leftwards of the parent supercell. Leftward motion of the tornado is likely a result of RFD surges, which continue to be generated after occlusion takes place. The tornado becomes decoupled from the RFGF at the onset of occlusion, isolating the tornado and low-level mesocyclone from the mechanism that was responsible for its movement along with the parent supercell. Consequently, the tornado becomes very susceptible to the influence of RFD surges, and the tornado is readily advected by the RFD surges in the direction of their movement. RFD surges typically follow a trajectory around the tornado circulation from their origin near the southern flank of the tornado towards the northern flank of the tornado. While this occurs, RFD surges continually spread out into the RFD and begin merging with the RFGF. Only a portion of the original surge momentum reaches the northern flank of the tornado and very little, if any, momentum is ever transported to the western flank of the tornado where it would be directed from the north. The result is that enhanced momentum occurring both to the south and north of the tornado counteract each other to varying degrees depending on the RFD surge trajectory, while enhanced southerly momentum east of the tornado is rarely compensated for by significant northerly momentum on the tornado's western flank. In response, the tornado tends to move north with respect to the parent supercell after occlusion occurs. Such a pattern of momentum and tornado movement is seen throughout D7 in the radar analyses that follow.

Leading up to occlusion in segment 4, potent RFD surges are likely present because of the occlusion downdraft. These powerful surges alter the tornado track even before occlusion occurs near 23:29 UTC. Then, after occlusion has occurred, even weak RFD

surges begin to exert considerable influence on the tornado track. As previously discussed regarding a possible track loop during early segment 3 and found by Kurdzo et al. (2015) and Lee and Finley (2022) in their studies, the specific arrangement of RFD surges and associated momentum around the tornado in space and time can cause the tornado to significantly change track or execute track loops. In Figure 6.5, RFD surge 1 is placing westerly momentum south of the tornado and southerly momentum east of the tornado as it pivots the circulation coincident with the start of the first track loop. During their analysis of the Moore 2013 tornado track loop, Kurdzo et al. (2015) also found a strong RFD surge moving north on the east flank of the tornado at the start of a track loop. As surge 1 moves north on the tornado's eastern flank, it promotes a northward shift in the tornado track. Then, as a portion of surge 1 is advected to the northern flank of the tornado, enhanced easterly momentum encourages westward movement of the tornado. However, the storm's eastward component of motion and tornado's westward motion counteract each other, resulting in near zero zonal movement. The momentum distribution of surge 1 and its impacts match closely to the start of the Kurdzo et al. (2015) conceptual model, which is adapted in Figure 6.6. Surge 1 in Figure 6.5 corresponds to the red surge in the model.

Following the first RFD surge, a second surge passes well south of the tornado. It is a potent surge; however, owing to its greater distance from the tornado, it has minimal direct impacts. Later, as surge 2 continues to spread outwards, some of the surge 2 momentum impinges north of the tornado, somewhat maintaining the high easterly momentum in place from surge 1. Right behind surge 2, momentum once again builds just to the west of the tornado, becoming apparent in the second analysis panel in Figure 6.5 at 2327:18 UTC. Surge 3 passes directly through the southern portion of the tornado

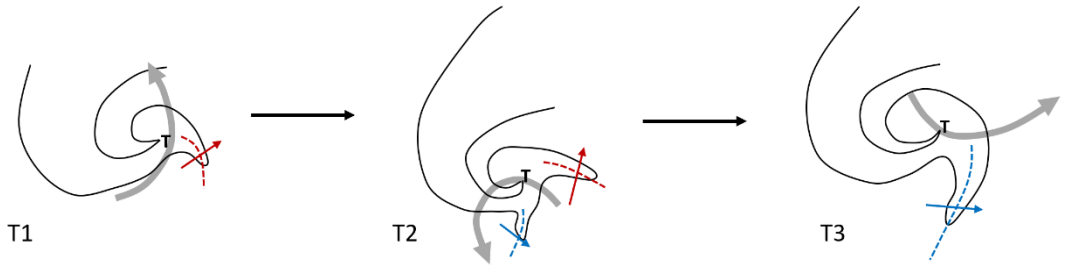

Figure 6.6: Conceptual model adapted from Kurdzo et al. (2015) to show the impact of surges at the 4° elevation during segment 4. During segment 4, RFD surge 1 from Figure 6.5 corresponds to the red surge while RFD surge 3 matches to the blue surge.

circulation while maintaining its initial easterly trajectory. While the surge is passing the tornado, the velocities on the south side of the vortex flare as the RFD surge momentum temporarily superimposes with it. Surge 3 is slow to move possibly because the air within it has a smaller negative temperature perturbation than other surges or because it is entirely momentum driven and the RFD surge is actually warmer than the surrounding environment. As a result, RFD surge 3 resides south of the tornado for almost 2 minutes before finally ejecting east of the tornado while pivoting towards the northeast. When RFD surge 3 was to the southwest of the tornado, it instigated southwestward movement of the tornado; once the surge settled to the south of the tornado, high westerly momentum south of the tornado spurred eastward motion. RFD surge 3 fills the role of the second surge highlighted in blue in the adapted Kurdzo et al. (2015) model in Figure 6.6.

The residence time of surge 3 south of the vortex also means that the influence of elevated momentum right near the tornado's southern flank lasts well after the loop is finished. During the latter part of segment 4, the tornado exits the track loop and then accelerates rapidly to the east as the momentum from surge 3 continues to carry the vortex. Eventually this movement comes to a sudden stop as the remnants of surge 3 pivot around the tornado and momentum instead starts to accumulate north of the tornado in the last

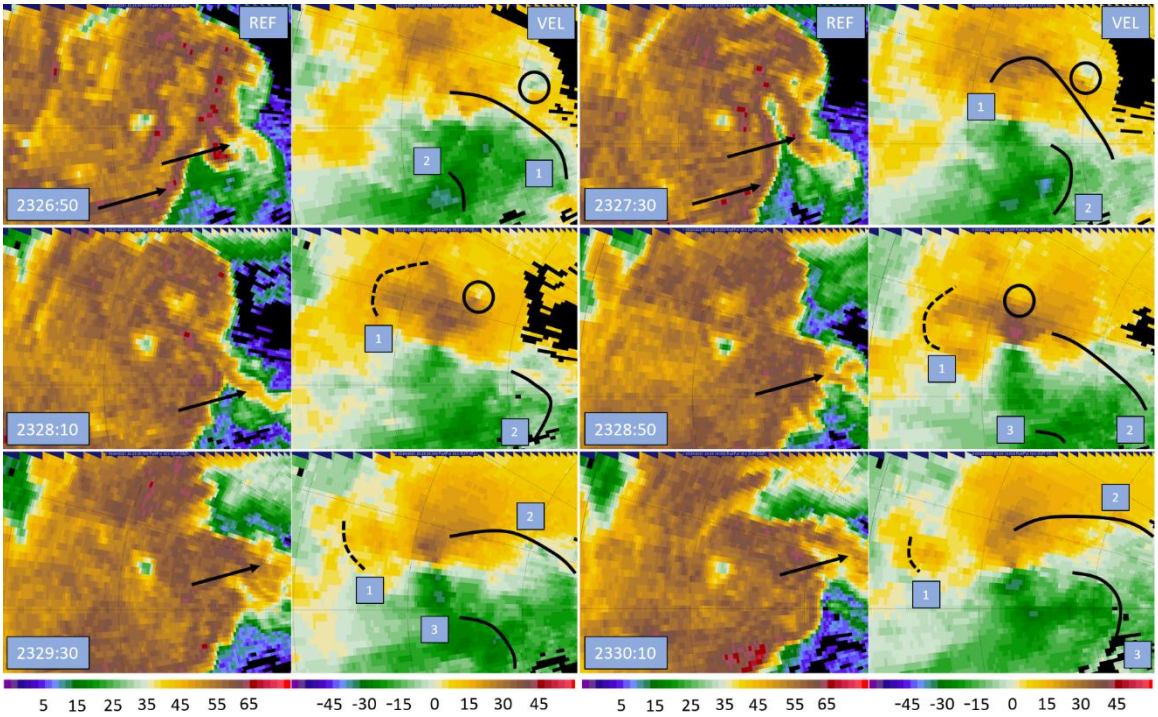

Figure 6.7: RaXPol imagery at the 16° elevation taken every 2 scans (40 s) during segment 4. In each radar panel, reflectivity is on the left and Doppler velocity on the right. Range ring spacing is 2.5 km. Black lines denote RFD surge fronts, which are also numbered. Black arrows also point to associated reflectivity appendages. Red lines mark the approximate positions of the forward flank and RFGF. A black circle also marks the location of an anticyclonic vortex, which will be investigated in section 6.4.

analysis panel of Figure 6.5. Because the tornado is now occluded and decoupled from the RFGF and since no other surges arrive to replace westerly momentum south of the tornado, the tornado immediately transitions from rapid eastward motion to a stationary phase. As surge 3 was advected around the circulation to its northern flank, easterly momentum increased north of the tornado, and without compensating increases to westerly momentum south of the tornado, the tornado came to a stop.

Figure 6.7 presents a similar radar analysis at the 16° elevation during the first cyclonic track loop. Overall, less surges are evident at the 16° level, but three relatively powerful surges do appear even at 1600 m ARL during segment 4. All three RFD surges

present in the analysis at the 16° elevation appear to be extensions of the RFD surges present at the 4° level since they appear in similar positions. Because the RFD outflow and RFD surges are near-surface features and become less potent further from the ground, many weaker RFD surges present at the ground do not extend vertically all the way to 1600 m ARL. However, the two strong surges that do appear in the first panel of Figure 6.7 appear to be extensions of exceptionally intense surges at the 4° elevation, revealing that only the strongest RFD surges have sufficiently large vertical extent to reach over 1.5 km ARL. Many of the surges that will be noted in the following 4° elevation radar analyses do not appear at the 16° level; as a result, the tornado sustains fewer short-lived, sharp track shifts and the tornado track is overall smoother and impacted by a relatively smaller number of strong RFD surges.

While fewer RFD surges appear at the 16° elevation, the few surges that do have sufficient vertical extent to reach 1600 m ARL result in the execution of a track loop. In the first radar panel of Figure 6.7, surge 1 is pivoting around the tornado on its eastern flank. Shortly thereafter, surge 1 makes it to the north side of the tornado where it causes momentum to build. The influence of RFD surge 1 is to move the tornado to the north and then west. While this is occurring, the second surge in the diagram passes to the south of the tornado, proceeding, like surge 1, to pivot the tornado. However, the primary thrust of RFD surge 2 is likely too far from the tornado to stimulate eastward movement; indeed, the tornado does not move east at this time but rather is continuing to move north and curve towards the west as it enters the track loop under the influence of RFD surge 1. Throughout the second (2327:30 UTC), third (2328:10 UTC), and fourth (2328:50 UTC) analysis times, surge 1 is advected all the way to the west side of the tornadic vortex, placing northerly

momentum on the tornado's western flank. Consequently, the tornado moves west and then south. This is confirmed by the 16° track map in Figure 6.1; the tornado is moving through the westward and southward portions of the loop during 2327 to 2328 UTC. By the fifth radar panel at 2329:30 UTC, a third momentum surge builds and transports enhanced westerly momentum to the southern flank of the tornado, causing a burst of eastward movement out of the track loop. Finally, surge 3 continues its northeasterly trajectory to the tornado's eastern flank, causing the tornado to resume on a north northeasterly heading. Because of differences in tornado position and lack of a defined RFGF, the configuration of momentum created by RFD surges is different at 16°; however, the result is the same as the tornado executes a clearly defined track loop.

6.2.2: Evolution in Mid D7 – Retrogression and Second Cyclonic Track Loop

Radar analysis at the 4° elevation covering the stationary and retrograding phases (segments 5 and 6) of the tornado at the 4° level is presented in Figure 6.8. The first panel picks up where Figure 6.5 ended, showing the two surges from the end of that analysis and a new third RFD surge that is building to the southwest of the tornado. All three RFD surges continue to be advected around the tornado as they spread out into the RFD and merge into the RFGF. Varying degrees of momentum from each surge manage to reach the north side of the tornado. Although none of the surges are particularly strong, they continuously supply enhanced easterly momentum north of the tornado. Throughout the first half of Figure 6.8 until 2332:58 UTC, new RFD surges continuously build southwest of the tornado and pass to its south as they are advected about the tornado circulation, continuing to balance some of the higher easterly momentum north of the tornado. While

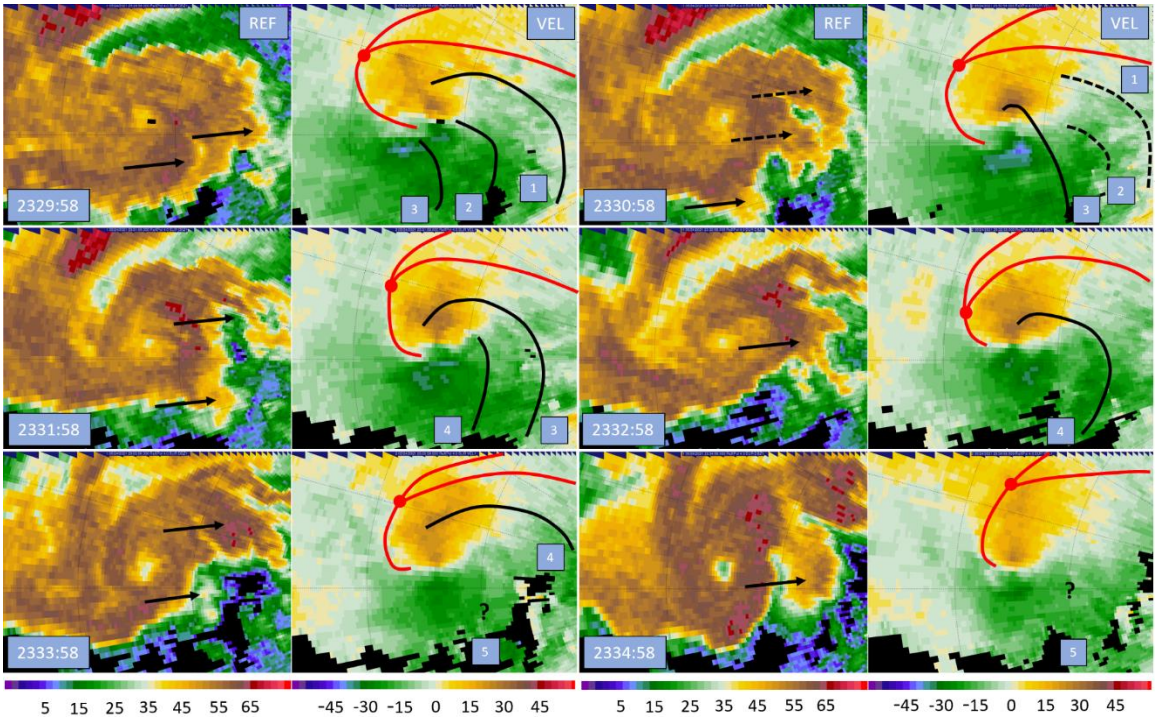

Figure 6.8: RaXPol imagery at the 4° elevation taken every 3 scans (60 s) during segments 5 and 6. In each radar panel, reflectivity is on the left and Doppler velocity on the right. Range ring spacing is 2.5 km. Black lines denote RFD surge fronts, which are also numbered. Black arrows also point to associated reflectivity appendages. Finally, red lines mark the approximate positions of the forward flank and RFGF.

this is occurring, the eastward component of motion being forced by the parent supercell and westward component of motion being forced by the RFD surge configuration are such that the tornado remains stationary. However, by the last two panels of the analysis in Figure 6.8, no new RFD surges are visible south of the tornado. While there may be surges ongoing, they are moving perpendicular to the radar beam. Consequently, the tornado is left without significant westerly momentum on its southern flank; the bounding momentum balance around the tornado is now completely dominated by high easterly momentum on the northern flank of the vortex, and the tornado tracks westwards to a greater extent than before. As a result, the tornado tracks west and its occlusion deepens rapidly as the triple point between the RFGF, forward flank convergence zone, and occluded portion of the

RFGF recedes from the tornado with time in Figure 6.8; the tornado becomes more deeply enveloped in outflow air and weakening continues.

In the last two panels of Figure 6.8, a new reflectivity appendage appears but does not seem to be associated with an RFD surge upon initial inspection of the data. However, the trajectory of the reflectivity appendage is almost perfectly perpendicular to the radar beam, meaning that any surge accompanying it would be invisible in the single-Doppler velocity field. In their analysis of the Moore 2013 tornado, Kurdzo et al. (2015) used minima in the correlation coefficient field to track surges; RFD surges passing near the tornado can disrupt and pick up debris from the tornadic circulation. Figure 6.9 presents a correlation coefficient analysis starting shortly after 2334 UTC. Although the Selden tornado is not lofting much debris and is relatively weak, two distinct minima in correlation coefficient appear in the analysis. The first moves due north in the first two panels of the analysis along with the reflectivity appendage noted in Figure 6.8 at 2334 to 2335 UTC, confirming the existence of another RFD surge. Because the first surge in Figure 6.9 is moving due north on a consistent south to north trajectory, the surge was never visible in the velocity field as it was moving perpendicular to the radar beam. Shortly after RFD surge 1 moves by on the eastern flank of the tornado, another RFD surge appears south of the tornado at 2335:18 UTC. Surge 2 quickly pivots around the tornado as it builds in strength, and momentum is transported to the tornado's eastern flank. As surge 2 departs, the RFD flow noticeably weakens as the tornado and supercell low-level mesocyclone near the end of the occlusion process; no further RFD surges were identified.

At 2335 UTC, the tornado undergoes a sharp turn towards the north at the 4° elevation. In Figure 6.9 it is seen that there are two surges coincident with the turn. RFD

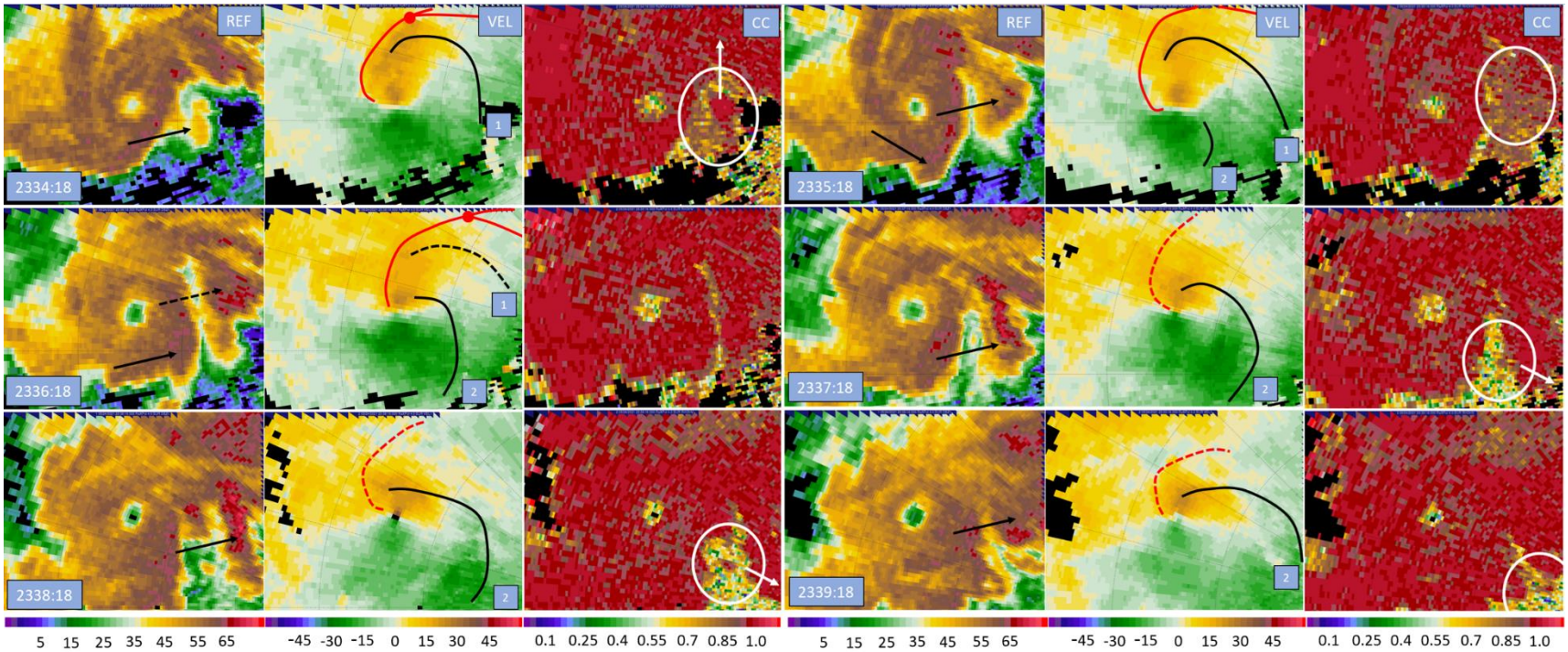

Figure 6.9: RaXPol imagery at the 4° elevation taken every 3 scans (60 s) during segments 6 and 7. In each radar panel, reflectivity is on the left, Doppler velocity is in the center, and correlation coefficient is on the right. Range ring spacing is 2.5 km. Black lines denote RFD surge fronts, which are also numbered. Black arrows also point to associated reflectivity appendages. Reded lines mark the approximate positions of the forward flank and RFGF. In the correlation coefficient images, the white circles denoted the correlation coefficient minima and white arrows indicate direction of movement.

surge 1 is weakening and has transported high momentum to the eastern and northern flanks of the tornado. At the same time, RFD surge 2 is gathering south of the tornado and quickly pivots around the southeastern flank of the tornado. As time progresses, RFD surge 2 becomes intense and moves to the northeast, transporting high southerly momentum to the eastern flank of the tornado. The configuration of momentum created by the 2 surges causes the tornado to make its sharp turn at the 4° elevation. Surge 1 has transported easterly momentum north of the tornado, contributing to the tornado's retrogression. Coincident with the turn, RFD surge 2 in Figure 6.9 is building south of the tornado where it slows the tornado's westward propagation and reverses it all together because westerly momentum is being enhanced on the southern flank of the tornado. Then, surge 2 is advected to the southeastern and eastern flank of the tornado, where the magnitude of enhanced momentum instigates the Selden tornado's new north northeastward track.

Notably, a similar RFD surge pattern is not observed at the 16° level, where no RFD surges were identified during this time. As a result, the 16° track does not contain a stationary or retrograde phase or undergo any sharp changes in motion. However, as the tornado makes a sharp northward turn at the 4° elevation, RFD surges once again become evident at the 16° level and the tornado executes a second cyclonic track loop aloft. Produced to show the disparate RFD surge distribution at the 16° elevation, Figure 6.10 shows that there are two distinct RFD surges in very different vortex relative locations from those at 4°. Despite this, both surges still appear to be extensions of those at the 4° elevation since RFD surges generally lean back with height; the differing positions of the surges at the 16° elevation are likely a result of vortex tilt. RFD surge 2 in both Figures 6.9 and 6.10 also clearly shows the evolution of a developing RFD surge. The surge first appears as a

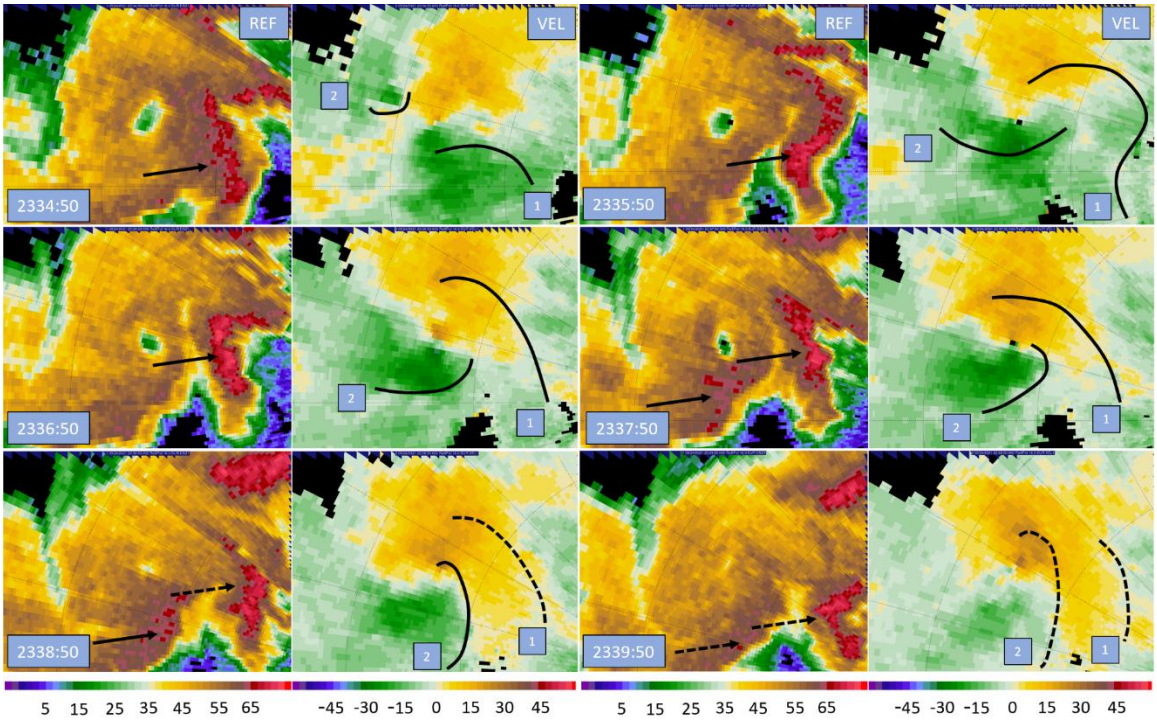

Figure 6.10: RaXPol imagery at the 16° elevation taken every 3 scans (60 s) during segments 5 and 6. In each radar panel, reflectivity is on the left and Doppler velocity on the right. Range ring spacing is 2.5 km. Black lines denote RFD surge fronts, which are also numbered. Black arrows also point to associated reflectivity appendages. Finally, red lines mark the approximate positions of the forward flank and RFGF.

compact area of enhanced momentum at the 16° level just to the west of the tornado sometime during 2334 UTC as an area of locally enhanced downdraft descends through the RFD. The locally enhanced portion of the downdraft continues to descend reaching the 4° scan elevation around 2335 UTC where the enhanced downdraft spreads out as it nears the surface. Upon reaching the surface, the surge is advected by the RFD flow and tornado circulation. While the area of enhanced downdraft that caused the RFD surge could have been driven by any number of physical mechanisms, such as a brief increase in evaporation of falling precipitation, RFD surge 2 in Figures 6.9 and 6.10 provides an exhibit of the formation of RFD surges from pockets of locally enhanced downdraft within the RFD as they descend and reach the surface.

The pattern of momentum created by RFD surges at the 16° elevation also explains the tornado's looping behavior. The first surge in Figure 6.10 is on a northward trajectory and spreads out over the next several scans to the north and east of the tornado. In the first panel at 2334:50 UTC, momentum is already building to the west of the tornado, and a second surge rapidly gathers. Surge 2 grows and moves south over the next minute, before pivoting around the tornadic circulation. From 2336:50 to 2338:50 UTC, surge 2 moves east on the tornado's southern flank, after which the surge dissipates as it spreads out east of the tornado. Surge 1 transports elevated southerly momentum to the east of the tornado, likely helping to maintain the northward track of the tornado at 16° in the lead up to the loop. Then, surge 2 significantly alters the bounding momentum around the tornado. A concentrated area of enhanced northerly momentum appears west of the tornado as surge 2 gathers and begins moving south, causing the tornado to jump southward in the absence of compensating southerly momentum east of the tornado. As RFD surge 2 pivots to the south of the tornado, the track vector reorients from southward to eastward, finishing the loop portion of the track at 16°. Finally, as surge 2 moves around to the east of the tornado and weakens, remnant southerly momentum in the absence of any new RFD surges causes the tornado to start tracking to the north northeast. The configuration of surges in Figure 6.10 is very similar to the adapted Kurdzo et al. (2015) model in Figure 6.6. While the trajectories are slightly different, two independent RFD surges appear one after the other, with the second surge appearing roughly 90° clockwise from the other around the tornado. The occurrence of two track loops with similar configurations of RFD surges reveals an identifiable pattern that can be used to anticipate tornado track loops. If a second RFD

surge appears roughly 90° clockwise from a leading surge around a tornado, then a track loop becomes likely, especially if the two surges occur in isolation from other RFD surges.

6.2.3: Evolution in Late D7 – Tornado Dissipation

By segment 7 at all elevations, the Selden tornado is beginning to succumb to occlusion. Near the end of analysis at 4° in Figure 6.9 and at 16° in Figure 6.10, the tornado is clearly weakening. Furthermore, the flow field around the tornado circulation is also decaying. There is a marked difference in strength of the RFD outflow from the second to the last analysis times in both Figures 6.9 and 6.10; when the last RFD surge passes the vortex and ejects to the east or northeast, the higher momentum within the RFD goes with it. The reflectivity field is also telling, as the supercell hook echo is no longer a hook appendage on the storm but rather has been absorbed into the southwestern terminus of the supercell as the hook echo has slowly moved to the west with respect to the storm.

During segment 4 in early D7, the tornado became occluded. The ramifications of this were two-fold. First, the tornado motion was altered significantly. Decoupling from the RFGF resulted in westward storm relative motion. The tornado also deviated significantly leftwards in response to RFD surges, which began exerting considerable influence on the tornado track after occlusion occurred and the RFGF became decoupled from the tornado. As was shown throughout D7 radar analysis, strong RFD surges were generated by the occlusion downdraft and possibly other mechanisms leading up to and after occlusion. Surges tended to move from the southern to the northern flank of the tornado as they were advected cyclonically around the circulation. As a result, surges repeatedly transported enhanced southerly momentum to the eastern flank of the tornado

and no significant compensating northerly momentum occurred near the tornado to counteract it, generating leftward movement. In this case, RFD surges are seen to play a crucial role in causing occlusion, and therefore, a crucial role in advancing the tornado lifecycle as documented by Lee et al. (2012) and Marquis et al. (2016). As in Skinner et al. (2014), the strong RFD surges and overall surge in RFD momentum around the tornado leading up to occlusion were likely the result of the outflow of the occlusion downdraft.

The second impact of occlusion was that relatively buoyant air was no longer feeding directly into the tornado. As outflow air completely enveloped the tornado at the end of segment 4 near 2330 UTC, the tornado began to weaken steadily as it struggled to lift less buoyant air. The weakening trend brought on by the tornado's occlusion from inflow is visible throughout the analysis in Figure 6.8, where ΔV_{max} for the tornado continuously decreases. Throughout the tornado lifecycle, the air around the tornado was slowly becoming more dominated by outflow air as the RFGF was displaced from the tornado and occlusion occurred; the conceptual model presented by Marquis et al. (2016) in Figure 1.4 summarizes the occlusion process that gradually occurred during the Selden tornado's lifecycle. However, the tornado continues to persist well after being surrounded by outflow. Numerous spikes in ΔV_{max} are also apparent (See Figure 4.5) throughout mid and late D7. As has been described by Finley and Lee (2004; 2008) and Lee et al. (2004), RFD surges are associated with significant enhanced convergence and vorticity. The numerous RFD surges that are observed in the Selden case are likely helping to sustain the vortex despite its occlusion. Marquis et al. (2012) observed this in their model, finding that tornadoes could persist even while surrounded entirely in outflow on bands of enhanced convergence associated with RFD surges. While RFD surges can aid tornadoes in this way,

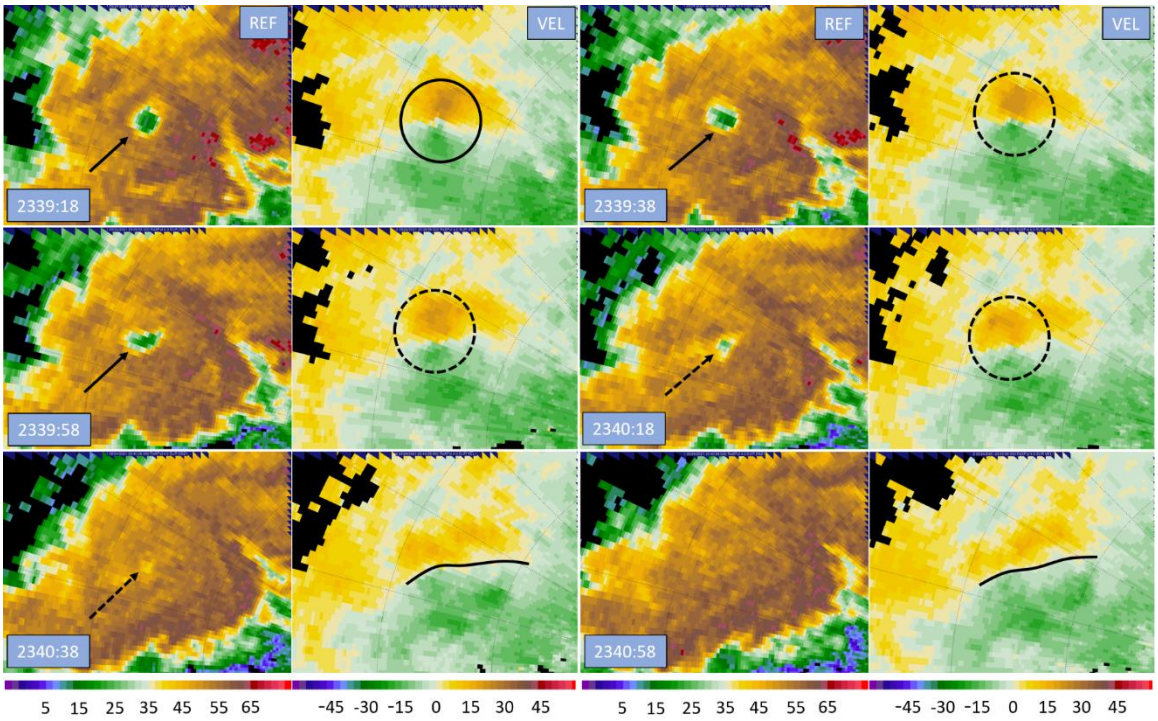

Figure 6.11: Radar analysis of RaXPol data at 4° elevation during the 2 minutes leading up to dissipation of the Selden tornado. Range ring spacing is 2.5 km. The vortex signature is marked by a black circle. Once the vortex signature breaks down, a line marks the remnant enhanced shear zone. A black arrow also points to the WEH in the reflectivity field.

they are an impetus for the occlusion process and their sum effect is to cause the tornado to decay.

A radar analysis for the dissipation phase of the tornado during late segment 7 and segment 8 is shown in Figure 6.11. Although the Selden tornado has persisted for a period of almost 10 minutes since its inflow channel had been occluded at the end of segment 4, the occlusion process has progressed so far that the flow field around the tornado is starting to decay. Matching closely to the last panel in the Marquis et al. (2016) conceptual model, the tornado and low-level mesocyclone have become very deeply occluded away from the RFGF and forward flank boundary apex, and the remnant extension of the RFGF extending back to the tornado has dissipated. This marks a completion of the occlusion process and

rapid decay will ensue (e.g., French et al. 2014; Marquis et al. 2012). Furthermore, the tornado and low-level mesocyclone have moved very far back into the parent supercell, no longer protruding as a hook echo. Consequently, the tornado and low-level mesocyclone have migrated into active downdraft areas within the parent supercell, causing the near vortex flow field to weaken rapidly. As shown in Figure 6.11, dissipation occurs acutely once the tornado migrates into the supercell downdraft; the tornado velocity signature breaks down into a shear zone in about 1.5 minutes and the WEH entirely collapses in about 1 minute, marking the completion of one cycle of occluding mesocyclogenesis.

6.3: Cross Section Analysis

6.3.1: Analysis During Segment 4 and Transition Back to Single Vortex

Figure 6.12 presents the average azimuthal cross section at the 4° elevation from segment 4; the 4° level is at approximately 420 m ARL and the cross-section accounts for a little over three minutes of time. The cross section in Figure 6.12 contains a very wide tornadic vortex nearing 800 m in diameter, or about one half mile. Although the width is large, it is in good agreement with NWS estimates based on damage indicators in the town of Selden. Much unlike cross sections presented in Tanamachi et al. (2007), the velocity maxima in Figure 6.12 are not well defined; velocities do not trail off quickly outside the RMW and the velocity maxima are just barely greater than the surrounding winds. Moreover, the tornado core region deviates significantly from solid body rotation during segment 4. Especially on the north side of the vortex, the rate of increase in winds outwards from the center is slow in the first 150 m before the rate approaches the expected solid

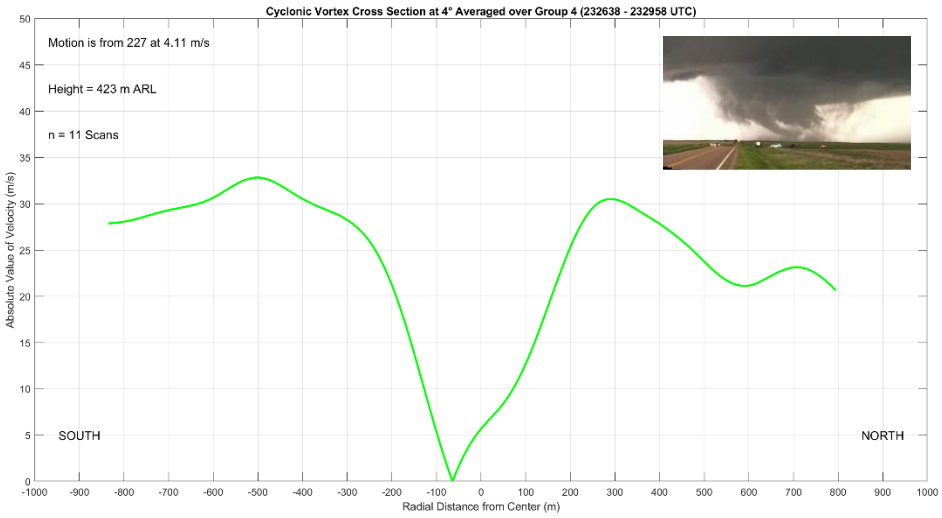

Figure 6.12: Azimuthal Cross Section through the Selden Tornado at 4° elevation for track segment 4. Photo courtesy of Howard Bluestein.

body rotation rate of increase. Another defining characteristic of the segment 4 profile is how off center the tornado is; the tornado's zero velocity center is observed to be about 75 meters south of the geometric center. The off-center shift of the profile does not appear to be the result of erroneous vortex velocity subtraction or biasing from superposition of strong flow on the vortex since the magnitude of both velocity maxima on either side of the tornado are nearly the same. Therefore, the tornado is significantly asymmetrical during segment 4. Considering the vortex asymmetry, its large size, and disruption to its core region, the tornado appears to still be in a multiple vortex phase where secondary vortices are causing flow irregularities to be captured in the average profile.

A photo taken of the tornado at 2327:22 UTC shown in Figure 6.13 strengthens the case for the Selden tornado remaining a multiple vortex tornado into D7. In the picture, a very large area of scoured dust and debris reveals a large tornadic flow field at the ground. Three different extensions of cloud down towards the ground may also evidence the existence of multiple cells within the tornado; each individual funnel or cloud extension

Figure 6.13: Photo of the tornado at 2327:22 UTC, mid-way through segment 4 at the end of the track loop. Photo is taken looking west from the D7 deployment location; the tornado is approximately 6 km away. Photo courtesy of Howard Bluestein.

possibly marks the location of a secondary vortex where locally intense vorticity is dynamically lowering the pressure enough to draw cloud down from the cloud base or cause a condensation funnel to form (Wurman 2002). The funnel on the left of the tornado is particularly defined and is highly tilted outward from the vortex center, marking the location of a particularly strong secondary vortex. The other two notable cloud extensions to the right may be inflow extensions rather than funnels. However, the overall appearance of the photo correlates well with prior visual observations of multiple vortex tornadoes; multiple cloud or funnel fragments reach down from the cloud base tilted inwards towards the center of the tornado that is apparent from the thickest area of lofted debris and dust (e.g., Bluestein et al. 2018). The secondary vortices noted in the photo in Figure 6.13 are visible for the first two radar scans at the 4° level before the vortex takes on a more symmetrical appearance (2326:38 and 2326:58 UTC scans, see first panel in Figure 6.5).

A breakdown of the segment 4 azimuthal cross section at the 4° scan elevation into the two segment 4 subsections in Figure 6.14 further support the notion that the Selden

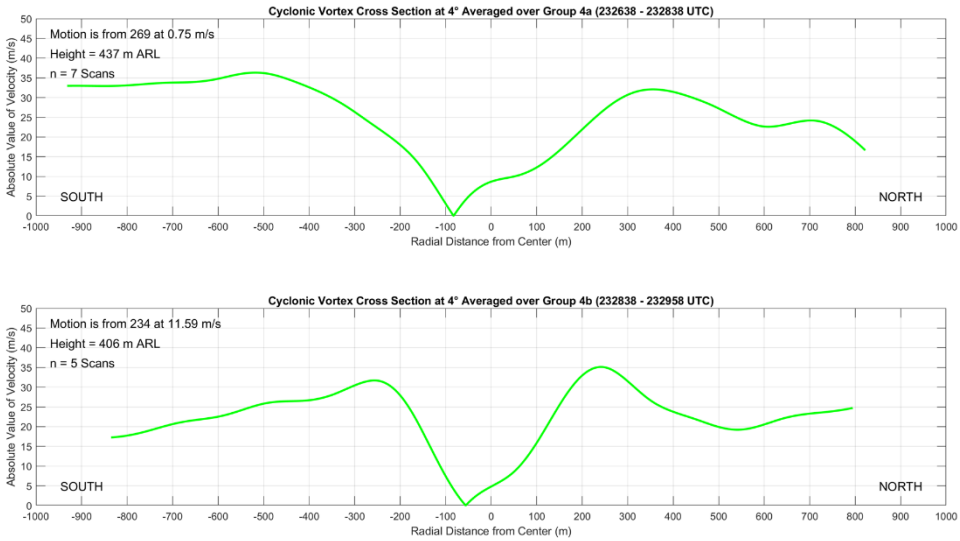

Figure 6.14: Azimuthal Cross Sections through the Selden Tornado at 4° elevation for track segment 4 subsections. The first subsection (top) represents the loop portion of segment 4, the second subsection (bottom) represents the rapid northeasterly movement after the track loop.

tornado remained a multiple vortex tornado into early D7 before resuming a single vortex structure. The first subsection profile in the top panel of Figure 6.14 appears largely like the total segment 4 profile; in the first subsection the tornado remains wide, the core region is still disrupted, and the tornado is still very asymmetrical. However, the second subsection profile representing the time right after the track loop is quite different. The tornado has contracted significantly, and it is less than 500 m wide. The velocity maxima on either side of the profile have also become better defined, the core region flow is beginning to recover towards solid body rotation, and asymmetry is decreasing when compared to the first subsection profile. Remarkably, despite the rapid increase in vortex motion, the profile remains balanced, lending more evidence for a noteworthy change in tornado behavior and structure. The great decrease in width of the tornado and increasing regularity of the profile such that it resembles more closely those in Tanamachi et al. (2007) are characteristic of a transition of the Selden tornado back to a single vortex structure.

Further indications that the tornado sustained a major change back to a single vortex structure during segment 4 can be found in the pattern of standard deviation within the segment 4 average azimuthal cross section (Figure not shown). The variability in measurements throughout the segment 4 cross section is high; the standard deviation is equal to or greater than ±10 m s^{-1} across the entire profile. The greatest amount of variability occurs near the RMW, indicating that the tornado is rapidly changing size. Smaller, but still large, standard deviations within the vortex interior also reveal a changing core structure. As the tornado undergoes transition to a single celled vortex, the tornado shrinks and secondary vortices disappear, which manifests as large standard deviation values throughout the azimuthal cross section, particularly near the RMW and within the vortex core.

The reasons for the tornado's transition back to single celled vortex structure remain unclear. During segment 4, the tornado occludes (See Figure 6.5), which results in outflow air enveloping the vortex. The less buoyant air around the tornado hinders radial inflow since the air cannot be lifted as easily in the tornado updraft and the swirl ratio continues to increase (Rotunno 1984). As suggested by Marquis et al. (2008), perhaps an RFD momentum surge instigated the transition to single vortex. The enhanced convergence and vorticity along surges, particularly at their northern ends near the tornado, certainly can increase radial inflow and decrease the swirl ratio (Finley and Lee 2004; 2008). However, this burst of inflow would only be temporary and the swirl ratio would once again increase, nudging the tornado back towards multiple vortex structure. Another way to force the swirl ratio down is to decrease the average azimuthal winds around the tornado. There is evidence for a weakening tornado; the velocities around the vortex do decrease

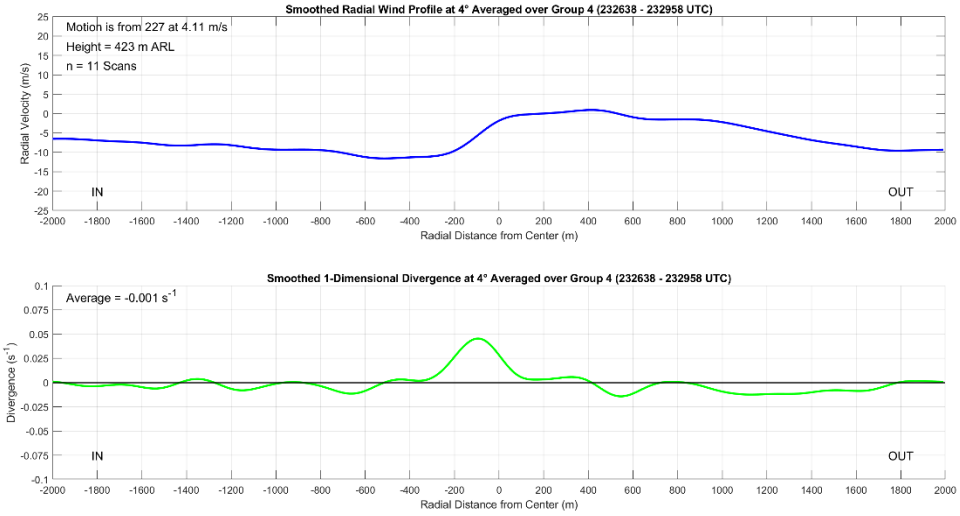

Figure 6.15: Radial wind cross section through the Selden tornado at the 4° elevation for segment 4 (top) and 1-D divergence (bottom).

starting in late segment 4 (See Figure 6.5) and ΔV_{max} begins decreasing (See Figure 4.5). Because of the weakening trend, it appears more likely that azimuthal winds decreasing at a higher rate than inflow were the primary factor in transition to single vortex, especially considering the increasingly unfavorable thermodynamic character of the air surrounding the tornado. However, this does not preclude a contribution from RFD surges; the strong surge passing by the tornado in late segment 4 which instigated the tornado's rapid increase in speed towards the northeast (surge 3 in Figure 6.5) could have caused tornado radial inflow to briefly increase, ultimately instigating the transition.

Figure 6.15 contains the corresponding radial wind cross section of the tornado during segment 4 at the 4° elevation. Reflective of the multiple vortex nature of the tornado during the first half of segment 4, there is a large area of divergence about 900 m wide centered on the tornado. However, there is now also a defined peak in the center of the broad area of divergence; the divergence spike has a magnitude approaching 0.5 s^{-1} and has a 400 m spatial extent. This spike is likely a result of the tornado transitioning back to

single vortex about halfway through the averaging period for the profile. As with previous radial wind profiles, the radial winds increase rapidly from inbound negative velocities to outbound positive velocities heading outwards from the radar within the tornado circulation. The overall character of the radial wind profile is slightly convergent tending towards neutral when compared to earlier profiles; the more neutral divergence contained within the whole profile reflects a low-level supercell mesocyclone that has reached peak intensity and is no longer strengthening, which agrees with radar analysis that showed occlusion occurring during segment 4.

6.3.2: Analysis During Mid D7

The azimuthal cross sections through the Selden tornado during segments 5 and 6 at the 6° elevation, which is approximately 600 m ARL during segments 5 and 6, are shown in Figure 6.16. The 6° elevation profiles were used in lieu of the 4° profiles because the 6° cross sections contained a higher quality vortex that was better defined; the higher elevation was within weaker RFD outflow winds, allowing for the tornado to appear within the cross section since weaker ambient winds were being superimposed on the tornadic circulation. Despite selecting a higher elevation for the segment 5 and 6 profiles, the wind maxima on either side of the profiles are still poorly defined. In particular, the segment 5 cross section shows winds south of the tornado continuing to increase outside the RMW. The trend for azimuthal cross sections to contain plateauing or even increasing winds outside the RMW reflects a weakening tornado embedded within the supercell mesocyclone circulation; as the tornado continues to weaken; its wind field becomes harder to distinguish from that of the mesocyclone since the tornado circulation was not isolated from other scales of flow

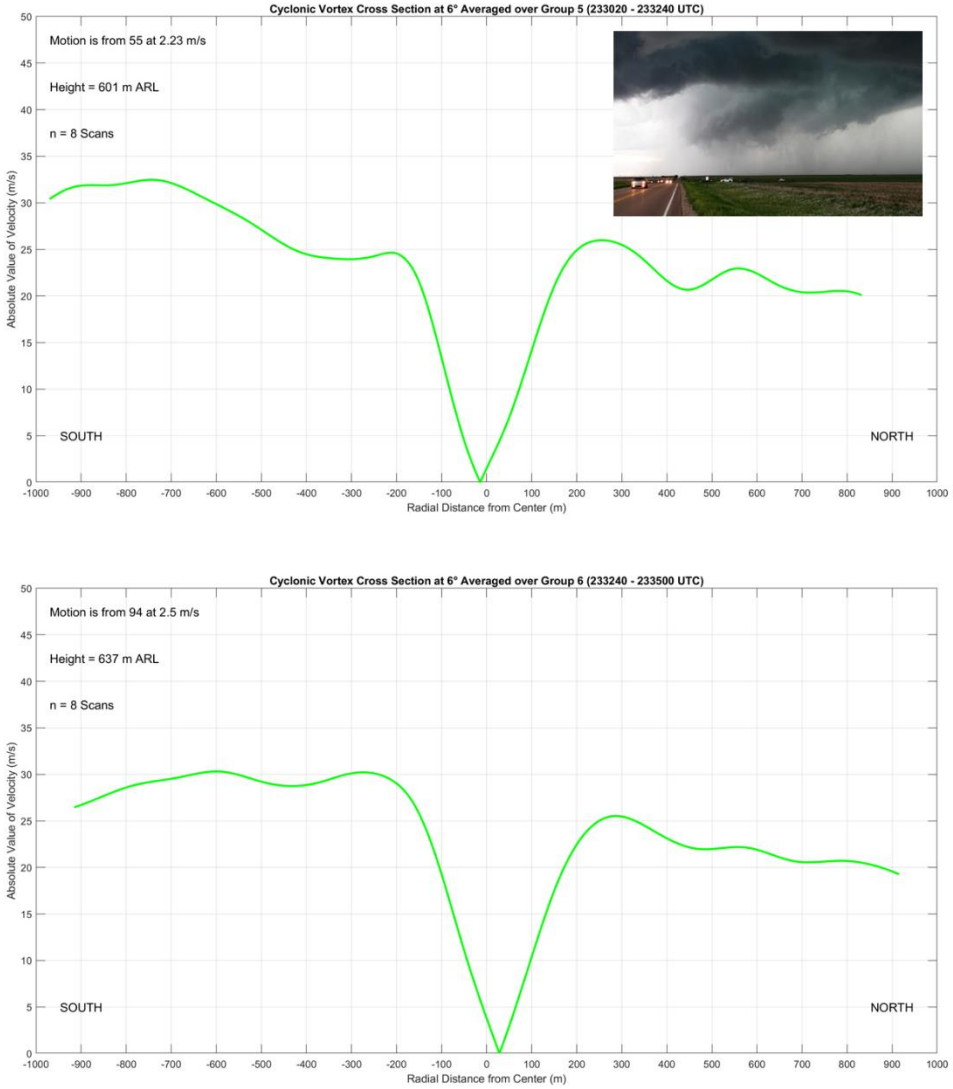

Figure 6.16: Azimuthal Cross Sections through the Selden Tornado at 6° elevation for track segments 5 (top) and 6 (bottom). A picture of the Selden tornado from segment 5 is also included. Photo courtesy of Howard Bluestein.

using GBVTD analysis as in Tanamachi et al. (2007). Indeed, the tornado is weakening as it continues to occlude, and the picture of the tornado in the top right of the segment 5 profile mirrors this. At the end of segment 4, the Selden tornado loses its condensation funnel and the area surrounding the tornado location appears outflow dominated, which is supported by radar analysis (See Figure 6.8).

Although the tornado becomes more difficult to detect in cross section analysis due to superposition of the supercell mesocyclone and RFD onto a weakening tornado flow field, the segment 5 and 6 profiles do reveal key details about the tornado. In the segment 5 cross section in Figure 6.16, the width of the vortex has reached a diameter of approximately 450 m as it continues to contract in its transition from multiple to single vortex at the end of segment 4. The width of the vortex then stabilizes, with the tornado circulation diameter remaining largely unchanged in the segment 6 profile. The core region of the tornado has also returned to solid body rotation, reflecting the complete transition of the Selden tornado's structure back to single vortex. Finally, the tornado is nearly symmetrical in both profiles, with any indicated asymmetry well within the margin of error of profile construction and vortex velocity subtraction.

The radial wind profiles for segments 5 and 6 at the 4° level shown in Figure 6.17 also reflect the ongoing occlusion of the tornado and low-level mesocyclone. Both radial wind profiles are overall divergent, indicating that the low-level supercell mesocyclone is starting to weaken. Moreover, the inflow convergence signature still present behind the tornado in both profiles has a smaller magnitude than it did before in segments 3 and 4. Another noteworthy signature appears within the divergence profiles. A broad area of enhanced divergence occurs in both profiles just to the inside of the tornado's position; the signature is consistent with descriptions of an occlusion downdraft. Klemp and Rotunno (1983) found that the occlusion downdraft commonly forms near the tornado, and a distinct outflow divergence signature can now be seen within the RFD outflow, possibly as the occlusion downdraft has been advected around the tornado circulation to its eastern flank.

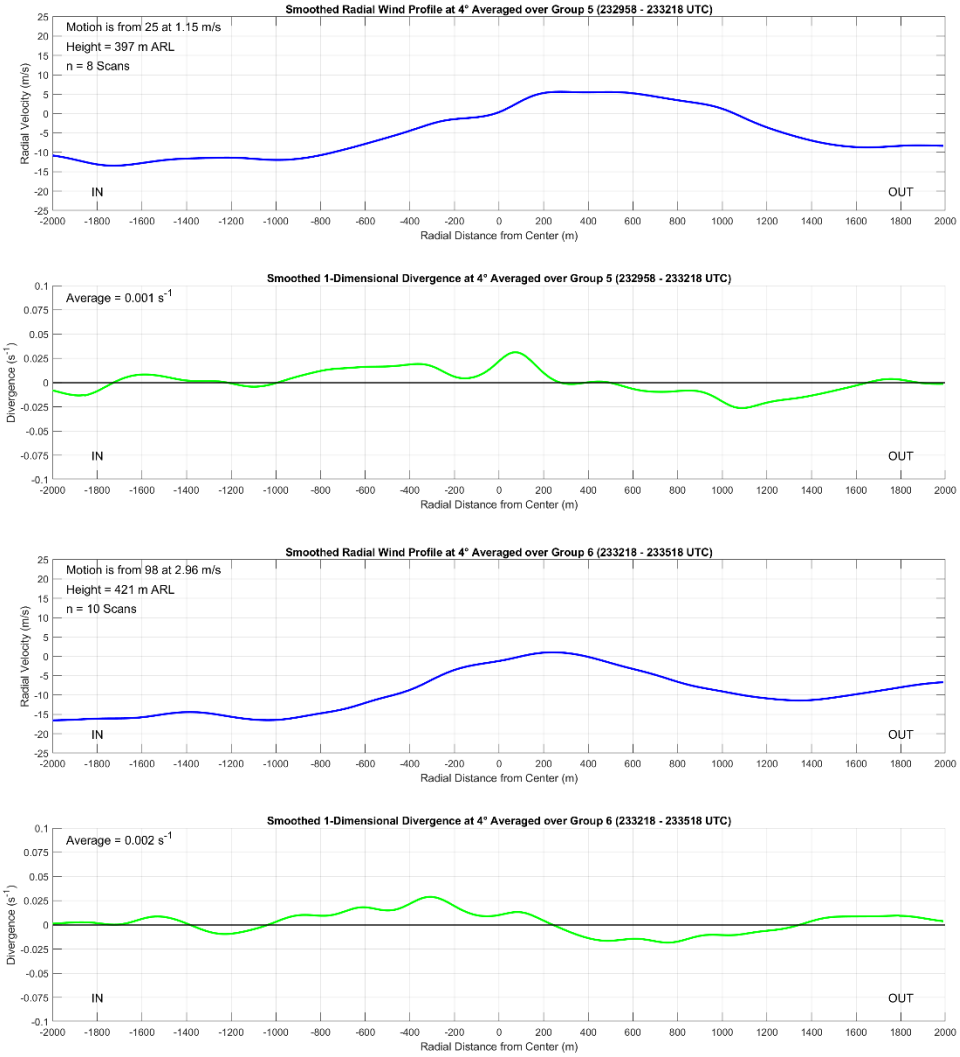

Figure 6.17: Radial wind cross sections through the Selden tornado at the 4° elevation for segment 5 (top) and segment 6 (bottom). 1-D divergence is also included.

However, the lack of dual Doppler synthesis makes it impossible to ascertain with certainty that an occlusion downdraft is present.

6.3.3: Analysis During Late D7

Figure 6.18 contains the azimuthal cross sections at the 4° elevation during segments 7 and 8. During late D7, the Selden tornado is continuing to weaken as occlusion continues; the tornado begins to decay more quickly throughout segment 7 and then

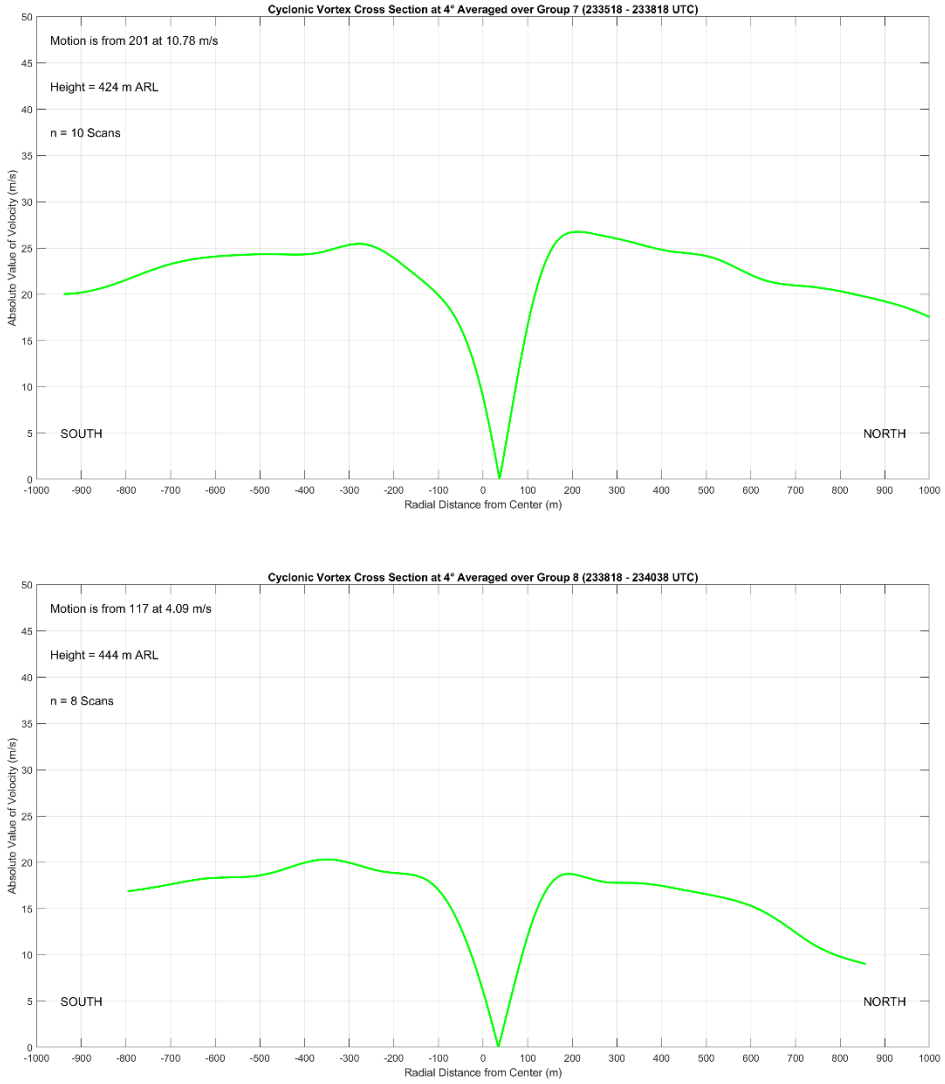

Figure 6.18: Azimuthal Cross Sections through the Selden Tornado at 4° elevation for track segments 7 (top) and 8 (bottom).

dissipates entirely at the end of segment 8 as the pace of decay increases markedly. In segment 7, the tornado is a similar width as before, remaining about 450 m wide. Despite the tornado's deepening occlusion, the tornado also maintains a ΔV_{max} near 50 m s^{-1}, which has continued to gradually decrease since segment 4. The persistence of the tornado throughout segment 7 reflects observations from radar analysis, which showed that the tornado continued to maintain significant strength for over 10 minutes after initial occlusion; RFD surges were found to potentially enable this trend because of the enhanced

convergence and vorticity associated with the surges (Finley and Lee 2004; 2008). The segment 7 profile is also balanced, with nearly the same magnitude of velocities on both sides of the tornado. Notably, the tornado made a sharp left turn just before segment 7 and picked up a large amount of speed. Yet, the drastically different vortex motion vector used to produce the segment 7 profile did not result in an asymmetrical cross section, indicating that the new track vector is representative of a change in the tornado's behavior.

The decay of the tornadic vortex becomes readily apparent in the segment 8 cross section. By segment 8, the velocity maxima on both sides of the vortex are slightly less than 20 m s^{-1}, which is below the 40 m s^{-1} tornadic shear threshold (French et al. 2014; Houser et al. 2015; Wurman and Kosiba 2013). Furthermore, the winds everywhere outside the RMW have also decreased as the RFD outflow has begun to collapse with the migration of the low-level mesocyclone into downdraft regions (See Figures 6.9 and 6.11). The size of the tornado wind field has also contracted significantly to roughly 300 m; however, the size is likely exaggerated due to superposition of the supercell mesocyclone circulation onto the tornado circulation.

Despite the seemingly large diameter of the tornado during segment 8, the width of the tornado still matches closely to the correlation coefficient derived track width in Figure 3.6, suggesting that the tornado wind field is still extensive. The large width of the vortex circulation and lingering substantial debris cloud may be the result of the tornado decay mode. Tanamachi et al. (2007) discussed two ways in which tornado decay can proceed. First is that dissipation occurs as both the vortex radius and azimuthal winds decrease while a second mode of decay occurred when the vortex radius increased while azimuthal winds decreased. The 300 m diameter of the wind field and large size of the remnant debris cloud

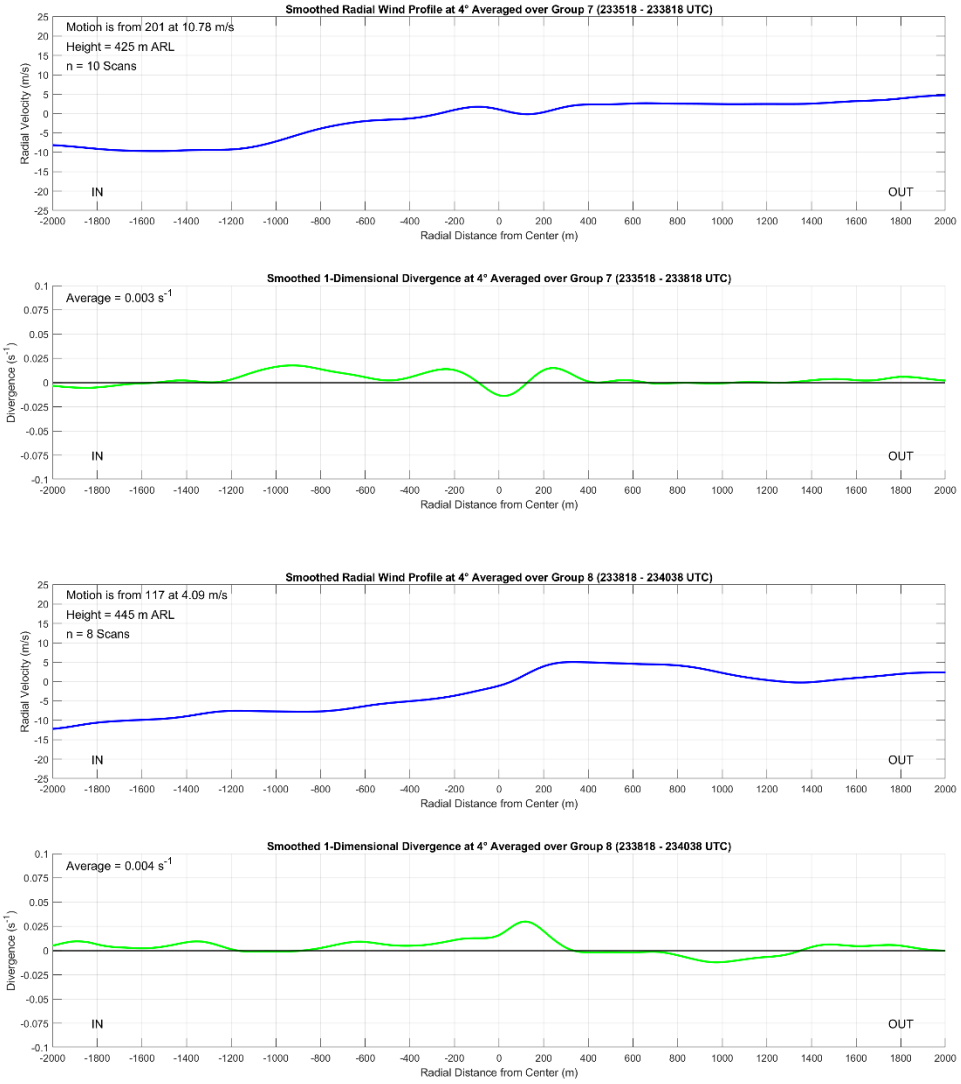

Figure 6.19: Radial wind cross sections through the Selden tornado at the 4° elevation for segment 7 (top) and segment 8 (bottom). 1-D divergence is also included.

are likely an indicator of a mode 2 decay and are not a signal for an intense vortex; large amounts of dirt and dust are briefly suspended as the RMW briefly increases during final dissipation.

Figure 6.19 shows the corresponding radial wind profiles for segments 7 and 8. Overall, both radial wind profiles are divergent, reflecting the decay of the supercell low-level mesocyclone as it occludes. Notably, the possible occlusion downdraft signature is still present, albeit weaker, with broad enhanced divergence still residing in between the

tornado and the radar. Although the tornado is weak in segment 8, the divergence spike around the tornado has nearly the same magnitude as those from several minutes earlier in segments 5 and 6. The segment 8 tornado proximate divergence may be an indicator of the tornado's final dissipation. The high magnitude of divergence centered on the tornado is reflective of a mode 2 decay (Tanamachi et al. 2007); when the Selden tornado dissipates, the vortex spreads out as the circulation loosens and vorticity decreases. As a result of this mode 2 decay, the vortex width remains large all the way to the end of the tornado's life and debris continues to be lofted even as the tornado dissipates entirely.

6.4: 'Rogue' Anticyclonic Vortex

At the start of D7, an unusually strong anticyclonic vortex is observed near the primary Selden tornado. Figure 6.20 presents observations of this vortex at the 8° elevation where it was the most defined. The anticyclonic vortex appears to orbit the primary tornado, moving from its eastern to northern flank over the course of nearly 3 minutes before dissipating to the northwest of the primary tornado. Throughout the duration of its lifespan, the anticyclonic vortex remained roughly 1.5 km from the center of the primary tornado while orbiting around it at a speed slightly greater than 20 m s^{-1}, which roughly matches the magnitude of the ambient flow immediately surrounding the 'rogue' vortex. Notably, the anticyclonic vortex was intense enough to have its own WEH, which can be tracked in the reflectivity field from the first scan in D7 at 2326:42 UTC through at least the fifth scan at 2328:02 UTC. The maximum ΔV of the anticyclonic vortex is nearly 45 m s^{-1}, qualifying it as a tornadic vortex, however only briefly. As the anticyclonic vortex begins to move to the northwest of the primary tornado, it dissipates rapidly as it is ingested

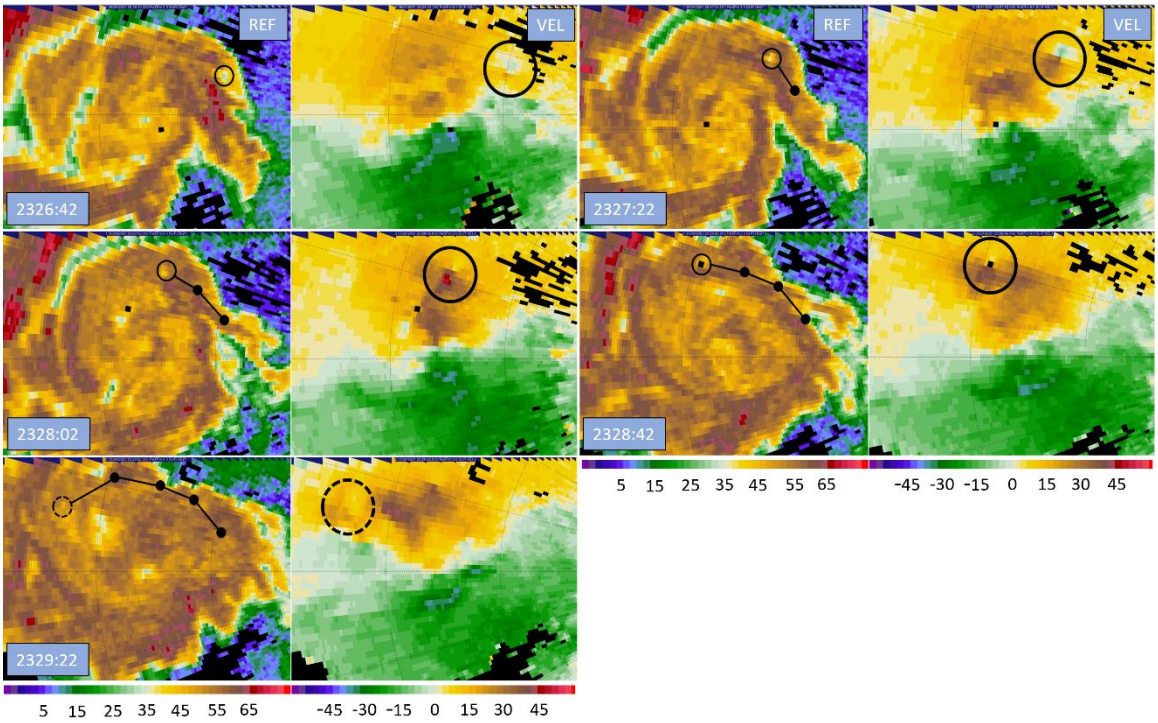

Figure 6.20: Radar analysis at 8° showing the 'rogue' anticyclonic vortex during early D7. Panels are taken every other scan, or 40 s apart. Range ring spacing is 2.5 km. The black circles denote the 'rogue' anticyclonic vortex, and its movement is tracked on the reflectivity field.

in the cyclonically rotating supercell updraft (See Figure 6.5). The position, track, and short lifespan of this anticyclonic vortex do not match what would be expected from a typical companion anticyclonic tornado, which occurs on the southern flank of the RFD away from the primary tornado and can persist along with the primary tornado for much of its total lifecycle (Bluestein et al. 2016; Wurman and Kosiba 2013). Instead, the early D7 anticyclonic vortex is a 'rogue' vortex; its pattern of behavior does not resemble common models of anticyclonic tornadoes in cyclonic supercells.

Numerous types of anticyclonic vortices have been observed in cyclonically rotating supercells. Aside from companion anticyclonic tornadoes, Wurman and Kosiba (2013) briefly discuss the occurrence of both cyclonic and anticyclonic satellite tornadoes. These smaller but still potent vortices tend to accompany intense supercells and orbit the

primary tornado during short lifespans. One case highlighted by Wurman and Kosiba (2013) showcases a cyclonic satellite tornado orbiting a primary tornado near Chickasha, Oklahoma on 3 May 1999; the satellite had a ΔV of 45 m s^{-1} and remained about 1 km from the primary tornado as it orbited around the eastern flank of the parent tornado. Tanamachi et al. (2012) also observed several satellite tornadoes around the Greensburg, Kansas tornado, 2 of which were anticyclonic. The satellites were very brief, often only remaining on the ground for 1 to 2 minutes with a pathlength of about 1 km; throughout their brief lifespans, satellites were found to systemically orbit about the eastern flank of the Greensburg tornado towards the north, only occurring on the flank of the primary tornado facing away from the rest of the parent storm. Furthermore, these satellites were found within 5 km of the center of the Greensburg tornado. Both the Wurman and Kosiba (2013) and Tanamachi et al. (2012) observations fit remarkedly well to the 'rogue' anticyclonic vortex observed near the Selden tornado; the 'rogue' vortex orbits about the eastern and northern flanks of the primary tornado before dissipating, it is short lived, and it orbits at a range of roughly 1.5 km at about the same speed as the flow immediately surrounding it.

Greenwood (2021) also documents an anticyclonic vortex with similar behavior to the one investigated here in their Amber-Bridge Creek case, although the anticyclonic vortex was found to be much farther from the primary cyclonic tornado at a range of 9 km and may have been associated with a shear zone located at the interface between the forward flank convergence zone and inflow channel. While the behavior of the vortex is like what is found with the 'rogue' vortex in the Selden case, its distance from the primary cyclonic tornado and deviation from an orbit around the primary cyclonic tornado

differentiate it from the Selden ‘rogue’ vortex. A lack of data during the genesis of the ‘rogue’ anticyclonic vortex precludes determining what feature may have been responsible for its formation, but it appears that the Selden ‘rogue’ anticyclonic vortex is different from the one identified in Greenwood (2021) and that it fits more with the observations of the satellite vortices in Wurman and Kosiba (2013) and Tanamachi et al. (2012).

The ostensible anticyclonic vortex in early D7 is likely an anticyclonic satellite of the Selden tornado. However, the lack of data from before the start of D7 remains problematic. It is unknown where the early D7 anticyclonic vortex came from or where it underwent genesis. It is possible that the anticyclonic vortex was generated at the southern flank of the RFGF as is the case for typical anticyclonic tornadoes (Bluestein et al. 2016). Then, for an unknown reason, the vortex was not anchored in position and was advected around the RFGF in the supercell inflow, where it would appear to orbit the primary Selden tornado as it neared the supercell updraft. However, the origin of satellite tornadoes is not well understood, so this possibility does not necessarily preclude the early D7 ‘rogue’ vortex from being a satellite tornado (Wurman and Kosiba 2013). Another limiting factor in analysis is that the ‘rogue’ anticyclonic vortex did not produce any visible cloud lowering or funnels, so there is no visual evidence to draw on to further analyze the ‘rogue’ vortex.

6.5: Weak Reflectivity Band

Late in D7, from approximately 2334:30 to 2336:58, a weak reflectivity channel feature was observed on the eastern flank of the Selden tornado. Figure 6.21 provides a scan-by-scan radar analysis of the band of weak reflectivity at the 4° elevation. Starting at

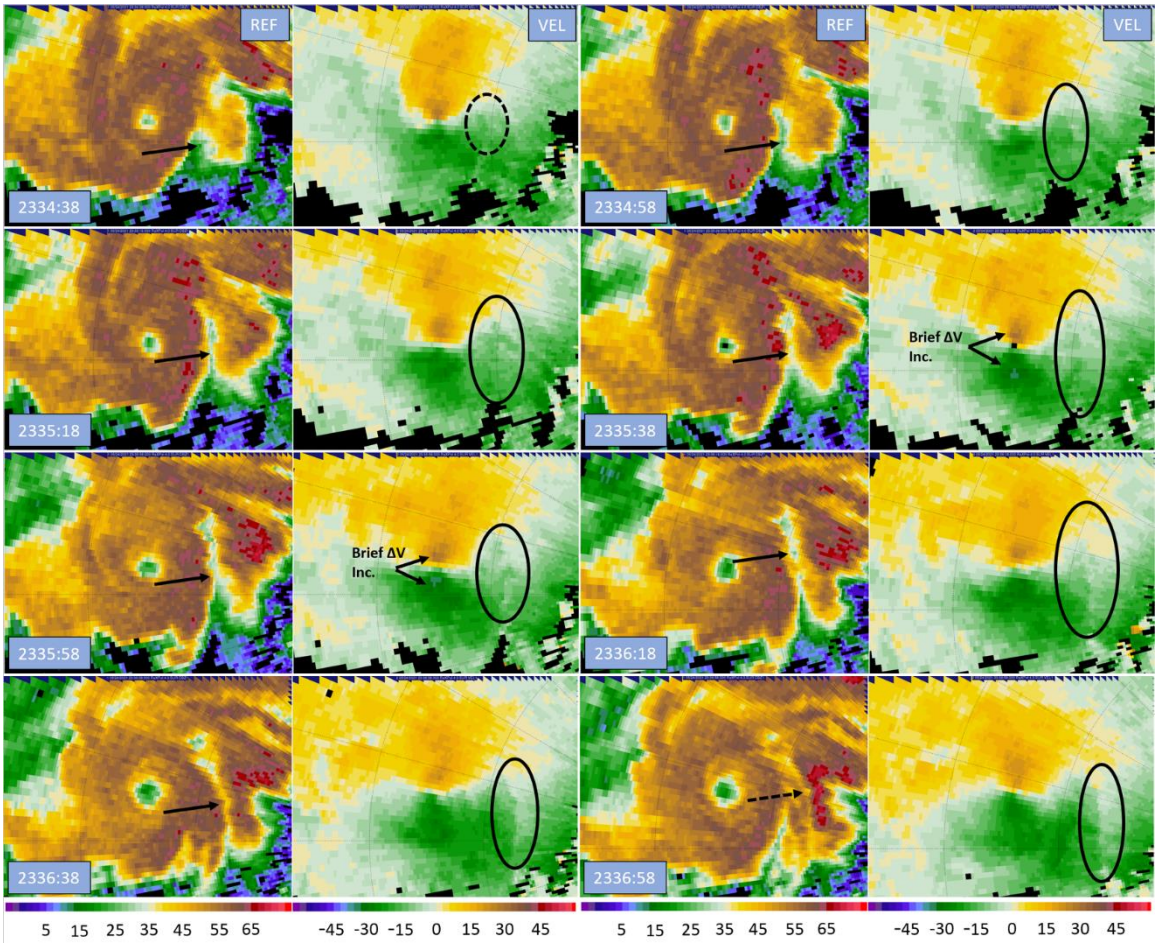

Figure 6.21: Reflectivity and velocity timeseries lasting about 2.5 minutes from 2334:38 to 2336:58 UTC. Black arrows on the reflectivity plots denote the WRB, while black circles on the velocity field mark the pronounced convergence signature. Range ring spacing is 2.5 km.

2334:38 UTC, a notch of lower reflectivity begins to form in the wake of an RFD surge induced reflectivity appendage. Just 20 seconds later, the trough of reflectivity has developed into a small channel and is collocated with a distinct convergence signature in the velocity field. The reflectivity trough continues to grow longer over the next three scans, reaching its greatest extent by 2335:58 UTC; the band is roughly 5 km from south to north and is only 150 to 200 m wide. During a brief two-scan, 40 second window, a coincident increase in the ΔV_{max} of the tornado occurs as marked in Figure 6.21 (See also Figure 4.5). Over the next few scans, the reflectivity trough begins to fill as another RFD

surge related reflectivity appendage emerges from the hook echo, but it remains associated with a pronounced convergence signature in the velocity field. Throughout its 2.5-minute lifespan, the reflectivity feature remained in place on the eastern flank of the tornado circulation, not moving much to the east or west as lower reflectivity developed from south to north slowly wrapping the vortex. This band of weak reflectivity appears to resemble the WRB feature first documented in Houser et al. (2016), which was observed to be a long and narrow reflectivity trough curving around the tornado circulation lasting for a period of roughly 3 minutes. To the best of the author's knowledge, the Selden case is only the second recording of a WRB feature.

In Houser et al. (2016), a horizontal circulation is responsible for the formation of the WRB, with the weak reflectivity being the result of the circulation's descending branch. The horizontal circulation was inferred from adjacent bands of divergence and convergence in the near surface Doppler velocity field; a leading band of divergence is followed by a narrow zone of convergence. The rising branch of the circulation occurred overhead of the convergence and descending branch over the divergence, which is where the WRB appeared. The velocity signature associated with the Selden WRB is remarkedly similar. Especially in later analysis times from 2336:18 to 2336:58 UTC, there is a sharp, narrow band of convergence situated just to the west of a broader area of enhanced divergence.

Houser et al. (2016) gave three potential explanations for the formation of the divergence and convergence bands and associated horizontal circulation; however, none of these seem to be the case here. While it is impossible to rule out the Houser et al. (2016) hypotheses due to the lack of thermodynamic data, the Selden WRB appears to be a coincidental feature that formed due to the specific arrangement of two RFD surges. In

initial analysis, it was noted that the WRB appeared to form because of the positioning of two RFD surges, with a trailing surge following immediately in the wake of a leading RFD surge; the RFD surge associated reflectivity appendages formed a narrow gap in between the two surges with relatively low reflectivity. Behind the initial RFD surge, there is a zone of enhanced divergence as momentum progressively decreases, which was then followed closely by a second surge, where divergence suddenly changed to convergence at the second RFD surge front. Since the RFD surges stayed near each other as they continued to pivot around the tornado, the bands of divergence and convergence persisted near each other for a few minutes, allowing for a horizontal circulation to form. As the horizontal circulation became established, it enhanced the gap in reflectivity between the two RFD surges in its descending branch, resulting in the WRB. While a DRC related surface outflow could reasonably create the divergence and convergence signature, no descending area of reflectivity was found; the appearance of the new reflectivity feature at the start of the analysis is not a DRC nearing the surface but rather an RFD surge generated reflectivity appendage. Considering these observations, it appears that WRBs may form whenever two RFD surges occur in rapid succession and then follow similar trajectories with both surges staying close to each other for an extended period, allowing for a horizontal circulation to form in between the two RFD surges.

While the WRB feature was present, Houser et al. (2016) noted that the tornado increased in intensity slightly. Houser et al. (2016) noted that this may be a consequence of the WRB horizontal circulation; the circulation sense is such that the horizontal vorticity is streamwise since flow passes through the WRB as it wraps in towards the tornado. However, Houser et al. (2016) was not able to conclusively tie the tornado intensity

increase to the horizontal circulation since other factors affecting tornado intensity could not be ruled out. A similar strengthening trend in the tornado velocities are noted during the Selden WRB. The WRB forms from south to north as the tornado circulation flow enters from the south and exits to the north; any horizontal vorticity would be streamwise and could reasonably be expected to cause a temporary increase in tornado ΔV. Furthermore, the Selden WRB occurs during the decay stage of the tornado where occlusion is causing the tornado to generally lessen in intensity. This is unlike the Houser et al. (2016) WRB, which occurred during the mature phase of the tornado where multiple other factors may have caused tornado intensification. Considering these observations, the Selden WRB appears to be responsible for the brief intensification given that the tornado should continue to weaken due to its occlusion. However, due to differences in time of development relative to the tornado's lifecycle and disparities in apparent formation mechanisms, it remains possible that the Selden WRB and Houser et al. (2016) WRB are in fact different features although their appearance and result are similar. Further cases of the WRB need to be documented to formally define the feature.

Chapter 7

The Companion Anticyclonic Tornado

7.1: Vortex Genesis

Early in D7 at roughly 2329 UTC, another anticyclonic vortex appears throughout all levels of radar data on the trailing flank of the RFGF. Unlike the 'rogue' anticyclonic vortex, this vortex appears far to the southeast of the cyclonic tornado and remains on the southern side of the RFD as it tracks northeasterly; the anticyclonic vortex fits the definition of an anticyclonic companion tornado as described in Bluestein et al. (2016). Companion anticyclonic tornadoes occur rarely in cyclonically rotating supercells. While the actual frequency is unknown, these tornadoes often catch storm chasers and NWS forecasters by surprise, which is a testament to their rarity. Of tornadic cyclonic supercells, perhaps only a few percent ever generate companion anticyclonic tornadoes. When they do occur, companion anticyclonic tornadoes often are ongoing at the same time as the primary cyclonic tornado but tend to occur later in the primary tornado's lifecycle. Companion anticyclonic tornadoes also generally track to the right of the motion of the cyclonic tornado as they remain on the opposite side of the RFD, resulting in tornado tracks that slowly diverge from each other. While strong anticyclonic companion tornadoes have occasionally been reported, such as the EF2 anticyclonic tornado that accompanied the El Reno 2013 tornado (Bluestein et al. 2015), companion anticyclonic tornadoes are generally

weak EF0 tornadoes. The Selden companion anticyclonic tornado fits these observations; it was concurrent with the cyclonic tornado and occurred in the latter portions of the cyclonic tornado's lifecycle, was only marginally tornadic at its peak strength, and tracked to the east northeast as it remained on the south side of the RFD.

Owing to their occurrence on the south side of the RFD, genesis of companion anticyclonic tornadoes has been attributed, at least partially, to RFD vortex ring tilting (Markowski and Richardson 2009; Bluestein et al. 2016). When idealized RFD vortex rings are tilted vertically by flanking line updrafts at the RFGF, a vortex couplet is created. Cyclonic vertical vorticity is generated on the north side of the RFD and has been implicated as a primary source of vorticity for cyclonic tornadogenesis (e.g., Markowski and Richardson 2009). On the southern side of the RFD, anticyclonic vertical vorticity is generated. Just as the cyclonic member of the vortex ring couplet supplies vertical vorticity for cyclonic tornadogenesis, the anticyclonic member of the couplet may be crucial for the occurrence of companion anticyclonic tornadoes. Once anticyclonic vertical vorticity is present, it can be concentrated and stretched to an extent by flanking line updrafts occurring along the RFGF, resulting in the formation of a weakly tornadic anticyclonic vortex (Bluestein et al. 2016).

However, Bluestein et al. (2016) offer an alternative hypothesis for the formation of companion anticyclonic tornadoes. RFD momentum surges have been noted to generate significant vorticity and shear at their northern and southern ends, which has been observed coincident with tornadogenesis and is likely an important factor in tornado formation (Finley and Lee 2008; Lee et al. 2012; Skinner et al. 2014). Cyclonic tornadoes have been frequently observed at the northern apex of RFD surges; however, anticyclonic tornadoes

have also been documented more rarely at the southern ends of RFD surges (Finley and Lee 2008). When an RFD surge impinges on the southern flank of the RFGF, the enhanced anticyclonic shear and vorticity at its southern end can be concentrated by flanking line updrafts and tornadogenesis can occur (Bluestein et al. 2016). Due to limited observations of companion anticyclonic tornadoes, it remains unknown what hypothesis for companion anticyclonic tornado formation better represents reality or if both processes work in tandem to result in tornadogenesis (Bluestein et al. 2016).

A radar series of the formation of the Selden companion anticyclonic tornado is shown in Figure 7.1. In the first panel at 2326:38 UTC, a particularly strong RFD surge is moving eastward through the middle of the RFD. It is farther from the cyclonic tornado than many of the surges documented earlier and is also very potent. As a result, the surge continues its eastward trajectory instead of wrapping around the cyclonic tornado and impinges the southern flank of the RFGF. Between the first and the second analysis time at about 2327 UTC, the southern end of the RFD surge begins encroaching on the RFGF on the southern flank of the RFD. When this occurs, the RFGF appears to kink in response to the anticyclonic vorticity present on the southern apex of the strong RFD surge as outbound Doppler velocities start to appear and intensify at the interface between the RFGF and RFD surge. The kink in the RFGF continues to become more defined as the RFD surge slowly passes and then dissipates. By the last analysis time at 2329:58 UTC, an incipient anticyclonic vortex is evident where the RFD surge had first impinged on the RFGF. Figure 7.1 indicates that the Selden anticyclonic vortex formed in a process resembling the second hypothesis in Bluestein et al. (2016); a strong RFD surge with attendant enhanced anticyclonic vorticity on its southern apex impinged on the RFGF. Flanking line updrafts

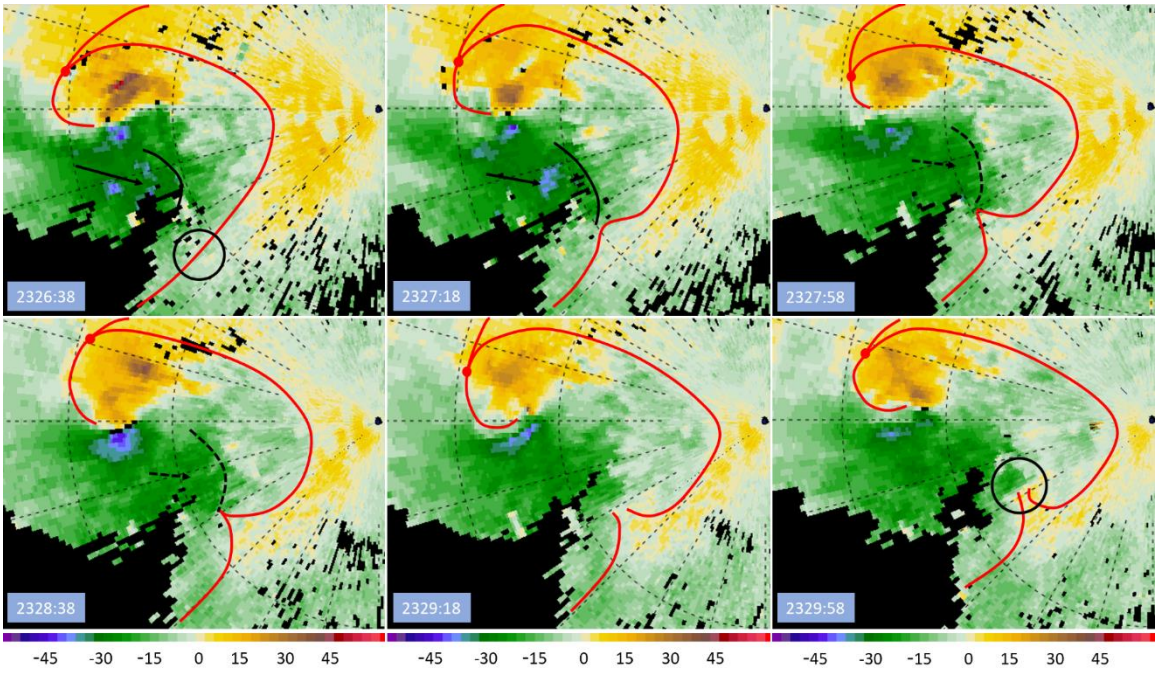

Figure 7.1: Radar analysis at the 4° level during early D7 showing development of an incipient anticyclonic vortex on the southern flank of the RFD. Panels are every 2 scans (40 s) and range rings are spaced every 2.5 km. Red lines mark the positions of the RFGF and forward flank boundary. The instigating RFD surge is marked in black, and a black arrow denotes the surge core. Dotted black lines and arrows mark the dissipating surge. In the first panel, a black circle marks slightly enhanced anticyclonic vorticity likely due to RFD vortex ring tilting, while the black circle in the last panel denotes the incipient anticyclonic vortex.

then concentrated the anticyclonic vorticity and stretched it resulting in vortex genesis roughly 3 minutes after the RFD surge initially reached the RFGF.

While Figure 7.1 clearly shows that an RFD surge was involved in anticyclonic tornadogenesis, it is unknown to what extent RFD vortex ring tilting contributed to vortex formation. It is apparent that weak ambient anticyclonic shear vorticity is present at the southern flank of the RFD, with very weak outbound Doppler velocities or weaker inbound Doppler velocities lying adjacent to stronger inbound Doppler velocities within the RFD. Some of the ambient anticyclonic shear vorticity exists simply because of the differing directions of the wind within the RFD and the ambient environment, but it is possible that

RFD vortex ring tilting is contributing to the vorticity as well. It is difficult to discern from the Doppler velocity field alone, but a small area of enhanced anticyclonic vorticity appears to be present along the southern flank of the RFD before the RFD surge impinges on the RFGF. This area of enhanced anticyclonic vorticity is marked in the first panel of Figure 7.1 and appears opposite to the cyclonic tornado, placing it in the expected position for RFD vortex ring tilting if the cyclonic member of the vortex ring couplet is taken to be located at the cyclonic tornado. However, this area of weak anticyclonic vorticity does not appear sufficient for flanking line updrafts to concentrate it into a discrete vortex since the amount of vorticity stayed nearly constant and a vortex was not generated until the RFD surge impinged on the RFGF; it appears that the RFD surge instigated the formation of the anticyclonic tornado by contributing additional anticyclonic vorticity that could then be concentrated and stretched along with the RFD vortex ring vorticity into a coherent vortex.

In the Selden case, it appears that both processes described in Bluestein et al. (2016) are occurring in tandem; although, the RFD surge is ultimately responsible for genesis. Weak anticyclonic vorticity is present along the southern flank of the RFGF from RFD vortex ring tilting; however, alone, it is not enough. Additional vorticity is required, which is supplied by a strong RFD surge. While vortex ring tilting provides the foundation for anticyclonic tornado formation by creating a zone of weak anticyclonic vorticity, the vorticity is rarely strong enough for anticyclonic tornadogenesis without additional contributions especially given the lack of a strong, persistent updraft to concentrate the vorticity. The additional vorticity comes from a strong RFD surge on a trajectory that enables the surge to thrust towards the southern flank of the RFGF, where the surge anticyclonic vorticity combines with the weak anticyclonic vorticity already present from

RFD vortex ring tilting to instigate tornadogenesis. Since RFD surges occur over a wide spectrum of intensity and trajectories, strong surges may only rarely be able to reach the southern flank of the RFGF; the requirement for a strong RFD surge on a particular trajectory is a possible explanation for why anticyclonic tornadoes occur only seldomly in cyclonic supercells. Furthermore, the Selden companion anticyclonic tornado occurred late in the cyclonic tornado's lifecycle, like many other documented cases (Bluestein et al. 2016). It is possible that an RFD surge capable of instigating anticyclonic tornadogenesis can only occur once the occlusion downdraft associated with the cyclonic tornado becomes established and begins enhancing momentum within the RFD. While there are no data to definitively connect the cyclonic tornado's occlusion downdraft to the RFD surge that caused the genesis of the anticyclonic tornado, it would be a possible explanation for why most companion anticyclonic tornadoes occur late in the lifecycle of primary cyclonic tornadoes since the occlusion downdraft does not form until the cyclonic tornado is maturing and reaching peak intensity. More stringent analysis of additional cases, preferably using dual-Doppler datasets, is needed to bolster these findings.

7.2: Track Behavior

The track of the anticyclonic tornado is remarkedly similar throughout its entire lifecycle; the tornado maintains a consistent east northeasterly heading, only gradually turning to the right with respect to supercell motion to a near due easterly heading at the end of D7 during dissipation. Figure 7.2 contains the track of the anticyclonic tornado and the track segments that were used for further analysis at the 4° scan elevation. A data gap is indicated on the map when the anticyclonic tornado passed directly overhead of the radar

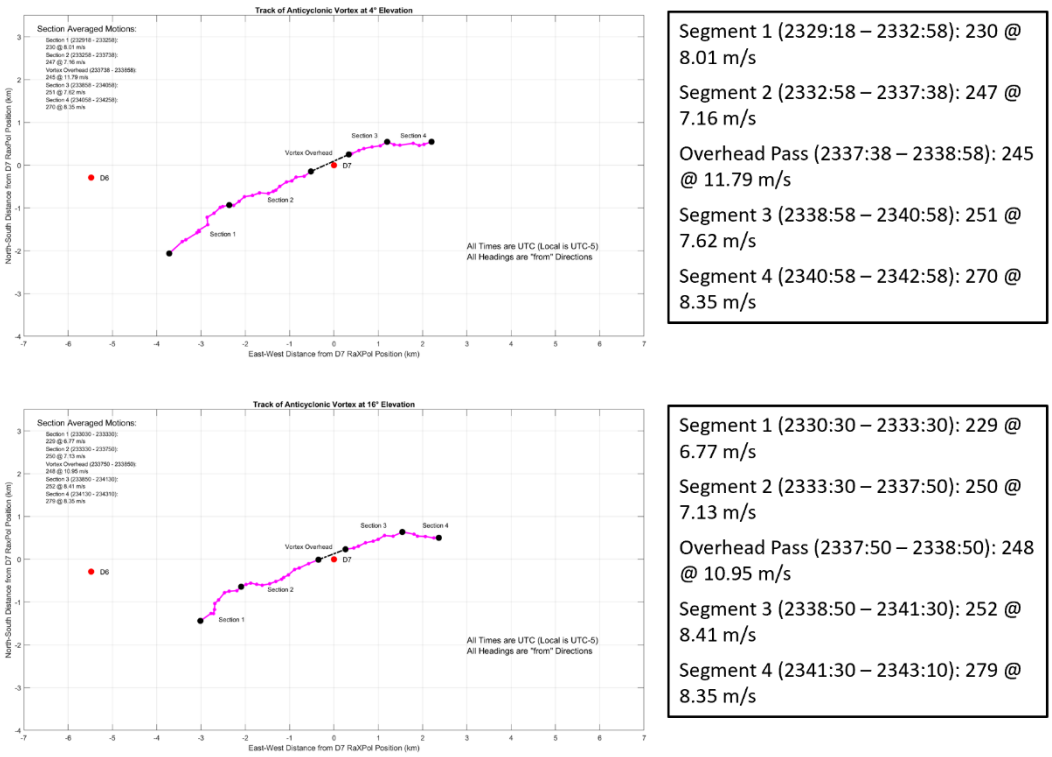

Figure 7.2: Track of the Selden companion anticyclonic tornado at the 4°(top) and 16° (bottom) elevation scans. Descriptions of the segment track vectors are provided to the right.

at roughly 2338 UTC. The vortex went unnoticed by the radar crew until it was nearly directly overhead, and the radar was enveloped in swirling, airborne chunks of vegetation; data were unreliable as the vortex passed into the radar's near field owing to ground clutter. The brief gap in data roughly bisects the tornado lifespan, providing at least two separate track segments for analysis. The anticyclonic tornado track was split further into four segments with two segments occurring before and after the vortex passed overhead based on subtle track changes and consideration for dividing the track to get a better representation of the vortex and its structural changes in cross section averaging. Segments 1 and 2 are differentiated by the consistency of the vortex track, with the track in segment 1 being more erratic than that in segment 2; a slight right turn also accompanies the segment change. Segments 3 and 4 are separated by another slight right turn.

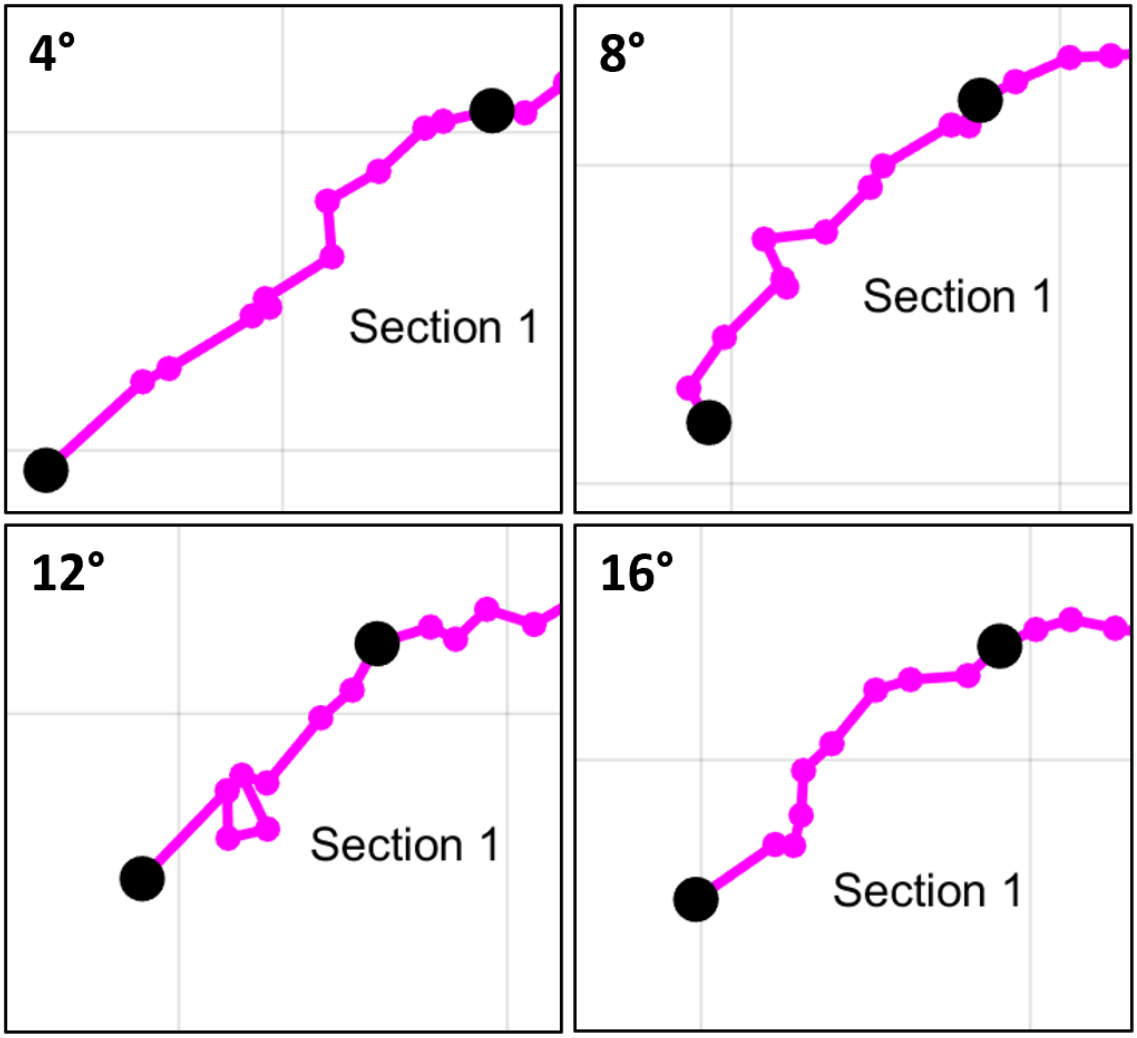

Figure 7.3: Comparison of the first anticyclonic tornado track segment at 4° increments. The segment 1 track is shorter with height reflecting longer development times aloft and is somewhat more erratic with height. Grid is at 1 km intervals.

Like the track behavior of the cyclonic tornado early in its lifespan, the segment 1 track for the anticyclonic tornado is somewhat erratic. The identifiable center of the vortex tends to jump around from scan to scan and the track appears less stable. Although the proximity of the radar to the vortex limits observations in the vertical, the track of the anticyclonic vortex appears to become more inconsistent with height. Figure 7.3 reflects these observations; the track at 4° (240 m ARL) is relatively smooth compared to the track at 8° (490 m ARL) and especially at 12° (740 m ARL) where the track meanders around

for three to four scans. However, at the 16° level (1000 m ARL) the trend is reversed, as the track becomes more consistent again. Regardless, the tendency is for the track to become more erratic with height, reflecting that the vortex is likely forming from the bottom up as suggested by Houser et al. (2015). Because the anticyclonic vortex appears to have been instigated by an RFD surge, which supplies vorticity near the surface, development first near the surface makes physical sense. Furthermore, the anticyclonic vortex is trackable earlier in lower elevation scans than at higher elevation ones, lending more evidence for a bottom-up development. As shown in Figure 7.3, the 4° elevation start time is 2329:18 UTC, at 8° it is 2329:22 UTC, at 12° it is 2330:06 UTC, and at 16° it is 2330:30 UTC. The anticyclonic vortex is first identified in the 16° elevation velocity field three scans later than at 4°, taking more than a minute after appearing at 240 m ARL to appear at 1000 m ARL. The difference in time of development grows when considering the top and bottom scan elevations in the data; the gap grows to 2 minutes with the vortex appearing at the 2° level at 2328:36 UTC and taking until 2330:32 to appear at 18°.

Finally, the track of the tornado takes a slight right turn at the end of segment 1 that has the same magnitude with height but is sharper at higher elevations (see Figure 7.3). At 4°, the track shifts from approximately 8 m s^{-1} from 230° (SW) to roughly 7 m s^{-1} from 250° (WSW); while the forward speed barely changes, the track direction changes by almost 20°. Meanwhile, the track at 16° goes from 7 m s^{-1} from 230° (SW) to 7 m s^{-1} from 250° (WSW), displaying a 20° track direction change. The right turn likely marks a point at which the anticyclonic vortex has become coherent with height and has reached a mature position at the apex of the RFGF kink, similar to the cyclonic tornado; as a result, the track

of the tornado becomes close to the motion of the parent supercell. This transition will be explored further in the following radar analysis section.

During segment 2, the anticyclonic tornado behavior becomes uniform with height and the vortex matures. The tornado tracks consistently to the east northeast, with headings that are no more than 5° different across all scan elevations, averaging from 250° (SW). Vortex forward speed also differs by less than 1 m s^{-1}, centered on roughly 7 m s^{-1}. However, the vertical extent of the measurements is also decreasing continuously as the anticyclonic vortex nears the radar; the heights of the bottom and top scans go from 105 m ARL and 975 m ARL at the start of segment 2 to 11 m ARL and 98 m ARL at the end of the segment. With less than 100 m of vertical depth at the closest scans, differences with height are expected to be minimal. Segment 2 also marks peak intensity for the anticyclonic vortex, with ΔV_{max} in between 35 and 40 m s^{-1}, placing the vortex just under the tornadic shear threshold in Wurman and Kosiba (2013). Furthermore, French et al. (2014) notes that the measured ΔV of an unchanging vortex will increase as distance to the radar decreases because of higher sampling resolution within the vortex. Therefore, the threshold for tornadic shear should increase as well to reflect the biased measurements. As a result, it is likely that the companion anticyclonic vortex did not complete development into a weak tornado and was instead an intense, sub-tornadic vortex. At 2337:30, the anticyclonic vortex passes within 0.3 km of the radar location and data become unreliable as the vortex enters the radar near field.

During the brief 2.5-minute gap while the vortex was overhead, the indicated speed of the tornado increases markedly. Both before and after the vortex passed over the radar, the vortex motion was 7 to 8 m s^{-1}, but while the vortex passed overhead forward speed

increases to over 10 m s^{-1} at all scan elevations. The increase in speed is greatest at the 2° level, with the vortex surpassing 12 m s^{-1} in forward speed. The reasons for the burst in speed are not entirely known, but its resemblance to the burst in forward speed of the cyclonic tornado during segment 4 as the result of a strong RFD surge suggest that an RFD surge may have been responsible. However, no sharp directional change occurred, and noisy data in the radar near field filled with ground clutter limit the ability to identify any near vortex features. Furthermore, the vortex center passes just to the north of the radar deployment location, creating unfavorable angles from the radar to any eastward moving RFD surge since any enhanced momentum would be oriented perpendicular to the radar beam. Hints of a momentum surge are still detectable however, and findings from radar analysis will be presented in the following section.

After the vortex passes overhead, segment 3 begins. The track heading and speed of the anticyclonic vortex return to those seen during segment 2; the 4° track vector was roughly 7 m s^{-1} from 250° (WSW) before the overhead pass and was approximately 8 m s^{-1} from 250° (WSW) after the overhead pass. As with segment 2, the track also remains unified across all scan elevations. However, the anticyclonic tornado does begin to weaken significantly during segment 3, backing off from marginal tornado intensity. Despite this weakening, it was not during segment 2 that disturbed dust and dirt was being lofted as indicated by the correlation coefficient derived damage paths in Figure 3.6, but during segment 3 after the vortex passed overhead that there was scouring of a small amount of dust and dirt by the vortex. As described by Tanamachi et al. (2007), the vortex could be dissipating in accordance with decay mode 2, where the RMW increases as azimuthal wind magnitude decreases. As the tornado's internal downdraft becomes dominant and inflow

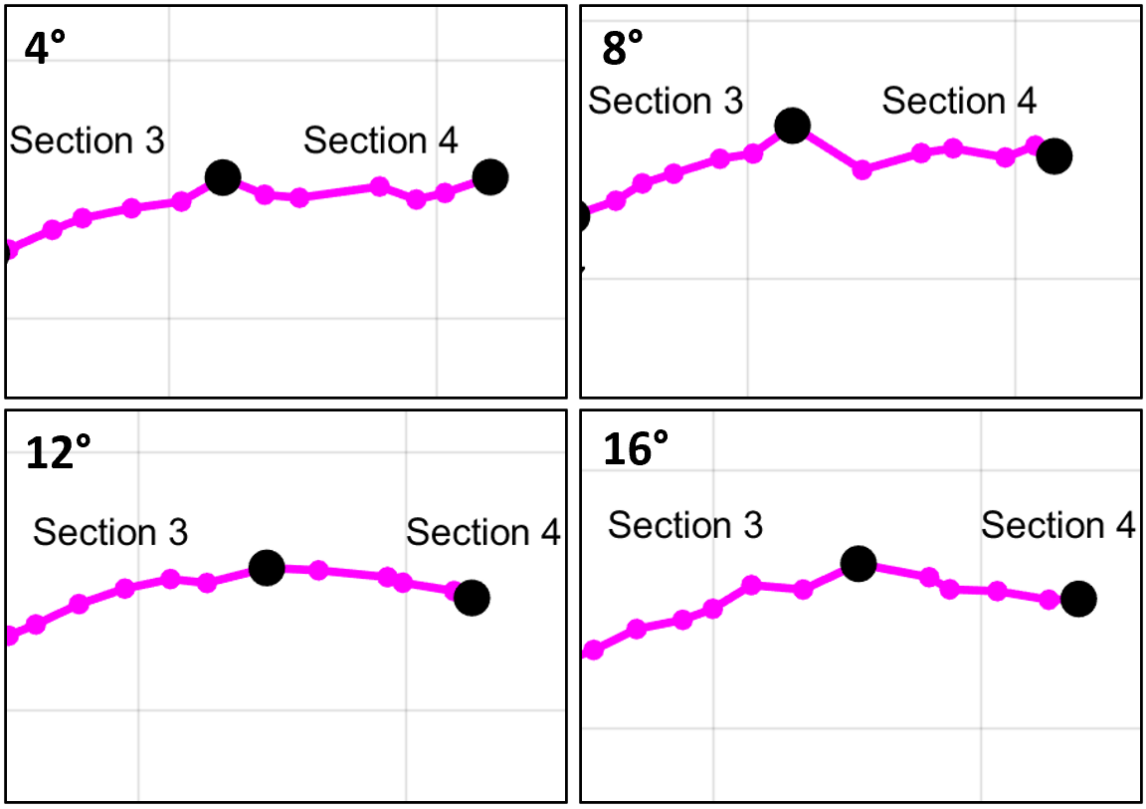

Figure 7.4: Comparison of the right turn between segments 3 and 4 at 4° increments. The right turn is persistent with height and generally sharp, occurring in 1 or 2 scans. Grid is at 1 km intervals.

ceases, the RMW increases, and more dust is lofted. Consequently, the damage path identified for the anticyclonic tornado may be a result of dissipation and not an actual damage path of a tornado. More details will be examined in cross section analysis in section 7.4 to determine if the vortex did follow a mode 2 decay.

At the end of segment 3, the sharpest directional shift in track of the anticyclonic vortex occurs. Figure 7.4 shows the rapid character of the track shift and its persistence with height; at the 4° elevation, the tornado track was 8 m s^{-1} from 250° (WSW) and shifted to 8 m s^{-1} from 270° (W). Across all scan elevations, the vortex turns an average of 25° to the right in 1 or 2 scans. The right turn is coincident with significant vortex weakening to a ΔV_{max} of less than 20 m s^{-1}. As the right turn is concurrent with significant weakening,

an occlusion from the RFGF has likely taken place in a process conceptually like the occlusion of the cyclonic vortex; indeed, the anticyclonic vortex is intense and likely generates an occlusion downdraft similar to the cyclonic tornado. Moreover, the average forward speed of the parent supercell is roughly 9.5 m s^{-1}, which is nearly 2 m s^{-1} faster than the average speed of the anticyclonic tornado; the anticyclonic tornado moves westward with respect to the parent supercell, reflecting the formation of an occlusion downdraft. The eventual decoupling of the anticyclonic vortex from the RFGF in an occlusion process like the cyclonic tornado will be explored in radar analysis.

7.3: Evolution of the Vortex and Near-Vortex Wind Field on Radar

A radar analysis showing the development of the companion anticyclonic tornado during segment 1 at the 4° level is shown in Figure 7.5. The first panel at 2329:18 UTC is the first scan in which a coherent anticyclonic vortex is trackable at the 4° elevation; over the next several scans the vortex strengthens and reaches a marginal tornadic intensity with ΔV_{max} over 35 m s^{-1}. By the third analysis time at 2330:38 UTC, a discrete area of outbound velocities has become established on the south side of the developing vortex. While the vortex remains broad, it rapidly begins to tighten and appears as a coherent anticyclonic vortex by the fifth analysis time at 2331:58 UTC. As the vortex strengthens, the kink in the RFGF continues to sharpen. The RFGF kink evolves and becomes coupled to the anticyclonic tornado, forming a distinct apex near the anticyclonic tornado where the portions of the RFGF ahead of the vortex (east) and behind the vortex (west) join. South of the apex, a marked inflow notch also becomes established. Like the apex between the RFGF and forward flank convergence zone near the cyclonic tornado, the apex at the sharp

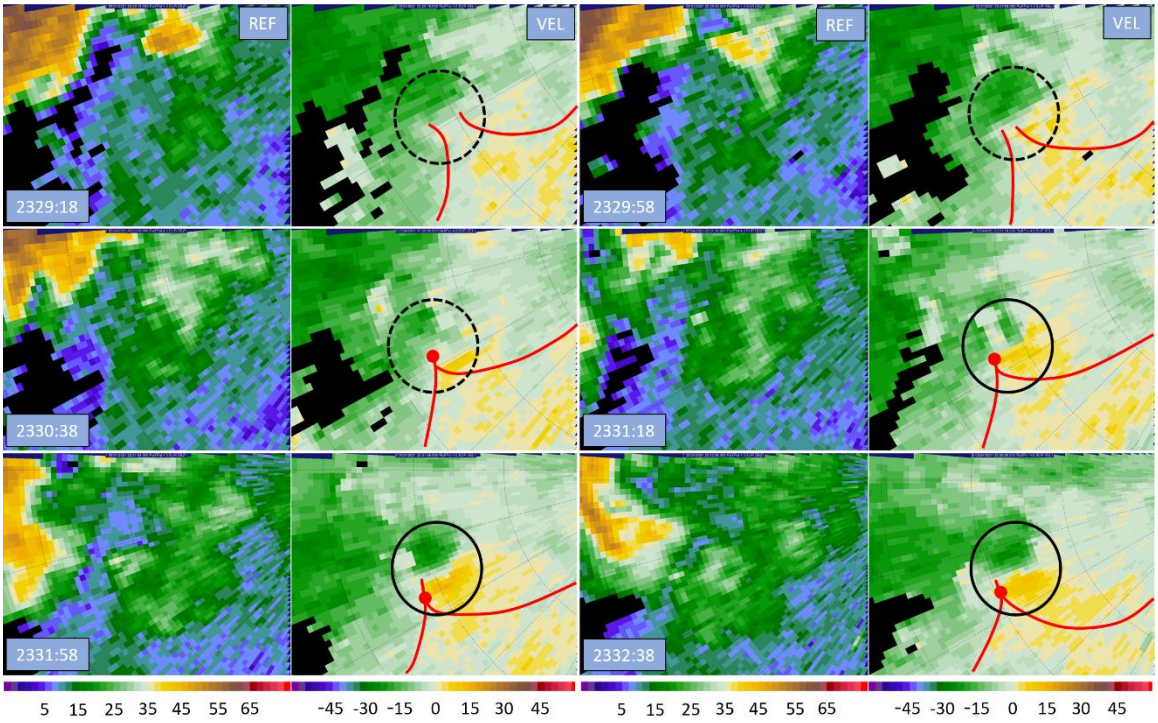

Figure 7.5: RaXPol imagery at the 4° elevation taken every 2 scans (40 s) during segment 1. In each radar panel, reflectivity is on the left and Doppler velocity on the right. Range ring spacing is 1.0 km. Black circles denote the anticyclonic vortex. Red lines mark the approximate positions of RFGF near the vortex.

corner of the RFGF kink near the anticyclonic tornado marks the inflow notch for the anticyclonic tornado and a zone of enhanced anticyclonic shear and vorticity underneath flanking line updrafts that support the continuation of the anticyclonic tornado. If the anticyclonic tornado can remain near the apex in the RFGF in proximity to flanking line updrafts, the vortex will continue to intensify or maintain strength; if the anticyclonic tornado moves away from or otherwise becomes decoupled from RFGF, the vortex will become occluded from its inflow and dissipate. Notably, the flanking line updrafts and enhanced convergence and vorticity located at the new RFGF apex are not as intense as similar features associated with the parent supercell located near the cyclonic tornado, so the overall potential for the anticyclonic vortex to intensify is probably not as great.

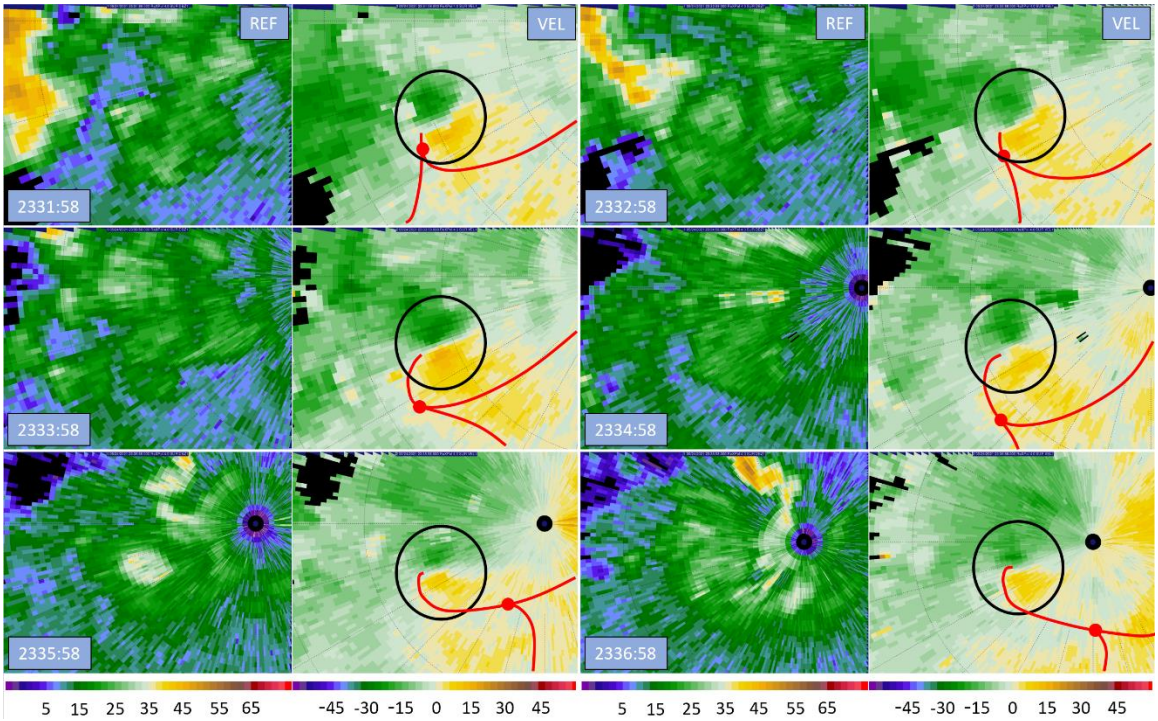

Figure 7.6: RaXPol imagery at the 4° elevation taken every 2 scans (40 s) during segment 2. In each radar panel, reflectivity is on the left and Doppler velocity on the right. Range ring spacing is 1.0 km. Black circles denote the anticyclonic vortex. Red lines mark the approximate positions of RFGF near the vortex.

A similar radar analysis during segment 2 while the anticyclonic vortex reaches maturity is produced in Figure 7.6. Throughout the analysis, the anticyclonic vortex visibly starts to lag the RFGF and apex that marks the inflow notch. During the first 2 analysis times, the anticyclonic tornado remains coupled to the RFGF and the inflow remains unobstructed; the vortex continues to intensify and reaches peak intensity around 2333 UTC. However, like the cyclonic tornado, the anticyclonic tornado represents a vorticity maximum and pressure minimum. Unlike the cyclonic tornado, there is no persistent mid-level mesoanticyclone above the anticyclonic vortex, and the magnitude of vorticity near the ground quickly surpasses that aloft. Consequently, a downward directed dynamic pressure gradient force likely develops rapidly and an occlusion downdraft becomes established. Because of the lack of vorticity aloft and subsequent rapid onset of the

downward directed pressure gradient force and formation of the occlusion downdraft, the anticyclonic tornado is not able to intensify much before occlusion takes place. The occlusion downdraft forms quickly, and the RFD surges it creates (See Figure 5.4) displace the RFGF from the anticyclonic tornado and occlusion occurs. As a result, the companion anticyclonic tornado only reaches a ΔV_{max} of 37 to 38 m s^{-1}; the early formation of the occlusion downdraft associated with companion anticyclonic tornadoes explains why most tornadoes of this type are relatively weak.

The motion of the anticyclonic tornado is evidence that an occlusion downdraft has become established. The vortex is moving at a consistent pace that is roughly 2 m s^{-1} slower than the parent supercell, which reflects westward storm relative movement of the vortex. Like the cyclonic tornado, this westward motion is likely a result of occlusion of the anticyclonic vortex, which has proceeded in a similar manner to the occlusion of the cyclonic tornado. The occlusion downdraft formed and generated RFD surges that decoupled the RFGF from the tornado, causing the occlusion to take place. Once occlusion occurs, the companion anticyclonic tornado slows down relative to the parent storm as it and the RFGF are no longer coupled. Again, the rapidity of occlusion and early onset of westward propagation reflects the more rapid lifecycle of the companion anticyclonic tornado as compared to the cyclonic tornado. Unfortunately, unlike with the cyclonic tornado, there are no direct indications of significant surging momentum within the RFD near the vortex. This may be because the surging momentum and occlusion downdraft related RFD surges are difficult to differentiate from the anticyclonic tornado in the data; the companion anticyclonic tornado, occlusion downdraft, and any surging RFD momentum generated by the occlusion downdraft are all smaller in scale and weaker than

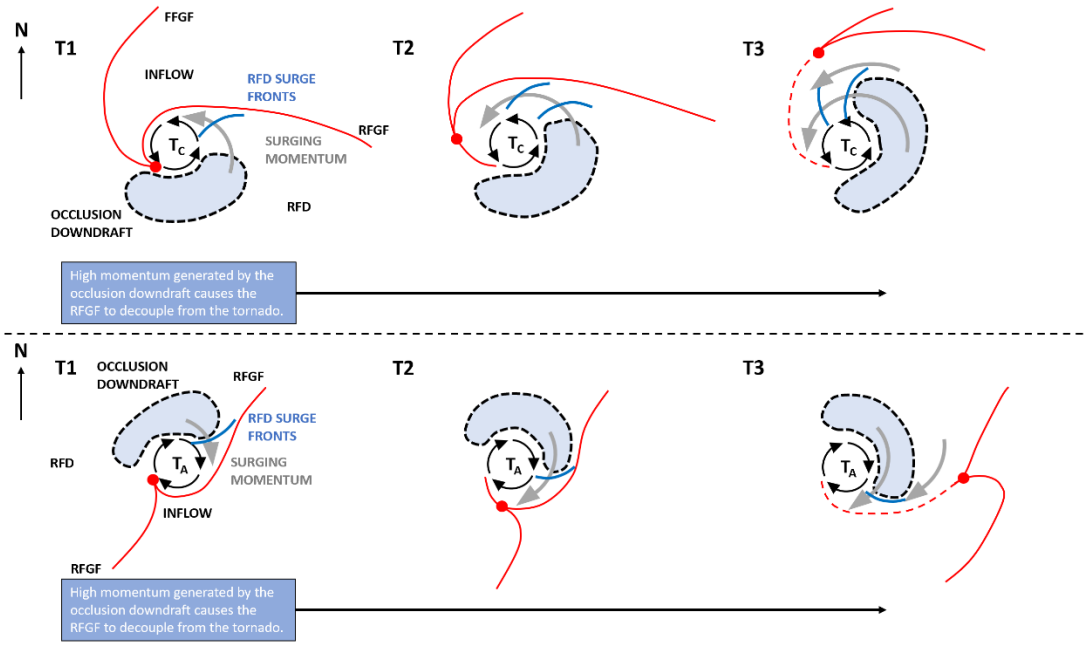

Figure 7.7: Conceptual diagram comparing the anticyclonic tornado occlusion process to the more familiar cyclonic tornado occlusion process. Red lines represent the major near-tornado boundaries. A dotted area shaded light blue denotes the approximate location of the occlusion downdraft. Gray arrows show where momentum is surging because of the occlusion downdraft. There is a scale difference between the two diagrams.

similar features associated with the cyclonic tornado. Moreover, as time passes, the companion anticyclonic tornado gets very close to the radar and then passes over it, making it difficult to discern features such as RFD surges since the interpretation of Doppler velocity changes as angles relative to the radar rapidly shift.

Throughout its lifecycle, the companion anticyclonic tornado follows an occlusion process conceptually like the one that the cyclonic vortex undergoes. Figure 7.7 presents a conceptual model comparing the occlusion of both the cyclonic and companion anticyclonic tornadoes. First, the intensity of the vortex increases and the magnitude of vorticity near the surface surpasses that aloft. A downward directed pressure gradient forms, leading to the development of the occlusion downdraft. The occlusion downdraft

often forms off-center from the tornado within the RFD, which could be the result of a tilt in the vorticity maximum with height or due to buoyancy contributions to the downward directed pressure gradient force (Adlerman and Droegemeier 1999; Bluestein 2013). Then, the occlusion downdraft generates strong RFD surges (e.g., Skinner et al. 2014). Figure 5.4 provided a possible physical mechanism for this, showing that pulsing occlusion downdraft outflow could generate RFD surges as the outflow pulses interacted with the RFD flow. The RFD surges are advected about the tornado circulation and reach the RFGF, displacing it. If the surging momentum is sufficiently strong as to overwhelm the near-surface convergence driven by the tornado's central low pressure, the RFD surges cause the RFGF to break away from the tornado and the two become decoupled. Once decoupling occurs, the tornado is occluded from relatively warm and buoyant inflow and the tornado begins to weaken.

However, there are a few key differences between the occlusion of the anticyclonic and cyclonic tornadoes. First is that the companion anticyclonic tornado is not overlain by a persistent mid-level mesoanticyclone like the cyclonic tornado. As a result, the magnitude of vorticity near the surface quickly surpasses the magnitude of vorticity aloft and a downward directed pressure gradient force develops rapidly at relatively low vortex intensities. Second, is that unlike the cyclonic tornado, the companion anticyclonic tornado did not deviate significantly in the direction opposite the RFD after occlusion occurred, which is rightwards in a storm relative sense. The lack of rightward motion appears to stem from the lack of significant or strong RFD surges near the anticyclonic tornado. Because the companion anticyclonic tornado is weaker than the cyclonic tornado, the associated features, such as the occlusion downdraft and surging RFD momentum, were likely weaker

as well and strong RFD surges may not have been generated. Moreover, the companion anticyclonic tornado is also located away from the parent supercell, isolated from other mechanisms that can generate RFD surges closer to the cyclonic tornado. As a result, there are few, if any, strong RFD surges near the anticyclonic tornado to affect its track.

The anticyclonic tornado also highlights a contradiction in a tornado's mere existence; as a tornadic circulation intensifies, it will drive the formation of an occlusion downdraft unless the magnitude of vorticity aloft is also exceptionally strong. In this way, the maximum potential intensity of most tornadoes is limited; as soon as the tornado intensifies to a point where near-surface vorticity grows stronger than that aloft, then the occlusion downdraft forms. The occlusion downdraft outflow creates RFD surges when interacting with the RFD flow (See Figure 5.4), and these surges are then advected around the tornado circulation where they can displace the RFGF and cause occlusion. For this reason, it is critical for a tornado to be overlain by an exceptionally strong mid-level mesocyclone. A strong mid-level mesocyclone delays the formation of a strong occlusion downdraft, allowing the tornado to grow more intense before the occlusion downdraft forms. This makes it more likely that the tornado will be able to drive enough surface convergence to stay coupled to the RFGF despite attempted displacement of the RFGF by the surging momentum caused by the occlusion downdraft. However, most supercells display cycling behavior to some degree, including the Selden supercell that underwent occluding mesocyclogenesis. Only in combinations of environmental shear and instability that are generally unrealistic in all but the most extreme synoptic patterns can supercells possess a strong enough mid-level mesocyclone to achieve non-cycling behavior (Adlerman and Droegemeier 2005). Because of the high directional and speed shear

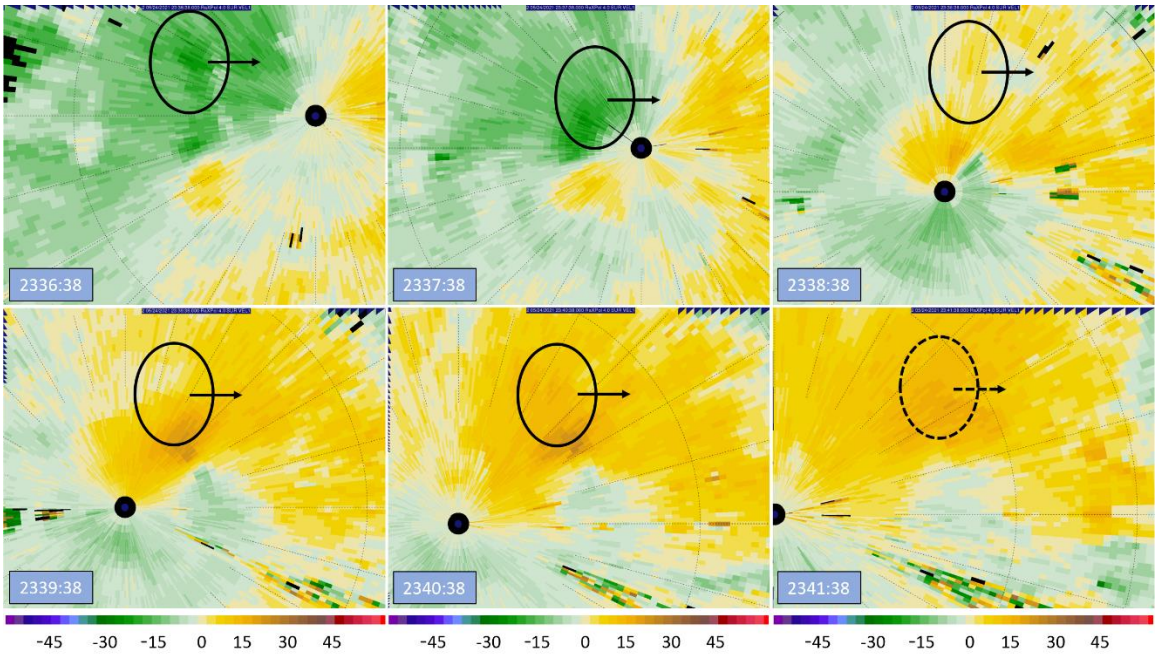

Figure 7.8: Radar analysis at the 4° scan elevation depicting a possible RFD surge brushing by the north side of the anticyclonic tornado. Black circles denote the area of enhanced momentum, while arrows indicate direction of movement. A dotted circle and arrow mark weakening of the possible surge in the last panel.

requirements of such supercells, steady non-cycling behavior is exceptionally rare; such a case was seen in December of 2021 when a steady non-cycling supercell developed and spawned the long track Mayfield, Kentucky tornado.

Following segment 2, the anticyclonic vortex is observed to accelerate significantly while it passes overhead of the radar. Figure 7.8 contains a radar analysis at the 4° level that may show evidence of an RFD surge brushing by the north side of the vortex that does not otherwise interact with the circulation by wrapping around it. In the first panel at 2336:38 UTC, a slight enhancement of momentum within the RFD north of the vortex is apparent. However, because the surge moves eastward north of the radar, momentum is oriented perpendicular to the radar, and it is difficult to determine with certainty whether a momentum surge is occurring. Because of this, only a small area of enhanced momentum just to the north of the vortex is identifiable at the second analysis time. The surge continues

eastwards until a weak area of enhanced outbound momentum emerges in the fourth panel at 2339:38 UTC as the surge passes to the northeast of the radar. The area of enhanced momentum continues to accompany the anticyclonic vortex to its north while it gradually decays. By 2341:38, any hint of a surge has all but disappeared as momentum north of the anticyclonic tornado returns closer to a baseline state. From these observations, it appears that a weak surge or extension of a stronger surge located farther to the north deeper within the RFD may have brushed by the northern side of the vortex from 2336:30 to 2341:30 UTC, moving only slightly faster than the vortex itself. The center of this time interval aligns well with when the vortex was directly overhead and forward speed briefly increased; it is possible that this surge was responsible for increasing momentum on the north side of the anticyclonic vortex, causing it to accelerate eastwards briefly.

After the anticyclonic tornado passes overhead of the radar location, it continues to weaken considerably. A radar analysis at the 4° elevation covering segments 3 and 4 is shown in Figure 7.9. Notably, the vortex becomes deeply occluded during the analysis; the apex in the RFGF is no longer visible anywhere near the tornado and the occluded extension of the RFGF reaching back to the anticyclonic vortex becomes less defined. As a result, the anticyclonic tornado dissipates to a point where the vortex signature is barely visible in the velocity field. Ironically, the reflectivity signature associated with the tornado is most visible as the vortex decays. The development of the reflectivity appendage is coincident with the start of the correlation coefficient drop indicated in the damage swaths in Figure 3.6, and it is likely that the disturbing of dust and dirt has finally allowed the vortex to develop a distinct reflectivity feature. While some reflectors are likely being pulled down from the north by the anticyclonic circulation, the vortex continues to decay;

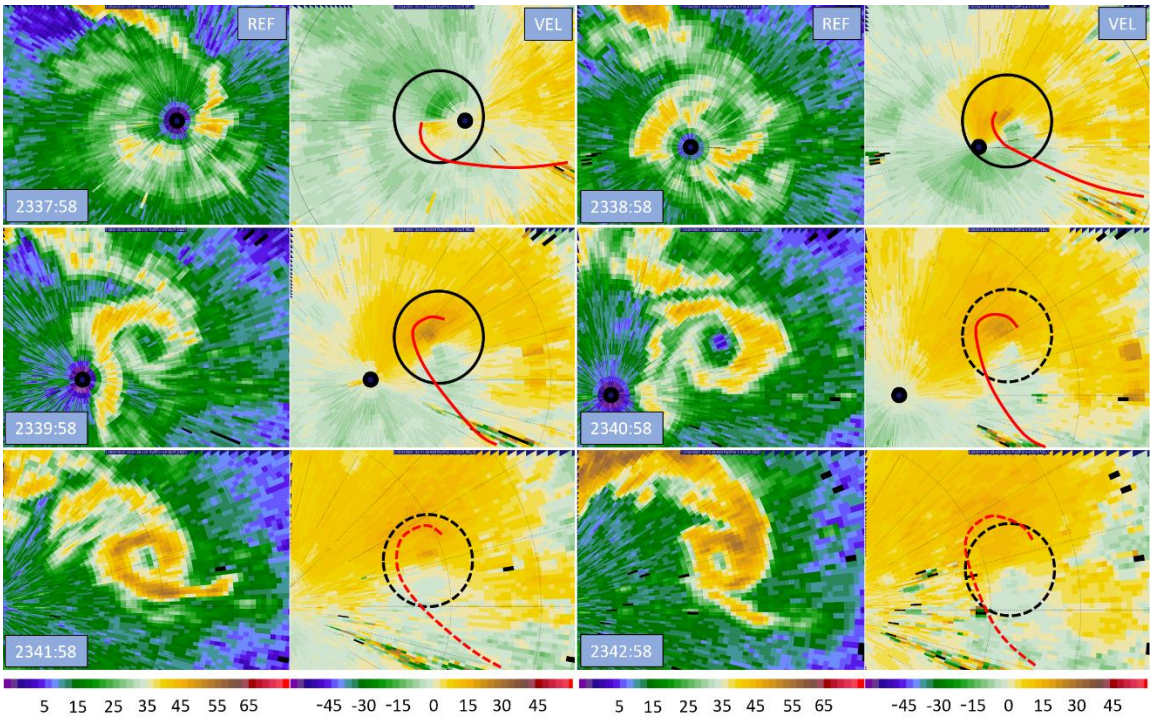

Figure 7.9: RaXPol imagery at the 4° elevation taken every 2 scans (40 s) during segments 3 and 4. In each radar panel, reflectivity is on the left and Doppler velocity on the right. Range ring spacing is 1.0 km. Black circles denote the anticyclonic vortex. Red lines mark the approximate positions of RFGF near the vortex.

this process would be expected to slow as the vortex weakened, not increase in intensity such that a full reflectivity feature could develop. As discussed previously, the increased presence of dirt and dust may be the result of a mode 2 decay where the vortex broadens as winds decrease (Tanamachi et al. 2007), so the appearance of the reflectivity appendage may be an indicator of dissipation rather than an intense vortex.

7.4: Cross Section Analysis

The averaged azimuthal cross sections at the 4° scan elevation for segments 1 and 2 are exhibited in Figure 7.10. The segment 1 cross section accounts for the first 3.5 minutes of the anticyclonic vortex lifecycle and averages 230 m ARL. Notably, the vortex width is relatively large, with an average diameter of roughly 370 m. Although this appears

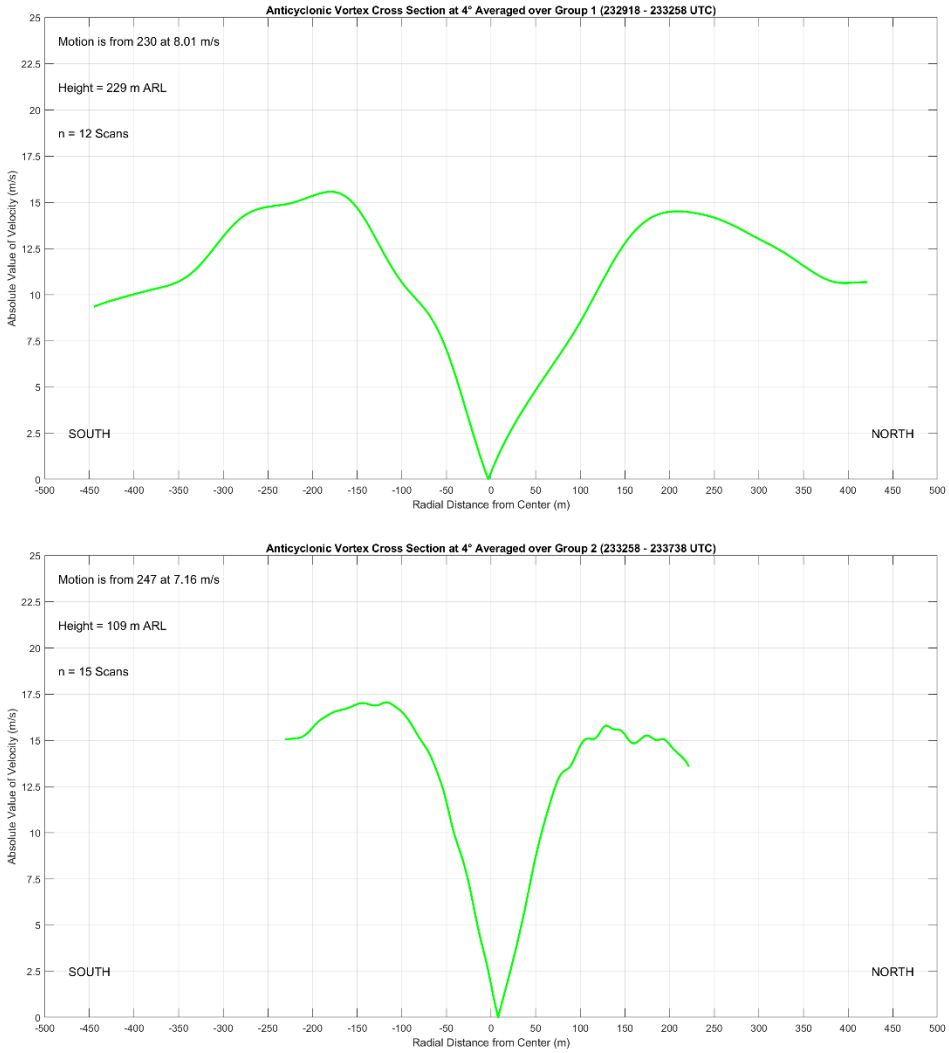

Figure 7.10: Azimuthal Cross Sections through the Selden anticyclonic Tornado at 4° elevation for track segments 1 (top) and 2 (bottom).

contradictory at first, the large width is indicative of a broad circulation that has yet to tighten into a coherent, intense vortex. For a majority of the first segment, the anticyclonic vortex is developing, and the radar appearance of the vortex (see Figure 7.5) is in good agreement with the cross section; the vortex remains broad as vorticity is supplied and slowly concentrated and stretched by flanking line updrafts. Another indication of vortex development is that the cross section departs from expected behavior in the vortex core, where winds are expected to obey solid body rotation (e.g., Tanamachi et al. 2007). Finally,

the average ΔV during segment 1 is less than 30 m s^{-1}, placing it well below tornadic thresholds.

The segment 2 azimuthal cross section in Figure 7.10 stands in sharp contrast to the segment 1 cross section. By segment 2, the anticyclonic vortex has tightened considerably, with a width of about 230 m. Despite the smaller diameter, the vortex width continues to be quite large compared to prior studies. In their analysis, Tanamachi et al. (2007) found that the RMW of their tornado was 100 to 150 m during peak intensity, resulting in a vortex diameter of 200 to 300 m while the vortex was mature. Furthermore, this diameter was for a larger cyclonic tornado; a small, marginally tornadic anticyclonic vortex should not have an RMW the same size as a mature cyclonic tornado. This finding highlights the differences between GBVTD analysis, where tornadic circulations are attempted to be isolated from larger scale flows, and cross section analysis from the unaltered Doppler velocity field, where flow of multiple scales is superimposed on the vortex. A further indicator that larger scale flow within the RFD is superimposing on the vortex circulation is that the profile winds do not decrease very rapidly outside the RMW as would be expected in GBVTD analyses, where a potential flow region is generally found outside the RMW (Kosiba and Wurman 2010, Tanamachi et al. 2007, Wakimoto et al. 2012). A similar observation was made in Wurman and Gill (2000), when they noted that winds outside the RMW did not decrease at the rates expected; when vortices are not isolated using GBVTD techniques, the size of the wind field and coverage of intense winds associated with the vortex are much larger. Otherwise, the segment 2 profile reveals a mature and healthy anticyclonic vortex verging on tornadic strength. The ΔV has continued to increase to approximately 33 m s^{-1} as the width of the vortex decreases, fitting a mode 2 intensification from Tanamachi

Figure 7.11: Picture of the anticyclonic vortex looking straight up as it passed overhead of the radar. The vortex is roughly in the center of the image, with a small funnel cloud or protrusion visible in the center of the vortex. Photo courtesy of Sam Emmerson.

et al. (2007). The vortex core region also reflects solid body rotation while the magnitude of velocity measured on both sides of the vortex is within 2 m s^{-1}.

After segment 2, the anticyclonic vortex passes directly overhead of the radar. Although data are unreliable as the vortex passes into the near field, a unique picture was taken looking straight up from the deployment site towards the cloud base as the vortex passed overhead and is shown in Figure 7.11. At the time when the vortex was overhead, the vortex was near its peak intensity; rotation within the cloud base is evident. Note that since the view is from the ground looking vertically, the rotation of the vortex will appear to be counterclockwise and not clockwise. A small protrusion of cloud is also visible at the center of the vortex, which may be a small funnel cloud forming in response to the intensity of the anticyclonic vortex. During the latter half of segment 2, the ΔV across the vortex was commonly 37 or 38 m s^{-1}, making it possible that the vortex was a marginal tornado

as it passed over the radar. Furthermore, small pieces of vegetation were being lofted when the anticyclonic vortex passed overhead, indicating that the vortex was intense, with marginally tornadic winds. Caution, however, must be exercised since the presence of any debris may be just as much a function of the onset of vortex dissipation as its intensity.

Figure 7.12 contains the averaged azimuthal cross sections at the 4° elevation for segments 3 and 4, from after the anticyclonic vortex passed to the east of the radar. The segment 3 profile appears much like the segment 2 profile, except that it contains a significantly greater amount of noise because it contains fewer scans that were all taken when the vortex was very close to the radar where pixel width was only a few meters. From segment 2 to segment 3, the anticyclonic vortex has begun to weaken, with a ΔV of approximately 28 m s^{-1}. The vortex width has also contracted to or slightly under 200 m. As the vortex weakens, it is also becoming less distinct from the background flow, so the winds do not decrease much outside the RMW. The segment 4 profile in Figure 7.12 is telling of a vortex that has almost entirely dissipated. The anticyclonic vortex has weakened considerably while broadening; the ΔV across the vortex is now less than 20 m s^{-1} and the vortex diameter has grown to at least 250 m. The vortex has followed a mode 2 decay, confirming that the appearance of the reflectivity feature on radar and presence of any debris is likely the result of vortex dissipation. This does not preclude small amounts of debris from being picked up by the sub-tornadic anticyclonic vortex as was noted by the radar crew when the vortex passed overhead of the radar, but the best-defined reflectivity signature that did not appear until segment 3 and was likely the result of decay and not due to the intensity of the vortex. The ΔV and diameter of the vortex are also difficult to discern, showing that the vortex has largely dissipated. The core region of the vortex no longer

Figure 7.12: Azimuthal Cross Sections through the Selden anticyclonic Tornado at 4° elevation for track segments 3 (top) and 4 (bottom).

obeys solid body rotation, and symmetry in the vortex profile has entirely disappeared; the vortex is both off center and the velocity magnitude on either side of the vortex is very different. Segment 4 reflects the occlusion of the vortex from the RFGF and inflow that was noted during radar analysis; the vortex has weakened rapidly in response and is barely a discernible vortex be the end of D7.

Chapter 8

Summary of the Selden Tornado, Conclusions, and Future Work

In May of 2021, the RaXPol mobile radar intercepted a supercell in northwestern Kansas that produced a tornado and companion anticyclonic tornado near the small town of Selden. In this thesis, the data collected by RaXPol during the Selden tornadoes were analyzed using multiple methods with the goal of explaining the behavior of both tornadoes throughout their lifecycles. Numerous features were identified, analyzed, and compared with prior literature to ascertain their potential influence on the behavior of both tornadoes. Some rarely documented phenomena with previously undetermined or uncertain impacts on tornado behavior were also observed, building on small sample sizes and limited understanding of potentially important features. Throughout analysis, particular emphasis was placed on how all identified features and their influences contributed to a summed whole, culminating in a comprehensive narrative for the Selden tornadoes. Throughout analysis, several key findings emerged. First was that RFD surges were critical for the evolution of both tornadoes, influencing track and advancing the occlusion process. Second was that the companion anticyclonic tornado formed only after a strong RFD surge impinged the southern flank of the RFGF, highlighting the possibility that companion anticyclonic tornadoes may be relatively scarce because they require vorticity from an RFD surge of sufficient strength and on a certain trajectory to form. Finally, it was found that both cyclonic and companion anticyclonic tornadoes followed conceptually similar

occlusion processes. The narrative of the Selden tornadoes that emerged from this study was based mostly on kinematic arguments, owing to the nature of the available data; there were certainly contributions to tornado behavior from thermodynamic or dynamic processes which could not be analyzed or investigated.

Over its roughly 35-minute life, the Selden tornado exhibited a plethora of behavioral changes and track shifts. RaXPol began observing the tornado at 2305 UTC, shortly after its genesis. During the early portions of the tornado's development, evidence was found for a near simultaneous or ascending pattern of intensification, such as been found in studies that focus on tornadogenesis such as Houser et al. (2022). Additionally, the tornado became less coherent above the 2 to 2.5 km level, reflecting observations in Houser et al. (2022) that tornadoes may not be very deep. This finding was postulated to be the result of the low shear synoptic environment. Through the first several minutes of the tornado lifespan, the supercell RFD continued to intensify, and the tornado turned slightly to the right as it reached its 'mature' position relative to the parent supercell (e.g., Dowell and Bluestein 2002; French et al. 2014). Additionally, the forward flank convergence boundary, which was not well established at the onset of the tornado, became rooted to the tornadic circulation by 2307 UTC. Consequently, the Selden tornado began to intensify while it maintained an advantageous position near the apex of the surface boundaries underneath the storm updraft.

While the Selden tornado was reaching a mature phase as described by numerous studies (e.g., Dowell and Bluestein 2002; Marquis et al. 2012; 2016), RFD momentum surges were also ongoing. Yet, the momentum associated with the surges was not yet enough to alter the tornado's course as in Kurdzo et al. (2015) or Lee and Finley (2022).

Also leading up to the D6 data gap, a DRC fitting the definition in Rasmussen et al. (2006) was identified. The impacts of this DRC are unknown as data collection stopped before the DRC reached the ground, but it appears to match the criteria for a category 1 DRC from Byko et al. (2009); the DRC may have had a significant impact on the tornado once reaching the surface. An additional finding from the early stages of the Selden tornado was that the averaged cross sections revealed a much wider vortex than in previous studies where cross sections were constructed. Because the cross sections were produced from the raw Doppler velocity field and not from GBVTD analysis as in Kosiba and Wurman (2010), Tanamachi et al. (2007), or Wakimoto et al. (2012), the tornadic circulation was not filtered or isolated and flow fields of larger scale circulations, such as the supercell mesocyclone, superimposed with the tornado. Consequently, winds in the azimuthal cross sections did not fall off exponentially outside the RMW and the indicated RMW was shifted outwards.

Immediately after data collection restarts following the D6 data gap at 2316 UTC, the tornado appears to be exiting a potential track loop. Although the D6 data gap precludes a definitive conclusion, the Selden tornado may have executed a track loop at the end of the data gap and exited it shortly after data collection restarted. An RFD surge present at the start of data collection after the data gap is supportive of the occurrence of a track loop, appearing in a similar position as the second RFD surge in the track loop conceptual model in Kurdzo et al. (2015) that causes the tornado to exit a loop. Analysis also indicates that the loop was most defined aloft, highlighting the subtleties inherent in small scale RFD surges; RFD surges have varying vertical extents, follow different trajectories, are

associated with widely varying magnitudes of enhanced momentum, and contain air with vastly different thermodynamic qualities (Finley and Lee 2004; 2008; Lee et al. 2004).

Shortly after 2318 UTC, the tornado undergoes a multiple vortex transition. Secondary vortices were observed both visually and in radar data, often displaying great shear magnitudes over incredibly small distances, matching the description of secondary vortices in Wurman (2002). The multiple vortex transition was coincident with a temporary but significant inflow disruption like in Marquis et al. (2008), which was instigated by an RFD surge that had been advected by the tornado circulation to the northern flank of the tornado where the RFGF was temporarily displaced from the tornado. Similar behavior has been noted by previous studies, such as Marquis et al. (2016) and Skinner et al. (2014), but a temporary and rapid inflow disruption tied to a multiple vortex transition has not been specifically documented before. When the tornado became briefly enveloped in outflow air, the swirl ratio of the tornadic circulation increased because radial inflow decreased as the tornado updraft struggled to lift less buoyant air, leading to a multiple vortex transition (Rotunno 1984). Shortly after multiple vortex transition, the inflow recovers and is no longer blocked, but the tornado remains a multiple vortex tornado. This was postulated to be the result of the tornado's central pressure; because of the tornado's larger size and an attendant decrease in the centrifugal force, the tornado's central pressure was not as low and was unable to drive enough vortex radial inflow to decrease the swirl ratio even after the tornado was no longer entirely enveloped in RFD air.

In between the D6 data gap and the end of D6 (2316 to 2319 UTC), another DRC was identified in the RaXPol data. This time, the DRC was able to reach the ground before data collection ended and a small increase in velocities on the side of the tornado closest

to the DRC was observed in the lowest scan elevation. While this would be expected since the DRC again fits the type 1 DRC definition from Byko et al. (2009), the lower limit of observations hinders the ability to make a definitive conclusion. Finally, with the tornado and forward flank at favorable angles from the radar and the supercell in a mature phase, reconstructed RHIs were made to search for a possible SVC. A small core of enhanced streamwise vorticity was found, particularly at the very end of D6 at 2319 UTC. The core of streamwise vorticity had a magnitude of approximately 0.15 s^{-1} and was located at roughly 600 m ARL right above the forward flank outflow just upwind of the tornado, which is in good agreement with models and observations of the SVC in Orf et al. (2017) and Schueth et al. (2021). However, the averaged RHI results were found to reflect more the presence of a density current rather than an SVC; the SVC is likely a transient structure that occurs in the heads of Kelvin-Helmholtz waves associated with the baroclinicity of the forward flank and is not a steady structure. Therefore, the average RHI plots do not reveal a defined SVC but simply reveal the defined density current associated with the forward flank cold pool, although, there are no temperature data to confirm this.

After a nearly 7-minute gap, D7 begins at 2326 UTC. Early in D7, the Selden tornado executes a cyclonic track loop. The track loop was accompanied by a configuration of surges that closely matches the model offered in Kurdzo et al. (2015). However, in the Kurdzo et al. (2015) case, the tornado ejected from the track loop to the right of the tornado's initial heading, preventing occlusion from taking place; in the Selden case, the tornado ejects from the loop on a similar heading to what it had before, and occlusion occurs. Immediately following the early D7 track loop a 'rogue' anticyclonic vortex appeared and orbited the Selden tornado. Although the origins of the vortex remain

uncertain due to the lack of data in between deployments, the ‘rogue’ anticyclonic vortex appears to be a satellite of the Selden tornado (e.g., Tanamachi et al. 2012).

At 2329 UTC, the tornado becomes occluded in response to a particularly strong RFD surge that had impinged north of the tornado. The appearance of significant surging momentum and potent RFD surges during segments 3 and 4 are likely the result of the occlusion downdraft, and by late segment 4, the surging momentum causes occlusion as the RFGF is displaced from the tornado and the two decouple from each other (e.g., Skinner et al. 2014). While small track deviations continue to occur, the trend of the tornado is to start moving rearward into the parent supercell now that the tornado is no longer coupled to the RFGF (Dowell and Bluestein 2002; French et al. 2014). Furthermore, since the tornado was severed from its more buoyant inflow and is being displaced from the zone of enhanced surface vorticity and convergence associated with the RFGF and forward flank boundary, it begins to slowly decay (Dowell and Bluestein 2002). Finally, the Selden tornado reverts to a single celled vortex, likely because of a decreasing swirl ratio resulting from azimuthal winds weakening at a greater pace than radial inflow.

After the Selden tornado begins occluding at 2329 UTC, the behavior of the vortex becomes disparate with height. At lower scan elevations, the tornado ejected rapidly east from the track loop on an RFD surge before suddenly stopping as momentum built on the northern flank of the tornado. Momentum continued to build on the tornado’s northern flank, eventually causing the tornado to retrograde starting at 2332 UTC. Finley and Lee (2022) documented a similar trend in which they observed tornadoes to undergo sharp track shifts when strong surges occurred and transported enhanced momentum around the tornadoes. After retrograding for about 2.5 minutes, the tornado then turns north because

of bounding momentum changes caused by another surge. Meanwhile, at higher scan elevations, the tornado ejected from the first track loop on a more northeasterly heading as the result of differences in the configuration of RFD surges aloft relative to the tornado. Then, the tornado underwent another track loop at upper levels at the same time as the tornado was retrograding and turning north at lower levels. Once again, the configuration of momentum proximate the tornado at upper scan elevations was like that in the Kurdzo et al. (2015) model.

Subsequent the second cyclonic track loop, the track of the Selden tornado once again becomes unified with height. At 2335 UTC as the tornado starts tracking north northeastward, a WRB appears in lower elevation scans; the WRB lasts for about 3 minutes, is narrow, and seems to cause a brief intensification of the tornado. While the observed WRB feature behaves largely like that in Houser et al. (2016), its formation appears to have occurred due to the positioning of 2 RFD surges, which was not noted in Houser et al. (2016). After the WRB dissipates, the Selden tornado begins to rapidly decay as the occlusion process completes; the tornado and low-level mesocyclone migrate into active downdraft areas and the tornado dissipates over a short time of roughly 1.5 minutes, completely disappearing by 2341 UTC.

Shortly after the start of D7 at 2326 UTC, a companion anticyclonic tornado developed to the southeast of the primary Selden tornado on the opposite side of the supercell RFD. Aligning with formation mechanism 2 from Bluestein et al. (2016), a strong RFD surge impinged on the southern flank of the RFGF instigating vortex genesis. However, it also appears that vortex arches from the RFD contributed to genesis (Bluestein et al. 2016; Markowski and Richardson 2009). Although vorticity from RFD vortex ring

tilting appears to be required for anticyclonic tornadogenesis, it only predisposes the environment to the possibility of anticyclonic tornadogenesis and is incapable of forming a tornado without additional vorticity contributions. Consequently, it appears that additional anticyclonic vorticity on the right side of a strong RFD surge is critical for anticyclonic tornadogenesis, a possible explanation for the rarity of companion anticyclonic tornadoes. Further studies are needed to validate this important finding; the requirement for RFD surge vorticity for companion anticyclonic tornado formation can help to explain the frequency of these types of tornadoes and has ramifications on their predictability.

After formation, the anticyclonic tornado established its own inflow notch and the RFGF became rooted to the tornado in a similar fashion as the cyclonic tornado. However, the anticyclonic vortex began to occlude rather quickly, as the occlusion downdraft likely formed due to the rapid onset of a downward directed dynamically driven pressure gradient force. Since there is no significant mid-level vorticity above the anticyclonic tornado as there is for the cyclonic tornado, vorticity near the surface quickly surpassed that aloft. All tornadoes are subject to this to some degree, since the existence of a strong circulation necessitates strong vorticity near the ground that is always threatening to exceed the vorticity aloft and drive the creation of the occlusion downdraft. Over the course of roughly 15 minutes, the anticyclonic vortex rapidly reaches a peak intensity just under tornadic thresholds and then steadily occludes, nearly completely dissipating by the end of D7 at 2343 UTC.

Thorough analysis of the Selden tornado's lifecycle prompts several points of discussion. First is the feasibility of using RFD surges to anticipate changes in tornado

motion in the near term to update NWS tornado warnings. A building number of cases show that RFD surges have a demonstrable effect on tornado behavior, and that the effect of any given surge or configuration of surges is at least somewhat predictable; the tornado tends to move in the same direction that the surge is moving. For example, Finley and Lee (2022) found that tornadoes turned significantly left when RFD surges passed in front of a tornado as they moved around the circulation; as surges passed from right to left in front of the tornado, they encouraged leftward motion with respect to the tornado track. Kurdzo et al. (2015) also showed that a specific arrangement of RFD surges can cause a tornado to execute a track loop. Similar patterns of behavior were documented with the Selden tornado, such as the observation that two RFD surges oriented 90° clockwise from each other about a tornado can cause a track loop to occur; however, the sample size of cases is not yet high enough to make generalizing conclusions. There are innumerable arrangements of RFD surges that could cause different tornado tracks, or perhaps, lead to a similar pattern of motion. The response of a tornado to an RFD surge also depends greatly on the surge trajectory and strength, which cover a wide spectrum (Finley and Lee 2004; 2008; Lee et al. 2004). Many more studies will need to be conducted on high resolution radar and thermodynamic data sets to begin ascertaining a true picture of RFD surges. Moreover, RFD surges are small features, requiring high resolution radar observations to detect. NEXRAD WSR-88D radars are simply too far from many storms to provide the necessary fidelity of measurement at heights close enough to the ground to capture all RFD surges.

A second key area of discussion that is related to using RFD surges to anticipate tornado behavior changes is how and why RFD surges form and where they originate.

Numerous studies have investigated the impacts of RFD surges on tornado behavior and lifecycle, and some have focused on the properties of surges directly (e.g., Finley and Lee 2004; 2008; Lee and Finley 2022; Kurdzo et al. 2015; Lee et al. 2004). However, the origin and formation processes for surges are still not well understood. One specific formation mechanism for RFD surges which was found in Skinner et al. (2014) and was also supported by this study was the occlusion downdraft. When the occlusion downdraft reaches the surface and generates outflow, RFD surges are generated; Figure 5.4 presents a conceptual model of this process. Another likely culprit are DRCs, which likely generate surges when they reach the surface and spread outwards; significant near-surface convergence is observed with DRCs in RFD surge-like bands (e.g., Rasmussen et al 2006 or Byko et al 2009). However, RFD surges of widely variable trajectory, source region, strength, and duration were noted in this study, highlighting the reality that RFD surges can result from many formation mechanisms. Furthermore, RFD surges have been observed to accompany air with a wide range of thermodynamic qualities, suggesting a wide range of different formation mechanisms.

While RFD surge formation is not yet fully understood, some possibilities are mentioned here. Perhaps most simply, higher momentum could be briefly mixed downwards to the surface from aloft, generating a surge. The storm could also advect higher momentum from aloft to the surface. Since downdrafts are largely driven by precipitation processes, it also stands to reason that local or short-lived perturbations to them could generate RFD surges. For instance, a brief increase in evaporative cooling as precipitation falls into dry air would briefly enhance the RFD locally as the air becomes even more negatively buoyant than the air immediately surrounding it. Additionally, a

simple increase in precipitation loading could also locally enhance the RFD and generate a surge. Vorticity near the surface within the RFD could also play a role. If a horizontal buoyancy gradient develops, then horizontal vorticity is generated, and the horizontal circulation creates enhanced momentum within the RFD near the surface if the circulation has the correct sense. Existing vertical vorticity could also be tilted into the horizontal near the surface for the same effect. Finally, an enhancement of the surface pressure gradient between the storm cold pool and updraft region could result in the generation of an RFD surge. This would require an intensification of either the supercell updraft, RFD, or both. Further work will be required to investigate these mechanisms. However, to investigate these mechanisms, it may be necessary to complete very high-resolution simulations or collect 3-dimensional observations of a supercell and its RFD, which may be out of reach given current technological limitations.

Finally, the spectrum of anticyclonic vortex behavior observed in this study warrants further investigation. Despite the relative unremarkable nature of the Selden case (the tornado was not particularly strong or violent), two entirely different anticyclonic vortices were found. The first vortex appeared to be a satellite tornado consistent with Tanamachi et al. (2012), but its origins are unknown. Only a few minutes after the first vortex appears, a second anticyclonic vortex undergoes genesis. However, this vortex is in an entirely different location in the storm and behaves dissimilarly to the first vortex; the vortex is a companion anticyclonic tornado fitting the description in Bluestein et al. (2016). Perhaps the most important finding in this study was that an RFD surge was observed to instigate the genesis of the companion anticyclonic tornado, and that the companion anticyclonic tornado only formed once the RFD surge vorticity added to the weak ambient

vorticity from RFD vortex ring. Studies focusing on anticyclonic tornadoes and the different types observed in cyclonic supercells need to be completed to answer questions concerning frequency, formation, and impacts on the primary cyclonic tornado. These questions are particularly salient for companion anticyclonic tornadoes, which can attain significant intensity on occasion (Bluestein et al. 2018) and are often difficult to anticipate owing to the potential role of RFD surges in their formation (Bluestein et al. 2016, Finley and Lee 2008). The two formation mechanisms given in Bluestein et al. (2016) certainly play a role in companion anticyclonic tornadogenesis as was seen in this study, but it remains unclear as to why some cyclonic supercells have companion anticyclonic tornadoes and others do not especially since RFD surges remain only partially understood.

There remains ample room for additional work surrounding the features identified in this study. As previously discussed, RFD surges remain poorly understood; questions regarding origins, frequency, and range of impacts on tornadoes are remain unanswered. Different types of studies, including simulation based and observational must be completed. However, some of the work that should be done, such as attaining full high-resolution 3-dimensional observations of an entire supercell RFD, remains out of reach. Yet, additional datasets become available from mobile weather radars every year, which are waiting to be analyzed. To further understanding of how RFD surges impact tornado behavior as well as to investigate the numerous other features identified in this study and others that may or may not yet have been discovered, these cases need to be analyzed. Polarimetric variables should also be considered to grasp a complete picture of a storm; for instance, microphysical information from polarimetric moments may reveal RFD surge formation mechanisms or highlight additional features. Furthermore, consideration should

be given to attempt dual Doppler analyses wherever possible to yield the full 2-dimensional horizontal velocities that make RFD surges much easier to discern, thereby increasing the accuracy and potential value of a study. Most importantly, this study focused on a kinematic explanation of tornado behavior. Thermodynamic processes, while certainly important to the behavior of tornadoes, were not a focus of this study owing to a complete lack of thermodynamic data. Furthermore, the occlusion of tornadoes is not a totally understood process (Adlerman and Droegemeier 2005). While RFD surges and the occlusion downdraft appear to play a large role in the occlusion process, it is possible that other mechanisms on multiple scales, from the synoptic environment down to the tornado itself, exert considerable influence on the occlusion process.

Bibliography

SPC Severe Weather Events Archive. Storm Prediction Center. https://www.spc.noaa.gov/exper/archive/events/ (Accessed October 27, 2022).

Adlerman, E. J., R. Davies-Jones, and K. K. Droegemeier, 1999: A numerical simulation of cyclic mesocyclogenesis. *J. Atmos. Sci.*, **56,** 2045-2069, https://doi.org/10.1175/1520-0469(1999)056%3C2045:ANSOCM%3E2.0.CO;2

Adlerman, E. J., and K. K. Droegemeier, 2005: The dependence of numerically simulated cyclic mesocyclongenesis upon environmental vertical wind shear. *Mon. Wea. Rev.*, **133,** 3595-3623, https://doi.org/10.1175/MWR3039.1.

Beck, J. R., J. L. Schroeder, and J. M. Wurman, 2006: High-resolution dual-Doppler analyses of the 29 May 2001 Kress, Texas, cyclic supercell. *Mon. Wea. Rev.*, **134,** 3125-3148, https://doi.org/10.1175/MWR3246.1.

Bluestein, H. B., 2013: *Severe Convective Storms and Tornadoes.* Springer-Praxis Books, Chichester, United Kingdom, 482 pp.

Bluestein, H. B., M. M. French, I. PopStefanija, R. T. Bluth, and J. B. Knorr, 2010: A mobile, phased-array Doppler radar for the study of severe convective storms: the MWR-05XP. *Bull. Amer. Meteor. Soc.*, **91,** 579-600, https://doi.org/10.1175/2009BAMS2914.1.

Bluestein, H. B., M. M. French, J. C. Snyder, and J. B. Houser, 2016: Doppler radar observations of anticyclonic tornadoes in cyclonically rotating, right-moving supercells. *Mon. Wea. Rev.*, **144,** 1591-1616, https://doi.org/10.1175/MWR-D-15-0304.1.

Bluestein, H. B., M. M. French, R. L. Tanamachi, S. Frasier, K. Hardwick, F. Junyent, and A. L. Pazmany, 2007a: Close-range observations of tornadoes in supercells made with a dual-polarization, X-band, mobile Doppler radar. *Mon. Wea. Rev.*, **135,** 1522–1543, https://doi.org/10.1175/MWR3349.1.

Bluestein, H. B., J. G. Ladue, H. Stein, D. Speheger, and W. F. Unruh, 1993: Doppler radar wind spectra of Supercell Tornadoes. *Mon. Wea. Rev.*, **121,** 2200-2222, https://doi.org/10.1175/1520-0493(1993)121%3C2200:DRWSOS%3E2.0.CO;2.

Bluestein, H. B., and A. L. Pazmany, 2000: Observations of tornadoes and other convective phenomena with a mobile, 3-mm wavelength, Doppler radar: the spring 1999 field experiment. *Bull. Amer. Meteor. Soc.*, **81,** 2939-2952, https://doi.org/10.1175/1520-0477(2000)081%3C2939:OOTAOC%3E2.3.CO;2.

Bluestein, H. B., A. L. Pazmany, J. C. Galloway, and R. E. McIntosh, 1995: Studies of the substructure of severe convective storms using a mobile 3-mm-wavelength Doppler radar. *Bull. Amer. Meteor. Soc.*, **76,** 2155-2170, https://doi.org/10.1175/1520-0477(1995)076%3C2155:SOTSOS%3E2.0.CO;2.

Bluestein, H. B., J. C. Snyder, and J. B. Houser, 2015: A multiscale overview of the El Reno, Oklahoma, tornadic supercell of 31 May 2013. *Wea. Forecasting*, **30,** 525-552, https://doi.org/10.1175/WAF-D-14-00152.1.

Bluestein, H. B., K. J. Thiem, J. C. Snyder, and J. B. Houser, 2018: The multiple-vortex structure of the El Reno, Oklahoma, tornado on 31 May 2013. *Mon. Wea. Rev.*, **146,** 2483-2502, https://doi.org/10.1175/MWR-D-18-0073.1.

Bluestein, H. B., K. J. Thiem, J. C. Snyder, and J. B. Houser, 2019: Tornadogenesis and early tornado evolution in the El Reno, Oklahoma, supercell on 31 May 2013. *Mon. Wea. Rev.*, **147,** 2045-2066, https://doi.org/10.1175/MWR-D-18-0338.1.

Bluestein, H. B., and W. F. Unruh, 1989: Observations of the wind field in tornadoes, funnel clouds, and wall clouds with a portable Doppler radar. *Bull. Amer. Meteor. Soc.*, **70,** 1514-1525, https://doi.org/10.1175/1520-0477(1989)070%3C1514:OOTWFI%3E2.0.CO;2.

Bluestein, H. B., C. C. Weiss, M. M. French, E. M. Holthaus, R. L. Tanamachi, S. Frasier, and A. L. Pazmany, 2007b: The structure of tornadoes near Attica, Kansas, on 12 May 2004: High-resolution, mobile, Doppler radar observations. *Mon. Wea. Rev.*, **135,** 475–506, https://doi.org/10.1175/MWR3295.1.

Bluestein, H. B., C. C. Weiss, and A. L. Pazmany, 2003: Mobile Doppler radar observations of a tornado in a supercell near Bassett, Nebraska, on 5 June 1999. Part I: Tornadogenesis. *Mon. Wea. Rev.*, **131,** 2954-2967, https://doi.org/10.1175/1520-0493(2003)131%3C2954:MDROOA%3E2.0.CO;2.

Bluestein, H. B., C. C. Weiss, and A. L. Pazmany, 2004: The vertical structure of a tornado near Happy, Texas, on 5 May 2002: High-resolution, mobile, W-band, Doppler radar observations. *Mon. Wea. Rev.*, **132,** 2325–2337, https://doi.org/10.1175/1520-0493(2004)132<2325:TVSOAT>2.0.CO;2.

Brandes, E. A., 1981: Finestructure of the Del City-Edmond tornadic mesocirculation. *Mon. Wea. Rev.*, **109,** 635-647, https://doi.org/10.1175/1520-0493(1981)109%3C0635:FOTDCE%3E2.0.CO;2.

Burgess, D. W., M. A. Magsig, J. Wurman, D. C. Dowell, and Y. Richardson, 2002: Radar observations of the 3 May 1999 Oklahoma City tornado. *Wea. Forecasting*, **17,** 456-471, https://doi.org/10.1175/1520-0434(2002)017%3C0456:ROOTMO%3E2.0.CO;2.

Byko, Z., P. Markowski, Y. Richardson, J. Wurman, and E. Adlerman, 2009: Descending reflectivity cores in supercell thunderstorms observed by mobile radars in a high-resolution numerical simulation. *Wea. Forecasting*, **24,** 155-186, https://doi.org/10.1175/2008WAF2222116.1.

Dowell, D. C., and H. B. Bluestein, 2002: The 8 June 1995 McLean, Texas, storm. Part II: Cyclic tornado formation, maintenance, and dissipation. *Mon. Wea. Rev.*, **130,** 2649–2670, https://doi.org/10.1175/1520-0493(2002)130<2649:TJMTSP>2.0.CO;2.

Doviak, R. J., and D. S. Zrnić, 1993: *Doppler Radar and Weather Observations.* 2nd ed. Dover Publications, Mineola, NY, 562 pp.

Davies-Jones, R., 1984: Streamwise vorticity: The origin of updraft rotation in supercell storms. *J. Atmos. Sci.*, **41,** 2991-3006, https://doi.org/10.1175/1520-0469(1984)041%3C2991:SVTOOU%3E2.0.CO;2.

Finley, C. A., and B. D. Lee, 2004: High resolution mobile mesonet observations of RFD surges in the June 9 Basset, Nebraska supercell during Project ANSWERS 2003. *22nd Conf. on Severe Local Storms*, Hyannis, MA, Amer. Meteor. Soc., P11.3, https://ams.confex.com/ams/11aram22sls/webprogram/Paper82005.html.

Finley, C. A., and B. D. Lee, 2008: Mobile mesonet observations of an intense RFD and multiple RFD gust fronts in the May 23 Quinter, Kansas tornadic supercell during TWISTEX 2008. *24th Conf. on Severe Local Storms*, Savannah, GA, Amer. Meteor. Soc., P3.18, https://ams.confex.com/ams/24SLS/techprogram/paper_142133.htm.

French, M. M., H. B. Bluestein, I. PopStefanija, C. A. Baldi, and R. T. Bluth, 2014: Mobile, phased-array, Doppler radar observations of tornadoes at X-band. *Mon. Wea. Rev.*, **142,** 1010-1036, https://doi.org/10.1175/MWR-D-13-00101.1.

Fujita, T. T., D. L. Bradbury, and C. F. Van Thullenar, 1970: Palm Sunday tornadoes of April 11, 1965. *Mon. Wea. Rev.*, **98,** 29-69, https://doi.org/10.1175/1520-0493(1970)098%3C0029:PSTOA%3E2.3.CO;2.

Fujita, T. T., 1981: Tornadoes and downbursts in the context of generalized planetary scales. *J. Atmos. Sci.*, **38,** 1511-1534, https://doi.org/10.1175/1520-0469(1981)038%3C1511:TADITC%3E2.0.CO;2.

Grazulis, T. P., 2001: *The Tornado: Nature's Ultimate Windstorm*. University of Oklahoma Press, Norman, OK, 315 pp.

Greenwood, T., 2021: Analysis of tornadic supercells using two rapid-scan, mobile Doppler radars. University of Oklahoma School of Meteorology.

Griffin, C. B., C. C. Weiss, A. E. Reinhart, J. C. Snyder, H. B. Bluestein, J. Wurman, and K. A. Kosiba, 2018: In situ and radar observations of the low reflectivity ribbon in supercells during VORTEX2. *Mon. Wea. Rev.*, **146,** 307-327, https://doi.org/10.1175/MWR-D-17-0201.1.

Grzych, M. L., B. D. Lee, and C. A. Finley, 2007: Thermodynamic analysis of supercell rear-flank downdrafts from project ANSWERS. *Mon. Wea. Rev.*, **135,** 240–246, https://doi.org/10.1175/MWR3288.1.

Hirth, B. D., J. L. Schroeder, and C. C. Weiss, 2008: Surface analysis of the rear-flank downdraft outflow in two tornadic supercells. *Mon. Wea. Rev.*, **136,** 2344–2363, https://doi.org/10.1175/2007MWR2285.1.

Houser, J. L., H. B. Bluestein, and J. C. Snyder, 2015: Rapid-scan, polarimetric, Doppler radar observations of tornadogenesis and tornado dissipation in a tornadic supercell: The "El Reno, Oklahoma" storm of 24 May 2011. *Mon. Wea. Rev.*, **143,** 2685-2710, https://doi.org/10.1175/MWR-D-14-00253.1.

Houser, J. L., H. B. Bluestein, and J. C. Snyder, 2016: A finescale radar examination of the tornadic debris signature and weak-echo reflectivity band associated with a large, violent tornado. *Mon. Wea. Rev.*, **144,** 4101-4130, https://doi.org/10.1175/MWR-D-15-0408.1.

Houser, J. L., H. B. Bluestein, K. Thiem, J. C. Snyder, D. W. Reif, and Z. B. Wienhoff, 2022: Additional evaluation of the spatiotemporal evolution of rotation during tornadogenesis using rapid-scan mobile radar observations. *Mon. Wea. Rev.*, **150,** 1639-1666, https://doi.org/10.1175/MWR-D-21-0227.1.

Klemp, J. B., 1987: Dynamics of tornadic thunderstorms. *Annu. Rev. Fluid Mech.,* **19,** 369-402, https://doi.org/10.1146/annurev-fluid-011212-140639.

Klemp, J. B., and R. Rotunno, 1983: A study of the tornadic region within a supercell thunderstorm. *J. Atmos. Sci.,* **40,** 359-377, https://doi.org/10.1175/1520-0469(1983)040%3C0359:ASOTTR%3E2.0.CO;2.

Klemp, J. B., R. B. Wilhelmson, and P. S. Ray, 1981: Observed and numerically simulated structure of a mature supercell thunderstorm. *J. Atmos. Sci.*, **38,** 1558-1580, https://doi.org/10.1175/1520-0469(1981)038%3C1558:OANSSO%3E2.0.CO;2.

Kosiba, K., and J. Wurman, 2010: The three-dimensional axisymmetric wind field structure of the Spencer, South Dakota, 1998 tornado. *J. Atmos. Sci.*, **67,** 3074-3083, https://doi.org/10.1175/2010JAS3416.1.

Kosiba, K., and J. Wurman, 2013: The three-dimensional structure and evolution of a tornado boundary layer. *Wea. Forecasting*, **28,** 1552-1561, https://doi.org/10.1175/WAF-D-13-00070.1.

Kosiba, K., J. Wurman, Y. Richardson, P. Markowski, P. Robinson, and J. Marquis, 2013: Genesis of the Goshen County, Wyoming, tornado on 5 June 2009 during VORTEX2. *Mon. Wea. Rev.*, **141,** 1157-1181, https://doi.org/10.1175/MWR-D-12-00056.1.

Kumjian, M. R., and A. V. Ryzhkov, 2008: Polarimetric signatures in supercell thunderstorms. *J. Appl. Meteor. Climatol.*, **47,** 1940–1961, https://doi.org/10.1175/2007JAMC1874.1.

Kurdzo, J. M., D. J. Bodine, B. L. Cheong, and R. D. Palmer, 2015: High-temporal resolution polarimetric X-band Doppler radar observations of the 20 May 2013 Moore, Oklahoma, tornado. *Mon. Wea. Rev.,* **143,** 2711-2735, https://doi.org/10.1175/MWR-D-14-00357.1.

Lee, B. D. and C. A. Finley, 2022: Tornado heading and speed changes associated with large and intense internal rear-flank surges in three supercells. *Wea. Forecasting*, **37**, 915-934, https://doi.org/10.1175/WAF-D-21-0174.1.

Lee, B. D., C. A. Finley, and C. D. Karstens, 2012: The Bowdle, South Dakota, cyclic tornadic supercell of 22 May 2010: Surface analysis of rear-flank downdraft evolution and multiple internal surges. *Mon. Wea. Rev.*, **140,** 3419-3441, https://doi.org/10.1175/MWR-D-11-00351.1.

Lee, B. D., C. A. Finley, and P. S. Skinner, 2004: Thermodynamic and kinematic analysis of multiple RFD surges for the 24 June 2003 Manchester, SD, cyclic tornadic supercell during Project ANSWERS 2003. *22nd Conf. on Severe Local Storms*, Hyannis, MA, Amer. Meteor. Soc., P11.2, https://ams.confex.com/ams/11aram22sls/webprogram/Paper82000.html.

Lee, W. C., B. J. D. Jou, P. L. Chang, and S. M. Deng, 1999: Tropical cyclone kinematic structure retrieved from single-Doppler radar observations. Part I: Interpretation of Doppler velocity patterns and the GBVTD technique. *Mon. Wea. Rev.*, **127,** 2419-2439, https://doi.org/10.1175/1520-0493(1999)127%3C2419:TCKSRF%3E2.0.CO;2.

Lemon, R. L., and C. A. Doswell III, 1979: Severe thunderstorm evolution and mesocyclone structure as related to tornadogenesis. *Mon. Wea. Rev.*, **107,** 1184-1197, https://doi.org/10.1175/1520-0493(1979)107%3C1184:STEAMS%3E2.0.CO;2.

Lewellen, D. C., W. S. Lewellen, and J. Xia, 2000: The influence of a local swirl ratio on tornado intensification near the surface. *J. Atmos. Sci.*, **57,** 527–544, https://doi.org/10.1175/1520-0469(2000)057<0527:TIOALS>2.0.CO;2.

Markowski, P. M., and Coauthors, 2012: The pretornadic phase of the Goshen County, Wyoming, supercell of June 2009 intercepted by VORTEX2. Part I: Evolution of kinematic and surface thermodynamic fields. *Mon. Wea. Rev.*, **140,** 2887-2915, https://doi.org/10.1175/MWR-D-11-00336.1.

Markowski, P. M., J. M. Straka, and E. N. Rasmussen, 2002: Direct surface thermodynamic observations within the rear-flank downdrafts of nontornadic and tornadic supercells. *Mon. Wea. Rev.*, **130,** 1692-1721, https://doi.org/10.1175/1520-0493(2002)130%3C1692:DSTOWT%3E2.0.CO;2.

Markowski, P. M., and Y. P. Richardson, 2009: Tornadogenesis: Our current understanding, forecasting considerations, and questions to guide future research. *Atmospheric Research*, **93,** 3-10, https://doi.org/10.1016/j.atmosres.2008.09.015.

Markowski, P., Y. Richardson, E. Rasmussen, J. Straka, R. Davies-Jones, and R. J. Trapp, 2008: Vortex lines within low-level mesocyclones obtained from pseudo-dual-Doppler radar observations. *Mon. Wea. Rev.*, **136,** 3513-3535, https://doi.org/10.1175/2008MWR2315.1.

Marquis, J., Y. Richardson, P. Markowski, D. Dowell, and J. Wurman, 2012: Tornado maintenance investigated with high-resolution dual-Doppler and EnKF analysis. *Mon. Wea. Rev.*, **140,** 3-27, https://doi.org/10.1175/MWR-D-11-00025.1.

Marquis, J., Y. Richardson, P. Markowski, J. Wurman, K. Kosiba, and P. Robinson, 2016: An investigation of the Goshen County, Wyoming, tornadic supercell of 5 June 2009 using EnKF assimilation of mobile mesonet and radar observations collected during VORTEX2. Part II: Mesocyclone-scale processes affecting tornado formation, maintenance, and decay. *Mon. Wea. Rev.*, **144,** 3441-3463, https://doi.org/10.1175/MWR-D-15-0411.1.

Marquis, J., Y. Richardson, J. Wurman, and P. Markowski, 2008: Single- and dual-Doppler analysis of a tornadic vortex and surrounding storm-scale flow in the Crowell, Texas, supercell of 30 April 2000. *Mon. Wea. Rev.*, **136,** 5017-5043, https://doi.org/10.1175/2008MWR2442.1.

McKeown, K. E., M. M. French, K. S. Tuftedal, D. M. Kingfield, H. B. Bluestein, D. W. Rief, and Z. B. Wienhoff, 2020: Rapid-scan and polarimetric radar observations of the dissipation of a violent tornado on 9 May 2016 near Sulphur, Oklahoma. *Mon. Wea. Rev.*, **148,** 3951-3971, https://doi.org/10.1175/MWR-D-20-0033.1.

Nixon, C. J., and J. T. Allen, 2021: Anticipating deviant tornado motion using a simple hodograph technique. *Wea. Forecasting*, **36,** 219–235, https://doi.org/10.1175/WAF-D-20-0056.1.

Orf, L., R. Wilhelmson, B. Lee, C. Finley, and A. Houston, 2017: Evolution of a long-track violent tornado within a simulated supercell. *Bull. Amer. Meteor. Soc.*, **98,** 45-68, https://doi.org/10.1175/BAMS-D-15-00073.1.

Oye, R., C. Mueller, and S. Smith, 1995: Software for radar translation, visualization, editing, and interpolation. *27th Conf. on Radar Meteorology*, Vail, CO, Amer. Meteor. Soc., 359–361.

Pazmany, A. L., J. B. Mead, H. B. Bluestein, J. C. Snyder, and J. B. Houser, 2013: A mobile rapid-scanning X-band polarimetric (RaXPol) Doppler radar system. *J. Atmos. Oceanic Technol.*, **30,** 1398-1413, https://doi.org/10.1175/JTECH-D-12-00166.1.

Rasmussen, E. N., J. M. Straka, M. S. Gilmore, and R. Davies-Jones, 2006: A preliminary survey of rear-flank descending reflectivity cores in supercell storms. *Wea. Forecasting*, **21,** 923-938, https://doi.org/10.1175/WAF962.1.

Rotunno, R., 1984: An investigation of a three-dimensional asymmetric vortex. *J. Atmos. Sci.*, **41,** 283–298, https://doi.org/10.1175/1520-0469(1984)041<0283:AIOATD>2.0.CO;2.

Rotunno, R., 2013: The fluid dynamics of tornadoes. *Annu. Rev. Fluid Mech.*, **45,** 59–84, https://doi.org/10.1146/annurev-fluid-011212-140639.

Rotunno, R., and J. Klemp, 1985: On the rotation and propagation of simulated supercell thunderstorms. *J. Atmos. Sci.*, **42,** 271-292, https://doi.org/10.1175/1520-0469(1985)042%3C0271:OTRAPO%3E2.0.CO;2.

Rotunno, R., P. M. Markowski, and G. H. Bryan, 2017: "Near ground" vertical vorticity in supercell thunderstorm models. *J. Atmos. Sci.*, **74,** 1757-1766, https://doi.org/10.1175/JAS-D-16-0288.1.

Ryzhkov, A. V., T. J. Schuur, D. W. Burgess, and D. S. Zrnic, 2005: Polarimetric tornado detection. *J. Appl. Meteor.*, **44,** 557–570, https://doi.org/10.1175/JAM2235.1.

Scheuth, A., C. Weiss, and J. M. L. Dahl, 2021: Comparing observations and simulations of the streamwise vorticity current and the forward-flank convergence boundary in a supercell storm. *Mon. Wea. Rev.*, **149,** 1651-1671, https://doi.org/10.1175/MWR-D-20-0251.1.

Skinner, P. S., C. C. Weiss, M. M. French, H. B. Bluestein, P. M. Markowski, and Y. P. Richardson, 2014: VORTEX2 observations of a low-level mesocyclone with multiple internal rear-flank downdraft momentum surges in the 18 May 2010 Dumas, Texas, supercell. *Mon. Wea. Rev.*, **142,** 2935-2960, https://doi.org/10.1175/MWR-D-13-00240.1.

Snyder, J. C., and H. B. Bluestein, 2014: Some considerations for the use of high-resolution mobile radar data in tornado intensity determination. *Wea. Forecasting*, **29,** 799-827, https://doi.org/10.1175/WAF-D-14-00026.1.

Snyder, J. C., H. B. Bluestein, V. Venkatesh, and S. J. Frasier, 2013: Observations of polarimetric signatures in supercells by an X-band mobile Doppler radar. *Mon. Wea. Rev.*, **141,** 3-29, https://doi.org/10.1175/MWR-D-12-00068.1.

Snyder, J. C., H. B. Bluestein, G. Zhang, and S. J. Frasier, 2010: Attenuation correction and hydrometeor classification of high-resolution, X-band, dual-polarized mobile radar measurements in severe convective storms. *J. Atmos. Oceanic Technol.*, **27,** 1979-2001, https://doi.org/10.1175/2010JTECHA1356.1.

Tanamachi, R. L., H. B. Bluestein, J. B. Houser, S. J. Frasier, and K. M. Hardwick, 2012: Mobile, X-band, polarimetric Doppler radar observations of the 4 May 2007 Greensburg, Kansas, tornadic supercell. *Mon. Wea. Rev.*, **140,** 2103-2125, https://doi.org/10.1175/MWR-D-11-00142.1.

Tanamachi, R. L., H. B. Bluestein, W. C. Lee, M. Bell, and A. Pazmany, 2007: Ground-Based Velocity Track Display (GBVTD) analysis of W-band Doppler radar data in a Tornado near Stockton, Kansas, on 15 May 1999. *Mon. Wea. Rev.*, **135,** 783-800, https://doi.org/10.1175/MWR3325.1.

Tanamachi, R. L., L. J. Wicker, D. C. Dowell, H. B. Bluestein, D. T. Dawson II, and M. Xue, 2013: EnKF assimilation of high-resolution, mobile Doppler radar data of the 4 May 2007 Greensburg, Kansas, supercell into a numerical cloud model. *Mon. Wea. Rev.*, **141,** 625-648, https://doi.org/10.1175/MWR-D-12-00099.1.

Trapp, R. J., G. J. Stumpf, and K. L. Manross, 2005: A reassessment of the percentage of tornadic mesocyclones. *Wea. Forecasting*, **20,** 680-687, https://doi.org/10.1175/WAF864.1.

Wakimoto, R. M. and Coauthors, 2016: Aerial damage survey of the 2013 El Reno tornado combined with mobile radar data. *Mon. Wea. Rev.*, **144,** 1749-1776, https://doi.org/10.1175/MWR-D-15-0367.1.

Wakimoto, R. M., N. T. Atkins, K. M. Butler, H. B. Bluestein, K. Thiem, J. C. Snyder, and J. L. Houser, 2015: Photogrammetric analysis of the 2013 El Reno tornado combined with mobile X-band polarimetric radar data. *Mon. Wea. Rev.*, **143,** 2657-2683, https://doi.org/10.1175/MWR-D-15-0034.1.

Wakimoto, R. M., N. T. Atkins, and J. Wurman, 2011: The LaGrange tornado during VORTEX2. Part I: Photogrammetric analysis of the tornado combined with single-Doppler radar data. *Mon. Wea. Rev.*, **139,** 2233-2258, https://doi.org/10.1175/2010MWR3568.1.

Wakimoto, R. M., P. Stauffer, W. C. Lee, N. T. Atkins, and J, Wurman, 2012: Finescale structure of the LaGrange, Wyoming, tornado during VORTEX2: GBVTD and photogrammetric analyses. *Mon. Wea. Rev.*, **140,** 3397-3418, https://doi.org/10.1175/MWR-D-12-00036.1.

Wakimoto, R. M., Z. Wienhoff, H. B. Bluestein, D. J. Bodine, and J. M. Kurdzo, 2020: Mobile radar observations of the evolving debris field compared with a damage survey of the Shawnee, Oklahoma, tornado of 19 May 2013. *Mon. Wea. Rev.*, **148,** 1779-1803, https://doi.org/10.1175/MWR-D-19-0215.1.

Wienhoff, Z. B., H. B. Bluestein, D. W. Reif, R. M. Wakimoto, L. J. Wicker, and J. M. Kurdzo, 2020: Analysis of debris signature characteristics and evolution in the 24 May 2016 Dodge City, Kansas, tornadoes. *Mon. Wea. Rev.*, **148,** 5063-5086, https://doi.org/10.1175/MWR-D-20-0162.1.

Wurman, J., 2002: The multiple-vortex structure of a tornado. *Wea. Forecasting*, **17,** 473-505, https://doi.org/10.1175/1520-0434(2002)017%3C0473:TMVSOA%3E2.0.CO;2.

Wurman, J., C. Alexander, P. Robinson, and Y. Richardson, 2007a: Low-level winds in tornadoes and potential catastrophic tornado impacts in urban areas. *Bull. Amer. Meteor. Soc.*, **88,** 31-46, https://doi.org/10.1175/BAMS-88-1-31.

Wurman, J., and S. Gill, 2000: Finescale radar observations of the Dimmitt, Texas (2 June 1995), tornado. *Mon. Wea. Rev.*, **128,** 2135-2164, https://doi.org/10.1175/1520-0493(2000)128%3C2135:FROOTD%3E2.0.CO;2.

Wurman, J., and K. Kosiba, 2013: Finescale radar observations of tornado and mesocyclone structures. *Wea. Forecasting*, **28,** 1157-1174, https://doi.org/10.1175/WAF-D-12-00127.1.

Wurman, J., K. Kosiba, P. Markowski, Y. Richardson, D. Dowell, and P. Robinson, 2010: Finescale single- and dual-Doppler analysis of tornado intensification, maintenance, and dissipation in the Orleans, Nebraska, supercell. *Mon. Wea. Rev.*, **138,** 4439-4455, https://doi.org/10.1175/2010MWR3330.1.

Wurman, J., K. Kosiba, P. Robinson, and T. Marshall, 2014: The role of multiple-vortex tornado structure in causing storm researcher fatalities. *Bull. Amer. Meteor. Soc.*, **95,** 31-45, https://doi.org/10.1175/BAMS-D-13-00221.1.

Wurman, J., Y. Richardson, C. Alexander, S. Weygandt, and P. F. Zhang, 2007b: Dual-Doppler and single-Doppler analysis of a tornadic storm undergoing mergers and repeated tornadogenesis. *Mon. Wea. Rev.*, **135,** 736-758, https://doi.org/10.1175/MWR3276.1.

Wurman, J., J. Straka, E. Rasmussen, M. Randall, and A. Zahrai, 1997: Design and deployment of a portable, pencil-beam, pulsed, 3-cm Doppler radar. *J. Atmos. Oceanic Technol.*, **14,** 1502-1512, https://doi.org/10.1175/1520-0426(1997)014%3C1502:DADOAP%3E2.0.CO;2.

Zrnic, D. S., and A. V. Ryzhkov, 1999: Polarimetry for weather surveillance radars. *Bull. Amer. Meteor. Soc.*, **80,** 389-406, https://doi.org/10.1175/1520-0477(1999)080%3C0389:PFWSR%3E2.0.CO;2.